Interfacial Energy Transfer in Small Hydrocarbon Collisions with Organic Surfaces and the Decomposition of Chemical Warfare Agent Simulants within Metal-Organic Frameworks

Guanyu Wang

Thesis submitted to the faculty of Virginia Polytechnic Institute and State University
in partial fulfillment of the requirements for the degree of

Doctor of Philosophy
in
Chemistry

John R. Morris, Chair
Alan R. Esker
Brian M. Tissue
Diego Troya

February 2019
Blacksburg, VA

Keywords: Self-assembled monolayer, Molecular beam, Ultra-high vacuum, Energy transfer, Nerve agent simulant, Metal organic framework

Interfacial Energy Transfer in Small Hydrocarbon Collisions with Organic Surfaces and the Decomposition of Chemical Warfare Agent Simulants within Metal-Organic Frameworks

Guanyu Wang

Abstract

A molecular-level understanding of gas-surface energy exchange and reaction mechanisms will aid in the prediction of the environmental fate of pollutants and enable advances toward catalysts for the decomposition of toxic compounds. To this end, molecular beam scattering experiments performed in an ultra-high vacuum environment have provided key insights into the initial collision and outcome of critical interfacial processes on model systems.

Results from these surface science experiments show that, upon gas-surface collisions, energy transfer depends, in subtle ways, on both the properties of the gas molecules and surfaces. Specifically, model organic surfaces, comprised of long-chain methyl- and hydroxyl-terminated self-assembled monolayers (SAMs) have been employed to test how an interfacial hydrogen bonding network may affect the ability of a gas-phase compound to thermally accommodate (typically, the first step in a reaction) with the surfaces. Results indeed show that small organic compounds transfer less energy to the interconnected hydroxyl-terminated SAM (OH-SAM) than to the organic surface with methyl groups at the interface. However, the dynamics also appear to depend on the polarizability of the impinging gas-phase molecule. The π electrons in the double bond of ethene (C_2H_4) and the triple bond in ethyne (C_2H_2) appear to act as hydrogen bond acceptors when the molecules collide with the OH-SAM. The molecular beam scattering studies have demonstrated that these weak attractive forces facilitate energy transfer. A positive correlation between energy transfer and solubilities for analogous solute-solvent combinations

was observed for the CH_3-SAM (TD fractions: $C_2H_6 > C_2H_4 > C_2H_2$), but not for the OH-SAM (TD fractions: $C_2H_6 > C_2H_2 > C_2H_4$). The extent of energy transfer between ethane, ethene, and ethyne and the CH_3-SAM appears to be determined by the degrees of freedom or rigidity of the impinging compound, while gas-surface attractive forces play a more decisive role in controlling the scattering dynamics at the OH-SAM.

Beyond fundamental studies of energy transfer, this thesis provides detailed surface-science-based studies of the mechanisms involved in the uptake and decomposition of chemical warfare agent (CWA) simulants on or within metal-organic frameworks (MOFs). The work presented here represents the first such study reported in with traditional surface-science based methods have been applied to the study of MOF chemistry. The mechanism and kinetics of interactions between dimethyl methylphosphonate (DMMP) or dimethyl chlorophosphate (DMCP), key CWA simulants, and Zr_6-based metal-organic frameworks (MOFs) have been investigated with *in situ* infrared spectroscopy (IR), X-ray photoelectron spectroscopy (XPS), powder X-ray diffraction (PXRD), and DFT calculations. DMMP and DMCP were found to adsorb molecularly (physisorption) to the MOFs through the formation of hydrogen bonds between the phosphoryl oxygen and the free hydroxyl groups associated with Zr_6 nodes or dangling -COH groups on the surface of crystallites. Unlike UiO-66, the infrared spectra for UiO-67 and MOF-808, recorded during DMMP exposure, suggest that uptake occurs through both physisorption and chemisorption. The XPS spectra of MOF-808 zirconium *3d* electrons reveal a charge redistribution following exposure to DMMP. Besides, the analysis of the phosphorus *2p* electrons following exposure and thermal annealing to 600 K indicates that two types of stable phosphorus-containing species exist within the MOF. DFT calculations (performed by Professor Troya at Virginia Tech), were used to guide the IR band assignments and to help interpret the XPS features, suggest that uptake is driven by nucleophilic addition of a surface OH group to DMMP with subsequent elimination of a methoxy substituent to form strongly bound methyl methylphosphonic acid (MMPA). With similar IR features of MOF-808 upon DMCP exposure, the reaction pathway of DMCP in Zr_6-MOFs may be similar to that for DMMP, but with the final product being methyl chlorophosphonic acid (elimination of the chlorine) or MMPA (elimination of a methoxy group). The rates of product formation upon DMMP exposure of the MOFs suggest that there are two distinct uptake processes. The rate constants for these processes were found to differ by approximately an order of magnitude. However, the rates of molecular uptake were found to be nearly identical to the rates of reaction, which strongly suggests that the reaction rates are diffusion limited. Overall, and perhaps most importantly, this research has demonstrated that the final products inhibit further reactions within the MOFs. The strongly bound products could not be thermally driven from the MOFs prior to the decomposition of the MOFs themselves. Therefore, new materials are needed before the ultimate goal of creating a catalyst for the air-based destruction of traditional chemical nerve agents is realized.

Interfacial Energy Transfer in Small Hydrocarbon Collisions with Organic Surfaces and the Decomposition of Chemical Warfare Agent Simulants within Metal-Organic Frameworks

Guanyu Wang

General Audience Abstract

A molecular-level understanding of gas-surface energy exchange and reaction mechanisms will aid in the prediction of the environmental fate of pollutants and enable advances toward catalysts for the decomposition of toxic compounds. Our gas-surface scattering experiments performed in an ultra-high vacuum environment have provided key insights into the outcome of critical interfacial processes on model systems. Results show that energy transfer upon gas-surface collisions depends on both the properties of the gas molecules and surfaces. Due to the formation of interfacial hydrogen bonding network in hydroxyl-terminated surface, the small organic compounds transfer less energy to it than to the organic surface with methyl groups at the interface. The dynamics also appear to depend on the properties of the impinging gas-phase molecule. The π electrons in the double bond of ethene and the triple bond in ethyne act as hydrogen bond acceptors when the molecules collide with the hydroxyl-terminated surface. The attractive forces facilitate energy transfer. A positive correlation between energy transfer and solubilities for analogous solute-solvent combinations was observed for the methyl-terminated surface, but not for the hydroxyl-terminated surface. The extent of energy transfer between ethane, ethene, and ethyne and the methyl-terminated surface appears to be determined by the degrees of freedom or rigidity of the gas, while gas-surface attractive forces play a more decisive role in controlling the scattering dynamics at the hydroxyl-terminated surface.

Furthermore, this thesis provides detailed surface-science-based studies of the mechanisms involved in the uptake and decomposition of chemical warfare agent (CWA) simulants on or within metal-organic frameworks (MOFs). Dimethyl methylphosphonate (DMMP) and dimethyl chlorophosphate (DMCP), key CWA simulants, physisorbed to the MOFs through the formation of hydrogen bonds between the phosphoryl oxygen and the free hydroxyl groups associated with inorganic nodes or dangling -COH groups on the surface of crystallites. The infrared spectra for UiO-67 and MOF-808 suggest that uptake occurs through both physisorption and chemisorption. The XPS spectra of MOF-808 zirconium *3d* electrons reveal a charge redistribution following exposure to DMMP. Besides, the analysis of the phosphorus *2p* electrons following exposure and thermal annealing to 600 K indicates that two types of stable phosphorus-containing species exist within the MOF. DFT calculations suggest that uptake is driven by nucleophilic addition of a surface OH group to DMMP with subsequent elimination of a methoxy substituent to form strongly bound methyl methylphosphonic acid (MMPA). With similar IR features of MOF-808 upon DMCP exposure, the reaction pathway of DMCP in MOFs may be similar to that for DMMP, but with the final product being methyl chlorophosphonic acid (elimination of the chlorine) or MMPA (elimination of a methoxy group). The rates of product formation suggest that there are two distinct uptake processes. The rate constants for these processes were found to be nearly identical to the rates of physisorption, which suggests that the reaction rates are diffusion limited. Overall, this research has demonstrated that the final products inhibit further reactions within the MOFs. The strongly bound products could not be thermally driven from the MOFs prior to the decomposition of the MOFs themselves. Therefore, new materials are needed before the ultimate goal of creating a catalyst for the air-based destruction of traditional chemical nerve agents is realized.

Acknowledgments

My completion of graduate school would not have been possible without the support of my family and friends.

First, I would like to thank my husband Guoming, for his love and encouragement. I know he has been and always will be there for me. I would like to thank my parents and my brother for their unconditional love and support in my life. They taught me how to persevere when the days are frustrating.

I would like to thank all Morris group members, past and present, notably Alec Wagner, Amanda Wilmsmeyer, Steve Burrows, Yafen Zhang, Joshua Abelard, Chikki Chan, Robert Chapleski, Angela Edwards, Cecilia Smith, Darren Driscoll, Conor Sharp, Tyler Grissom. Nathan Jones, Stacy Farley, Nicholas Sapienza, Graham Frazier, and Andrew Maynes. Thank you all for all your extensive help and making work in lab enjoyable. Thank you for being my second family. I would like to acknowledge Prof. Diego Troya for his advanced knowledge and expertise in theoretical chemistry that helped me tremendously in developing a deeper understanding of my research. I would like to thank my committee members, Prof. Brian Tissue and Prof. Alan Esker, for their encouragement and inspirations.

Finally, I would especially like to thank my advisor, Prof. John Morris. His intelligent leadership, patience, academic expertise, and dedication to science have always inspired me. I thank him for being both a superb teacher and a good friend, for encouraging me and keeping me motivated. He put faith in me even when I had doubts myself. In those overwhelming days, he believed in me, gave me confidence, and pushed me forward. I could never have asked for a better advisor. I am truly grateful for his tremendous help.

Table of Contents

List of Figures

List of Tables

Index of Acronyms

BDC	1,4-Benzenedicarboxylate
BPDC	4,4' Biphenyl-dicarboxylate
BTC	Benzene-1,3,5-tricarboxylate
CCW	Counterclockwise
CW	Clockwise
CWA	Chemical warfare agent
DFT	Density functional theory
DMCP	Dimethyl chlorophosphate
DMMP	Dimethyl methylphosphonate
FTIR	Fourier transform infrared
FWHM	Full width at half maximum
IMPA	Isopropyl methyl phosphonic acid
IR	Infrared
IS	Impulsive scattering
LD	Lethal dose
MB	Molecular beam

MCS	Multichannel scaler
MCT	Mercury-cadmium-telluride
MMPA	Methyl methylphosphonic acid
MPA	Methylphosphonic acid
MPFA	Methyl phosphonofluoridic acid
MOF	Metal organic framework
OP	Organophosphorus
PES	Potential energy surface
PXRD	Powder X-Ray Diffractometer
QMS	Quadrupole mass spectrometer
RAIRS	Reflection Absorption Infrared Spectroscopy
RGA	Residual gas analyzer
SAM	Self-assembled monolayer
SBU	Secondary building unit
TD	Thermal desorption
TOF	Time of flight
UHP	Ultrahigh purity

UHV	Ultrahigh vacuum
XPS	X-ray photoelectron spectroscopy/spectrometer

Chapter 1 Introduction and Motivation

Thesis Statement

Molecular-beam surface science based experimental methods have been directed at developing a fundamental understanding of gas-surface interactions to help predict the fate of atmospheric organic pollutants and to reveal the limitations of new materials designed for use as air-based catalysts for the decomposition of chemical warfare agents.

1.1 Gas-Surface Energy Exchange at Organic Surfaces

1.1.1 Overview

The goal of developing a complete description of gas-surface interactions has driven the development of new experimental and computational methods for decades. Interactions and reactions between gases and surfaces not only play an essential role in the maintenance of the atmospheric balance and the control of air pollutant concentrations, but also have significant practical applications in catalysis, material science, and astrochemistry.[1-14] As such, progress toward the objective of developing a mechanistic understanding of important gas-surface interactions will benefit wide-ranging fields from atmospheric sciences to commodity chemical production.

In the real world, surfaces of materials are bombarded continuously by atmospheric gases that impinge at random impact angles and with a thermal distribution of translational energies. Further, the surfaces of materials are highly heterogeneous in terms of structure and chemical functionality. A systematic study of gas-surface reaction dynamics requires model systems that offer control over the chemical and physical properties of the system. As shown in Figure 1.1, in my experiments, molecular beams (MBs) and self-assembled monolayers (SAMs) model the impinging gas and the surface, respectively.

Molecular beam methods are widely employed in the research of gas-surface interactions. A molecular beam is created by expanding gas of interest into a vacuum chamber through a small aperture. After the expansion, a steady stream of gas molecules is formed. This gas stream has a well-defined cross sectional area, unified direction, and well characterized average translational energy. Molecular beams help ensure the gas source used in the experiments is well defined.

Self-assembled monolayers are highly ordered, well-characterized and highly reproducible thin layers. They are commonly used as models of organic surfaces in many types of interfacial studies.[15-17]

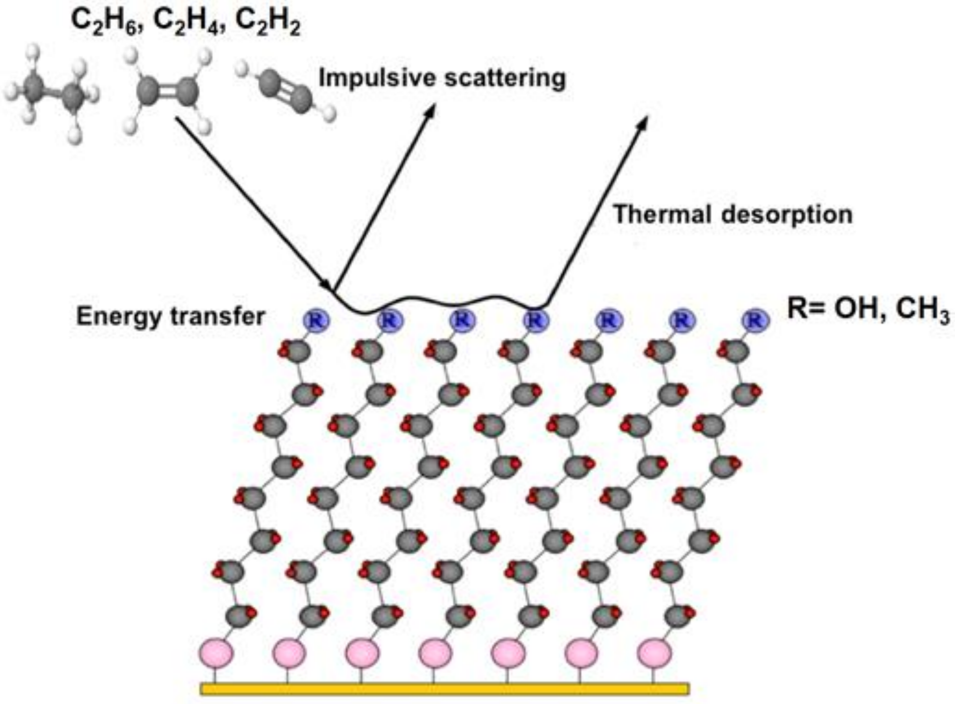

Figure 1.1 Schematic representation of the systems under investigation.

The combination of MBs and SAMs is the foundation of the research presented in the first portion of this thesis. By applying MBs and SAMs, the complex situation (uncharacterized gas molecules and complicated surfaces) is simplified, which affords one the ability to study how surface and gas properties affect the interactions systematically.

The experiments are performed by directing a molecular beam, composed of the compound of interest, at a SAM that contains a functional group of interest. Previous work showed that there are two possible non-reactive pathways for the incident gas molecules in the gas-surface interactions. One is referred to as "thermal desorption" (TD), and the other one is "impulsive scattering" (IS). The gas molecules may hit on the surface then directly recoil back to the gas phase without further interactions. These gas molecules are described as impulsively scattered molecules. On the other hand, before leaving the surface, the gas molecules that go through the thermal-desorption pathway first reach thermal equilibrium with the surface prior to evaporation back into the gas phase.

By using different gas sources and modifying the functionality of the SAMs, I am able to explore the influence of both gas-phase and surface properties on the outcome of the collision. I am particularly interested in how the surface functionality affects the energy transfer and thermal accommodation efficiency of small organic compounds. Further, small changes to the structure of the gas-phase molecule may also affect the outcome of the interfacial collision. I have investigated both aspects of this vital problem.

Overall, the research project presented in this thesis is aimed at developing a fundamental understanding of the dynamics of interactions between gases and surfaces. Small hydrocarbon molecules (ethane C_2H_6, ethene C_2H_4, and ethyne C_2H_2) and model organic surfaces (OH-terminated and CH_3-terminated SAMs) are employed as the gas sources and model surfaces, respectively, to help decipher factors that affect gas-surface energy exchange and thermal accommodation. Furthermore, my research may show correlations between gas-surface accommodation and bulk phase properties (solubility). Such correlations can be a powerful means of predicting the fate of other types of gas-surface collisions from well-known properties. Much more complex gas-materials interactions augment these fundamental studies on accommodation and energy exchange. I am particularly interested in extending the surface science experimental methods to the study of gas uptake and decomposition within metal-organic frameworks.

1.1.2 **Background**

1.1.2.1 Gas-Surface Interactions: the fundamentals

Interfacial collisions, as the first step of all gas-surface reactions, are one of the most critical factors that affect the equilibrium between gases and surface-adsorbates. Therefore, interfacial collisions and the subsequent interactions play essential roles in material degradation and the regulation of pollutant concentrations.[18,19] As such, a complete understanding of interfacial reactions requires studies into the dynamics of gas-surface interactions. Extensive experimental and theoretical investigations over the past century have shed light on key factors that affect gas-surface collision dynamics and energy transfer processes. [20-44] While many of these studies have explored interfacial collisions at metal and metal-oxide surfaces, the primary focus of this thesis is on exploring interactions between small gas-phase molecules and organic surfaces.

In some of the first research into this topic, Day et al. studied how surface functional groups on model organic surfaces affect the gas-surface energy transfer process.[45] In that work, comparisons of scattering dynamics of argon atoms from alkanethiol SAMs with varying terminal groups such as CH_3-SAMs, CH_2=-SAMs, OH-SAMs, and COOH-SAMs were made under identical experimental conditions. The results showed that the energy transfer between argon atoms and CH_3-SAMs is markedly more efficient than the energy transfer with the polar SAMs.[45] They concluded that this phenomenon is caused by the formation of intra-monolayer hydrogen bonds in the OH-SAMs and COOH-SAMs. Hydrogen bonds make the surface more rigid, which limits the energy transfer from gas molecules to the surface.

Further study of the terminal group effect is demonstrated in the work of Lu et al.[46] They studied the scattering of triatomic molecules on CH_3-SAMs, OH-SAMs, and CF_3-SAMs. Compared with the CH_3-SAM and OH-SAM, they found a significant decrease in the thermal accommodation efficiency for scattering from the CF_3-SAM. Apparently, the larger mass of the CF_3 terminal group results in higher rigidity and less efficient energy transfer.[46] Further, and in contrast to the argon scattering studies cited above, they did not observe a thermal accommodation difference for triatomic scattering from the CH_3-SAM versus the OH-SAM. Even though the OH-SAM is more rigid due to the formation of intra-monolayer hydrogen bonds, the attractive forces between the polar triatomic gas molecules (CO_2, O_3, and NO_2), and the OH-SAM were responsible for bringing more molecules into thermal equilibrium. Their work demonstrated that energy transfer depends on the properties of both the incident gas molecules and the surfaces.

Further research has been conducted to help unveil how the properties of gas molecules affect gas-surface interactions. As shown in the work of Alexander et al., changing the mass of incident gas molecules (Ne, Ar, and Kr) significantly varied the final scattering results.[47] The increase of molecular mass facilitated the transfer of energy and resulted in a higher thermal desorption fraction. This result can be explained by using the concept of momentum. The energy transfer in gas-surface interactions for a simple model can be approximated by equation (1). In equation (1), ΔE stands for the energy transferred from the gas molecules to the surface, it is defined as the difference between the incident energy and final energy of the gas molecules; μ is the mass ratio of gas molecule and surface terminal group, m_g/m_s; E is the incident energy.

$$\frac{\Delta E}{E} = \frac{4\mu}{(\mu + 1)^2} \qquad \textbf{(1)}$$

In gas-surface collisions, the effective mass of the surface (the mass of the surface segment that interacts with gas molecules) is necessarily higher than the mass of gas molecules. However, heavier gas molecules correspond to a smaller mass difference between the gas, and the surface. Equation (1) predicts that smaller mass differences lead to greater energy transfer. Therefore, under the same experimental conditions and neglecting gas-surface forces, the gas molecules with higher mass transfer more energy to the surface.

Further studies into how the properties of gases affect energy transfer have been performed by Saecker et al. [48] They focused on the study of interactions between polar or non-polar gas molecules and liquid organic surfaces. Their research demonstrated that the stronger the intermolecular forces (dipole-dipole interactions) between the gas molecules and the liquid surfaces are, the more efficient the energy transfer during the collision.

1.1.2.2 Impulsive Scattering and Thermal Desorption

As described above, the gas molecules that bounce on the surface once or multiple times, then recoil back into the gas phase without further interactions are considered as following the mechanism of impulsive scattering. These types of gas molecules only transfer part of their incident translational energy to the surface and retain the remainder. Alternatively, gas molecules may completely dissipate their excess incident translational energy to the surface through multiple collisions. At this point, they become thermally accommodated on the surface. Then, after gaining energy from thermal fluctuations of the surface, the molecules can desorb back into the gas phase. These thermally desorbed gas molecules maintain the same statistical energy distribution as the surface, which is the Boltzmann distribution at the surface temperature. An arbitrary potential energy surface of gas-surface interaction is provided in Figure 1.2.

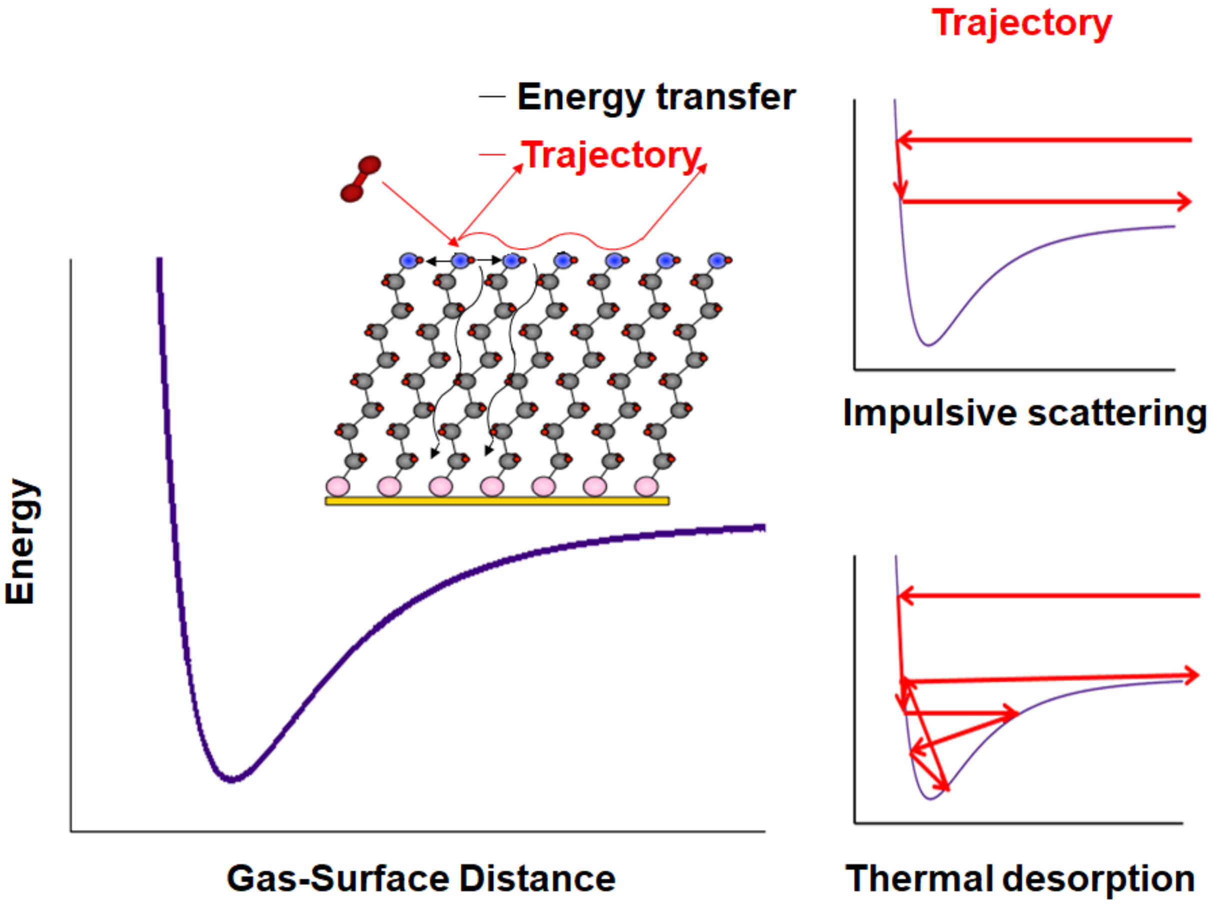

Figure 1.2 Arbitrary potential energy surface (PES) of gas-surface interaction.

The description above shows the general idea about IS and TD. The potential energy surface (PES) governs these two pathways. As a gas molecule approaches a surface, the molecule typically experiences attractive forces due to dispersive or dipolar interactions. The attractive energy well accelerates the gas molecule toward the surface. After the initial acceleration, the gas molecule experiences a potential energy wall due to highly repulsive interactions between the gas-surface electrons. Upon collision, the repulsive wall reflects the molecule back into the gas phase, but not before absorbing some fraction of the impinging energy (purely elastic scattering does not occur in these systems where a very high number of energy states at the surface are available for excitation). After the energy transfer process, the scattering gas molecules exit along the attractive tail of the potential energy surface. If the gas molecule only loses part of its initial translational energy to the surface, and the retained energy is higher than the potential well, it will be able to escape and return to the gas phase. This type of molecules is considered as going through the IS pathway. However, if a gas molecule loses all of its excess energy to the surface, then during this reflection, it will need to gain energy from the thermal fluctuations of the surface. Before desorption, when the gas molecule obtains enough energy, they will desorb into the gas phase with a Boltzmann distribution of energies at the surface temperature.

The probability of gas molecules to follow IS, and TD pathways ultimately determine the fate of the gas-surface interaction. Compared with gas molecules that go through IS pathway, the TD gas molecules lose more of their initial energy to the surface. The overall amount of energy transferred to a surface, the "energy transfer fraction," affects the overall trajectory and, ultimately, interfacial reactions.

The energy transfer fraction is represented by the Greek symbol alpha (α) and defined by equation (2).[45] In equation (2), E_i and E_f are the initial and final average translational energy of the gas molecules, respectively.

$$\alpha = \frac{E_i - E_f}{E_i} \qquad \textbf{(2)}$$

The energy transfer fraction is the difference between the initial and final translational energy per initial energy. As shown by equation (2), with specific initial energy, higher final energy corresponds to a lower energy transfer fraction.

1.1.3 **Gas-Surface Scattering Models**

Various methods including classical mechanics have successfully modeled the dynamics of gas-surface interactions.[49,50] By using classical models, the interaction processes can often be described by properties of the system that can be experimentally determined. Such models, once validated, enable predictions of the outcomes of gas-surface interactions.

1.1.3.1 Hard-Cube Model

After gas-surface scattering experiments emerged during the late 1960s,[51,52] a theory was needed to help interpret the scattering data. Therefore, Logan and Stickney[53] developed a model based on classical mechanics to fulfill the requirement at that time. This model is now known as the hard-cube model.

In this model, the gas molecules are treated as rigid spheres, and they impinge on the flat upper surface of a cube, which is also rigid. As shown in Figure 1.3, the momentum of the gas molecules in the direction that is parallel to the cube's surface is conserved throughout the interaction, $V_{pi}=V_{pf}$. The energy transfer is considered to occur in the normal direction with respect to the surface. Furthermore, the incident angle and final angle (θ_i and θ_f, respectively) are both defined for given surface temperature, T_{surf}, and the initial momenta of both the surface and the gas molecule. At this point, the only adjustable parameter is the mass ratio of the gas molecule and the surface. Hence, this enables the simplification of the original problem to a one-variable problem. As shown in equation (1), μ is this mass ratio with m_g as the mass of one gas molecule and m_{surf} as the effective surface mass.

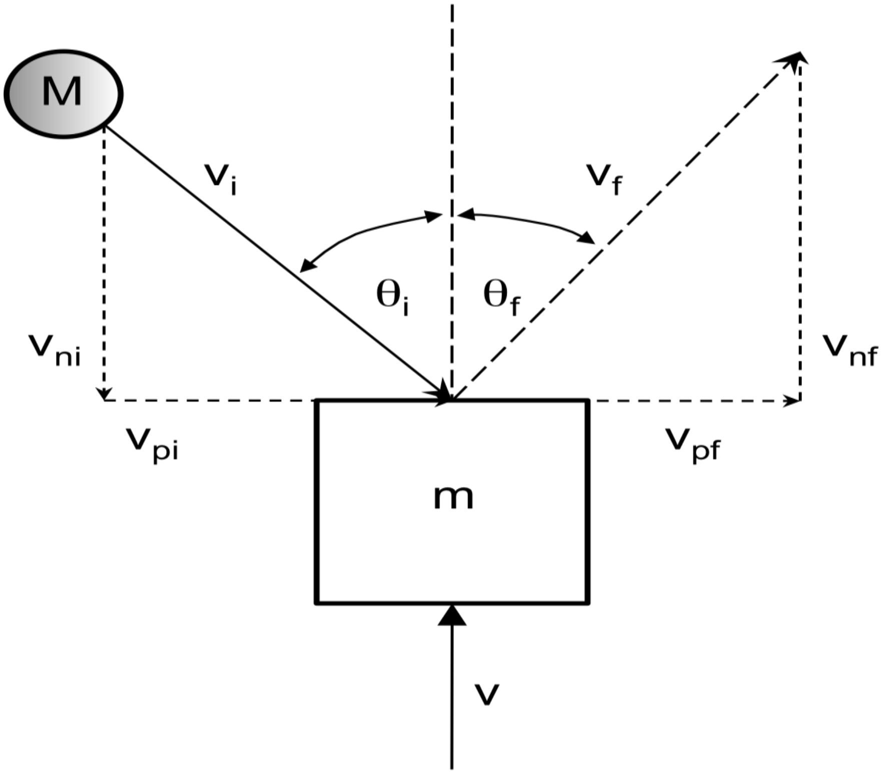

Figure 1.3 Schematic of the hard-cube model.[50]

The main accomplishment of this model is that it provides a direct conclusion: the energy transfer between gas molecules and solid surfaces are maximum when the mass of the gas molecules is equal to the mass of the surface site with which it collides (μ=1), see equation **(1)**. In scattering experiments, if one can probe the amount of energy transferred during the collision, one may be able to apply this result to help predict how many surface groups are involved in the interactions. Despite the rudimentary nature of this model, it provides a rough prediction of how the mass ratio of the gas and the surface affects energy transfer and has proved successful in limited cases.[53-54]

1.1.3.2 Soft-Cube Model

As an improvement to the hard-cube model, the soft-cube model includes additional aspects of the system. The soft-cube model was devised by Logan and Keck in 1968.[53] Instead of representing the surface as a vertical infinitely high potential energy surface. This model approximates the interaction as one composed of an initially attractive well followed by an exponentially repulsive component.[55]

As shown in Figure 1.4, in the soft-cube model, the cube is attached to a rigid wall through a linear spring. Therefore, rather than an isolated cube, this model simulates the solid-solid interactions that occur within the surface during the collision. Overall, this model simulates the interaction between an incident gas molecule and a one-dimensional cube oscillator with a frequency ω. When a gas molecule approaches the oscillator, it experiences the potential well illustrated by the box in the lower right side of Figure 1.4. The interaction between the gas molecule and the cube oscillator is initially attractive and then becomes exponentially repulsive. Thus, there are two adjustable parameters in this model in addition to μ–the oscillation frequency ω and the potential well depth D.

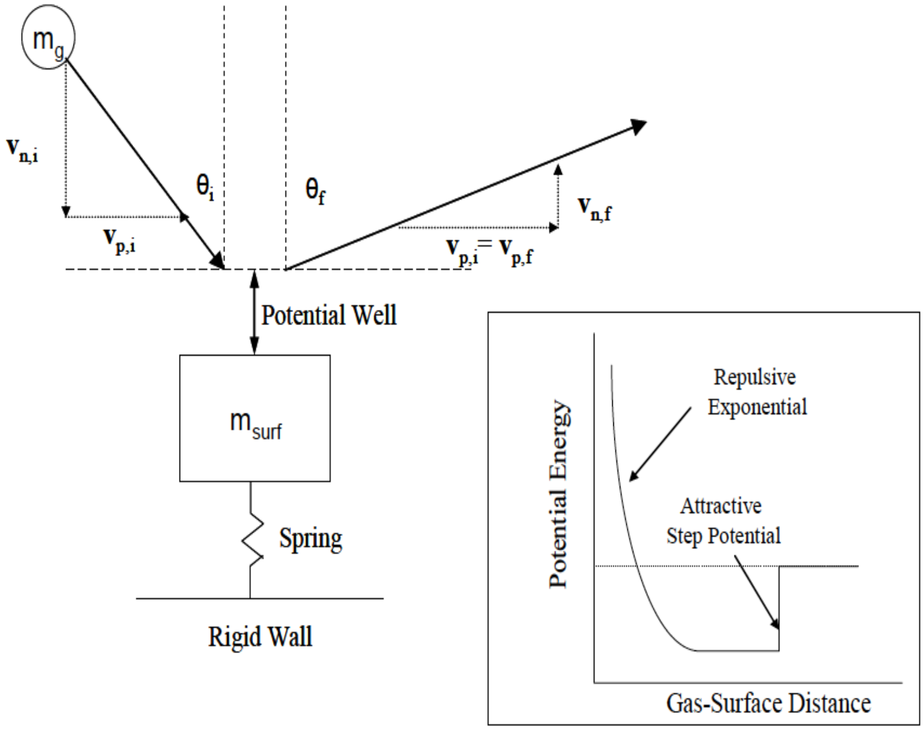

Figure 1.4 Schematic of the soft-cube model.[45]

1.1.3.3 Hard Sphere Model

Both the hard-cube and soft-cube models are built on the assumption that the surface behaves like a flat solid cube. However, that is not always an appropriate approximation. There are conditions under which a surface can be highly corrugated. For example, a gas molecule may only interact with an individual terminal functional group of the surface that protrudes into the gas phase. [18,56] In this case, the gas molecule and the surface are more likely to behave as two rigid spheres rather than a sphere and a flat surface. To model this type of gas-surface interaction, the hard sphere model was developed.

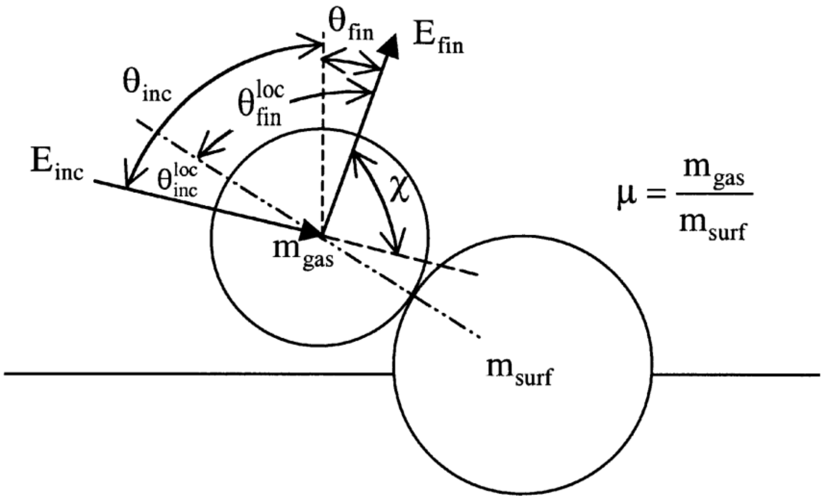

Figure 1.5 Schematic of hard sphere model.[56]

A schematic of the hard sphere model is provided in Figure 1.5. In this model, the calculation of the amount of energy transferred between gas molecules and surfaces is similar to the procedure demonstrated in the cube-models, as shown in equation (3). When a gas molecule of mass m_{gas} collides with a surface molecule of mass m_{surf} with an initial kinetic energy of E_{inc} at an angle of θ_{inc} with respect to the normal of the global surface plane, the energy transfer is directly related to the mass ratio and another parameter called deflection angle, χ. And the gas molecule after the collision will leave the surface molecule with a kinetic energy of E_{fin} at an angle of θ_{fin} with respect to the normal of the global surface plane. There is no potential well involved in the energy transfer equation for this model, so the collision between these two spheres is treated as being completely impulsive.

The definition of the deflection angle is $\chi = 180° - \theta_{i,loc} - \theta_{f,loc}$, with $\theta_{i,loc}$ and $\theta_{f,loc}$as the local approach and final angle with respect to the line of centers between the gas and the surface spheres. Equation (3) indicates that the energy transfer is maximized when χ equals 180° and minimized when χ is 0°. That is, based upon Figure 1.5, the energy transfer will be greatest when the two spheres undergo a head-on collision. When the collision is glancing, the energy transfer is the least efficient. This model has been successfully applied to the study of thermal roughening effects on the angular distribution of scattering in gas-liquid collisions by the Nathanson group.[57]

$$\frac{E_{inc} - E_{fin}}{E_{inc}} = \frac{2\mu}{(1+\mu)^2}\left[1 - \cos\chi(1 - \mu^2 sin^2\chi)^{1/2} + \mu sin^2\chi\right] \tag{3}$$

1.1.3.4 Washboard Model

Developed by Tully,[58] the washboard model is another extension of the classical hard-cube model. However, this model accounts for the corrugation of the surface.

To simulate the corrugation of the surface, the impact interface is modeled as a cosine wave. As illustrated by Figure 1.6, the flat surface of the cube is defined by the local incident and final angle; the tangential momentum is conserved with respect to the local normal but depends as for the global normal. The cosine-wave shape of the surface is defined by equation (4), where a represents for the lattice spacing for a repeated united of the surface structure, x is the position of the impact site, and A is the amplitude that determines the strength of surface corrugation. This cosine-wave function, $Z(x)$ represents for the location of the interaction hard wall in this model.

$$Z(x) = A\cos\left(\frac{2\pi x}{a}\right) \tag{4}$$

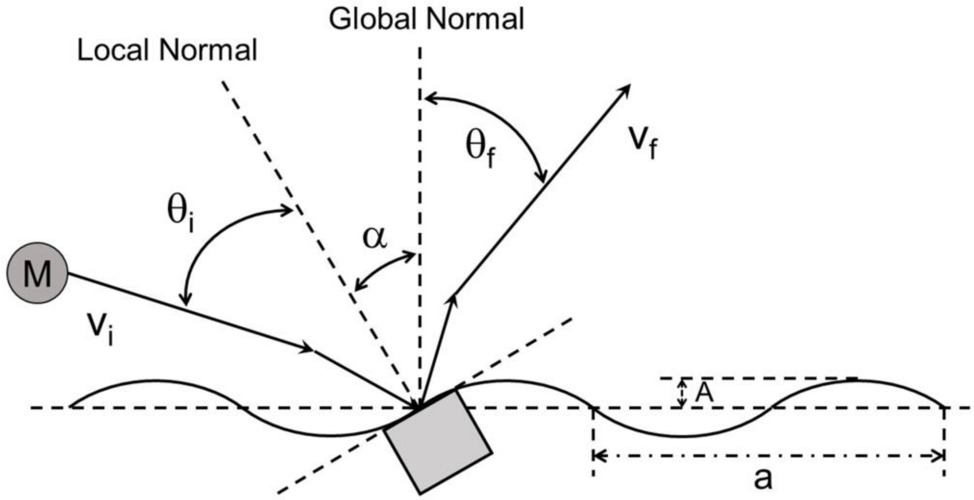

Figure 1.6 The schematic of the washboard model.[59,58, 60]

Once the incident gas molecule crosses a defined point, its direction may change due to the existence of a potential well. Within the washboard model, three parameters affect energy transfer. They are the mass ratio (μ), the potential well depth (D), and a parameter called the "corrugation strength parameter" (α_m). As shown in equation (5), the definition of this parameter is the maximum obtainable angle between the local surface normal and the global surface normal.

$$\alpha_m = \tan^{-1}\left(\frac{2\pi A}{a}\right) \tag{5}$$

To apply the washboard model to the analysis of experimental scattering results, other parameters must be defined. These parameters are the momentum distribution of the surface, surface temperature, and the incident angle of the gas molecules. Even though it is an obvious oversimplification to simulate a corrugated surface as a cosine wave, this model has demonstrated that surface roughness and corrugation are essential for the modeling of gas-surface interactions. For example, by applying the washboard model, Kondo et al. studied the effect of molecular structure on gas-surface scattering,[61] and Yan et al. further developed a washboard model that takes the surface moment of inertia into account. By employing this model, they successfully modeled Ar and Ne scattering from an alkylthiolate self-assembled monolayer surface and reproduced the major results obtained by classical trajectory simulation of the same system.[59]

The models described above provide helpful qualitative, and in some case quantitative, information about how properties (collision energy, approach angle, well depth, bond rigidity, mass) affect energy exchange in the initial gas-surface collisions. Following the initial impact, intermolecular forces dominate the fate of the molecule. Others have shown that the gas-organic surface intermolecular forces may be predicted to some extent by the relative solubilities of gases in liquids composed of organic molecules that mirror the properties of the compounds present at the surface. Therefore, the next section reviews the solubilities of the organic gases in a variety of liquid phases, which will provide an essential context within which to discuss thermalization probabilities and scattering characteristics in subsequent chapters.

1.1.4 C_2H_6, C_2H_4, and C_2H_2 Interactions with Liquids

Solubility is a property related to the extent to which a solid, liquid or gaseous chemical (solute) dissolves into another solid, liquid or gaseous phase (solvent) to form a homogeneous solution. The value of solubility is commonly used to indicate the extent to which a solute can dissolve into a unit amount (volume or mass) of solvent. As such, the solubility of a substance depends upon the physical and chemical properties of both the solute and the solvent. Other than factors like pressure, temperature, and pH, the intermolecular force is also one of the most important factors that affect the solubility.

Intermolecular forces are attractive and repulsive forces between neighboring particles and are electrostatic in nature. Even though intermolecular forces are not as strong as intramolecular forces such as covalent bonds, they are still quite critical for atomic level and molecular level interactions. There are several types of intermolecular forces, such as dipole-dipole forces, hydrogen bonds, ion-dipole forces, and London dispersion forces.

Dipole-dipole forces only exist between molecules that possess permanent dipole moments. This type of force is an electrostatic force that tends to align the molecules to maximize the attraction. Dipole-dipole interactions are the strongest intermolecular force of attraction for neutral species. Consider two polar molecules interacting with each other, the potential energy possessed by the system depends upon the dipole moment, μ, of each molecule and the separation, according to equation (6),[62] where ε is the permeability of space.

$$V = -\frac{2\mu_1\mu_2}{4\pi\varepsilon_0\gamma^3} \tag{6}$$

One typical example of dipole-dipole interactions is the formation of hydrogen bonds. This is a special kind of dipole-dipole interaction that occurs specifically between a hydrogen atom attracted to an electronegative atom, such as oxygen, nitrogen, and halogen atoms, and groups with excess electron density. Hydrogen bonding is a relatively strong force of attraction between molecules, and considerable energy is required to break hydrogen bonds (a typical hydrogen bond is about 20 kJ/mol). Hydrogen bonds are often cited as the strongest type of dipole-dipole interaction.

Ion-dipole forces are interactions between ions and molecules with dipole moments. Moreover, the charge of an ion can also distort a non-polar molecule to form an induced dipole moment in this molecule. In this case, the interactions are described as ion-induced dipole moment interactions. The energies of both an ion-permanent dipole interaction and an ion-induced dipole interaction are inversely proportional to the fifth power of the distance ($1/r^5$).[63]

Beyond the types of interactions that involve dipolar molecules, weak interactions caused by instantaneous fluctuations in the electron density of a molecule also play a significant role in solubility (and gas-surface interactions). In 1930, Fritz London (1900–1954) established the foundation of intermolecular forces between nonpolar molecules. London proposed that temporary fluctuations in the electron distributions within atoms and nonpolar molecules could result in the formation of short-lived instantaneous dipole moments, which produce attractive forces called London dispersion forces between otherwise nonpolar substances.[64] London dispersion energies are also proportional to the inverse sixth power of the distance.

The balance of intermolecular forces does not only play an important role in the determination of solute solubility in a specific solvent, but they also are the key factor in determining the fate of gas-surface collisions. One of the primary thrusts of this work is to build an understanding of the energy transfer and thermal accommodation for small organic compounds on organic surfaces that contain polar and non-polar functional groups. I am particularly interested in whether the same properties that control the uptake of these gases in liquids (as predicted by their solubilities) can be used to predict the outcome of gas-solid collisions. Thus, water and *n*-hexane are used as examples for polar and nonpolar solvents, respectively. The solubilities of C_2H_6, C_2H_4, C_2H_2 in both water and *n*-hexane at room temperature and atmospheric pressure are shown in Table 1.1.

The solubility data shows that, while the three gas molecules have similar solubilities in hexane, their solubilities in water differ by orders magnitude. This interesting observation can be explained by the differences in the intermolecular forces between the molecules and the condensed solvent. The interactions between the non-polar gas molecules and *n*-hexane, which is also non-polar, are mainly induced dipole-induced dipole interactions (London-dispersion forces). For the three gas molecules, the polarizability increases in the order of $C_2H_2<C_2H_4<C_2H_6$. The magnitude of the induced dipole increases with polarizability. Thus, the solubility of the compounds in *n*-hexane decreases in the order predicted by the polarizability of each compound $C_2H_6 > C_2H_4 > C_2H_2$. However, with water as the solvent, the primary interactions between the gas molecules and the solvent are electrostatic in nature. The specific attractive forces are governed by interactions between the π electrons and the polar O-H bonds of water. The high electron density in C_2H_4 and C_2H_2 makes them good electron donators for the formation of hydrogen bonding with water molecules. So the solubilities of C_2H_4 and C_2H_2 in water are much higher than the solubility of C_2H_6, and the solubility of C_2H_2 is higher than C_2H_4.

Table 1.1 Properties C_2H_6, C_2H_4, and C_2H_2.[65]

Gas	C_2H_6	C_2H_4	C_2H_2
Solubility in water (×10^{-3} mole fraction)	0.0362	55.1	251
Solubility in hexane (×10^{-3} mole fraction)	32.0	20.5	13.0
Mass (g/mol)	30	28	26
C-C bond order	1 (1 σ)	2 (1σ, 1π)	3 (1σ, 2π)
C-C Bond length (Å)	1.54	1.35	1.21
C-C Bond strength (kcal/mol)	83	125	230
Polarizability(10^{-40} Cm^2/V)	5.00-5.06	4.69-4.76	3.74-3.94
pKa	>51	44	25

Conceptually, a deeper potential well is beneficial for more efficient gas-surface energy transfer. However, these concepts have yet to be systematically tested for small organic compounds colliding with organic surfaces. I hypothesize that the dynamics of small non-polar hydrocarbon collisions on organic surfaces will depend on the polarizability of the colliding species and the surface functional group located precisely at the interface. This hypothesis will be tested by studying the energy transfer efficiency in the scattering of C_2H_2, C_2H_4, and C_2H_6 molecules on CH_3-terminated organic surfaces. Ultimately, this research will explore whether the same properties that affect bulk-phase solubility can be employed to predict the accommodation efficiency of gases at solid organic surfaces.

1.2 Chemical Warfare Agents, Simulants, and MOFs

While the studies described above will probe the nature of gas-surface collisions, energy transfer, and accommodation efficiency from a highly fundamental perspective, my more recent studies have focused on the more practical application of surface science to the study of materials that may sequester and decompose chemical warfare agents (CWAs). Here, the motivation for this next stage of work is provided, as well as an introduction to the key scientific questions we aim to probe with this new research.

1.2.1 Background

The threat of CWAs, assured by their ease of synthesis and effectiveness as a terrorizing weapon, will persist long after the once-tremendous stockpiles in the U.S. and elsewhere are finally destroyed.[66-68] Therefore, there exists a pressing and continual need for strategies capable of combatting these weapons. Soldier and civilian protection, battlefield decontamination, and environmental remediation from CWAs remain top military priorities. Therefore, new chemical approaches for the fast and complete destruction of CWAs has been an active field of research for many decades and new technologies, highlighted recently in prominent research journals, have generated immense interest.[69-75] In particular, Zr_6-based metal-organic frameworks (MOFs) have been shown to be active for catalyzing the rapid hydrolysis of chemical warfare nerve agents.[76-82]

1.2.2 Nerve Agents and Simulants

The first nerve agents were invented by accident in the 1930s when the German researchers were attempting to develop alternatives to common insecticides.[83] The working mechanism of nerve agents is to disable the enzyme, acetylcholinesterase ultimately. Acetylcholinesterase is responsible for removing acetylcholine, which is used to send messages between cells to maintain a functional nervous system. Nerve agents can perform as irreversible acetylcholinesterase inhibitors, and therefore disrupt the central nervous system. Nerve agents can be absorbed through inhalation or skin contact.

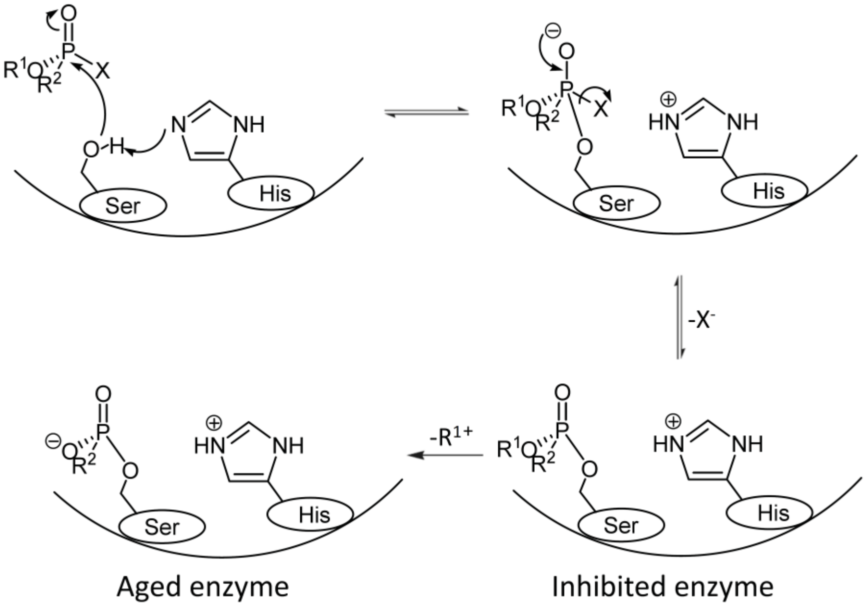

Figure 1.7 Pathway for organophosphonate nerve agent inhibition of acetylcholinesterase through irreversible binding at the serine residue.[84-85]

As shown in Figure 1.7, once in contact with the human body, the nerve agents can bind to a serine residue at the active site of the cholinesterase enzyme. The phosphorylated enzyme may then lose an alkylic carbonium ion through the cleavage of the PO-C bond. At this point, the enzyme is irreversibly inhibited. Because the agent blocks the active site, acetylcholine no longer binds to the enzyme, and acetylcholine accumulates in the human body. With the first symptoms appearing in seconds after acute exposure, elevated acetylcholine levels first cause miosis and rhinorrhea, then tremor, respiratory difficulty, and finally death.[86]

There are two major classes of nerve agents, G-series and V-series. The members of these two classes share similar properties. My studies focus on the surface chemistry of the G-series of CWAs. Common G-series nerve agents are given both a common name (such as sarin) and a two-character NATO identifier (such as GB). The chemical structures of the G-series nerve agents are shown in Figure 1.8.

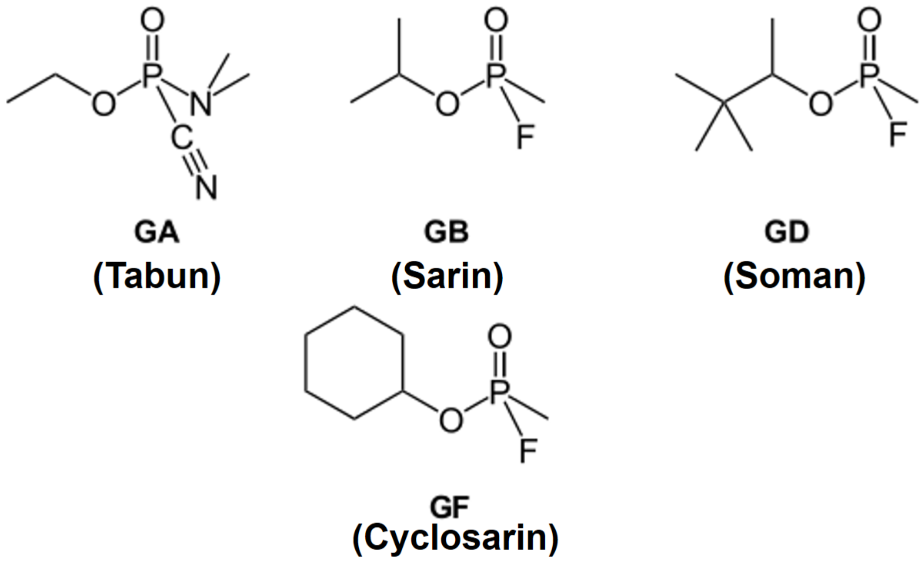

Figure 1.8 Chemical structures of the G-series nerve agents.

Nerve agents are organophosphonate compounds with the phosphorus atom bound to a hydrocarbon group. They share similar chemical and physical properties. At room temperature, common nerve agents are volatile, colorless and viscous liquids. The difficulty in distinguishing them from regular non-toxic liquids makes them even more dangerous. The physical properties of the nerve agents shown in Figure 1.8 are provided in Table 1.2.

Table 1.2 Physical properties and LD_{50} of nerve agents[86-91] (LD_{50}: the dose required to kill half the members of a tested population after a specified test duration)

Nerve Agent	Vapor Pressure (torr)	Melting Point (°C)	Boiling Point (°C)	Molecular Weight (g/mol)	LD_{50} (mg/70kg person)
GA (Tabun)	0.07 (25.0 °C)	-50	248	162.1	4000
GB (Sarin)	2.9 (25.0 °C)	-56	158	140.1	1700
GD (Soman)	0.40 (25.0 °C)	-42	198	182.2	300
GF (Cyclosarin)	0.06 (25.0 °C)	-30	239	180.2	150

Because of their tremendous toxicity, the "live" CWAs are seldom directly studied in laboratory settings; rather, surrogates of the nerve agents, or "simulants" have been developed for use in academic studies. Simulants are molecules that maintain the same bond of interest with the live nerve agents, possess similar physical and chemical properties, but with much less toxicity due to their inability of binding to the acetylcholinesterase. Although simulants do not exactly reproduce each live agent property, the simulants can be used to mimic particular functional groups. Studies then strive to construct a relationship between the molecular structure and chemical functionality in an effort to predict how the live agents will behave under specific circumstances. The simulants used in the research presented here are dimethyl methylphosphonate (DMMP) and dimethyl chlorophosphate (DMCP). The chemical structures of these two compounds are shown in Figure 1.9. Moreover, the comparison of their physical properties with sarin can be found in Table 1.3.

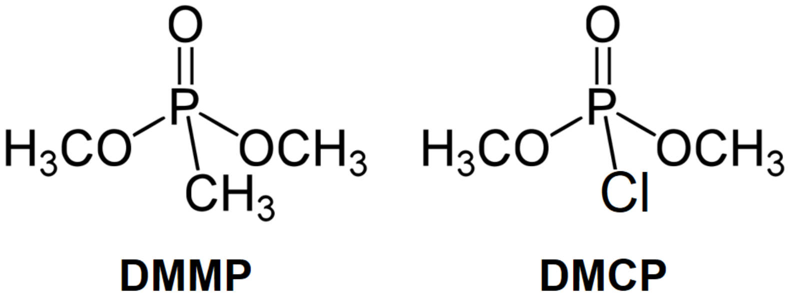

Figure 1.9 Chemical structures of nerve agent simulants.

Table 1.3 Physical properties and LD_{50} of sarin and nerve agent simlulants[89, 92]

Nerve Agent/Simulants	Vapor Pressure (torr) (at 25.0 °C)	Melting Point (°C)	Boiling Point (°C)	Molecular Weight (g/mol)	LD_{50} (mg/kg) (rat)
GB (Sarin)	2.9	-56	158	140.1	0.55
DMMP	0.96	-50	181	124.1	8210
DMCP	-	-	80	144.5	-

1.2.3 Metal Organic Frameworks (MOFs)

MOFs are a relatively new class of hybrid organic-inorganic materials with high porosity, chemical tenability, tailorable pore environments, and extraordinarily large surface areas.[93-97] Some of the most thermal and chemically stable MOFs are constructed from Zr_6-based nodes linked together by carboxylate-terminated struts.

The most well-studied example is UiO-66, which consists of $Zr_6(O)_4(OH)_4$ nodes and benzene dicarboxylate linkers.[98] The node connectivity and structure of UiO-66 is illustrated in Figure 1.10. UiO-66 exhibits two pore environments: octahedral cavities composed of six inorganic nodes, and smaller tetrahedral cavities with four nodes. In the pristine MOF, four bridging hydroxyl groups are located at the corners of the tetrahedral cavities. Also, a small fraction of terminal hydroxyl groups is likely to present at under-coordinated zirconium sites (defects). Transport through the pores of UiO-66 requires movement through the small triangular windows at the cavity walls. As described in a recent publication from our group indicated this MOF has been shown to be stable up to 500 °C, as well as in a variety of organic solvents, acidic solutions, and basic media.[99-100] Furthermore, UiO-66 catalyzes the hydrolysis of organophosphorus (OP) nerve agents and nerve agent simulants in basic solutions.[77] The catalytic activity of UiO-66 was attributed to the strongly acidic Zr^{IV} ions that are key for the activation of coordinated OP compounds.[97]

Following the demonstration of UiO-66 as a catalyst for CWA decomposition, a variety of other Zr_6-based MOFs emerged with much greater turnover frequencies for OP compound hydrolysis. Researchers speculated that the small, 6 Å, pore apertures of UiO-66 (the product of 12 short linkers per node) limit access to the active centers and thus catalysis occurs almost exclusively on the external surface of UiO-66.[77] Therefore, several studies pursued Zr_6-based MOFs with more open pore structures. In particular, UiO-67, a 12-connected MOF that is isoreticular to UiO-66, but constructed from extended biphenyl dicarboxylate linkers, was shown to be much more active for OP compound hydrolysis.[100] The apertures for UiO-67 are 11.5 Å.[100] Researchers hypothesize that hydrolysis occurs at “missing linker” defects within the MOF where substitutionally labile aqua ligands afford the simulants access to the acidic Zr^{IV} ions.[78, 101-102]

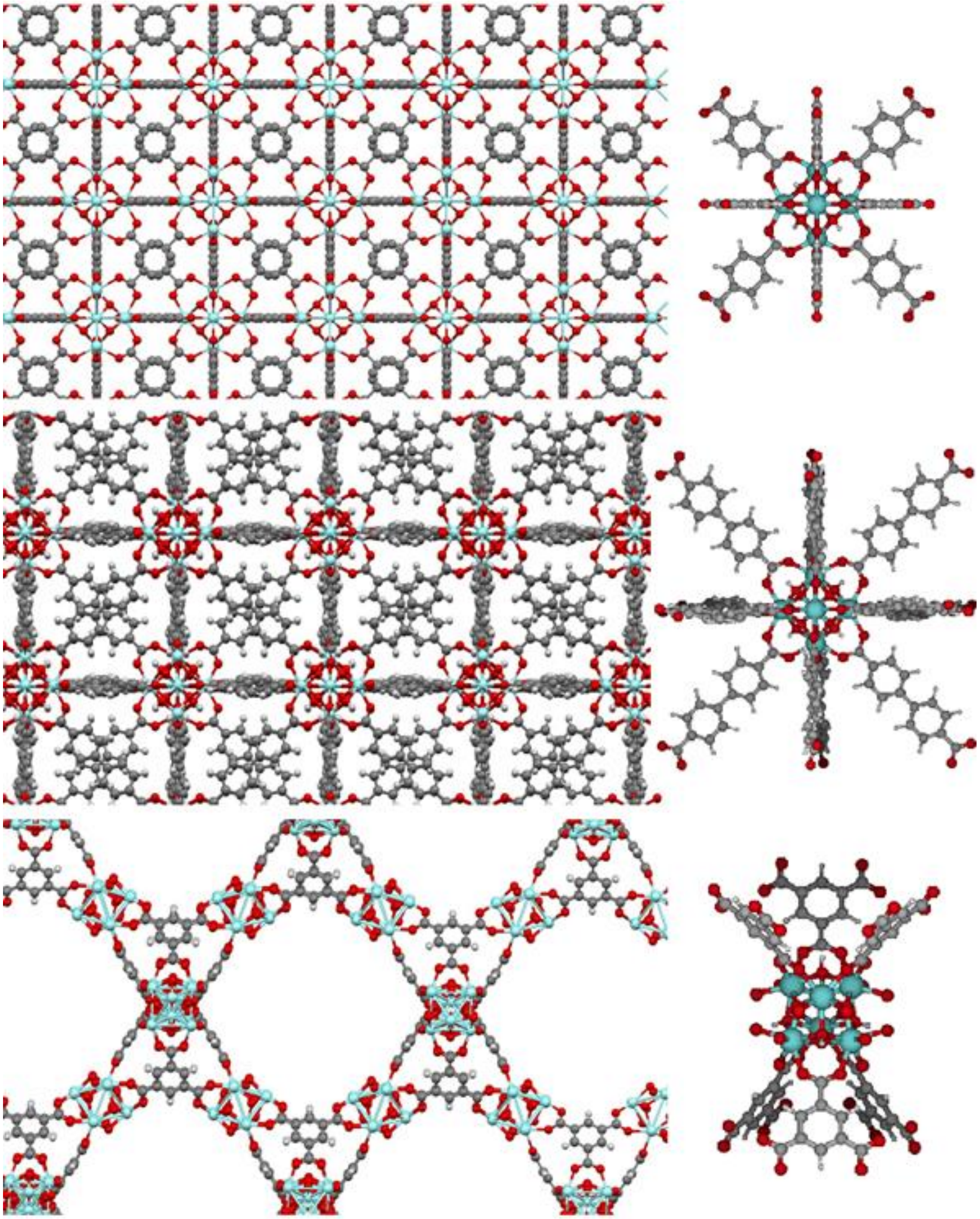

Figure 1.10 Representations of the UiO-66 (top), UiO-67 (center), and MOF-808 (bottom) MOF structures (left), and their secondary building units (right). Hydrogen atoms in the repeating UiO-66 structure have been omitted for clarity. Atom colors are C: gray, O: red, H: white, Zr: blue. Figure adapted from paper referenced.[103]

Based upon the hypothesis that labile aqua ligands are required for catalyzing OP hydrolysis at Zr_6-MOFs, scientists recently explored these reactions as catalyzed by the 6-connected MOF, MOF-808. MOF-808 is composed of the same secondary building unit (SBU) as the UiO series of MOFs, but with benzene-1,3,5-tricarboxylate (BTC) serving as the organic linkers. The tricarboxylate groups link three nodes to each ligand, which creates an open crystalline structure with pores as large as 18 Å.[104-106] Once activated (by removing formate ions that remain from the synthesis), the resulting 6-connected nodes have multiple water and hydroxide ligands that decorate the circumference of the nodes (See Figure 1.10). These ligands, along with the high accessibility of the nodes to the reactants, are likely responsible for the remarkably high decomposition rates of CWA simulants in the presence of this catalyst."

Although, as described above, several Zr_6-based MOFs have been shown to be catalytically active for the hydrolysis of CWAs in aqueous solution, the reactions have yet to be extensively explored for hydrolyzing CWAs or OP simulants in the gas phase. One may hypothesize that the same rapid hydrolysis rates could accompany gas-MOF heterogeneous catalysis. Motivated both by the practical importance of exploring strategies for destroying vaporous CWAs and a fundamental interest in catalysis within MOFs, I have employed ultrahigh vacuum-based surface-science methods in a systematic study of organophosphonate-MOF chemistry at the gas-MOF interface. Specifically, infrared spectroscopy has been used to characterize several MOFs, then track bond rupture and formation during exposure of the Zr_6-MOFs to a controlled flux of dimethyl methylphosphonate, a common simulant for the nerve agent sarin. Besides, X-ray photoelectron spectroscopy was employed to provide insight into the elemental abundance of the material following exposure and show how the oxidation state of the nodes is affected by exposure to DMMP and DMCP. These experimental methods have helped to benchmark parallel computational studies performed by Prof. Diego Troya, that map the energetics of initial DMMP binding and subsequent hydrolysis reaction pathways by employing density functional theory (DFT).

1.3 Summary and Research Goals

Despite their simple structure and well-documented properties, surprisingly little is known about how small hydrocarbons behave at the gas-surface interface, and how their fate is affected by properties of the surface itself. I have therefore embarked on work to uncover the dynamics of small-molecule interfacial collisions. Key research objectives for this project include:

(1) Determine if molecular rigidity–*i.e.*, molecules with single, double, or triple bonds, affects the extent of energy transfer in the initial gas-surface collision.
(2) Probe how the electron density along a C-C bond influences the thermal accommodation efficiency.
(3) Explore if surfaces functionalized by methyl groups behave differently, as collision partners, than the surfaces terminated with hydroxyl groups.
(4) Study how molecular scattering behavior may be correlated with the solubility of the compounds in hexane and water.

Following these highly fundamental studies, and motivated by the pressing and continual need for strategies capable of combatting chemical warfare agents (CWAs), protecting soldier and civilians, decontaminating battlefield, and remediating environmental contamination, I developed a new area for my group that focused on more practical applications of surface science to the study of materials that may sequester and decompose CWAs. To the best of my knowledge, these studies represent the first UHV-based exploration of MOFs as sorbents for nerve agent sequestration and destruction. The key scientific objectives that I aimed to probe with this new research include:

(1) Demonstrate the application of traditional UHV-based surface science methods to the study of highly porous, high surface area, particulate materials with a special emphasis on Zr_6-based metal-organic frameworks.
(2) Determine if a CWA-simulant, like dimethyl methylphosphonate, upon collision with a Zr-based MOF, diffuses into the material or simply scatters from the crystallite surfaces.
(3) Characterize reaction products that may form upon DMMP-MOF interactions.
(4) Show if there is a catalytic activity for the decomposition of a CWA simulant at the gas-MOF interface, as has been reported in solution-based studies.
(5) Uncover the rate and rate-limiting step for the CWA uptake on Zr_6-MOFs.

Chapter 2 Experimental Setup

2.1 Gas-Surface Interactions

The fundamental goals of studying gas-surface energy transfer, accommodation efficiency, and reactivity require experimental methods that afford a systematic approach where the energetics and chemical nature of the system is highly controlled. My approach is to combine ultrahigh vacuum surface science methods with molecular beam scattering techniques and model surfaces. In this way, I systematically explore how parameters such as collision energy and surface functionality affect the outcome of the gas-surface interaction. These studies can then be correlated to develop an overall understanding of the roles of specific chemical and physical properties in determining the outcome of interfacial processes. Below, the methods are described in sufficient detail such that future students may have a guide for reproducing and furthering this work.

2.1.1 Ultrahigh Vacuum

The experimental approach for the investigation of gas-surface interaction dynamics has been described in previous papers,[87,88,107,108] and will be presented in detail in this chapter. As indicated in Figure 2.1, the experiments are performed under ultrahigh vacuum (UHV) conditions. Ultrahigh vacuum enables surface samples, once clean, to remain free from background contamination for sufficient durations for experimental studies. To clarify this point, if one assumes a sticking probability of gas molecules at a particular surface to be unity, the minimum time to form one monolayer on a clean surface at atmospheric pressure (760 Torr) is about 1 ns. My target pressure for the ultrahigh vacuum chamber is 10^{-10} Torr, which changes the formation time of one monolayer to 3 hr.

In addition to maintaining a well-characterized surface, UHV conditions ensure that gas-phase chemistry plays an insignificant role in my studies. That is, based upon the mean free path equation for air at 20° C[109] (shown in equation (7)), a lower pressure corresponds to a longer mean free path of gas molecules.

$$\lambda \approx \frac{5}{P(mtorr)} cm \tag{7}$$

Mean free path is the characteristic distance a molecule can travel before it hits another molecule. During my experiments, the mean free path of gas molecules can be as long as approximately 500 km (pressure is 10^{-10} Torr) in the main chamber, which ensures the gas molecules in the incident molecular beam travel toward the surface without colliding with background gases. Hence, both the incident energy distribution and the travel direction of the molecular beam can be maintained before the gas molecules collide with the surfaces.

Finally, the application of the UHV system also enables us to implement surface analytical techniques. For these studies, I employ X-ray photoelectron spectroscopy (XPS) and mass spectroscopy (MS) to characterize the surface adsorbates and gas-phase species, respectively.

2.1.2 The Main Chamber, Detector Chamber, and Load Lock System

Figure 2.1 shows the top-view schematic of the UHV chamber that is employed in my gas-surface interaction study project, and the detailed side-view schematic is shown in Figure 2.2. There are four important parts in this UHV chamber: (1) main chamber, (2) detector chamber, (3) load lock sample transfer system, and (4) sample manipulator.

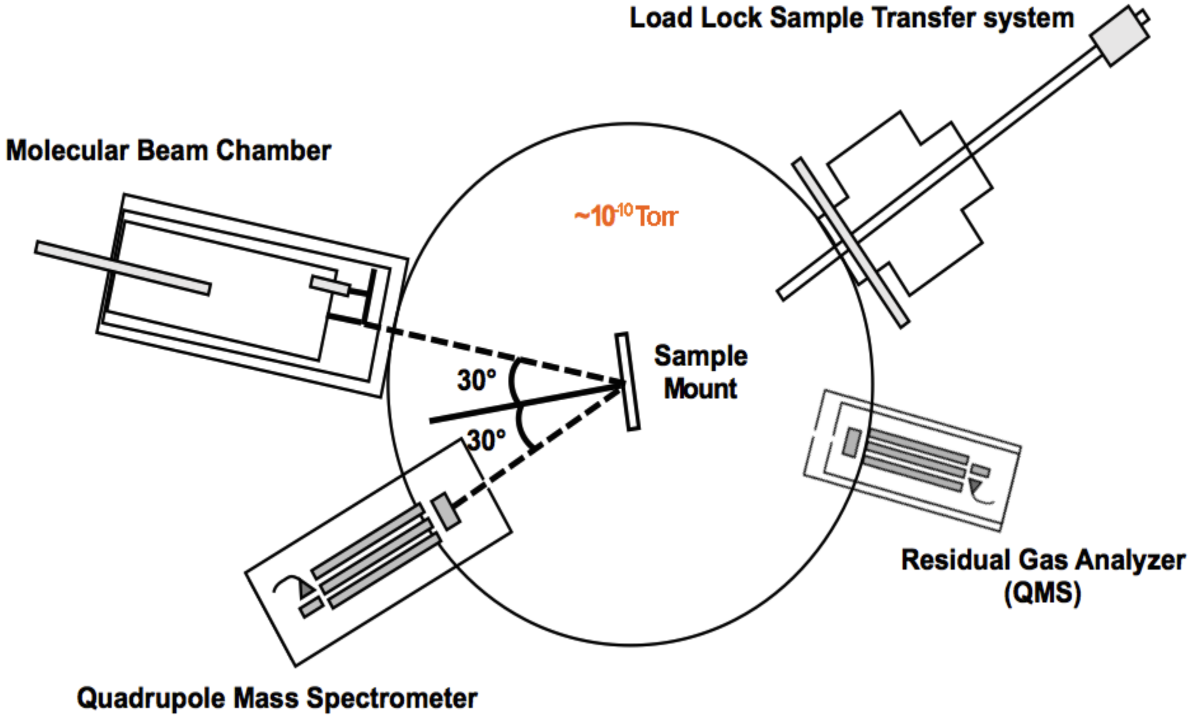

Figure 2.1 Top view schematic of the UHV chamber for surface-gas molecules interactions.

The main chamber is equipped with a 1500 L/s turbomolecular pump (Pfeiffer TMU1601P). This pump helps maintain the pressure in the main chamber below 1×10^{-9} Torr. A sample manipulator (McCallister MA2012) is located on top of the main chamber; it can be used to change the coordinates of the sample mount. Therefore, other than providing a clean environment for gas-surface interactions and minimize background interferences, the main chamber also functions as the tool to adjust the position of the surface to achieve good gas-surface alignment.

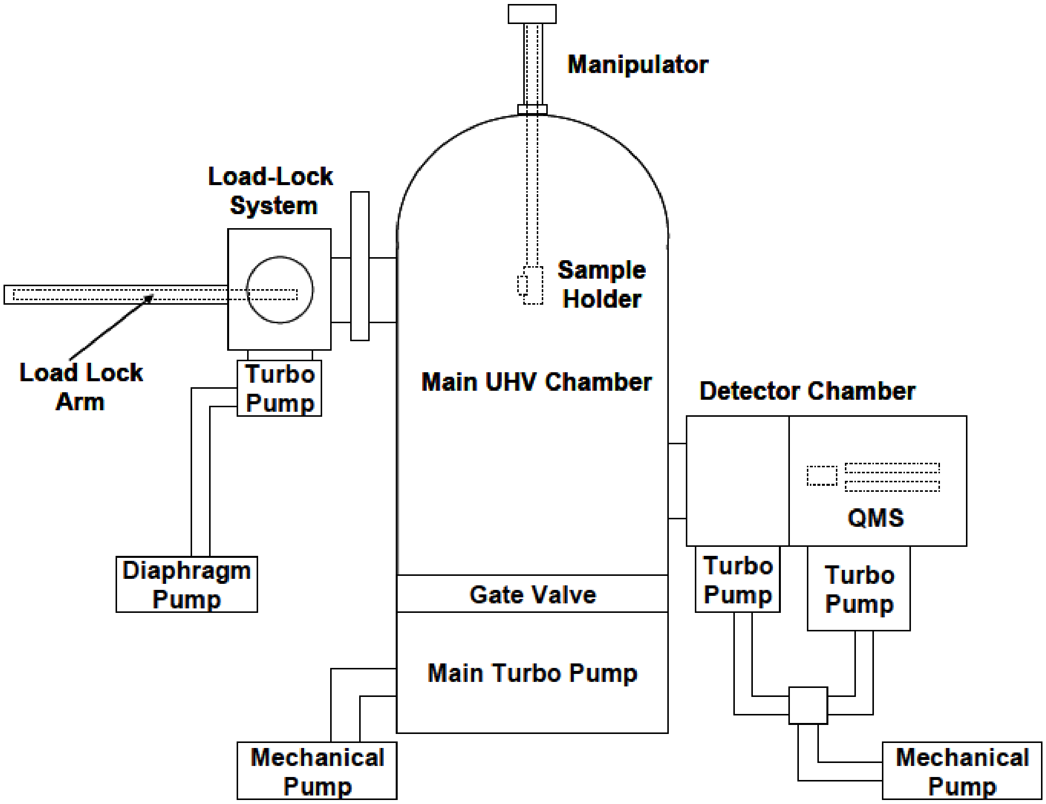

Figure 2.2 Schematic of the ultrahigh vacuum main chamber.[45]

The detector chamber is connected to the main chamber through a 4.3 mm diameter aperture. Gas molecules scattered from the surface may travel into the detector chamber through this aperture, and go through the first differential pumping stage. Then, these molecules may pass through another aperture with a diameter of 4.7 mm to enter the second stage of the detector chamber. The first stage is equipped with a small turbomolecular pump (Pfeiffer TMU261P) with a 250L/s pumping speed, and the second stage is equipped with a 500L/s turbomolecular pump (Pfeiffer TMU521P). The combination of the turbomolecular pumps in the main chamber and the detector chamber helps maintain the pressure in the detector chamber at 1×10^{-10} Torr throughout the experiments. The Extrel QMS is located in the second stage of the detector chamber. This QMS is set to detect the scattered gas molecules with a certain mass-charge ratio. The MS signal from the scattered molecules as a function of time is recorded via a multichannel scaler (MCS) to provide the final TOF distribution.

Both the detector chamber and the main chamber are monitored and controlled by a LabVIEW program. This program helps make sure the pressures in both chambers are always below certain thresholds. The pressure limits can be set in the software as set points. Once the pressure in any chamber increases and exceeds the setpoint value, the software will automatically shut down the system to protect the instruments.

Before starting experiments, surface samples need to be transferred into the main chamber. However, directly exposing the main chamber to the atmosphere will cause an immediate pressure jump and possible chamber contamination. Hence, a technique that helps prevent the main chamber from being exposed to the atmosphere is needed during sample transfer. The load lock system in my apparatus is employed to fulfill the experimental requirement of transferring the sample without breaking the vacuum in the main chamber. The procedure of sample transfer is explained in detail in Section 2.1.5.2 of this thesis.

2.1.3 Molecular Beam

In order to investigate gas-surface interaction dynamics, a well-characterized gas source is necessary. As shown in Figure 2.1, a molecular beam chamber is attached to the UHV main chamber as the source of gas molecules. A molecular beam is a stream of gas molecules with unified direction, near single energy, and well-controlled cross sectional area.[110] In my experiments, I seed the gas of interest in UHP (ultra-high purity) H_2 (Airgas). The prepared mixture is then introduced into the molecular beam chamber, which is a high vacuum chamber with a pressure of 10^{-7} Torr. In the molecular beam chamber, gas molecules are supersonically expanded through a 0.05 mm diameter nozzle. A 0.4 mm diameter conical skimmer is located 6 mm downstream from the nozzle. This skimmer selects the core of the gas stream. Then, a rotating 2-slit mechanical chopper wheel converts the continuous gas beam into gas pulses. The period of one gas pulse is about 50 μs, for a rotation frequency of 250 Hz. After passing another differential pumping stage, the molecular beam is introduced into the UHV main chamber.

2.1.3.1 Supersonic Molecular Beam

In my experiments, the supersonic molecular beam technique is employed to acquire a well-characterized incident gas source. This technique requires the application of a nozzle and a pressure difference between the gas source and the differentially pumped molecular beam chamber. The backing pressure for the nozzle is set to approximately one atmosphere. In this condition, the mean free path of the gas molecules is smaller than the diameter of the nozzle. As a result, the flow of the gas molecules is hydrodynamic, which means this flow follows the same dynamics with liquid fluid. The gas molecules will be pushed through the hole and enter the first differential pumping stage.[45] The vacuum condition of this differential pumping stage makes the flow of the gas molecules change from a continuum flow to a molecular flow. Then, the skimmer located downstream from the nozzle selects the core of the gas flow and produces the supersonic molecular beam. The continuum flow and molecular flow here are defined by using the Knudsen number, K_n. As shown in equation (8),[111] K_n is equal to the mean free path of the gas molecules (λ) over the size of the chamber (L).

$$K_n = \frac{\lambda}{L} \tag{8}$$

When $K_n < 0.001$, the gas is considered to be in the continuum regime, and the molecular flow regime occurs when $K_n > 10$.[111] At one atmosphere; therefore, λ is approximately 10^{-8} m. The dimension of the nozzle is about 10^{-2} m. Hence, the corresponding K_n equals 10^{-6}, which places the gas source in the continuum regime. After the gas source enters the differential pumping stage of the molecular beam chamber, which has a pressure of 10^{-6} Torr, the λ of the gas molecules increases significantly to about 50 m. Since the size of the molecular chamber is no bigger than 1 m, the K_n of the gas molecules is much larger than 10. Therefore, after the supersonic expansion, the gas molecules are in the molecular flow regime.

Because of the pressure drop from the gas source to the molecular chamber, the gas molecules are accelerated when they pass through the nozzle and enter the high vacuum chamber. This occurs due to continuum flow mechanics. If gas molecules flow through an aperture and there is a significant pressure difference (around a ratio of 2) between the two stages, the speed of the gas molecules will be accelerated to around the local speed of sound.[112]

During expansion, the highest pressure is reached at the throat of the nozzle aperture. When the gas molecules enter the high vacuum chamber, the dramatic pressure difference makes them go through an expansion to get adjusted to the low pressure of the vacuum chamber. This expansion lowers the pressure and increases the velocity of the gas. When the velocity is approximately constant, the mean free path of gas molecules at this low pressure is large enough to avoid intermolecular collisions in the molecular beam. Therefore, the unified direction and well-ordered cross sectional area are maintained in the molecular beam.

The velocity of the gas molecules increases upon expansion, and the average translational energy of the expanded gas is predicted by employing Equation (9). In this equation, the T is the temperature of the nozzle, γ is the heat capacity ratio (C_p/C_v) of the gas species, and R is the gas constant. This equation is developed under the assumption that the gas molecules behave ideally.[45]

$$E = \frac{RT\gamma}{(\gamma - 1)} \qquad \textbf{(9)}$$

From equation (9), one can tell that the energy is proportional to the temperature of the nozzle. Therefore, I can tune the average translational energy of the expanded gas beam to desired values by controlling the nozzle temperature. Other than this method, the energy of a beam can also be manipulated by using the seeding technique. The detailed procedure of this technique is described in Section 2.1.5.1.

2.1.3.2 Molecular Beam Chamber Structure

A side view schematic of the molecular beam chamber is shown in Figure 2.3. There are three pumping stages in the molecular beam system. The first stage is equipped with a 5000 L/s VHS10 diffusion pump (Varian Vacuum Technologies). Gas molecules are introduced into the chamber with an initial pressure of approximately 1 atm through a Teflon tube. They enter the first pumping stage right after being expanded through a 0.05 mm diameter nozzle, where a molecular beam is created through a supersonic expansion. This beam then travels toward the 0.4 mm diameter conical skimmer that is located 6 mm downstream from the nozzle. This skimmer only allows the molecules that travel toward the main chamber to pass. As a result, after being selected by the skimmer, the modified molecular beam has a unified direction and a well-defined cross sectional area.

The second pumping stage is equipped with a 1500 L/s Diffstak MK2 Diffusion Pump (BOC Edwards). After flowing through the skimmer, the continuous molecular beam is modulated by a two-slit chopper wheel located about 1.5 cm from the skimmer. There is a resulting gas pulse created every 2.02 ms (corresponding to a frequency of 495 Hz).

After further collimation by a 1.5 mm aperture, the gas pulses enter the final differential pumping stage of the molecular beam chamber. This pumping stage is equipped with a 250 L/s turbomolecular pump (TMU 261P, Pfeiffer) and separated from the UHV main chamber by a 2.2 mm aperture. A gate valve is applied to cover this aperture, so when experiments are not being performed, the gate valve is kept closed to isolate the main chamber from the molecular beam chamber. This can help maintain the low pressure in the main chamber and avoid contamination. During an experiment, the gate valve is open to connect the molecular beam chamber and the main chamber through the 2.2 mm aperture. Gas molecules that travel through this small aperture produce a 1 cm^2 spot on the surface sample, which is pre-aligned with the incident molecular beam.

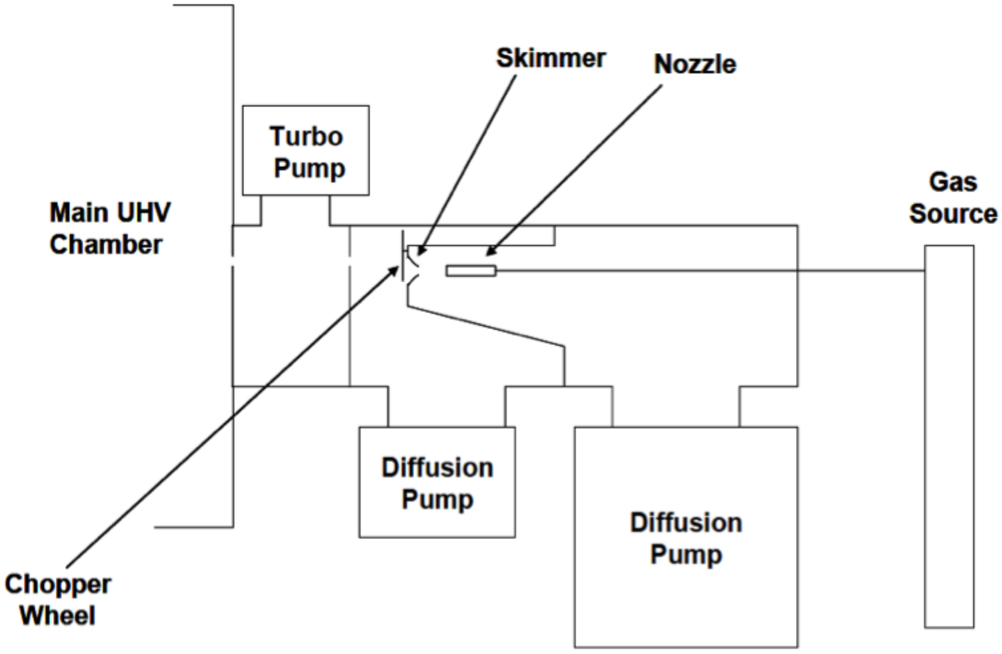

Figure 2.3 Side view of the molecular beam chamber.[45]

2.1.3.3 Molecular Beam Characterization

As mentioned in the previous section, the incident energy of a molecular beam can be tuned by modifying the ratio of the gas of interest and the carrier gas, the detailed experimental procedure of gas source preparation is provided in section 2.1.5.1. Facilitated by the sample manipulator, the coordinates of the sample mount in the UHV chamber can be modified, as shown in Figure 2.2. With the surface mount away from the pathway of the molecular beam, the RGA can be employed to measure the TOF distribution of the incident beam. A schematic of the experimental setup is provided in Figure 2.4.

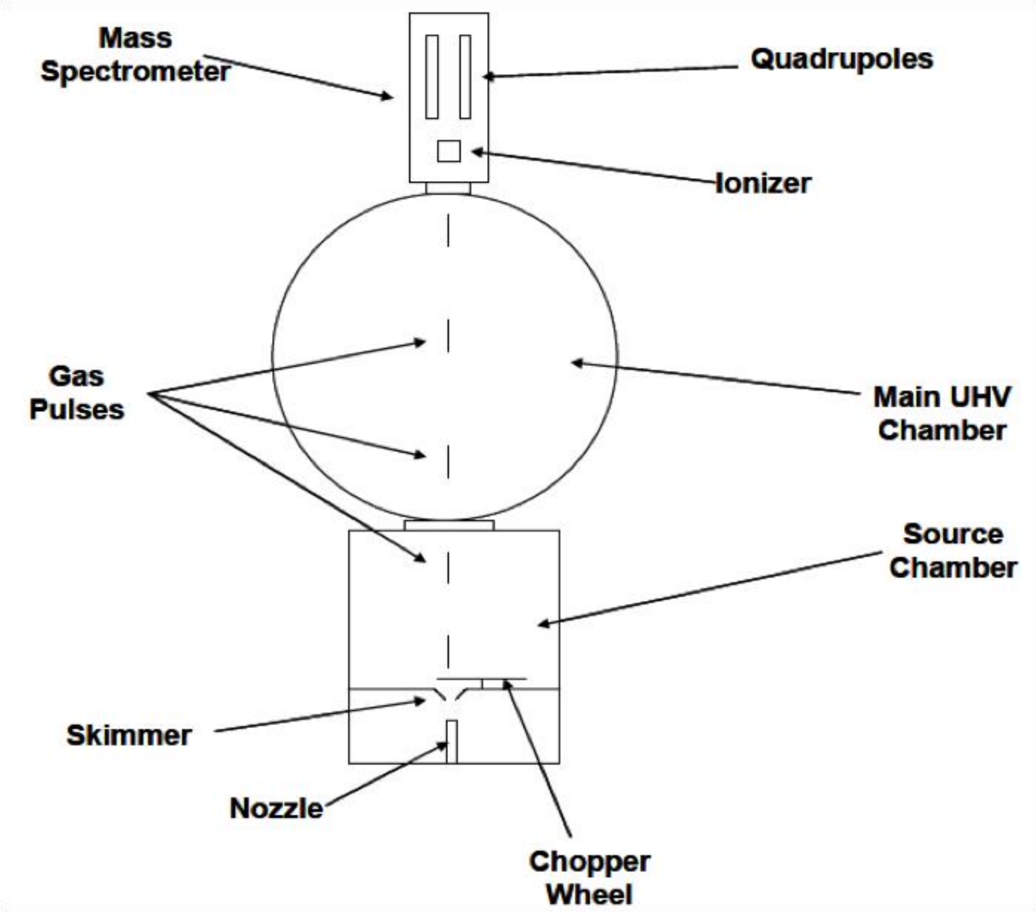

Figure 2.4 Top view of the in-line beam energy characterization system.[45]

In order to gain a well-controlled gas source, the characterization of the incident molecular beam is set to be the first step of the experiments. To characterize the incident beam, the sample mount is moved away from the path of the beam. Therefore, as depicted in Figure 2.4, after entering the UHV main chamber, instead of colliding with the sample surface, the incident beam travels directly through the main chamber and enters the RGA. By analyzing the recorded TOF distribution of the incident beam, the travel time, t, of gas molecules from the chopper wheel to RGA can be acquired. The distance from the chopper wheel to the RGA, L, is known from the chamber dimensions. Therefore, by using equation (12), the energy of the incident beam can be characterized.

2.1.4 **Self-Assembled Monolayer (SAM)**

2.1.4.1 Structure and Characterization of Self-Assembled Monolayers on Gold

SAMs are well-ordered organic surfaces that enable researchers to gain the control necessary to study the dynamics of gas-surface energy transfer. Previous research has shown that SAMs have high stability and reproducibility.[113] The chemical functionality of the end groups of the alkanethiols informs the chemical and physical properties of the monolayer. SAMs employed in this thesis are formed from adsorption of ω-functionalized alkanethiols onto gold substrates, and have been studied extensively and proven to be a well-characterized system.[114] Therefore, as previously described, the SAMs that are employed in my research project are model organic surfaces. In this type of SAM (*n*-alkanethiols on gold), the sulfur atoms at the end of each long carbon chain bond to a pre-cleaned Au (111) surface. The sulfur-gold spatial relationship is depicted in Figure 2.5.

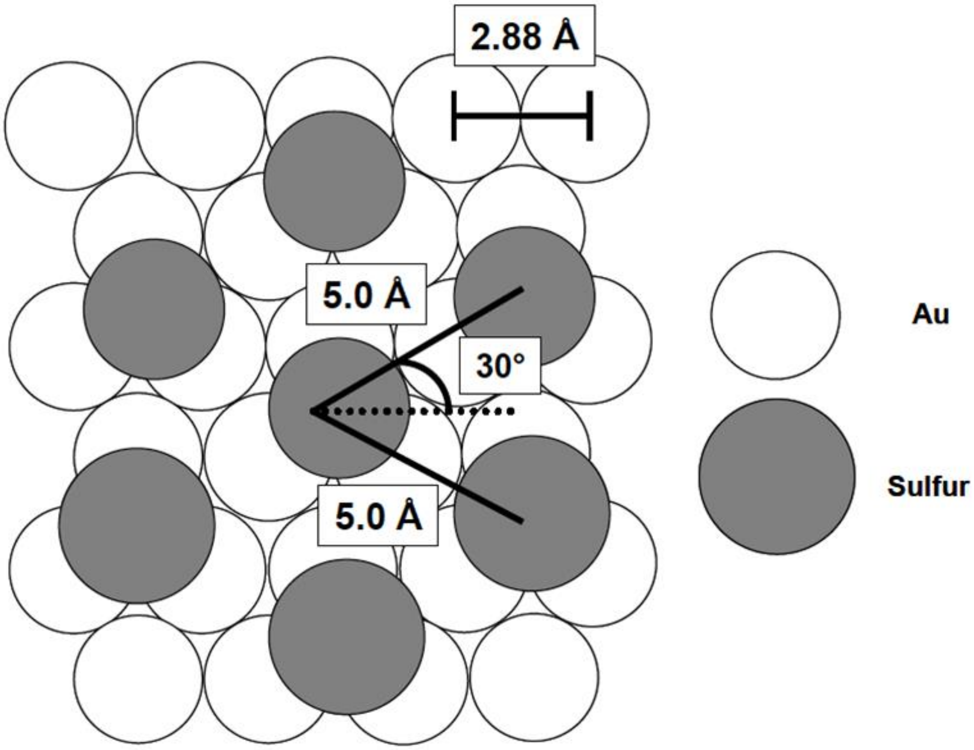

Figure 2.5 Schematic of sulfur-gold spacing in SAM.[45]

The formation of Au-S covalent bonds produces a final average intermolecular alkane chain distance of 5 Å. As shown in Figure 2.5, each of the sulfur atoms interacts with three gold atoms on the substrate. The nearest spacing of the top sulfur atoms is √3×2.88 Å (the nearest spacing of the bottom Au atoms), and the sulfur lattice is rotated 30° relative to the gold lattice. Therefore, the overlay of sulfur and gold atoms forms an overall (√3×√3) R30° lattice.[45] After the formation of bonds between the alkanethiols and the gold substrate, the conformation of the alkane chains is optimized and stabilized at the lowest energy state. For OH-SAMs and CH_3-SAMs, the optimized structure is reached when the tilt angle of chains is approximately 30° to 34° with respect to the surface normal, as shown in Figure 2.6.

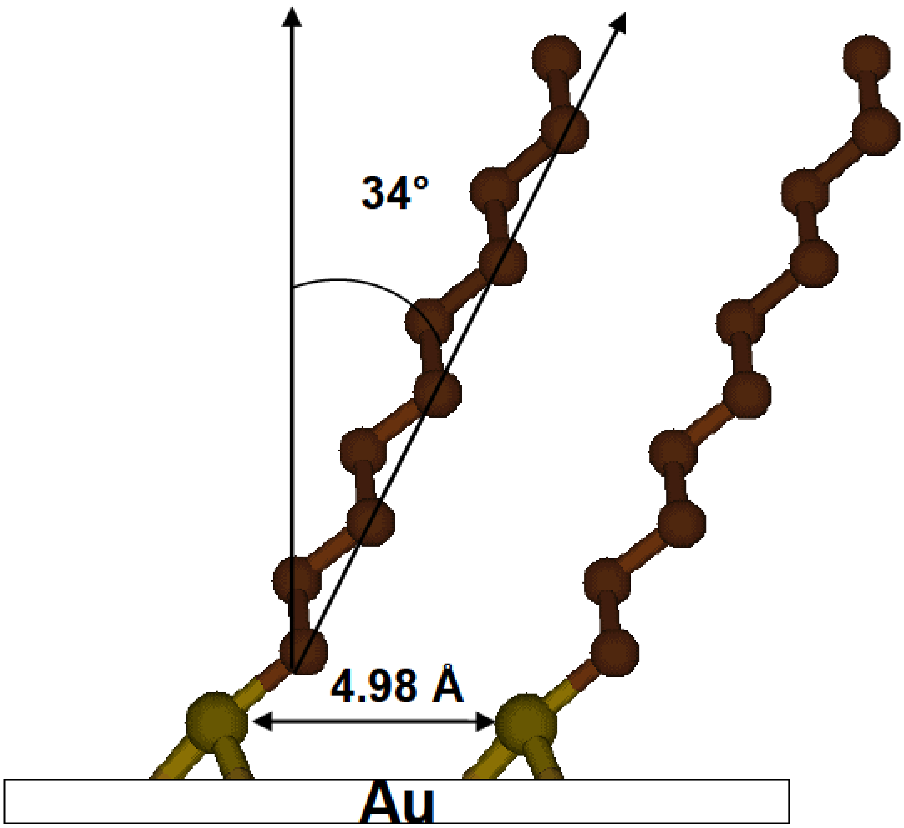

Figure 2.6 Schematic of SAM on gold.[45]

Previous literature shows that, when the alkane chain of an alkanethiol contains 6 or more carbons, the formed SAMs exhibit very high stability and crystal-like long-range order.[115] Since the alkanethiols that are employed in this research project are 1-octadecanethiol ((Sigma-Aldrich), CH_3-SAMs) and 16-mercapto-1-hexadecanol ((Sigma-Aldrich), OH-SAMs), which contain 18 and 16 carbons in the alkane chains, respectively, the SAMs that are prepared based on the method described above most likely produce highly ordered structures.

Characterization of the SAMs is critical for verifying their structures before performing a gas-surface collision experiment. Therefore, reflection absorption infrared spectroscopy (RAIRS), which is a non-destructive surface analysis technique, was employed. RAIRS contains a Michelson interferometer that can make a full scan over the entire infrared region, then output a time-domain interferogram. Through Fourier transformation, this interferogram can be transformed into a frequency-domain spectrum. The exploitation of reflection in RAIRS can provide information about the chemical environment and the orientation of surface-bound molecules. Based on the surface-selection rule discovered by Greenler in the 1960s, compounds on a surface could absorb incoming infrared light with specific frequencies.[116] Upon radiation, the polarized IR light will be reflected off a substrate surface, and be resolved into two components: A P-polarized component (E_p, parallel to the incident plane), and an S-polarized component (*Es*, perpendicular to the incident plane). There is a phase change of 180˚ at nearly all angles of incidence for the *Es*. This results in its destructive interference and amplitude canceling out. On the other hand, the phase change of the Ep depends on the incident angle. A grazing incidence of 88° induces a phase change of about 90° for Ep, which allows the P-component light to interfere constructively with itself. Therefore, the surface environment can be monitored by recording the change in IR reflection. The reflected radiation was detected by a mid-range (750-4000 cm^{-1}) mercury cadmium telluride (MCT) detector, which was cooled by liquid nitrogen prior to each experiment.

As shown in Figure 2.7, the IR spectrum of a highly ordered CH_3-SAM shows clear and sharp peaks for the symmetric and asymmetric C-H stretch for both CH_3 groups and CH_2 groups. In the spectrum of an OH-SAM, the two peaks for the C-H stretch of CH_2 groups can be identified. The wavenumbers of these modes in highly ordered SAMs have been reported previously.[117] The peak positions in the IR spectra, Figure 2.7, agree well with the literature values (as shown in Table 2.1). Therefore, I am confident that the SAMs I employed in my experiments were well ordered.

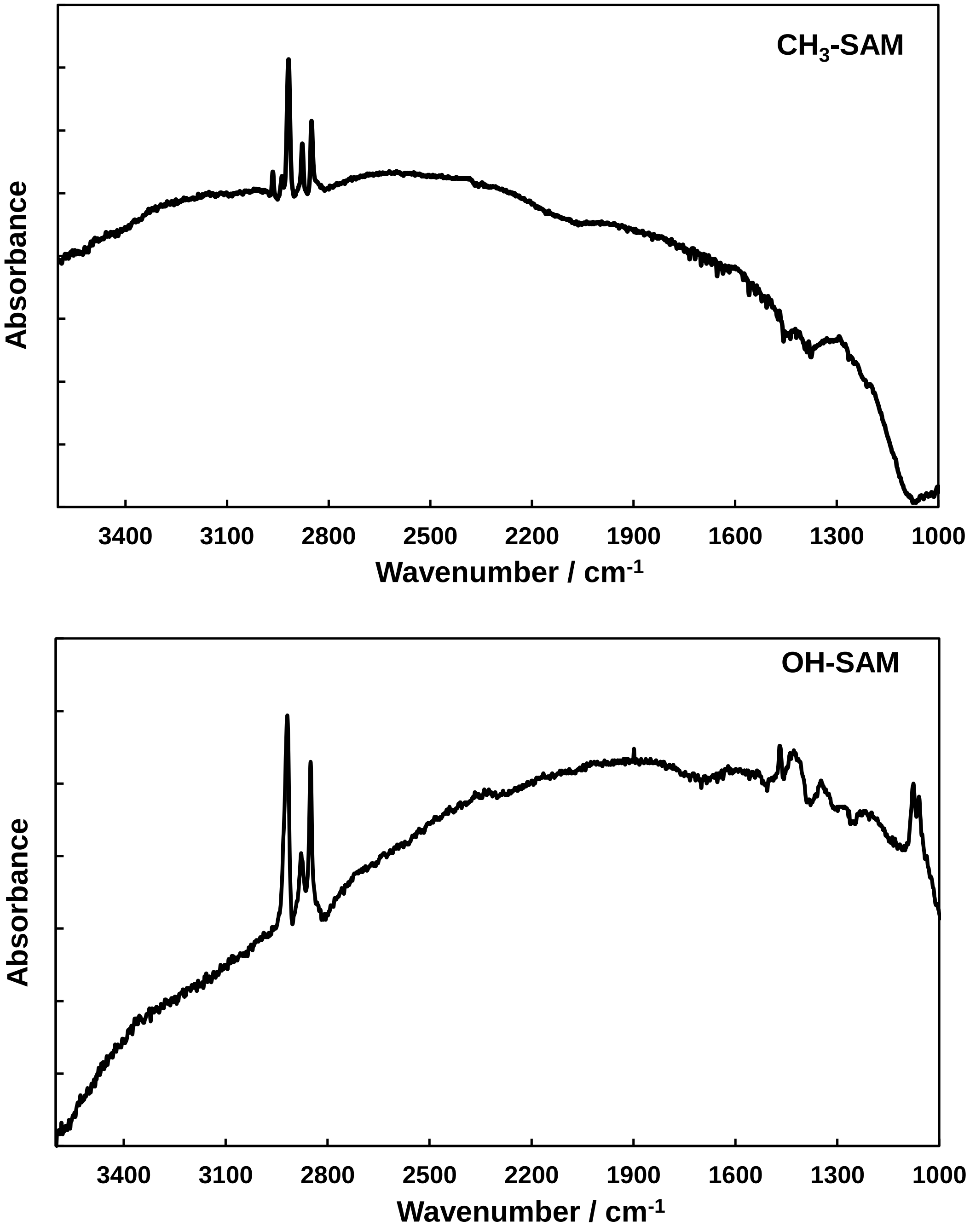

Figure 2.7 IR spectra of CH$_3$-SAM (top) and OH-SAM (bottom).

Table 2.1 Comparison of IR peak positions of the observed and well-ordered SAMs.

CH_3-SAM			OH-SAM		
Observed Wavenumber (cm^{-1})	Well-ordered SAM[117] Wavenumber (cm^{-1})	Mode Assignment	Observed Wavenumber (cm^{-1})	Well-ordered SAM[117] Wavenumber (cm^{-1})	Mode Assignment
2850	2851	CH_2 C-H str (sym)	2850	2850	CH_2 C-H str (sym)
2878	2878	CH_3 C-H str (sym)	2919	2920	CH_2 C-H str (asym)
2918	2919	CH_2 C-H str (asym)	1471	1472	CH_2 scissors
2964	2958	CH_3 C-H str (asym)	1078	1073	C-O str

2.1.5 Experimental Approach

The procedure of the experiments presented in the thesis is described in this section. Generally, a well-characterized incident molecular beam and a model organic surface are prepared first. Then, the surface is aligned with the molecular beam, and the energy distribution of the recoiling gas molecules after they interact with the surface is determined. Information about the dynamics of the gas-surface collision can be obtained by detailed comparisons between the incident and final energy distributions.

2.1.5.1 Preparation of Gas Sources

Preparation of the gas source is the first step of an experiment. The seeding gas technique is employed. The key point of this technique is: one can increase the incident energy of a gas beam by mixing the gas molecules with a higher velocity carrier gas. At a specific temperature, different types of gas molecules all possess the same amount of average translational energy. Accordingly, based upon equation (10), equation (11) can be derived to show that the gas molecules with different mass have a different velocity.

$$E = \frac{1}{2}mv^2 \tag{10}$$

$$v = \sqrt{\frac{2E}{m}} \tag{11}$$

More specifically, the higher the molecular weight, the lower the corresponding velocity for the same kinetic energy. For example, at room temperature, where the average kinetic energy of gas molecules is approximately 4 kJ/mol, the velocity of argon atoms is far lower than the velocity of helium atoms.

In this work, molecular beams of different gases with unified incident energy are required. The mixing ratio of the gas of interest and carrier gas is modified to tune the incident energy of a molecular beam to the desired value. The carrier gas employed in my experiments is UHP H_2. H_2 molecules have the lowest molecular weight, so they travel faster than all the other types of gas molecules. In the mixture, H_2 carries the gas of interest at higher velocities than that of the pure gas under static condition. As a result, the incident energy of the gas beam increases. The incident energy of all the molecular beams employed in this research project was tuned to 48±5 kJ/mol with the full width at half maximum (FWHM) of 10 kJ/mol. (The details of the determination of the beam energy are presented in section 2.1.5.5).

A schematic of the apparatus for the preparation of the gas source is provided in Figure 2.8. Taking the preparation of the C_2H_6 (UHP, Airgas) - carrier gas (UHP H_2) mixture as an example, the preparation procedure of the gas source is described as follows.

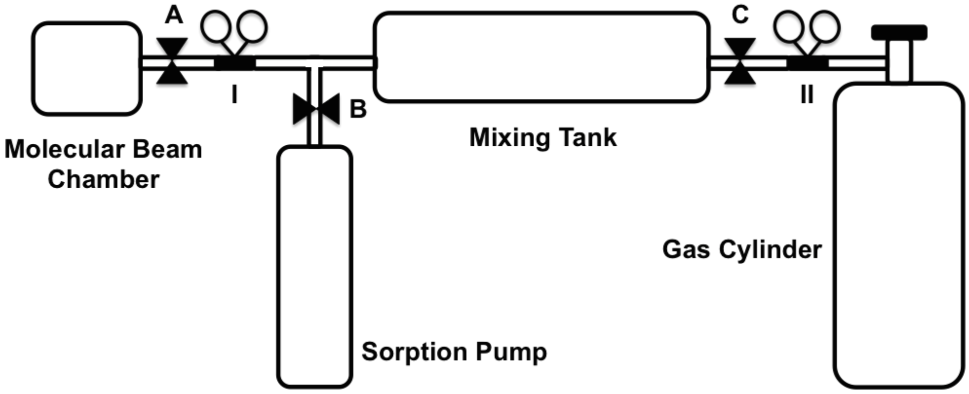

Figure 2.8 Schematic of apparatus for gas source preparation.

a) Liquid nitrogen is used to cool a sorption pump for 30 mins. Open valve B, with valve A and C closed. The pre-cooled sorption pump is then employed to pump down a stainless steel mixing tank (Swagelok, DOT-3A1800) for another 30 min. Then valve B is closed. At this point, the pressure in the tank is far lower than atmospheric pressure. Thus, when the mixing tank is connected to a gas cylinder, this pressure difference will cause the gas molecules to flow into the mixing tank. Furthermore, pumping down the tank before making the gas mixture significantly lowers the interferences from other gas molecules and keeps the gas mixture clean.

b) Then, C_2H_6 is introduced through regulator II at about 10 psi. The pressure in the mixing tank is allowed to stabilize for about 30 s; then valve C is closed.

c) The carrier gas (UHP H_2) is then connected to the mixing tank. Valve C is kept closed, and regulator II is employed to increase the delivery pressure to about 50 psi gradually.

d) Then, valve C is opened to connect the H_2 gas cylinder and the mixing tank. Since the delivery pressure of H_2 (50 psi) is much higher than the pressure in the mixing tank (10 psi), H_2 molecules will flow into the mixing tank. During this time, the delivery pressure of H_2 is gradually increased to about 250 psi. The pressure in the mixing tank is allowed to stabilize for approximately 30 s.

e) Valve C and the H_2 cylinder are both closed after 30 s. At this point, the mixing tank contains 250 psi of C_2H_6 - H_2 gas mixture. This mixture is the gas source for the study of interactions between C_2H_6 and model organic surfaces.

2.1.5.2 Preparation of SAMs

SAMs employed in this experiment were prepared by using alkanethiols and "gold slides" (Au evaporation onto Cr-coated glass slides).[46] To clean the gold slides, they were immersed into piranha solution, which is the mixture of 70% sulfuric acid and 30% hydrogen peroxide (volume/volume ratio) for at least 1 hr, and then rinsed by copious amounts of deionized water followed by ethanol to get rid of the piranha solution residue. Then, the cleaned gold slides were placed into a 1 mM ethanolic solution of alkanethiols (1-octadecanethiol (Sigma-Aldrich) for CH_3-SAMs and 16-mercapto-1-hexadecanol (Sigma-Aldrich) for OH-SAMs).[118] The gold slides remained in the alkanethiol solution for at least 24 hr prior to use. During this 24 hr period, the alkanethiols in the solution chemisorbed to the surface of the gold slides by forming a covalent bond through sulfur atoms at the end of the chains. Furthermore, 24-hour immersion ensures the SAMs possess good chain order and packing density. After removal from the solution, the slides were rinsed thoroughly by ethanol, blown dry by ultra-high purity (UHP) nitrogen (Airgas), placed on a sample mount, and immediately transferred into the UHV chamber through the load lock sample transfer system. In the UHV chamber, a high precision manipulator was employed to precisely modify the coordinates of the sample mount to satisfy experimental needs.

The preparation method of SAMs described above has been confirmed to be reliable by several previous research projects. [118, 90, 119] The prepared SAMs were highly ordered in both long range and short range. To optimize the chain-chain interactions, the distance between each chain turns out to be about 5Å,[91] and in both the CH_3-SAMs and OH-SAMs that are employed in this experiment, all the chains tilt approximately 30° with respect to the surface normal. [120]

2.1.5.3 Sample Transfer

The load-lock system is employed to achieve the goal of transferring samples without breaking the vacuum in the UHV chamber. A schematic of this system is shown in Figure 2.9. As shown in Figure 2.9, a gate valve, A, is located between the load-lock chamber and the main chamber. When there is no need for sample transfer, valve A is kept closed to maintain low pressure in the UHV chamber. The detailed procedure for transferring samples into and out from the chamber is provided here by steps:

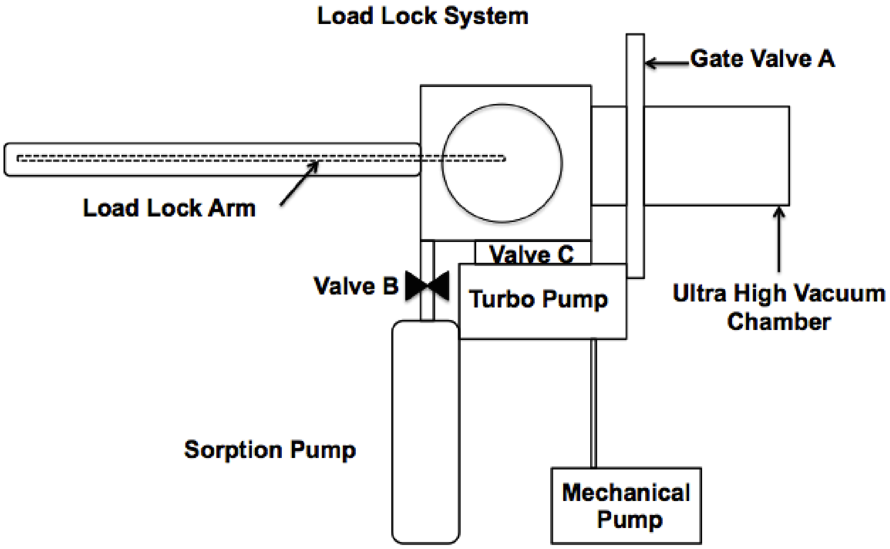

Figure 2.9 Schematic of the load lock system.

a) To transfer surface samples out from the UHV chamber, the first step is to pump down the load lock chamber. A sorption pump is cooled by liquid nitrogen for 30mins, then valve B is opened to connect the sorption pump and the load lock chamber for another 30 min or until the pressure in the load lock chamber is approximately 10^{-4} Torr.

b) After valve B is closed, valve C is opened to let a turbomolecular pump further pump down the load-lock chamber to about 10^{-7} Torr.

c) Then, the sample mount coordinates are modified in the UHV chamber to achieve a good alignment with the load-lock arm. At this point, due to the significant pressure difference between the main chamber (10^{-10} Torr) and load-lock chamber (10^{-7} Torr), once the gate valve A is opened, there will be an immediate pressure rise in the main chamber. To prevent the system from being instantly shutdown, the set point for the main chamber pressure is temporarily set to a higher value (1×10^{-6} Torr).

d) Then, gate valve A is opened, and the load-lock arm is pushed into the main chamber until it holds the sample mount. A lock-in-key mechanism then engages the sample mount for removal from the sample manipulator. After steadily pulling out the load-lock arm (containing the sample mount) from the main chamber, valve A is closed to isolate the main chamber from the load lock chamber.

e) Valve C is then closed. The load-lock chamber is vented to atmospheric pressure by UHP nitrogen (UHP300). Then the gate of the load-lock chamber is opened. After taking out the sample mount, this gate is kept closed during sample preparation to avoid contamination.

After the clean sample surfaces are positioned on the sample mount, they can be transferred to the UHV chamber and prepared for the gas-surface scattering experiments. In my experimental apparatus, as shown in Figure 2.10, two sample surfaces can be placed on the same sample holder. During experiments, the alignment of a molecular beam and each surface can be achieved by modifying the sample mount coordinates. Therefore, the interaction dynamics between the gas molecules and different surfaces can be studied under the same experimental conditions.

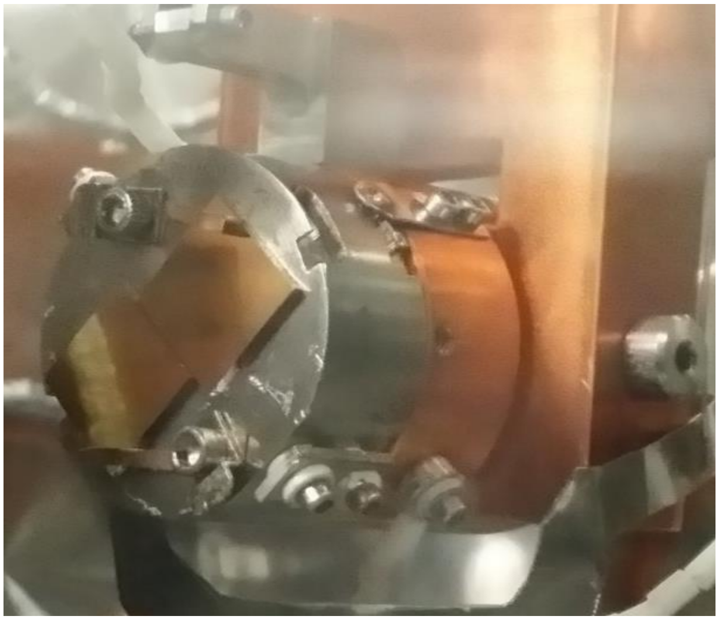

Figure 2.10 Picture of the sample mount.

The procedure of putting the sample mount back is quite similar to the procedure for removal. After mounting the sample holder back on to the load-lock transfer arm, the sample mount can be transferred back to the UHV chamber by following steps a), b), c) and d) provided above. After the sample installation, the set point of the main chamber should be set back to the original value in the LabVIEW program.

2.1.5.4 Instrumental Alignment

To ensure that the molecular beam collides with the surface sample, and the reflected gas molecules are detected by the QMS located in the detector chamber, the whole system must be aligned before performing any experiments. A laser source is employed to accomplish this alignment. The whole experimental setup is built to have the centers of all the apertures aligned. Therefore, if I shine a laser through the apertures in the detector chamber and let it hit a reflective surface with a specific angle, the reflected laser should go directly through the apertures in the molecular beam chamber, as shown in d) of Figure 2.11. Therefore, at this point, if a molecular beam enters the main chamber and collides on the surface, the reflected gas molecules will follow the same pathway to enter the detector chamber, pass through the two apertures and undergo analysis by the QMS.

The detailed procedure of performing alignment is shown in Figure 2.11. This is the view along the Z-axis. The first step of the alignment is to find the zero degrees position. When the shined laser hits the surface with an incident angle of 0° with respect to the surface normal, as shown in (a) of Figure 2.11, the surface is considered as being located at the zero degrees position. To identify the zero degrees angle, the reflection of the laser is employed. The reflection follows the same path of the incident laser and travels back to the laser source. Therefore, the angle of the sample mount is altered until the reflected beam is co-linear with the primary beam.

The second step of the alignment is the modification of the Y coordinate of the sample surface. Therefore, the Y coordinate of the surface is modified through the sample manipulator to make sure that the laser hits right at the center of the surface, as shown in graph (b) of Figure 2.11.

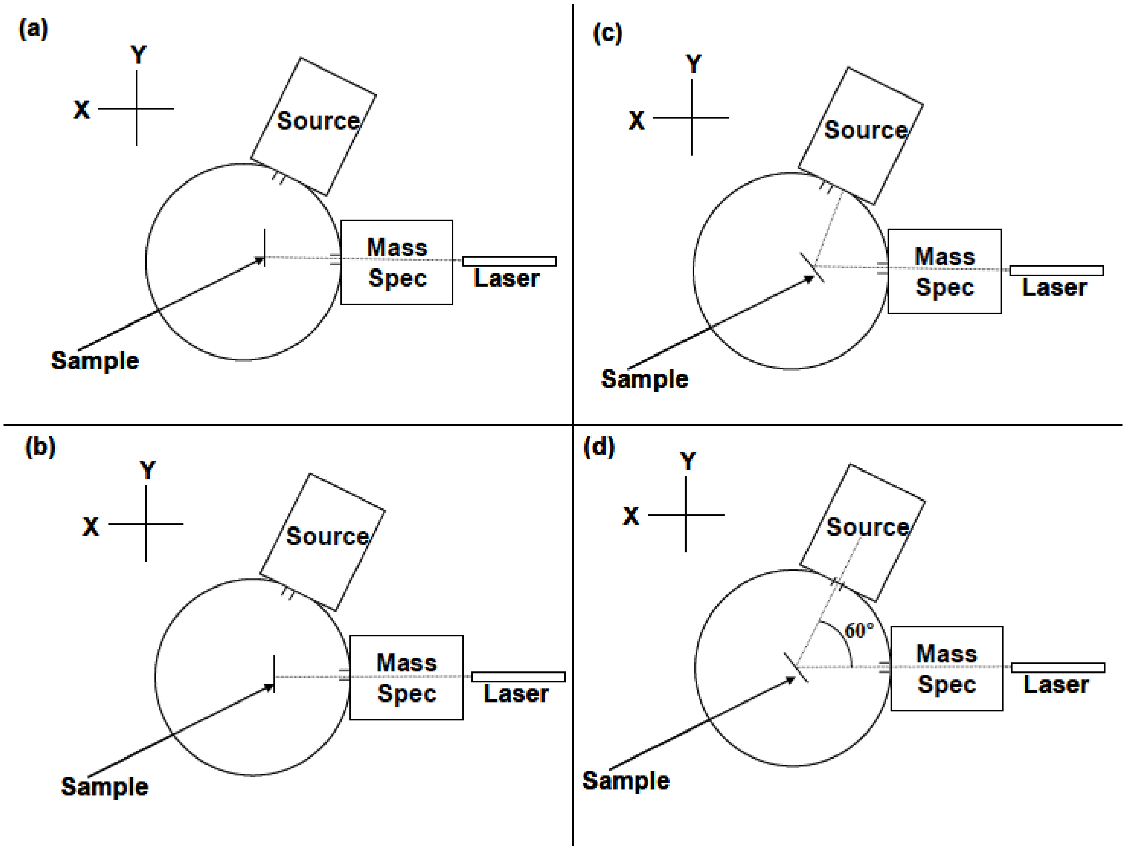

Figure 2.11 Z-axis view of the sample alignment schematic. [45]

The surface is then rotated 30° counterclockwise as shown in (c) of Figure 2.11. At this point, the laser goes through the detector chamber, hits on the surface center and is reflected. As shown in (c) of Figure 2.11, the reflected laser may hit on the inner wall of the UHV chamber at this stage. To fulfill the experimental requirements, the laser needs to go directly into the molecular beam chamber. Thus, the fourth step of the alignment is to adjust the X coordinate of the sample until the reflected laser passes into the aperture in between the main chamber and the molecular beam chamber, as shown in (d) of Figure 2.11. Finally, the Z coordinate of the sample is adjusted to ensure that the laser hits the vertical center of the sample. Hence, in a well-aligned system, a generated molecular beam will enter the UHV main chamber through an aperture and hit on the center of the sample surface. Further, the mass spectrometer views a spot at the center of the surface sample.

2.1.5.5 Incident Beam Energy Measurement

The determination of the incident energy of a molecular beam is critical for studying the dynamics of gas-surface interactions. Using the sample manipulator, I am able to change the position of the surface inside the main chamber. As shown in Figure 2.1, with the sample mount away from the gas pathway, the molecular beam passed directly into a Residual Gas Analyzer (RGA) (Stanford Research System), which is a quadrupole mass spectrometer (QMS). During experiments, the RGA is set to record the time of flight (TOF) distribution of particles with a specific mass-charge ratio. Based upon the dimensions of the chamber, the distance from the mechanical chopper wheel to the RGA is 45.3cm. Therefore, after acquiring TOF distribution, the incident kinetic energy of the molecular beam can be determined according to the relationship shown in equation (12).

$$E_{in} = \frac{1}{2}mv^2 = \frac{1}{2}m\left(\frac{L}{t}\right)^2 \tag{12}$$

The detailed procedure for obtaining an incident beam with specified incident energy is explained here by taking the preparation of an argon beam as an example.

The RGA is set to detect particles with a mass-to-charge ratio of 40, which is the molecular weight of the argon molecules. The data collected by this RGA is simultaneously output by the pre-installed MCS software to generate a graph of total RGA counts versus time for the particles with the set mass-charge ratio. When the incident molecular beam is 2%Ar/98%H_2 (Airgas, specialty gas), Figure 2.12 is the generated plot by the MCS.

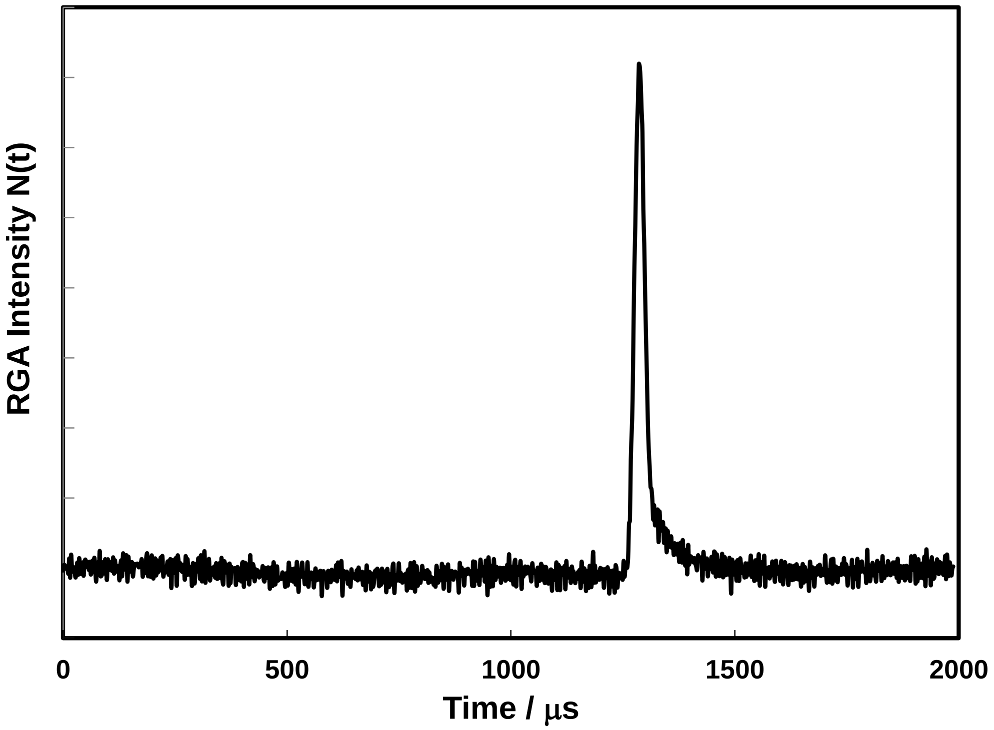

Figure 2.12 TOF distribution of Ar in a 2%Ar/98%H_2 molecular beam detected by RGA.

For the data shown here, the parameters in the MCS software are preset=200,000, path length=198, and dwell=10 μs. The preset indicates the total number of runs in each data file. By setting the dwell time as 10 μs, the software is arranged to collect the data in 10 μs bins, summed them and then output one data point. The path length of 198 means the software will collect 198 data points in one period, which makes the period of one run 198×10 μs=1980 μs=1.98 ms. After the collection of 198 data points, the software starts a new period. Each data file is the sum of 200,000 periods.

There is one gas pulse generated every 2.02 ms. Consequently, the real period is 40 μs longer than the detected period set in the software. Right after the detection of one period, the computer and the other electronic parts need some response time to start a new period. This difference is set to ensure the computer has enough time to start a new period so that each pulse can be detected after being generated.

To determine the incident energy of a specific molecular beam, the position of the peak in the distribution recorded by the MCS is employed. However, instead of selecting the direct reading of the peak position, there are several timing corrections required to get the true arrival time. The details of timing corrections are presented in Section 2.1.6.1. After all the timing corrections, the arrival time of the incident beam can be obtained. The velocity of the incident molecular beam is calculated by using the corrected arrival time and the distance from chopper wheel to RGA. Then the incident beam energy can be easily calculated by applying equation (12).

2.1.5.6 Molecular Beam Scattering

After characterization of the incident molecular beam, the sample mount is repositioned to the pre-aligned coordinates. At this point, the scattering experiments of molecular beams on sample surfaces can be performed following the procedure presented here.

a) After connecting the prepared gas source (as presented in Section 2.1.5.1) to the molecular beam chamber, the mechanical chopper wheel and the electronic trigger can be turned on. The rotational frequency of the chopper wheel is typically tuned to 495 Hz (2.02 ms).

b) The gate valve between the molecular beam chamber and the main chamber can then be opened to introduce the molecular beam into the UHV chamber. Since the sample position has been aligned, the incident molecular beam should collide with the center of the model surface. After the collisions with the surface, the gas molecules recoil back into the gas phase. Among these recoiled gas molecules, the ones with a final angle of 30°, with respect to the surface normal, can go through two collimating apertures, enter the detector chamber, and get analyzed by the Extrel QMS.

c) The TOF distribution of the scattered gas molecules can be recorded by employing the Extrel QMS and MCS software.

2.1.5.7 Quadrupole Mass Spectrometry

The recorded, raw time of flight distribution of Ar molecules (in 2%Ar/98%H_2 beam) scattered from an OH-SAM is shown in Figure 2.13.

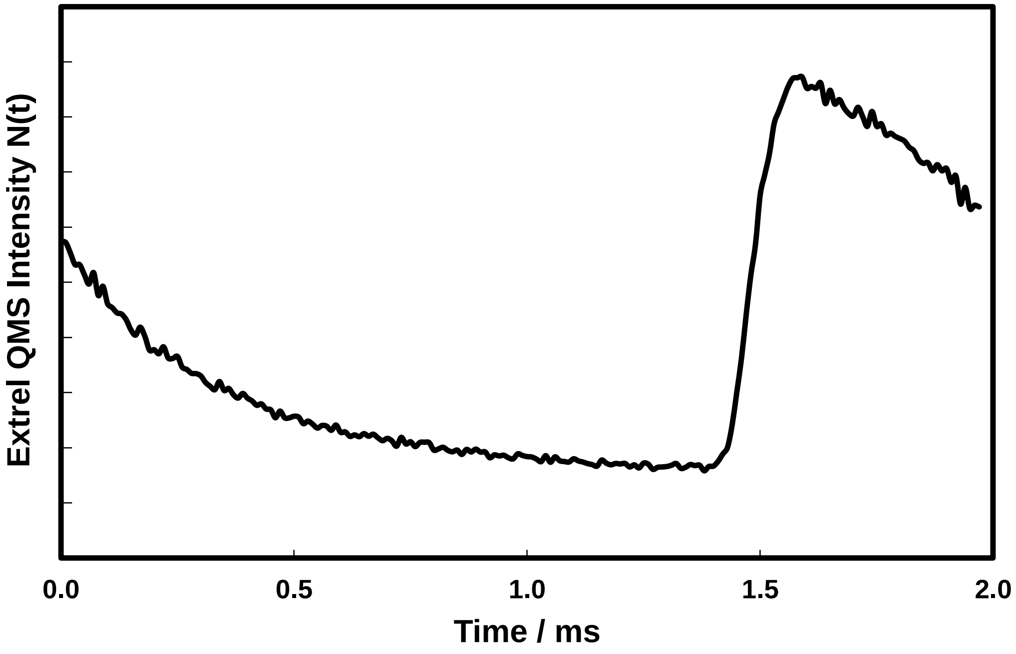

Figure 2.13 TOF distribution of an Ar (2%Ar/98%H_2) beam scattered from an OH-SAM.

The ionizer of the Extrel QMS is located 29 cm away from the surface; it views an approximately 1cm^2 spot of the surface through the two apertures in the detector chamber. To obtain the TOF distribution shown in Figure 2.13, the mass-to-charge ratio (m/z) of argon is set as 40. Analysis of this raw data is accomplished by the following the general guidelines in Section 2.6.1, which describe corrections for timing and intensity aspects of the experiments.

2.1.6 **Data Analysis**

2.1.6.1 Timing

The molecular beam passes through the aperture of the skimmer and then is chopped into gas pulses by a 2-slit chopper wheel. During the rotation of the chopper, as shown in Figure 2.14, the gas molecules pass through the slits to form a pulse every time the slit of the chopper wheel is aligned with the skimmer aperture.

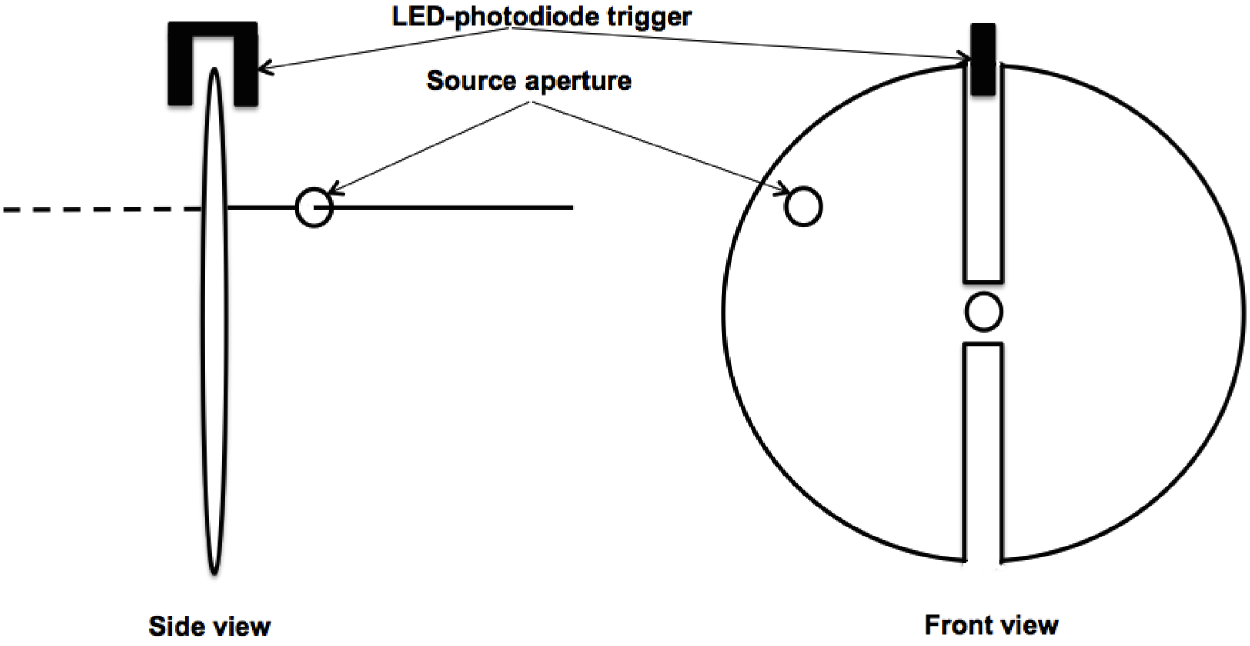

Figure 2.14 Side view and front view of the chopper wheel and trigger.

There is a LED-photodiode trigger located at the edge of the chopper wheel. This trigger is connected to a computer and an oscilloscope. It triggers the computer to start a new period of data collection by sending an electronic signal every time a chopper slit is aligned with the trigger (the position that is shown in the front view of Figure 2.14) The voltage of the trigger is 4.5 V and the trigger frequency of the chopper is set to be 495 Hz.

There are two slits on the chopper. In one rotation, each slit passes the trigger once, so there will be two gas pulses generated. After the gas pulses enter the main chamber and collide with the surface, the desorbed gas molecules are detected by the QMS. Since the MCS software starts to collect data every time a slit of the chopper wheel is aligned with the trigger, the time of this alignment is the “time zero” for the raw data of Figure 2.13.

There are four main timing corrections in my experiments: electronic time offset, chopper wheel time offset, chopper-surface time offset, and mass spectrometer time offset. The electronic time offset is caused by the employment of the LED-photodiode trigger. When a slit of the chopper wheel is aligned with the trigger, the trigger will send an electronic signal to the computer to start a new run. However, due to the response time of the electronics, there will be a delay for this procedure. Based on previous literature, this time offset is estimated to be approximately 2 μs.[45] Although the electronic time offset is included in the overall analysis, the data is summed into 10 μs bins. Therefore, this offset has a negligible influence on the final TOF distribution.

The chopper wheel time offset is the time difference between trigger-chopper slit alignment and skimmer-chopper slit alignment. As demonstrated in Figure 2.15, in my experiments, the chopper is set to rotate counterclockwise (CCW). The LED-photodiode trigger will generate a trigger pulse to make the computer start a new run every time a chopper slit is aligned with it. The “time zero” in Figure 2.13 is the moment of this alignment. However, the gas pulse is generated when the chopper slit is aligned with the skimmer aperture. Therefore, the beam pulse is generated *after* the computer starts a new run, which is a significant timing offset for which the data must be corrected.

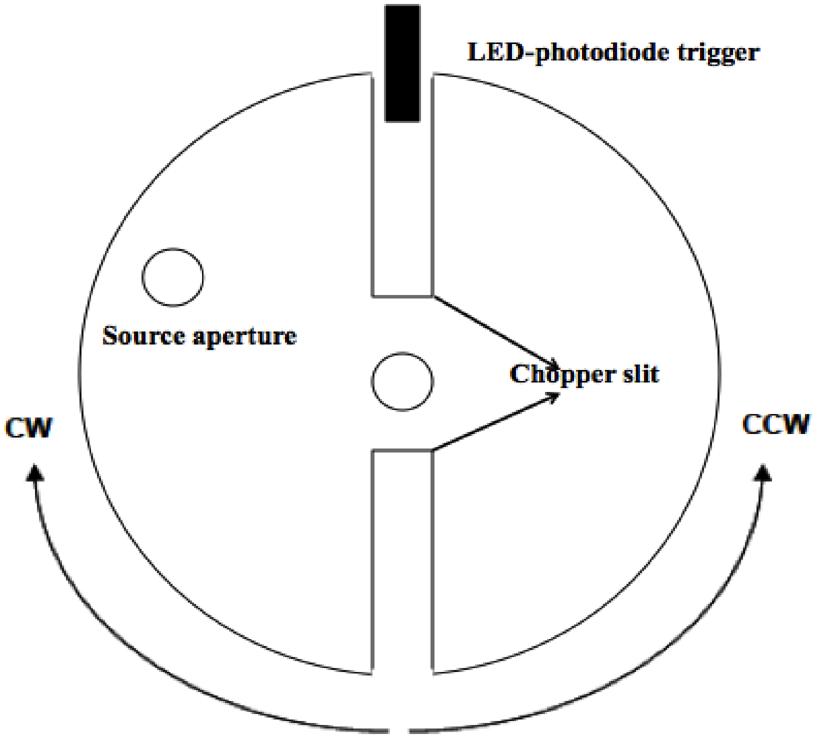

Figure 2.15 Front view of the chopper wheel for the demonstration of the time lag between the beam pulse and the trigger pulse.

To calculate the chopper wheel time lag, the pulse frequency is set to 495 Hz. As shown in Figure 2.16, if the chopper wheel rotates CCW, the travel time of one slit from the trigger to the source aperture is considered as y, and x is the time from this source-slit alignment to the moment when the other slit is aligned with the trigger. So, y should be the time lag that I have in the experiments. Since the beam pulse is after the signal pulse, y should be deducted from the total time. On the other hand, if the chopper wheel rotates CW, y will be the travel time of the slit from the source aperture to the trigger, and x is the time from this slit-trigger collimation to the moment when the other slit is aligned with the source aperture. Then, in this case, x will be the time lag. Since the beam pulse is still after the signal pulse, x should also be subtracted from the total time.

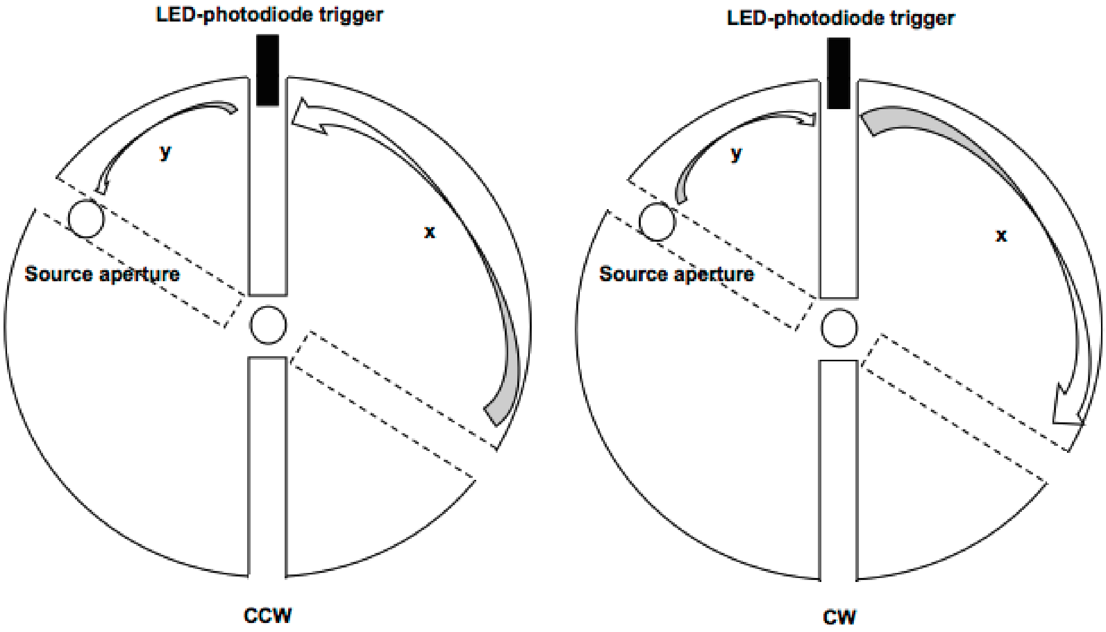

Figure 2.16 Schematic of the chopper wheel time offset calculation.

By employing an oscilloscope, I observe a pulse signal every time a slit passes the trigger. Therefore, the rotation period of the chopper with two slits should be equal to the time difference between the first pulse signal and the third following signal.

The rotation period can also be defined by using x and y in Figure 2.16 as 2(x+y). To solve y, another equation relating x and y is needed. Therefore, experiments that measure the TOF distribution of an incident beam under both CCW and CW conditions are performed. The TOF distributions of the incident molecular beams, as shown in Figure 2.17, are measured by employing the RGA. By comparing the peak positions of the TOF distributions measured under these two conditions, the time difference, x-y, can be obtained. By combining these two equations, x and y can be solved. Since in my research, the chopper wheel is set to rotate CCW, y is the time lag that needs to be subtracted from the total time.

The chopper-surface time is the next offset that needs to be considered. This time offset is the time it takes for the molecular beam to travel from the chopper wheel to the surface. Before performing gas-surface scattering experiments, the velocity of the molecules is calculated by using the arrival time and the distance from the chopper to the RGA. With the known velocity and the distance from the chopper wheel to the surface, which is 31 cm, the flight time of gas molecules from the chopper wheel to the surface can be obtained.

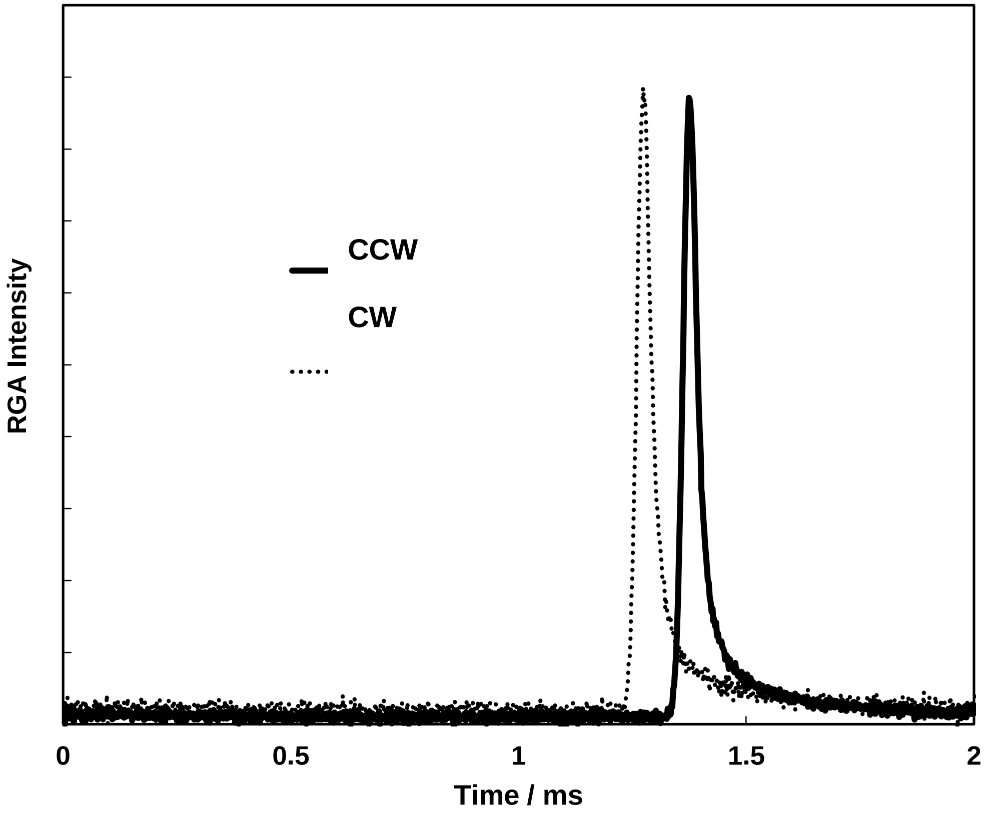

Figure 2.17 TOF distributions of a molecular beam under CCW and CW rotation of the chopper wheel.

After the reflected gas molecules enter the QMS, they require time for the ions to reach the detector. Therefore, the flight time of the gas ions in the QMS (mass spectrometer time offset) also needs to be subtracted from the total time. Based on previous literature,[45] an ion's flight time in a QMS before arriving at the detector can be calculated by applying equation (13).

$$t_q = \left(L_q \sqrt{\frac{1}{2E}} \sqrt{m} \right) \tag{13}$$

L_q is the effective length of the flight path in the quadrupoles, E is the translational energy of the ion and m is the mass-charge ratio. However, it is not necessary to obtain the exact values of L_q and E. As shown in equation (13), the flight time in quadrupoles is in proportional to the square root of the mass-charge ratio. So, if the pre-factor, $L_q\sqrt{\frac{1}{2E}}$ is known, the flight time of a specific ion can then be obtained by employing equation (13).

The value for this pre-factor has been determined in previous literature as 6.5.[45] I re-tested this value by performing argon (Airgas) scattering on a CH_3-SAM. In this experiment, a pure Ar beam is employed as the incident beam. Due to the low velocity and translational energy, the Ar atoms will collide and get fully accommodated with the surface. Therefore, after all the time corrections, the final TOF distribution should be a Boltzmann distribution at the surface temperature. As shown in Figure 2.18, by setting the pre-factor as 6.5, the corrected TOF distribution and the corresponding final energy distribution are both well fitted by the Boltzmann distribution at 298 K (surface temperature). Thus, it is reasonable to set the pre-factor as 6.5 in the data analysis.

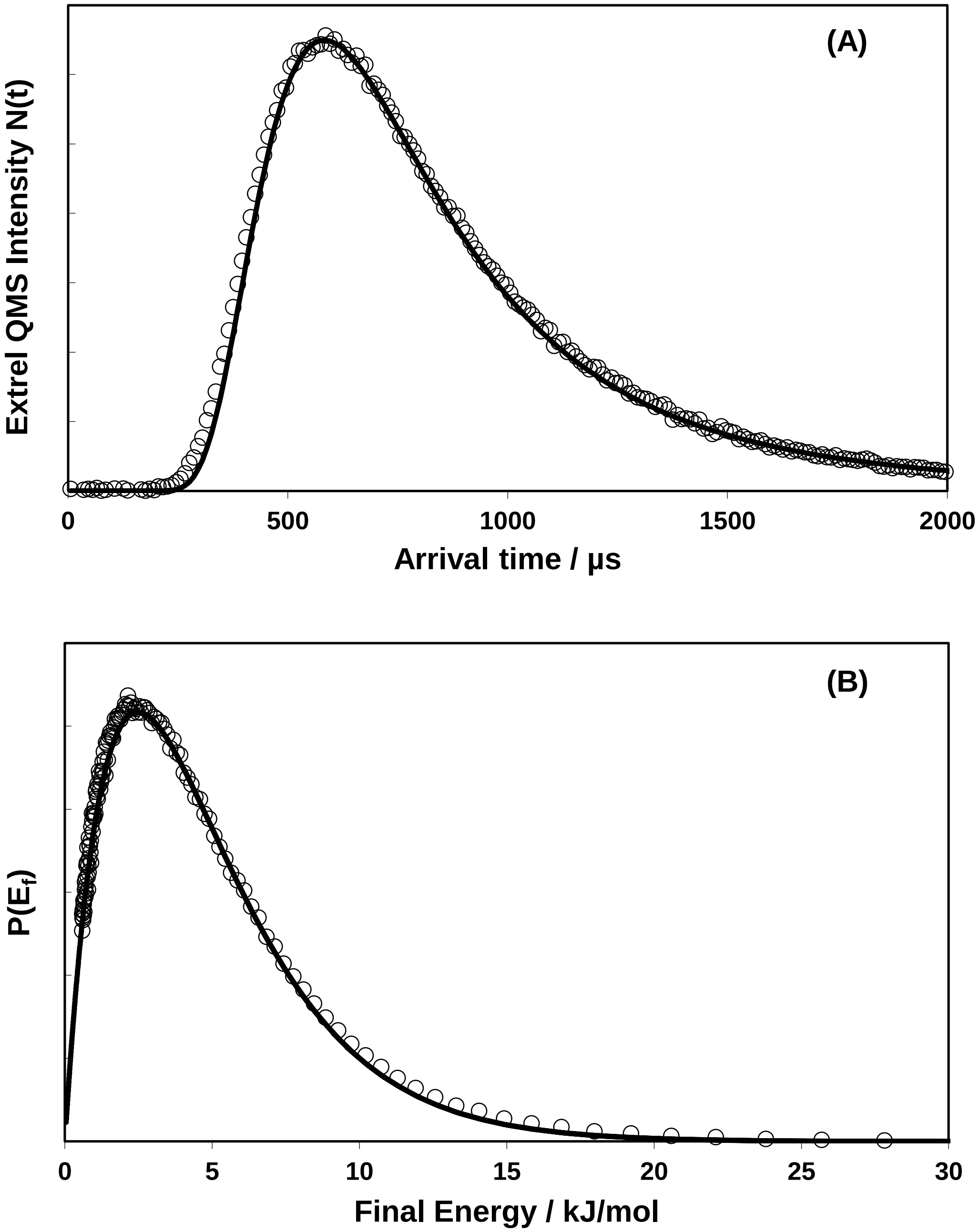

Figure 2.18 The TOF distribution (A) and the final energy distribution (B) of pure Ar scattering on an OH-SAM. The open circles represent the experimental data, and the solid lines are the Boltzmann distributions at the surface temperature.

Based upon all timing correction-related descriptions above, the time-axis of TOF distributions that are measured by the QMS in the detector chamber should be corrected by using equation (14). In this equation, t_{arrival} is the flight time for reflected gas molecules to travel from the surface to the entrance of the QMS; t_{total} is the measured flight time, which is the x-axis of Figure 2.13.

To sum up, $t_{\text{electronic}}$ is the response time of the LED-photodiode trigger, $t_{\text{chopper-wheel}}$ is the time difference between the beam pulse and the trigger pulse; $t_{\text{chopper-surface}}$ is the flight time from the chopper to the surface, and $t_{\text{mass-spec}}$ is the flight time in the quadrupoles before reaching the detector. The directly measured t_{total} originally contains all these time factors. By doing the time corrections shown in equation (14), the travel time from the surface to the detector entrance can be obtained. This corrected time can provide straightforward information about the behavior of gas molecules after their collisions with the surface. The corrected TOF distribution of Ar atoms (in 2%Ar/98%H_2 beam) after they collide with an OH-SAM is provided in Figure 2.19.

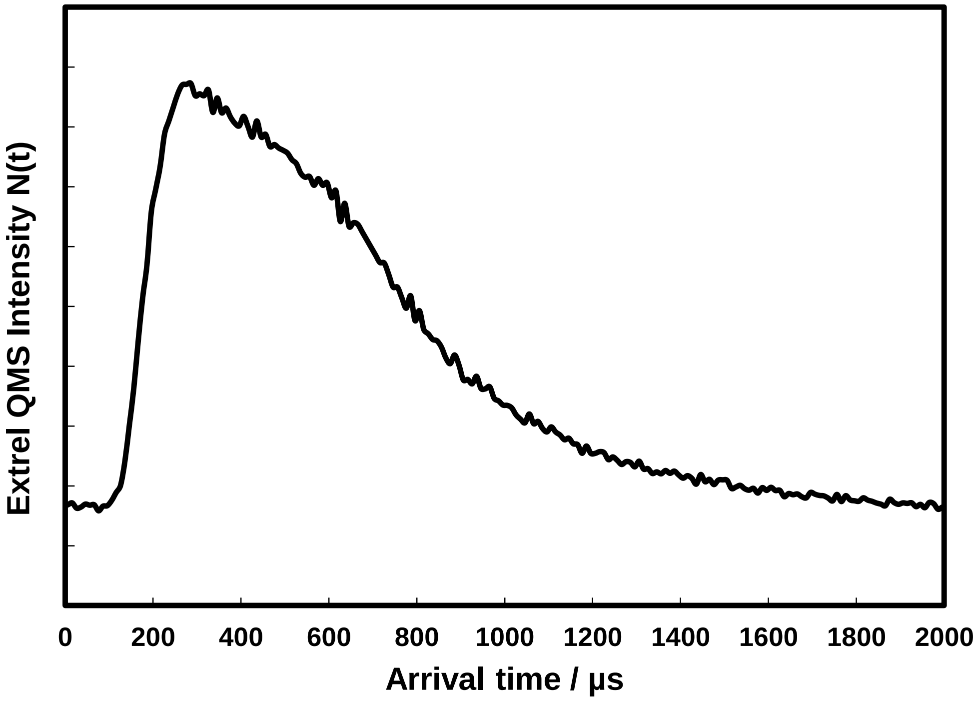

Figure 2.19 Time-corrected TOF distribution of Ar in the 2%Ar/98%H_2 beam after colliding with an OH-SAM.

The distance from the surface to the entrance of QMS is known as 29 cm. Therefore, based upon the corrected TOF distribution and this distance, the final energy distribution of the reflected gas molecules can be calculated. The energy transfer fraction during the gas-surface interactions can then be calculated by using equation (2).

$$t_{arrival} = t_{total} - \left(t_{electronic} + t_{chopper-wheel} + t_{chopper-surface} + t_{mass-spec}\right) \qquad \textbf{(14)}$$

2.1.6.2 Incident Beam Energy

The procedure of measuring the incident beam energy has been presented in Section 2.5.4. A 2%Ar/98%H_2 beam is employed as an example here to show exactly how to calculate this value.

The original TOF distribution of this beam is measured by the in-line RGA as shown in Figure 2.12. Since the calculation of the incident beam energy requires the flight time from the chopper to the RGA and the distance between these two parts, the time-axis of this TOF distribution must be corrected. In the raw data plot, the time shown in Figure 2.12 includes the electronic response time of the trigger, the chopper wheel time lag, and the flight time in the quadrupoles of the RGA before the ions reach the detector. To acquire the flight time from the chopper wheel to the entrance of the RGA, all these timing corrections must be subtracted according to equation (15).

$$t'_{arrival} = t'_{total} - \left(t_{electronic} + t_{chopper-wheel} + t_{RGA}\right) \qquad \textbf{(15)}$$

Both the electronic time offset and the chopper wheel time offset have been described above. However, the RGA and the Extrel mass spectrometer have different dimensions. Therefore, before reaching the detectors, the same ions' flight time in the two quadrupole mass spectrometers will be different. Equation (13) can be applied to calculate the time correction term, t_{RGA}. The slope of this equation was previously determined to be 3.6.[45] After all the time corrections, the TOF distribution of Ar in the 2%Ar/98%H_2 incident molecular beam is shown in Figure 2.20.

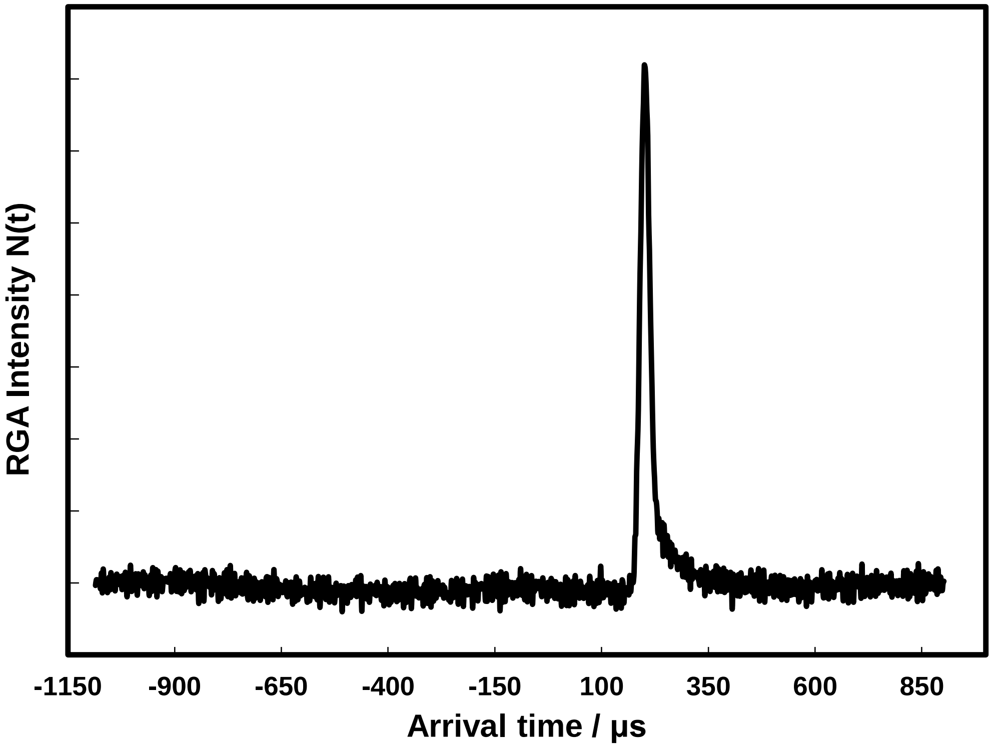

Figure 2.20 Time corrected TOF distribution of Ar in an incident 2%Ar/98%H_2 molecular beam detected by RGA.

As shown in Figure 2.20, after making all the time corrections, the flight time from the chopper wheel to the entrance of RGA can be determined, which in this case is 200 µs. The distance from the chopper wheel to the entrance of RGA is 45.3 cm. So, the energy of this incident Ar beam is determined to be 103±5 kJ/mol.

2.1.6.3 Analysis of TOF Data Detected by the Extrel QMS

With the pre-characterized incident molecular beams and SAMs, the final TOF distribution of the reflected gas molecules can be analyzed to acquire information to help interpret the dynamics of gas-surface interactions. Here, the scattering data of the 2%Ar/98%H_2 beam is employed to demonstrate how the final TOF distributions are analyzed.

As explained in Section 1.1.2.2 of this thesis, there are two possible pathways for the gas molecules to go through, impulsive scattering and thermal desorption. The gas molecules that are thermalized with the surface have a final TOF distribution that is the same as a Boltzmann distribution at the surface temperature. Therefore, the final TOF distribution can be fit by two components, the Boltzmann distribution at the surface temperature and the TOF distribution of the gas molecules that goes through the impulsive scattering pathway.

The detected signal in the final TOF distribution is proportional to the number density of the gas molecules, N(t). With the known arrival time and distance from the surface to the QMS, the final energy of the gas molecules can be obtained. The intensity of the final energy distribution, P (E_f), is proportional to t^2N (t). This correlation is related to the ionization probability of gas molecules when they enter the QMS that has an electron impact ionizer.[121] The probability of ionization is determined by the time the neutral species spend in the ionizer of the mass spectrometer. Compared with the high-speed gas molecules, the gas molecules that travel slower have a higher probability of ionization.

Figure 2.21 (A) shows the TOF distribution of Ar atoms after a 2%Ar/98%H_2 molecular beam is scattered from an OH-SAM. As previously mentioned, the data of Figure 2.21 (A) can be transformed to provide the final energy distribution, shown in Figure 2.21 (B). The data in Figure 2.21 (B) is then modeled with two limiting scattering pathways: impulsive scattering and thermal desorption. The two corresponding fitting components, impulsive scattering component (IS) and thermal-desorption component (TD) in Figure 2.21 (B) can then be transformed back to the TOF distribution.

In Figure 2.21 (B), the final energy distribution of the gas molecules is separated into an IS component and a TD component. After complete thermalization with the surface, the gas molecules have an identical energy distribution to that of the surface, which is the Boltzmann distribution at the surface temperature. Therefore, the first step of this fitting is to assign the Boltzmann distribution to the final energy distribution. At the surface temperature (298K), the translational energy Boltzmann distribution can be calculated by using equation (16). Then the IS component is determined by taking the difference between the total experimental energy distribution and the TD distribution.

$$P_{TD}(E_f) = \frac{E_f}{RT_{surf}} exp\left(-\frac{E_f}{RT_{surf}}\right) \quad \textbf{(16)}$$

Based upon the final energy distribution, the energy that is below 2.5 kJ/mol (RT_{surf}) is all assigned to the Boltzmann distribution, which means, $P_{IS}(E_f)=0$ for $E_f \leq 2.5$ kJ/mol. In Figure 2.21 (A), the IS (the sharp, high-velocity component with a peak position of approximately 256 μs (solid line)) and TD (the broad peak with later arrival time) in the final TOF distribution is transformed from the IS and TD in Figure 2.21 (B). In both (A) and (B) of Figure 2.21, the dashed lines are the Boltzmann distributions at the surface temperature, and the solid lines represent the impulsive scattering components.

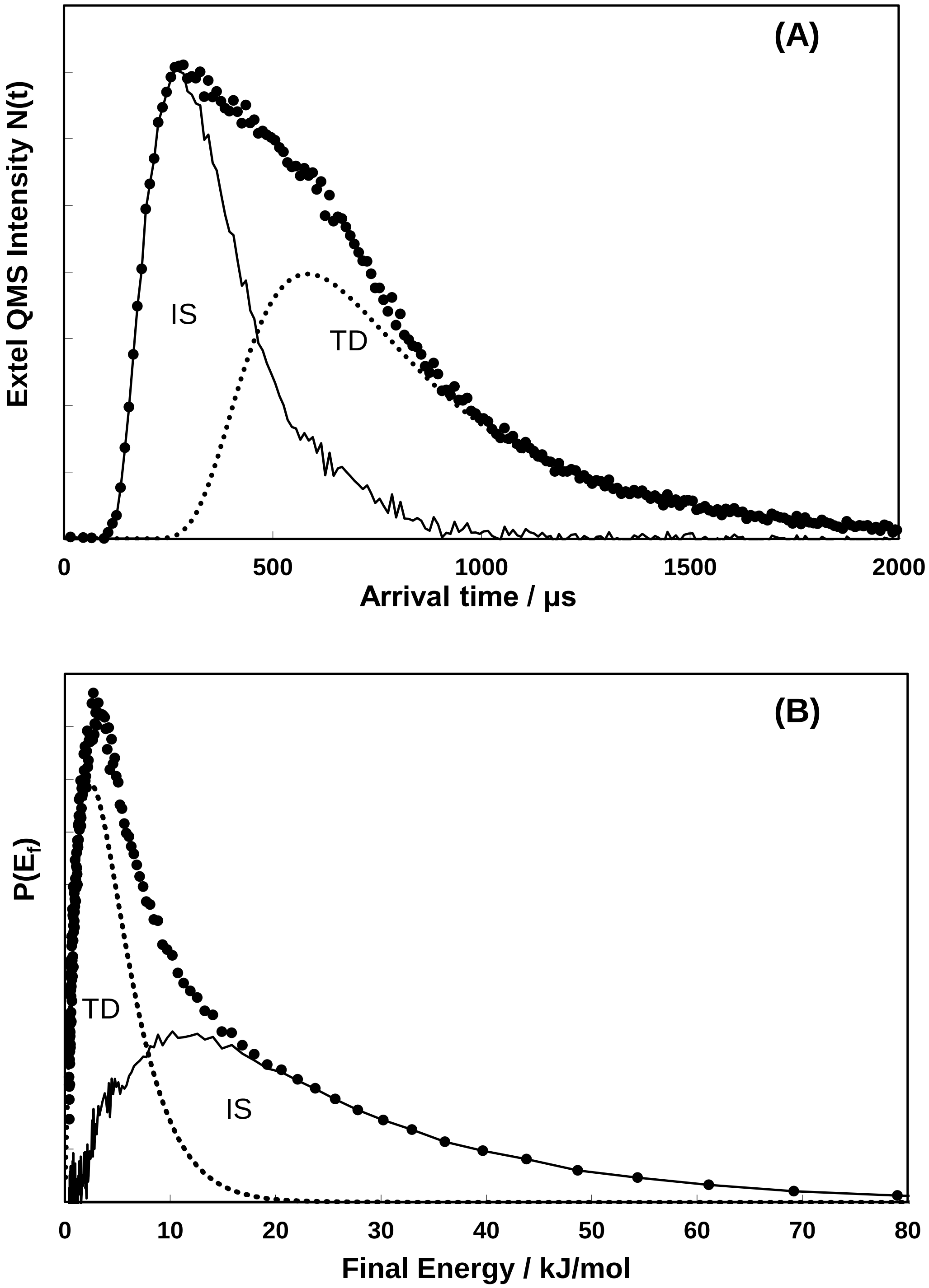

Figure 2.21 (A) TOF distribution of Ar atoms in a 2%Ar/98%H_2 beam after scattering from an OH-SAM; (B) The corresponding translational energy distribution $P(E_f)$ from (A).

The most important parameter employed in the next chapter to facilitate the understanding of the dynamics is the thermal-desorption (TD) fraction in the final energy distribution. The TD fraction is defined as the area fraction of the Boltzmann distribution in the final energy distribution.

The TD component in a specific gas-surface interaction provides information about how well the incident gas molecules thermalize with the surface, the rigidity of the surface, the ability of the surface to dissipate the energy transferred from the gas molecules, and the percentage of incident gas molecules that go through the thermal desorption pathway. The other parameter defined here is the IS fraction. The IS fraction is equal to the difference between the probability of the whole distribution (which is 1) and the calculated TD fraction.

$$TD = \frac{\int_0^\infty P_{TD}(E_f)dE_f}{\int_0^\infty P(E_f)dE_f} \qquad (17)$$

By performing different molecular beam scattering experiments from clean, well-characterized organic surfaces, the work described in this thesis has provided insight into the energy transfer efficiency between different gas molecules and surfaces. Overall, this information is providing a comprehensive understanding of how gas properties and surface structure and functionality affect the outcome of gas-surface interactions.

2.2 Nerve Agent Simulants-MOFs Interactions

2.2.1 Experimental Setup

Every gas-surface interaction starts from the initial collision. So I started with the simple gas-surface collision experiments to build a fundamental understanding of this step. Based on this understanding of interactions between small hydrocarbon molecules and model organic surfaces, the research was then furthered to much more complex materials, which are the metal organic frameworks.

Instead of RAIRS, transmission infrared spectroscopy is needed for proper characterization of this bulky material. To study the interaction mechanisms of chemical warfare agent simulants and MOFs, a slightly different experimental approach is needed.

Experiments were also performed in an ultrahigh vacuum (UHV) surface-science instrument as well, which enables a highly controlled flux of a gas of interest onto a particular material, and *in situ* monitoring of surface-bound products.[122-126] The instrument base pressure of 10^{-9} Torr ensured that background contamination remained below trace levels throughout the experiment. The MOF samples were prepared by pressing (~60 psi) approximately 15 mg of MOF powder into a 50-μm thick tungsten mesh grid (Tech-Etch) that could be resistively heated and cooled. During the experiment, the temperature of the sample was monitored by a type K thermocouple (chromel and alumel wires) spot welded adjacent to the sample.

The same as the molecular beam chamber, this chamber is also controlled by a custom-built computer interface and a LabVIEW program. So all the pumps and instruments are protected from unexpected instrument failures, power outage and potential leaks. In order to dose gas of interest directly onto the MOF, a vapor dosing system was attached to the main chamber as shown in Figure 2.22. The schematic of the dosing system can be found in Figure 2.23.

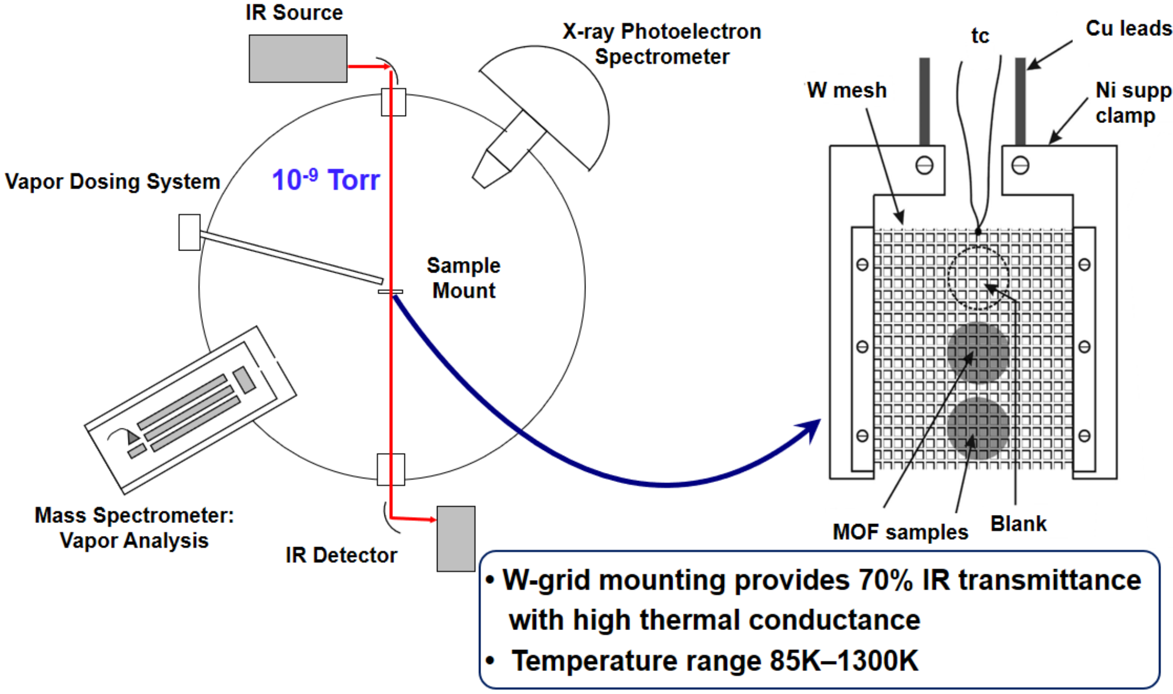

- W-grid mounting provides 70% IR transmittance with high thermal conductance
- Temperature range 85K–1300K

Figure 2.22 Top view schematic of the UHV chamber for CWA simulant-MOF interactions (left), and the zoomed view of the sample holder (right).

Before dosing, start with valve 7-9 and the pneumatic gate valve closed, and all other valves open, the manifold will be first pumped down by pre-cooled (by liquid nitrogen) sorption pump for about 30 minutes. Then close the right angle valve and the butterfly valve, open the pneumatic gate valve to further pump down the manifold to approximately 1×10^{-7} Torr. This may take another 30 minutes. The manifold will then be ready for dosing. Before dosing, All the valves should be closed first. Then gently open the two valves above the simulant of interest and valve 2. By adjusting valve 1 and monitoring the main chamber pressure through LabVIEW, the dosing pressure can be controlled.

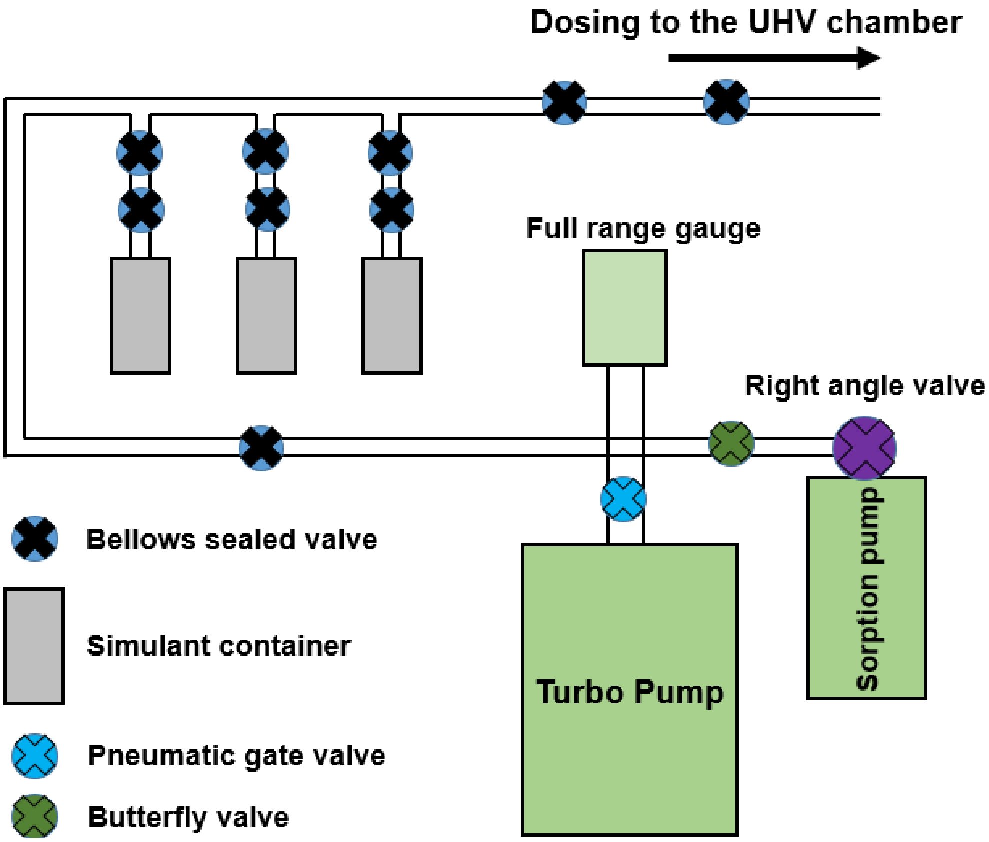

Figure 2.23 The schematic of the simulant dosing manifold.

2.2.2 Metal Organic Frameworks and Chemical Warfare Agent Simulants

The samples, UiO-66, UiO-67, and MOF-808, were synthesized by Dr. Weiwei Guo and Prof. Craig Hill (Department of Chemistry, Emory University) according to standard procedures that have been published in the previous literature.[100, 105] Before being pressed onto the tungsten mesh, the MOFs were activated by solvent exchange with methanol, followed by heating under vacuum at 100 °C for 1 hour. After being pressed and loaded into the UHV chamber, the MOFs were further heated to 100 °C for 10 minutes to drive off residual water.

DMMP (97%, purchased from Sigma-Aldrich) and DMCP (96%, purchased from Sigma-Aldrich) were each stored in a glass bulb attached to a bellows-sealed valve on a stainless steel gas-handling manifold. A stainless steel directional doser with a capillary array positioned approximately 5 mm from the sample was used to dose specific vapor to the sample. The schematic and dosing procedure can be found in section 2.2.1. The more detailed description of the heated manifold and doser can be found in previously published literature.[127] The flux of DMMP for these experiments was estimated to be 3×10^{15} molecules/s.

2.2.3 **Powder X-ray Diffraction**[103]

Prior to the experiments, each MOF was characterized by powder X-ray diffraction (PXRD). The characterizations and data analysis were performed by Dr. Anna Plonka, Dr. Qi Wang, and Prof. Anatoly Frenkel (Department of Materials Science and Chemical Engineering, Stony Brook University). All three samples used for further experiments were pure phase as no additional reflections were observed (Figure 2.24, Figure 2.25, and Figure 2.26). The unit cell values were in good agreement with those previously published (Table 2.2), indicating good quality and crystallinity of the samples.

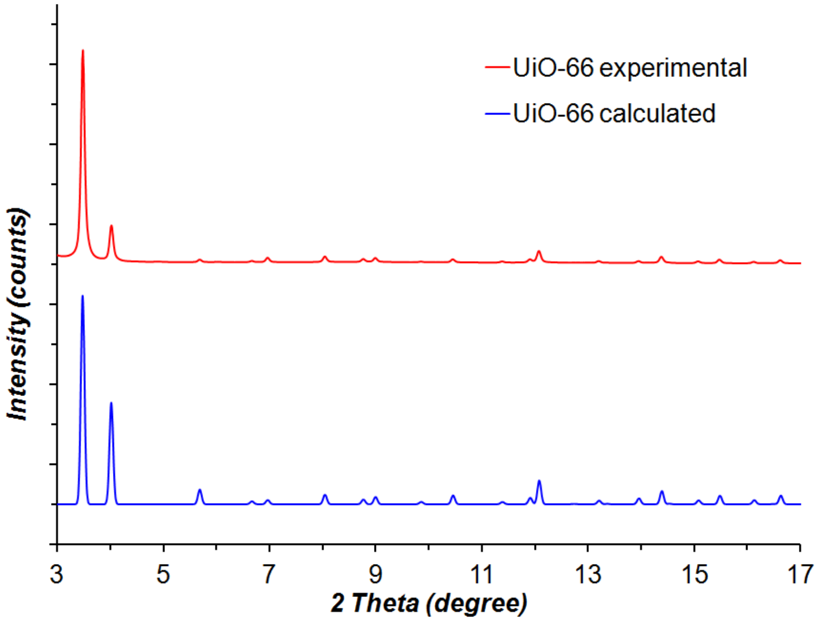

Figure 2.24 Experimental PXRD pattern of UiO-66 compared with the pattern calculated from the single crystal structure. No additional peaks indicate the purity of the sample.

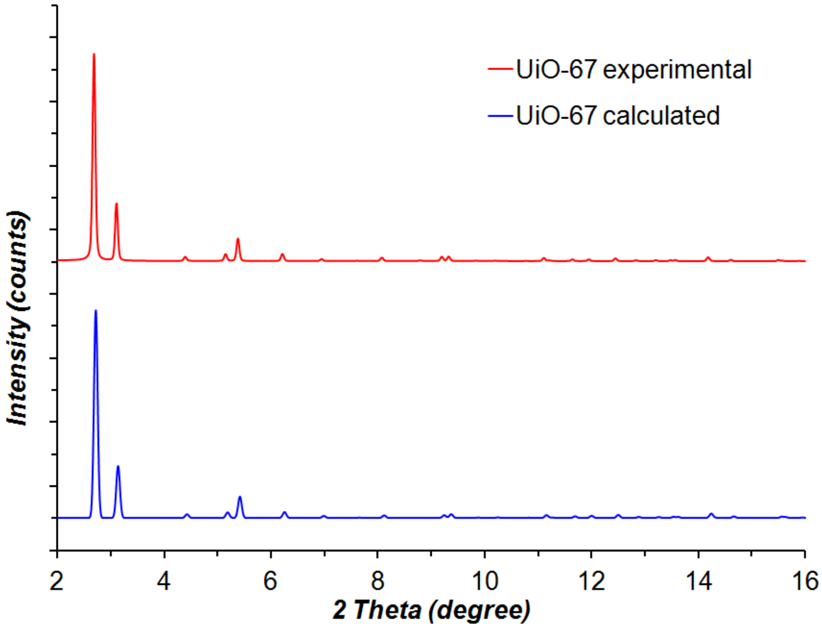

Figure 2.25 Experimental PXRD pattern of UiO-67 compared with the pattern calculated from the single crystal structure. No additional peaks indicate the purity of the sample.

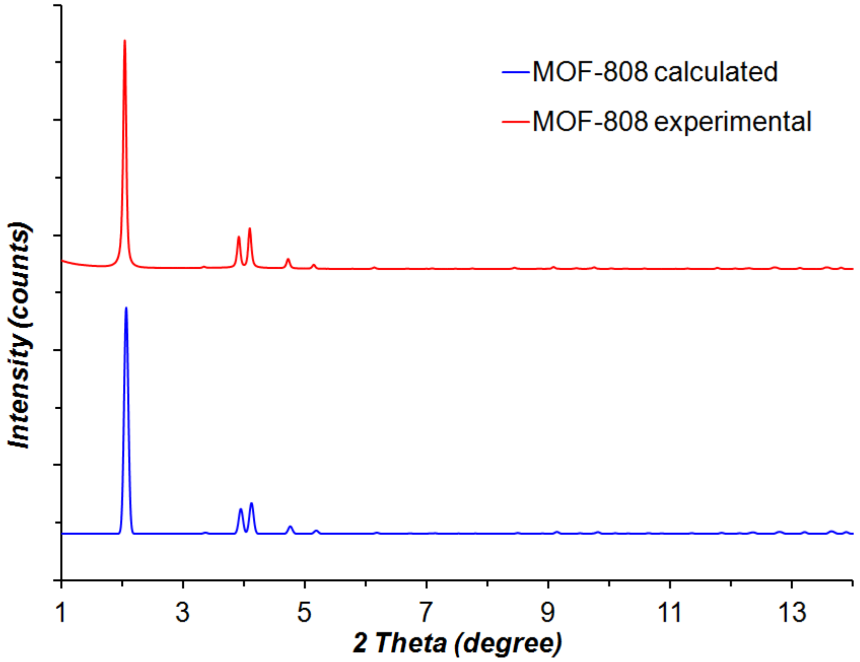

Figure 2.26 Experimental PXRD pattern of MOF-808 compared with the pattern calculated from the single crystal structure. No additional peaks indicate the purity of the sample.

The powder XRD measurements were performed with synchrotron X-rays at the 17-BM beamline at the Advanced Photon Source (APS) at Argonne National Laboratory with the fast and large 2D detector, using the beam of λ=0.72959 Å, and were analyzed using the GSAS-II software.[128] The unit cell parameters of all three MOFs were obtained from LeBail fitting, where peak shapes were refined with pseudo-Voigt function and peak asymmetry corrected with Simpson functions using the Jana2006 software.[129] The background was modeled manually using 50 points. The PXRD patterns of UiO-66, UiO-67, and MOF-808 are consistent with those of the ideal structures, as verified by comparison to models.[130-132]

Table 2.2 Unit cell parameters of UiO-66, UiO-67, MOF-808 from this study, compared with published results. Small differences in values arise from different temperatures of data collection.

MOF	this study		published	
	lattice parameter *a* (Å)	T(K)	lattice parameter *a* (Å)	T (K)
UiO-66	20.7582(6)	298	20.7465(2)*	100
UiO-67	28.845(1)	298	26.783(3)**	100
MOF-808	35.371(2)	298	35.0764(10)***	100

*[130], **[131], ***[132]

2.2.4 **Transmission Infrared Spectroscopy**

Interactions between DMMP/DMCP and the MOFs were monitored in real time by a Bruker IFS 66v/S spectrometer, in conjunction with a mercury cadmium telluride (MCT) detector, that was coupled to the UHV chamber via KBr viewports located on either side of the sample. Each of the spectra shown below was the average of 100 scans at a resolution of 2 cm^{-1}, with a 5 mm aperture and 20 kHz scan frequency. The spectra of MOFs in this paper were recorded by using a blank spot on the tungsten mesh as the background, while the clean, pre-exposed MOFs were employed as the background for data presented as difference spectra.

2.2.5 **X-ray Photoelectron Spectroscopy**

The XPS spectra were recorded using the monochromatic radiation (beam diameter 100 μm, 15 kV) from a Versa Probe III (Physical Electronics). To control charging of the samples, an electron neutralizer (1 eV) and an argon ion gun (10 eV) were used during the measurements. The plots below represent the average of 900 scans for the phosphorus *2p* electrons and 30 scans of zirconium *3d* electrons.

Chapter 3 The Energy Transfer and Thermal Accommodation in Collisions of Hydrocarbon Gases at Organic Surfaces

3.1 Introduction

Interfacial reactions between organic particles and atmospheric gas molecules play a central role in regulating atmospheric gas concentrations, processing aerosols, and aging materials. The interactions may result in changes in particulate composition, size, and physical properties. These changes affect human health, visibility, climate, and the global carbon cycle.[133] Energy transfer (thermal accommodation) is the first step in many gas-surface interfacial reactions, as well as in condensation events that lead to the growth of aerosol particles. Therefore, the primary goal of my research was to develop a fundamental understanding of the chemical and physical properties of molecules that affect interfacial energy transfer and thermal accommodation. I am particularly interested in whether bulk properties, such as solubility, can be employed to predict accommodation efficiencies when the molecules collide with polar and non-polar organic surfaces.

In the research presented in my master's thesis, I discussed the gas-surface energy transfer dynamics of diatomic gas molecules and organic surfaces, and factors that play a role in this process. The effect of dipole moment on gas-surface energy transfer was investigated by scattering diatomic gas molecules on the same OH-SAM and recording the TD fractions. $^{14}N_2$ has the same molecular weight as CO, and $^{15}N_2$ has the same molecular weight as NO. However, CO and NO have permanent dipole moments that may lead to dipole-dipole interactions with the terminal groups of a hydroxyl –terminated surface (as modeled by an OH-SAM—see Chapter 1). $^{14}N_2$, $^{15}N_2$, CO, and NO gas-surface scattering experiments were performed under the same conditions (same incident beam energy, incident angle, temperature, etc.). If intermolecular force plays an essential role in determining gas-surface interaction dynamics, then CO and NO may exhibit higher thermal accommodation efficiencies than $^{14}N_2$, $^{15}N_2$, respectively. The experimental results of $^{15}N_2$, $^{14}N_2$, NO and CO scattering on an OH-SAM are summarized inTable 3.1, and the corresponding final energy distribution comparisons are provided in Figure 3.1.

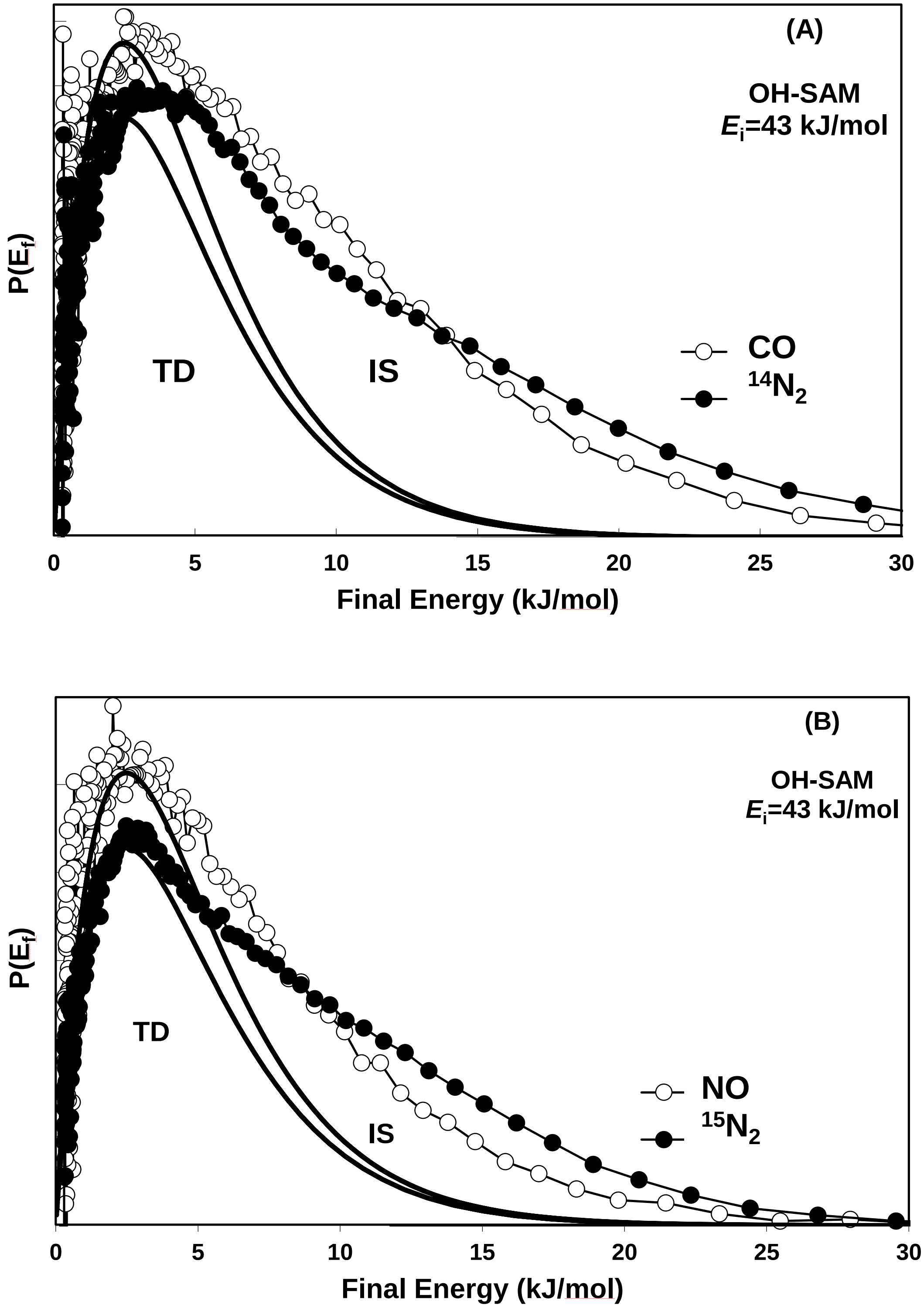

Figure 3.1 The final energy distributions comparison: $^{14}N_2$ and CO (A), $^{15}N_2$ and NO (B). Solid lines represent the TD components.

Table 3.1 Comparison between $^{15}N_2$ and NO, $^{14}N_2$ and CO scattering on an OH-SAM for E_i=43kJ/mol.

Gas source	Dipole moment (D)	TD (±0.02)	Gas source	Dipole moment (D)	TD (±0.02)
$^{15}N_2/H_2$	0	0.62	$^{14}N_2/H_2$	0	0.61
NO/H_2	0.169	0.67	CO/H_2	0.101	0.64

The experimental results demonstrated that the TD fraction is higher for molecules with a dipole moment (NO and CO). Thus, intermolecular forces play a role in energy exchange. This idea is reinforced by the comparison between NO and CO. Compared with CO, NO possesses a higher dipole moment, a higher TD fraction.

Furthermore, in the study of diatomic gas molecules (O_2, N_2, CO and NO) scattering on organic surfaces, a correlation was observed between energy transfer efficiency (TD fraction) and the solubilities of gas molecules in specific solvents. The solubilities of O_2, N_2, CO and NO in both water and hexane decrease in the order of $S_{NO} > S_{O2} > S_{CO} > S_{N2}$. I found that the same trend describes the relative TD fractions for these molecules scattering from the OH-SAM and CH_3-SAM. The thermal accommodation fractions for the gases upon colliding with the OH-SAM (CH_3-SAM) are plotted, versus the solubility of the gas molecules in water (hexane), in Figure 3.2 (**Error! Reference source not found.**). This correlation supports the notion that, for O_2, N_2, CO, and NO, larger solubility corresponds to higher thermal accommodation efficiencies, and, as a result, more efficient energy transfer.

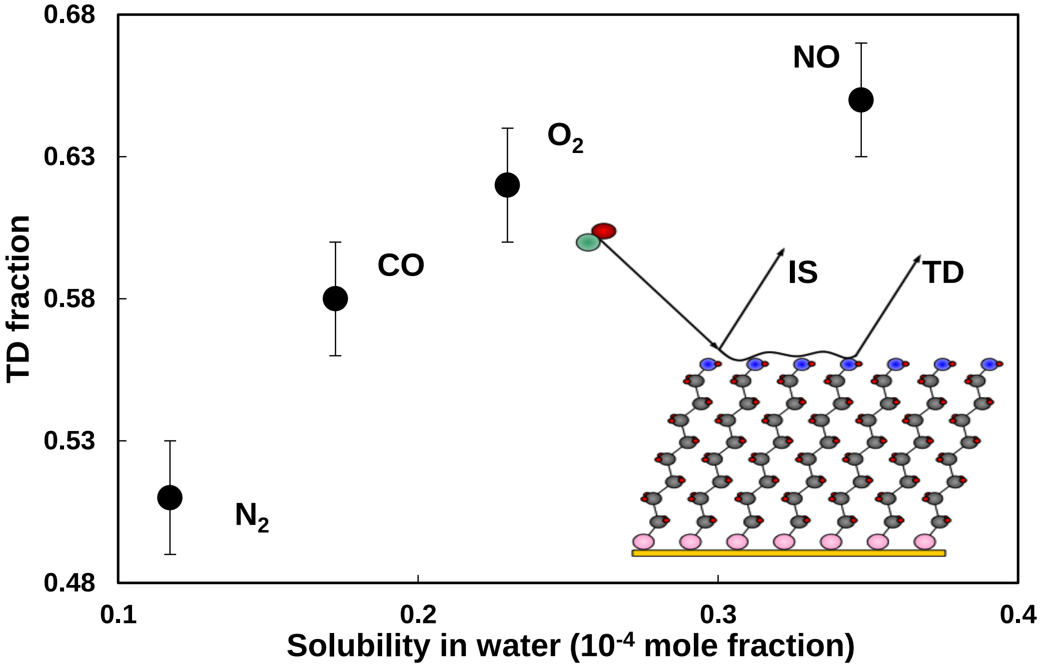

Figure 3.2 Thermal desorption fractions of gas scattering on an OH-SAM versus the solubilities of gas molecules in water. [134]

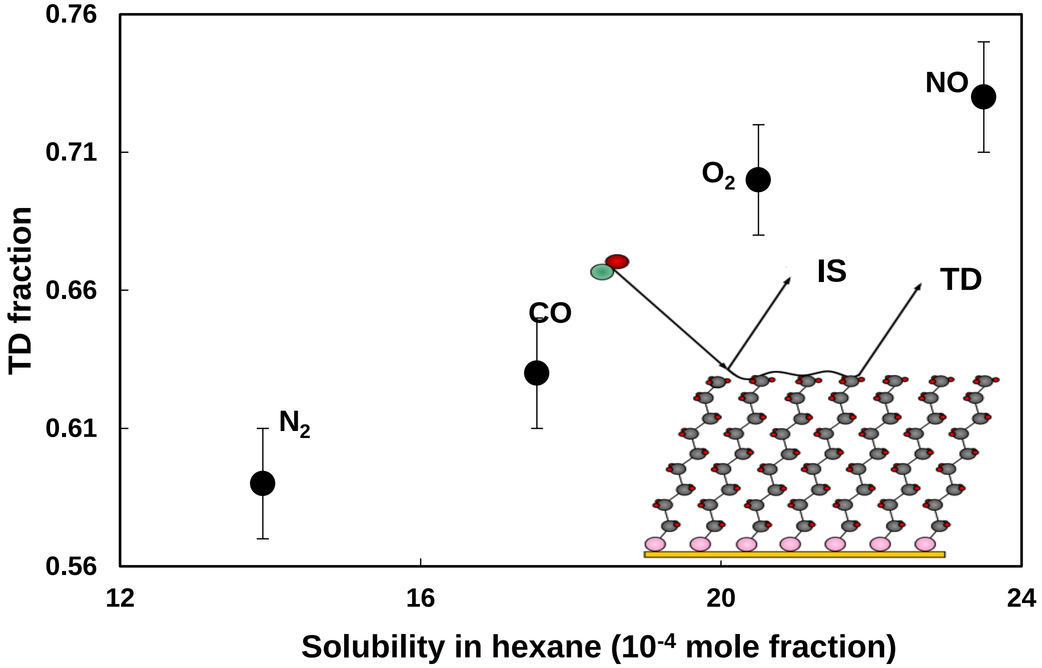

Figure 3.3 Thermal desorption fractions of gas scattering on CH_3-SAM versus the solubilities of gas molecules in hexane. [135, 136, 137, 138]

The correlation between gas-surface energy transfer efficiency and solubility in analogous solvents for simple diatomic gas molecules leads one to hypothesize that similar trends may apply to more complex systems. The research presented in this thesis furthers the investigation to small hydrocarbon gas molecules. I tested this hypothesis with a systematic study of the collision dynamics of the three small hydrocarbons, ethane (C_2H_6), ethene (C_2H_4), and ethyne (C_2H_2). These molecules were selected because they are similar in size and mass, yet they have some key differences in their chemical properties, as provided in

Table 3.2.

Table 3.2 Properties of C_2H_6, C_2H_4, and C_2H_2.[65]

Gas	C_2H_6	C_2H_4	C_2H_2
Dipole moment (D)	0	0	0
Solubility in water ($\times10^{-3}$ mole fraction)	0.0362	55.1	251
Solubility in hexane ($\times10^{-3}$ mole fraction)	32.0	20.5	13.0
Mass (g/mol)	30	28	26
C-C bond order	1 (1 σ)	2 (1σ, 1π)	3 (1σ, 2π)
C-C Bond length (Å)	1.54	1.35	1.21
C-C Bond strength (kcal/mol)	83	125	230
Polarizability(10^{-40} Cm^2/V)	5.00-5.06	4.69-4.76	3.74-3.94
pKa	>51	44	25
Molar heat capacity (at 300 K, $J\cdot mol^{-}1\cdot K^{-1}$)	52.71	43.08	44.17
Boiling point (K)	184.6	169.5	-
Melting point (K)	90.4	104.0	192.3

At room temperature, all three non-polar molecules are colorless, odorless, and flammable. Furthermore, they also share similar molecular weights and molar heat capacities. Their distinguishing characteristics, due to different bond orders, are their ionization potentials. The chemical structures of C_2H_6, C_2H_4, and C_2H_2 are provided in Figure 3.4. The double bond and triple bond in C_2H_4 and C_2H_2 are regions of high electron density. Thus they are susceptible to attack by electrophiles. While C_2H_6 has a three-dimensional structure, C_2H_4 is planar, and C_2H_2 is linear. The solubilities of these three molecules in water and *n*-hexane also vary in interesting ways as previously mentioned in section 1.1.4.

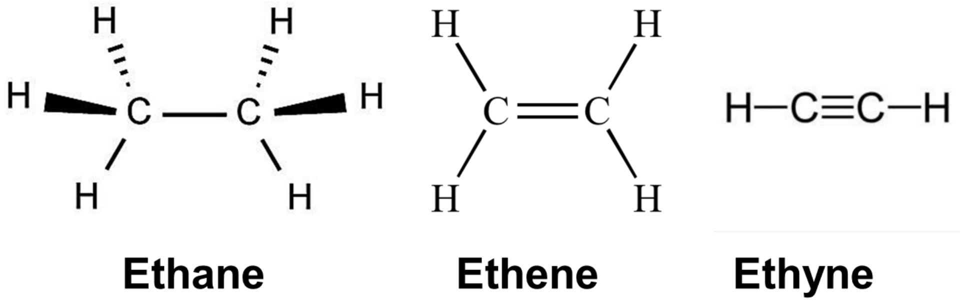

Figure 3.4 Chemical Structures of ethane, ethene, and ethyne.

Despite the simple structure and well-documented properties of small hydrocarbon molecules, surprisingly little is known about how small hydrocarbons behave at the gas-surface interface, and how their fate is affected by properties of the surface itself. A previous study by B. Scott Day et al. shows that intra-surface hydrogen bonding plays a major role in the gas-surface energy transfer for rare gas scattering on hydroxyl-terminated organic surfaces. As shown in Figure 3.5, the thermal desorption (TD) component is much larger for the 40 kJ/mol Ar atoms scattering from the CH_3-SAM than it is in the scattering from the OH-SAM, which indicates a more efficient energy transfer in the Ar-CH_3-SAM scattering.[26] Further study on the scattering of

Ne, deuterated methane (CD_4) , deuterated water (D_2O), and deuterated ammonia (ND_3) on hydrogen bonding and hydrocarbon SAMs were done by Megan E. Bennett et al. Their results show that the gas-surface energy transfer depends on the balance between the surface rigidity (determined by the intramonolayer hydrogen bonding) and the gas-surface attractive forces (determined by the intermolecular interactions). While the intramonolayer hydrogen bonding remains the dominating factor affecting energy transfer when Ne and CD_4 colliding on the OH-SAM and the NH_2-SAM, the deep potential energy well of polar gases, ND_3 and D_2O, makes them become trapped very efficiently on the OH- and NH_2-SAMs. As a result, ND_3 and D_2O overcame the rigid nature of the surface, imposed by the intra-surface hydrogen bonding network, and transferred the majority of their excess collision energy to the surface.[139] The analogous studies have not been done with small hydrocarbon gases.

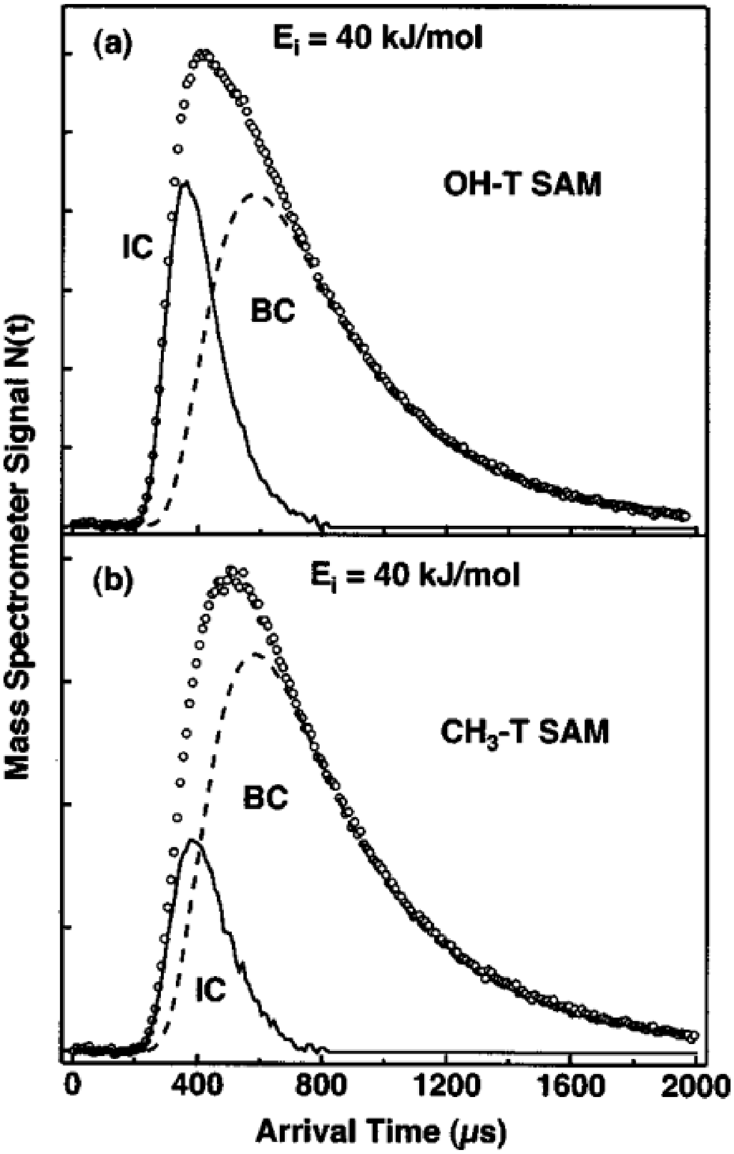

Figure 3.5 Comparison of Ar scattering from (a) an OH-SAM and (b) a CH_3-SAM. The dashed lines represent the TD components. Figure adapted from reference.[26]

My goals have been to extend this previous work to uncover the dynamics of interfacial collisions of small hydrocarbon molecules. Key research objectives for this project include:

(1) Determine if molecular rigidity and electron density–*i.e.*, molecules with single, double, or triple bonds, affect the extent of energy transfer in the initial gas-surface collision.
(2) Explore if surfaces functionalized by methyl groups behave differently, as collision partners, than the surfaces terminated with hydroxyl groups.
(3) Study how molecular scattering behavior may be correlated with the solubility of the compounds in hexane and water.

The research presented here will investigate these questions by measuring the energy transfer and thermal accommodation efficiencies for the three organic compounds when they collide with well-ordered model organic surfaces. The results will help researchers predict the transport rate of organic pollutants in the environment, the ability of small organic species to form secondary aerosol particles in the atmosphere, and the details of heterogeneous reactions at the gas-surface interface.

3.2 Experimental

The experimental apparatus was presented in section 2.1 of this thesis. The application of the ultrahigh vacuum chamber ($<10^{-9}$ Torr) enables the investigation of gas-surface interaction dynamics without interferences from background gases and surface contaminants. The SAMs (preparation procedure presented in section 2.1.5.2), used as model organic surfaces, were transferred to the main UHV chamber via a load-lock system and mounted on a precision manipulator.

The well-defined molecular beams were created by expanding the small hydrocarbon molecules, seeded in H_2 carrier gas, through a 0.05 mm diameter nozzle. After going through two differential pumping stages, as presented in section 2.1.3.2, the beam then passed through a 2.2 mm aperture to enter the main chamber and produce a 1 cm^2 spot size on the surface sample. The surface samples were aligned so that the normal is coplanar with the source and detector and at $\theta_i = \theta_f = 30°$ to the molecular beam and QMS. A fraction of the gas molecules that scattered from the surface was intercepted by a doubly differentially pumped Extrel mass spectrometer oriented at 60° to the incident beam such that $\theta_f = 30°$. The time-of-flight distribution of the incident gas beam was recorded by a residual gas analyzer (RGA) mass spectrometer, which was in line with the molecular beam.

3.2.1 Incident beam characterization

In work described here, the incident gas beams (C_2H_6, C_2H_4, and C_2H_2) were all generated with H_2 as the carrier gas. The H_2-seeded beams were found to provide excellent stability and narrow energy distributions. The data analysis procedure for the incident beam energy characterization is shown here by employing the C_2H_2/H_2 gas beam as an example.

The original time of flight (TOF) distribution of C_2H_2 in an incident C_2H_2/H_2 molecular beam was detected by a mass spectrometer in-line with the axis of the beam. The distribution (raw experimental data) is provided in Figure 3.6. As described in section 2.1.6.2, the time correction equation, as shown in equation (15), was employed to account for experimental timing offsets including the electronic response time of the LED-photodiode trigger ($t_{electronic}$=2.0 μs), the time difference between the beam pulse and the trigger pulse ($t_{chopper\text{-}wheel}$=1065.4 μs), and the flight time in the RGA (t_{RGA}). While the first two components are determined by the experimental apparatus, the flight time in the mass spectrometer is related to the molecular mass of a gas molecule and can be calculated based on equation (13). With M_{C2H2}=26.0 g/mol, and the pre-factor determined to be 3.60, the flight time in the mass spectrometer was determined to be 18.4 μs. Therefore, the corrected arrival time should be the measured time minus 1085.8 μs (2.0+1065.4+18.4 μs).

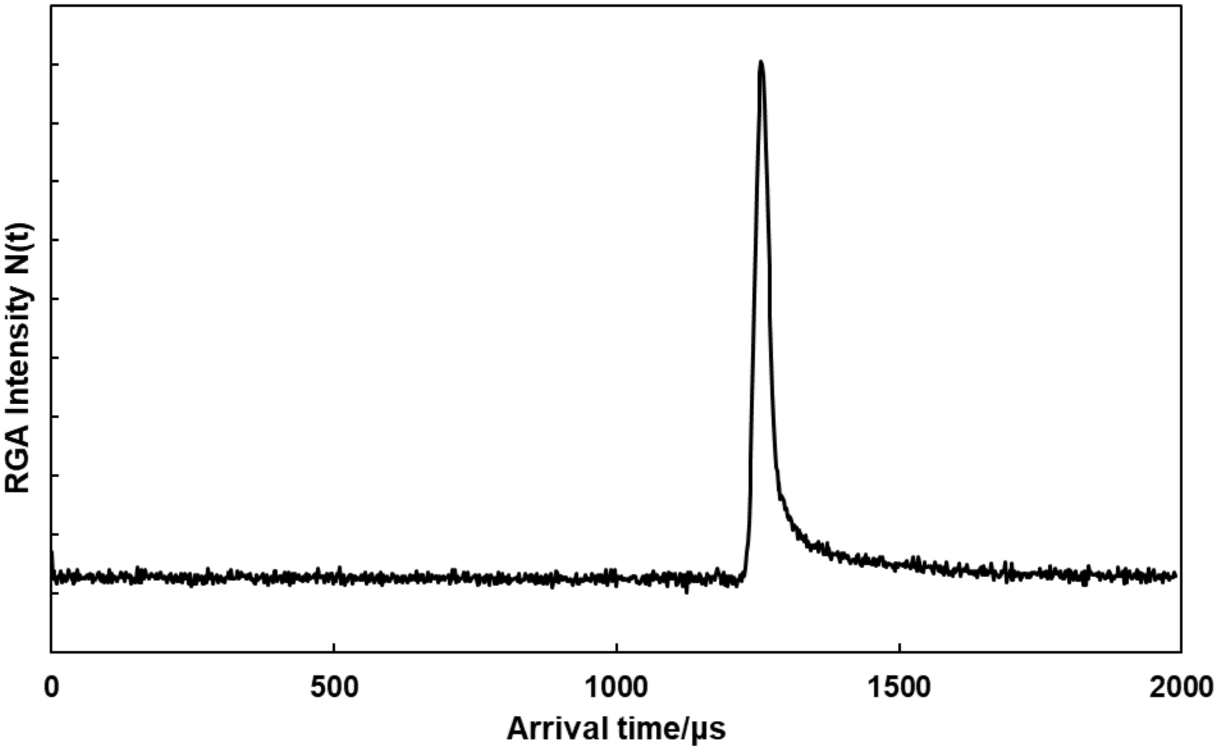

Figure 3.6 The original time of flight distribution of C_2H_2 in an incident C_2H_2/H_2 molecular beam detected by RGA.

The time-corrected TOF distribution of the C_2H_2/H_2 beam is shown in Figure 3.7. After the time correction, the peak position (corrected arrival time of C_2H_2 to the detector) is determined to be 168.2 μs. Based on the dimensions of the experimental apparatus, the distance from the chopper wheel to the entrance of the mass spectrometer is 0.4530 m. Therefore, the velocity of the C_2H_2 is 2693 m/s (0.4530 m/ 168.2 μs), and the corresponding incident beam energy is approximately 94.3 kJ/mol ($1/2m\upsilon^2$). This beam energy is very similar to that anticipated based on a 0.99 H_2:C_2H_2 seeding ratio in the beam and the kinetic theory of gases for expansion through a nozzle.[140]

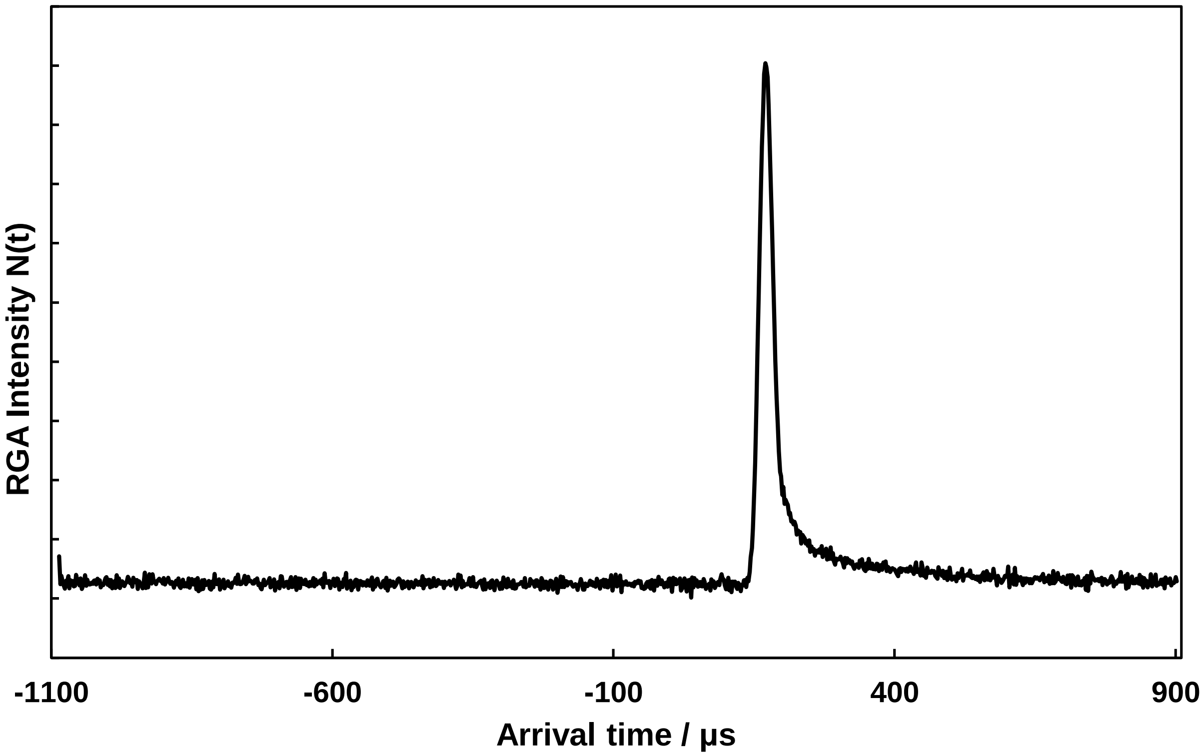

Figure 3.7 The time-corrected TOF distribution of C_2H_2 in the incident C_2H_2/H_2 molecular beam detected by RGA.

3.2.2 TOF distribution of surface scattered gas molecules

Upon the characterization of the incident beam, the gas beam was then applied to the study of gas-surface interactions. Mounted on the precision manipulator, the sample surface can be adjusted in position by changing the coordinates inside the UHV chamber, as shown in Figure 2.2. After characterizing the incident beam, the sample surface was lowered and rotated so that the normal is coplanar with the source and detector at $\theta_i = \theta_f = 30°$. The quadrupole mass spectrometer recorded a TOF distribution of the scattered gas molecules after they interacted and desorbed from the surface. A sample TOF distribution (C_2H_2 in the 95 kJ/mol beam scattered from a CH_3-SAM) is shown in Figure 3.8. Similar to the corrections described in the incident beam characterization procedure, the arrival time here in the TOF distribution was corrected for experimental timing offsets.

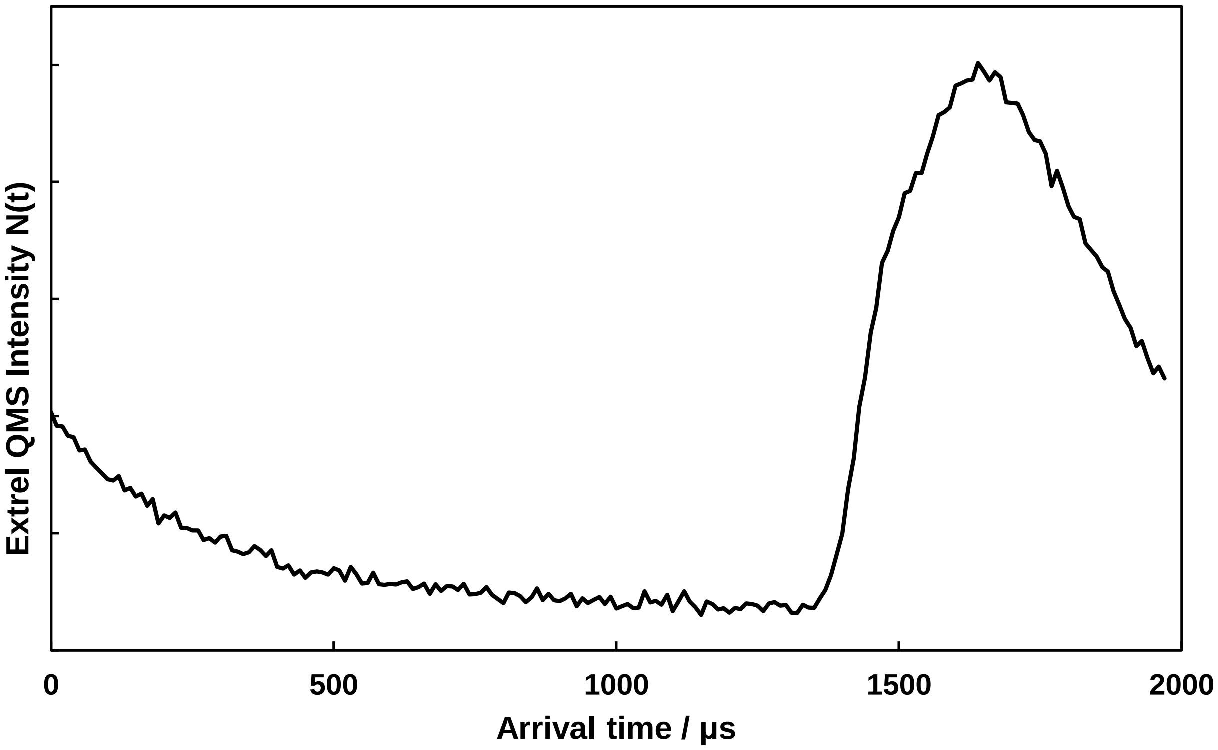

Figure 3.8 The original TOF distribution (raw data, as recorded) of C_2H_2 in the C_2H_2/H_2 beam after colliding with a CH_3-SAM.

As described by equation (14), there are four time components that are employed for determination of the true arrival time, the electronic response time ($t_{electronic}$=2.0 μs), the time difference between the beam pulse and the trigger pulse ($t_{chopper\text{-}wheel}$=1065.4 μs), the flight time in the QMS ($t_{mass\text{-}spec}$), and the flight time from chopper wheel to surface ($t_{chopper\text{-}surface}$). The first two components are the same as previously described for the incident beam characterization. The

$t_{mass\text{-}spec}$ was determined to be 33.1 μs by equation (13) with a molecular mass of 26.0 and pre-factor of 6.50 for the Extrel QMS. Based on the dimensions of the experimental apparatus, the distance from the chopper wheel to the surface is 0.3100 m. The velocity of the C_2H_2 beam was calculated to be 2693 m/s, based on the incident beam characterization. Therefore, the $t_{chopper\text{-}surface}$ was determined to be 115.1 μs. Overall, the corrected arrival time includes the measured arrival time minus 1215.6 μs ($t_{electronic}$ 2.0 μs + $t_{chopper\text{-}wheel}$ 1065.4 μs + $t_{mass\text{-}spec}$ 33.1 μs + $t_{chopper\text{-}surface}$ 115.1 μs). The time-corrected TOF distribution of the scattered C_2H_2 from a CH_3-SAM is shown in Figure 3.9.

Figure 3.9 Time- corrected TOF distribution of C_2H_2 in the C_2H_2/H_2 beam after colliding with a CH_3-SAM.

3.2.3 **Conversion from TOF distribution to final energy distribution**

Based on the time-corrected TOF distribution of the scattered C_2H_2 molecules, the final energy distribution can be derived. The final energy is calculated from the time-corrected arrival time from equation **(18)**, with L (29 cm) as the distance from the surface to the QMS ionizer, m is the molecular weight of the incident gas molecule, and $t_{corrected\text{-}arrival}$ is the flight time from surface to the ionizer (X-axis of the time-corrected TOF distribution).

$$E = \frac{1}{2} m \left(\frac{L}{t_{corrected-arrival}} \right)^2 \tag{18}$$

For each calculated final energy value, the corresponding probability can be calculated by using equation **(19)**, with N(t) as the QMS counts.

$$P(E) = \frac{t_{corrected-arrival}^2 N(t)}{mL} \tag{19}$$

Equation **(19)** is derived based on the fact that the following three distributions have the same integrated area. *I(t)* is the true intensity at the QMS, which can be derived from N(t) by equation **(20)**. The ionization probability of gas molecules in the QMS is inversely proportional to the velocity (proportional to 1/ v).

$$I(t)\ vs.t$$

$$I(v)\ vs.v$$

$$P(E)\ vs.E$$

$$\frac{1}{v} I(t) = N(t) \tag{20}$$

The fact that the integrated areas of these three distributions are the same can be expressed by equation **(21)**. And by plugging equation **(20)** into **(21)**, equation **(22)** can be derived.

$$\int_0^\infty I(t)dt = \int_0^\infty I(v)dv = \int_0^\infty P(E)dE \tag{21}$$

$$I(t)dt = vN(t)dt = \frac{L}{t}N(t)dt = P(E)dE \tag{22}$$

$$\frac{dE}{dt} = \frac{d\left[\frac{1}{2}m\left(\frac{L}{t}\right)^2\right]}{dt} = \frac{1}{2}m\frac{d(\frac{L}{t})^2}{dt} = -\frac{mL^2}{t^3} \tag{23}$$

Take the differentiation on both sides of equation **(18)** with respect to time, and the results are then shown in equation **(23)**. Moreover, by plugging equation **(23)** into equation **(22)**, a correlation between P(E) and N(t) can be derived as shown in equation **(19)**. Since *P(E)* cannot be negative, the negative sign in equation **(23)** can be ignored.

In this way, a final energy distribution (*P(E) vs. E*) can be derived from the time-corrected TOF distribution. In this chapter, both the TOF distribution and the final energy distribution will be provided. From these distributions, the fractional energy transfer and thermal accommodation efficiencies (for the scattering geometry employed in this work) will be determined.

3.3 **Results**

3.3.1 **C_2H_6, C_2H_4, and C_2H_2 Collisions with a CH_3-SAM**

This experiment was performed under UHV conditions to maintain the clean surface and minimize the interferences from background gases. The gas of interest (C_2H_6, C_2H_4, or C_2H_2) was seeded in the H_2 carrier gas of various seeding ratios, to create two distinct incident energies, 76 kJ/mol, and 96 kJ/mol. As described in Chapter 2, SAMs were employed in the experiments as model organic surfaces because they can be reproducibly synthesized with a specific functional group located precisely at the gas-surface interface. The *n*-alkanethiols employed for making SAMs were commercially available, with nominal purity > 97%, and used without further purification. The CH_3-SAM was prepared by first cleaning a flat Au substrate in piranha solution (70% sulfuric acid and 30% hydrogen peroxide). The substrate was then placed into a 1mM ethanolic solution of 1-octadecanethiol (Sigma-Aldrich) for 24 hours to ensure good chain order and packing density, followed by ethanolic rinsing and ultra-high purity nitrogen drying. Once created, the SAMs surface sample was installed into the UHV chamber via the load-lock system. Once aligned with the mass spectrometer, the molecular beam was introduced into the main chamber. The ionizer of the mass spectrometer was located 29 cm from the SAM surface and viewed a 1cm^2 spot size on the surface through two collimating apertures. The time-of-flight distribution of the scattered molecules was measured under specular scattering conditions ($\theta_i = \theta_f = 30°$) by the QMS and then analyzed to provide information that helps to investigate gas-surface interaction dynamics.

As previously mentioned, there are two possible pathways for the gas molecules after they strike a surface, thermal-desorption (TD) and impulsive scattering (IS). These two pathways are governed by the gas-surface potential energy surface (PES), the rigidity of the surface, and the efficiency of energy redistribution upon collision. As a gas molecule approaches a surface, the molecule typically experiences attractive forces due to dispersive or dipolar interactions. The attractive potential-energy well accelerates the gas molecule toward the surface. After the initial acceleration, the gas molecule experiences a potential-energy wall due to highly repulsive interactions between the gas and surface electrons. Upon collision, the repulsive wall reflects the molecule back into the gas phase, but not before absorbing some fraction of the impinging energy (purely elastic scattering does not occur in these systems where a very high density of energy states at the surface are available for excitation). After the energy transfer process, the scattering gas molecules exit along the attractive tail of the potential energy surface. If the gas molecule only loses part of its initial translational energy to the surface, and the retained energy is higher than the potential well, it will escape and return to the gas phase. This type of trajectory is considered as going through the IS pathway. However, if a gas molecule loses all of its excess energy to the surface, then during this reflection, it must gain energy from the thermal fluctuations of the surface. When this type of gas molecule obtains sufficient energy, they desorb into the gas phase with a Boltzmann distribution of energies at the surface temperature. The percentages of gas molecules that follow IS and TD pathways ultimately determine the fate of the gas-surface interaction. Therefore, in non-reactive gas-surface collisions, the gas molecules either follow the IS pathway or the TD pathway. Compared with gas molecules that go through IS pathway, the TD gas molecules lose more of their initial energy to the surface. The overall amount of energy transferred to a surface, the "energy transfer fraction," affects the overall trajectory and, ultimately, interfacial reactions.

The scattered gas molecules are analyzed by monitoring the quadrupole mass spectrometer (Extrel) signal at the parent mass (or largest fragment) as a function of time. With the integration interval of 10 μs, the time-corrected (procedure provided in section 3.2.2) time-of-flight distribution of the three small hydrocarbons upon scattering from a CH_3-SAM are shown in Figure 3.10. The solid lines in the figure represent a Boltzmann distribution at the surface temperature, which is referred to as the low-energy part of the final energy distribution shown in Figure 3.11. The molecules that emerge from the surface with a Boltzmann distribution of final energies are likely thermally accommodated with the surface following the dissipation of their excess translational energy and are considered as the thermal desorption (TD) component. The intensity of the TD component, as well as the arrival time of the leading edge of the TOF distributions, clearly depend on the specific hydrocarbon. Therefore, the energy transfer efficiency of C_2H_6, C_2H_4, and C_2H_2 are different. This will be further illustrated by showing the final energy distributions of these three molecules.

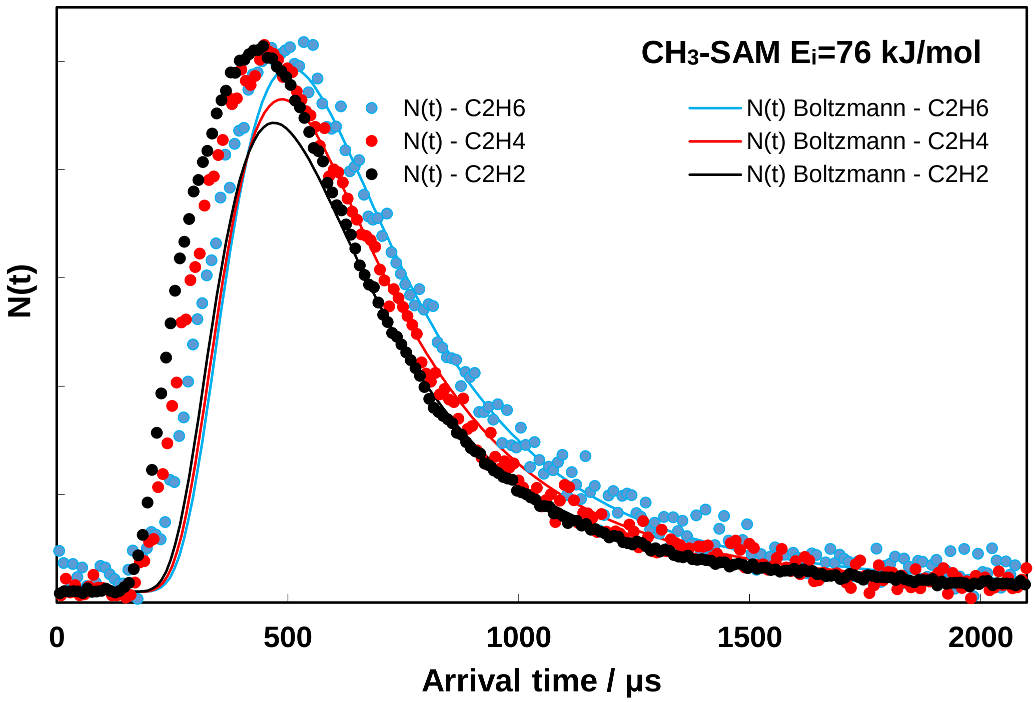

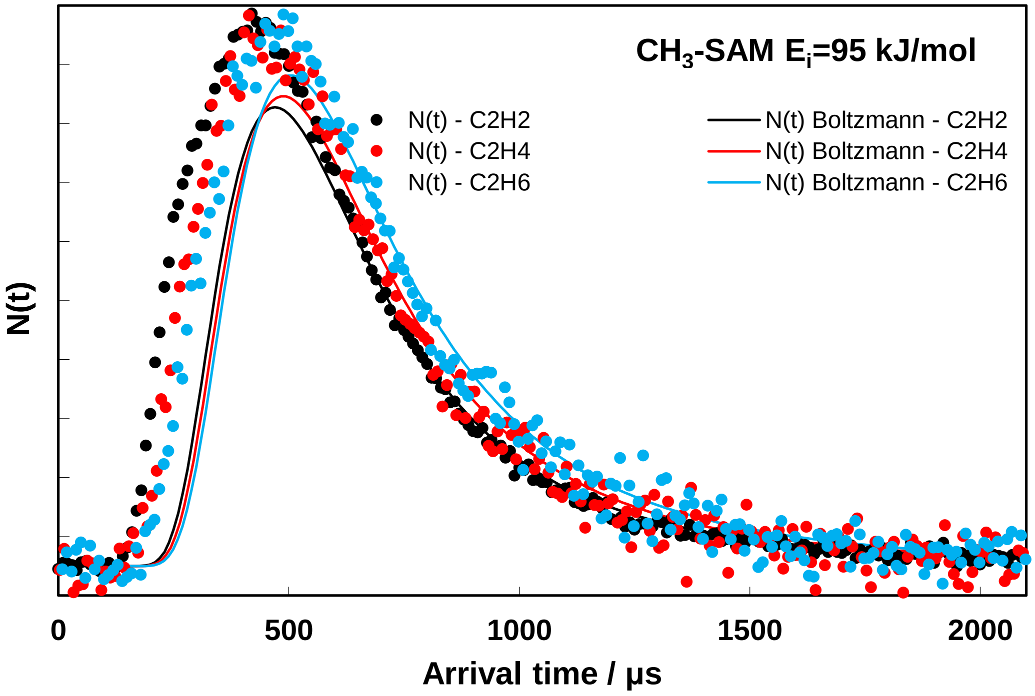

Figure 3.10 Time of flight distributions of C_2H_6, C_2H_4, and C_2H_2 scattering from a CH_3-SAM with the incident energy of 76 kJ/mol (top) and 95 kJ/mol (bottom). Solid lines represent the TD components (Boltzmann distributions at surface temperature), and the solid circles represent the experimental time of flight distributions.

The time-of-flight distributions in Figure 3.10 can be converted to final energy distributions, which provide direct and quantitative insight into the energy transfer efficiency. The final energy distributions for C_2H_6, C_2H_4, and C_2H_2 molecules after colliding with a CH_3-SAM are provided in Figure 3.11. In Figure 3.11, the TD component is described well by a Boltzmann distribution at the surface temperature (solid lines). The IS component is represented by the difference between the experimental data and the TD component. The fractions of TD and IS are determined by integration of each component. The TD fraction is equal to the area of the TD component over the total area, as shown in equation **(24)**. The overall final energy distribution is the sum of TD component and IS component, see equation **(25)** and **(26)**.

$$\alpha_{TD} = \frac{Area_{TD}}{Area_{Total}} \tag{24}$$

$$1 = \alpha_{TD} + \alpha_{IS} \tag{25}$$

$$Area_{Total} = Area_{TD} + Area_{IS} \tag{26}$$

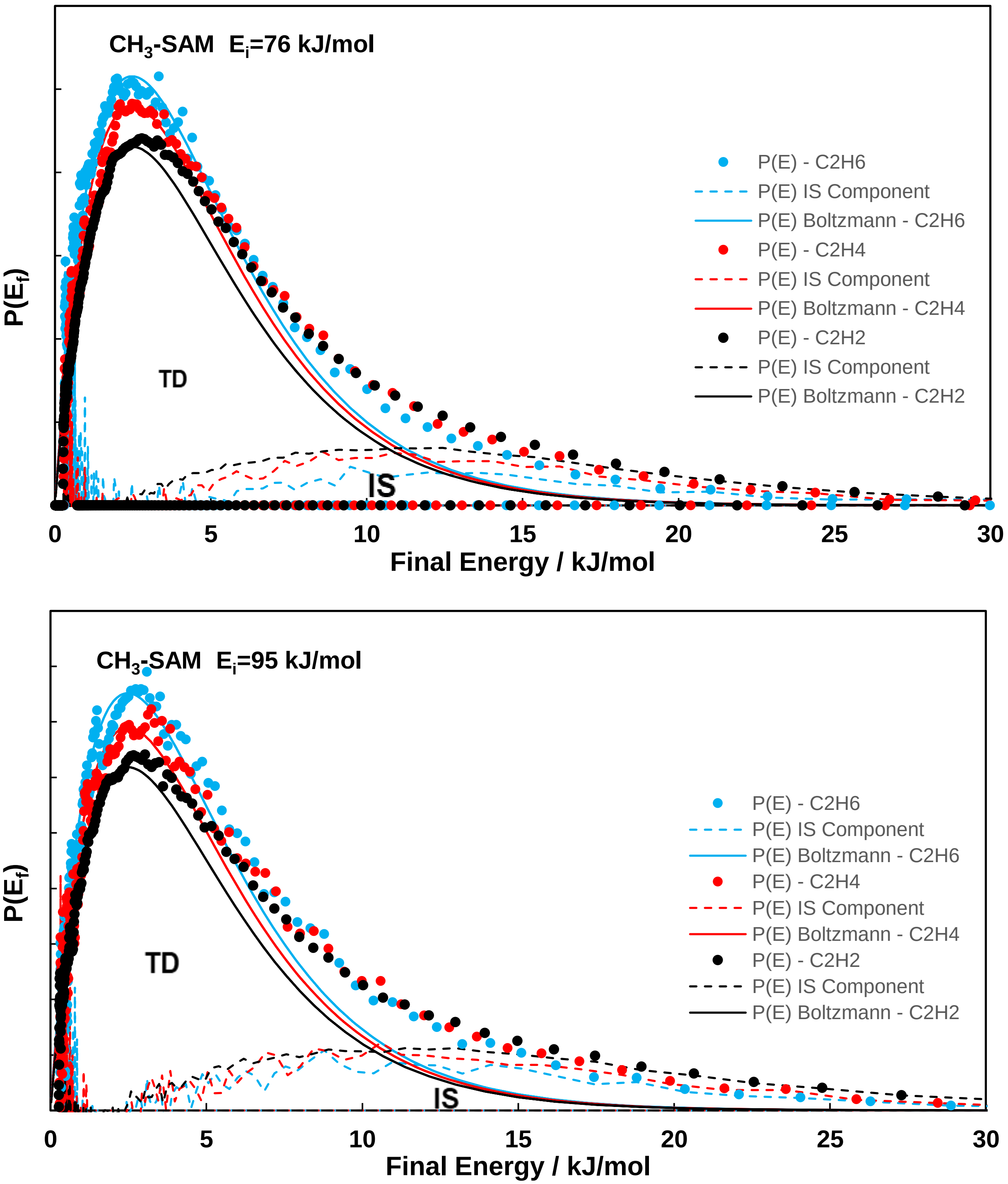

Figure 3.11 Final energy distributions of C_2H_6, C_2H_4, and C_2H_2 scattering from a CH_3-SAM with the incident energy of 76 kJ/mol (top) and 95 kJ/mol (bottom). Solid lines represent the TD components, dashed lines represent the IS components, and the solid circles represent the experimental final energy distributions.

Although not dramatically different, the final energy distributions were found to depend on the identity of the gas when they impinge on CH_3-SAM. Because the final energy distribution is directly correlated to the efficiency of thermal accommodation for each gas-surface system, this result indicates that these molecules thermalize and transfer energy to a different extent when colliding with the same surface. Table 3.3 shows that, for both incident energies, the TD fractions (area) decrease by according to the order $C_2H_6 > C_2H_4 > C_2H_2$. So, during the interactions with a CH_3-SAM, C_2H_6 molecules accommodate best with the surface and transfer the most of energy (±0.02 is experimental error bar), followed by C_2H_4, and C_2H_2 shows to be the least efficient regarding energy transfer. That is, the extent of energy transfer depends (albeit weakly) on the number of hydrogen atoms on the molecules.

Table 3.3 TD and IS fractions of C_2H_6, C_2H_4, and C_2H_2 scattering on a CH_3-SAM.

Gas source	Incident beam energy (±2 kJ/mol)	TD (±0.02)	IS (±0.02)
C_2H_6/H_2	76	0.87	0.13
C_2H_4/H_2	76	0.82	0.18
C_2H_2/H_2	76	0.75	0.25
C_2H_6/H_2	95	0.85	0.15
C_2H_4/H_2	95	0.78	0.22
C_2H_2/H_2	95	0.70	0.30

3.3.2 C_2H_6, C_2H_4, and C_2H_2 Collisions with an OH-SAM

The results and TD trends observed in scattering from the non-polar, CH_3-terminated surface, raise the question of whether the same trend holds for scattering from polar surfaces. The key difference between the OH- and CH3-SAMs is that the extended hydrogen bonding network at the surface of the OH SAM anchors the chains, which presents a more rigid collision partner to the incoming gas. As described above, in some cases, that increased surface rigidity is balanced by a larger attractive PES which ultimately leads to enhanced thermal accommodation.

These two competing factors were probed in my hydrocarbon scattering work. The same experiments as conducted for the CH3-SAM were performed on an OH-SAM under identical experimental conditions.

To prepare an OH-SAM, Au was also employed as the substrate, and the same procedure as the one used for the CH_3-SAM was followed. After cleaning, the substrate was immersed in an ethanolic solution of 16-mercapto-1-hexadecanol (Sigma-Aldrich) to make well-ordered OH-SAMs. Two molecular beams with different incident energies, for each gas, were used for the experiments. The flight time distributions for each gas molecule scattering from the OH-SAM were recorded, and these distributions are shown in Figure 3.12.

While the TOF distributions are similar to those for scattering from the CH_3-SAM, there are important differences. In particular, C_2H_2 appears to have a larger TD fraction than C_2H_4. These differences are also borne out in the final energy distributions.

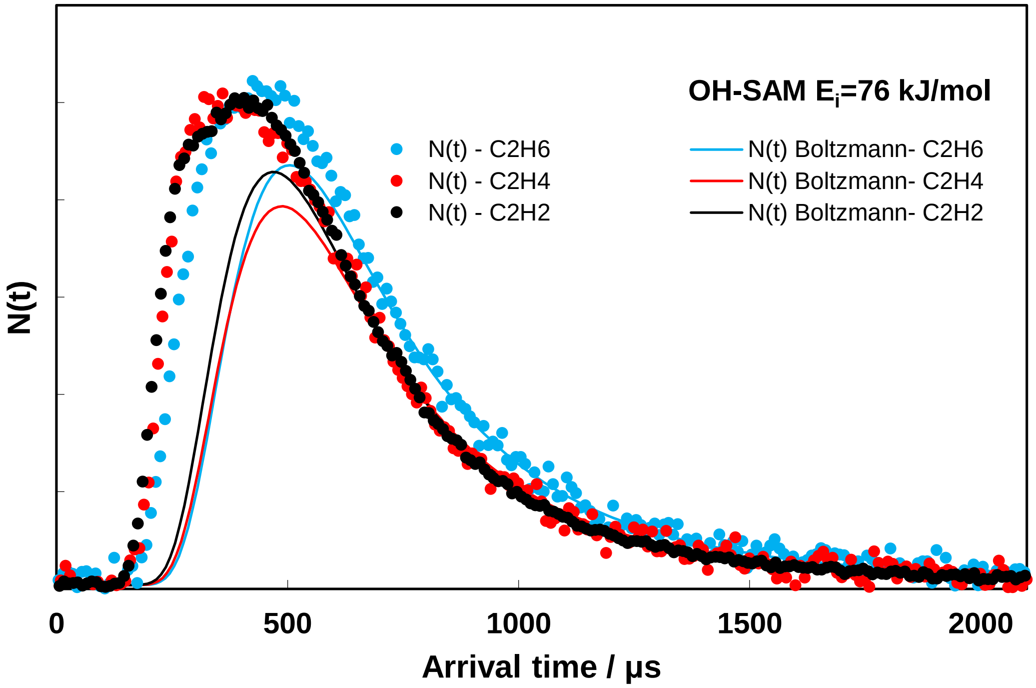

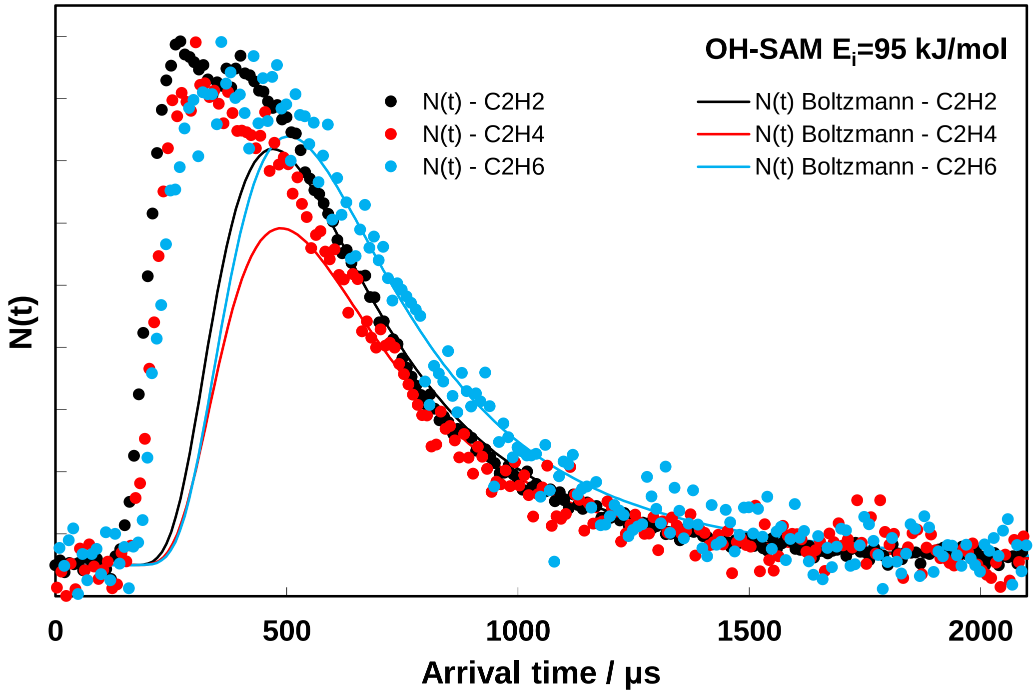

Figure 3.12 Time of flight distributions of C_2H_6, C_2H_4, and C_2H_2 scattering from an OH-SAM with the incident energy of 76 kJ/mol (top) and 95 kJ/mol (bottom). Solid lines represent the TD components (Boltzmann distributions at surface temperature), and the solid circles represent the experimental time-of-flight distributions.

The time-of-flight distributions in Figure 3.12 can be converted to final energy distributions, which provide direct and quantitative insight into the energy transfer efficiency. The final energy distributions for C_2H_6, C_2H_4, and C_2H_2 molecules after colliding with an OH-SAM are provided in Figure 3.13. In Figure 3.13, the TD component is described well by a Boltzmann distribution at the surface temperature (solid lines). The IS component is represented by the difference between the experimental data and the TD component. Equation **(24)**, **(25)**, and **(26)** are still used to obtain the TD fraction and IS fraction here. The overall final energy distribution is still the sum of the two components. Regarding the TD fractions in Figure 3.13, the trend observed is consistent with the one from the time-of-flight distribution. Upon collision with an OH-SAM, C_2H_6 yields the largest TD component, followed by C_2H_2, then C_2H_4.

The TD and IS fractions for C_2H_6, C_2H_4, and C_2H_2 scattering on the OH-SAM are provided in Table 3.3. The table highlights the trend observed in final energy distributions. The TD fraction for C_2H_6 scattering on the OH-SAM is higher than the other two molecules. The TD fraction for C_2H_4 scattering is lower than C_2H_2, indicating that ethyne thermally accommodates more efficiently to the OH-SAM than does ethene, which is counter to the trend observed for scattering from the CH_3-SAM.

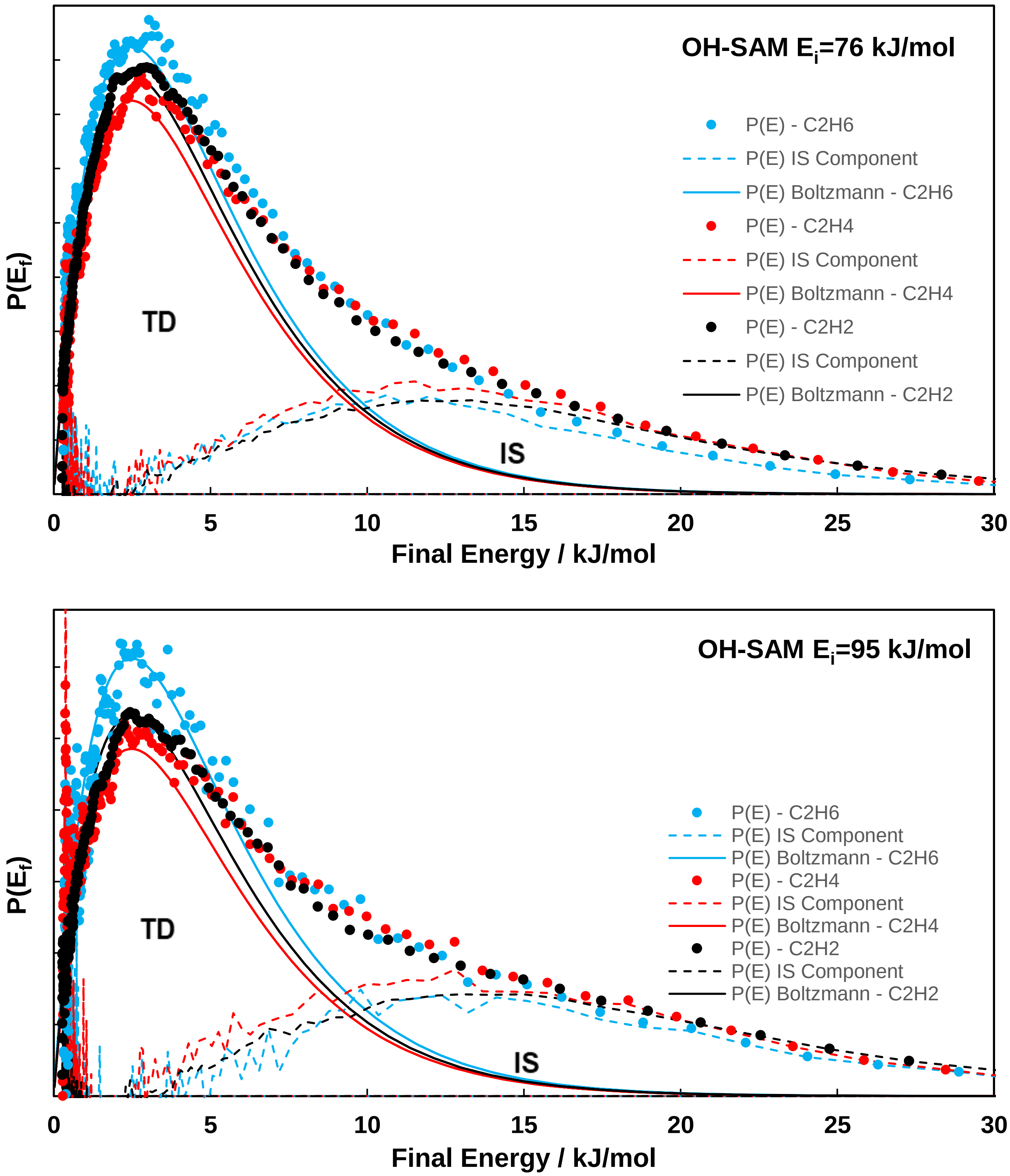

Figure 3.13 Final energy distributions of C_2H_6, C_2H_4, and C_2H_2 scattering from an OH-SAM with the incident energy of 76 kJ/mol (top) and 95 kJ/mol (bottom). Solid lines represent the TD components, dashed lines represent the IS components, and the solid circles represent the experimental final energy distributions.

Table 3.4 TD and IS fractions of C_2H_6, C_2H_4, and C_2H_2 scattering on an OH-SAM.

Gas source	Incident beam energy (±2 kJ/mol)	TD (±0.02)	IS (±0.02)
C_2H_6/H_2	76	0.70	0.30
C_2H_4/H_2	76	0.63	0.37
C_2H_2/H_2	76	0.67	0.33
C_2H_6/H_2	95	0.65	0.35
C_2H_4/H_2	95	0.58	0.42
C_2H_2/H_2	95	0.61	0.39

The scattering experiments on both CH_3-SAM and OH-SAM were performed with molecular beams of two different incident energies, 76 kJ/mol, and 95 kJ/mol. The energy transfer results (shown in Table 3.3 and Table 3.4) indicate that, under the same experimental conditions, more gas molecules become thermally accommodated (higher TD fractions) with the surface in the beam with lower incident energy. As previously published, this is due to the shorter surface residence time of gas molecules in the higher energy beam.[141] The differences in TD values and trends for two surfaces will be discussed further in section 3.4.

3.4 **Discussion**

The gas-surface molecular beam scattering experiments described above demonstrate that the pathway to interfacial thermal accommodation depends on both the nature of the incident gas, the molecule's translational energy, and the identity of the functional group at the interface. To the best of my knowledge, these experiments are the first to show that the change of degree of saturation for vaporous hydrocarbons affects the energy transfer dynamics. These effects may be due to differences in the rigidity (or degrees of freedom) of the molecules, small changes in molecular mass, small varieties regarding molecular sizes, or differences in the gas-surface attractive forces. Below, I provide a review of previous results in an effort to better understand the specific role of each property in controlling the scattering dynamics.

3.4.1 **Effect of Small Mass Differences of the Gas-phase Species**

The molecular mass of C_2H_6 (30 g/mol), C_2H_4 (28 g/mol), and C_2H_2 (26 g/mol) are slightly different. The effect of mass differences on gas-surface energy transfer has been previously studied by William A. Alexander et al. Facilitated by simulations, the interpretation of the scattering data of Ne (20 g/mol), Ar (40 g/mol), and Kr (84 g/mol) colliding on a CH_3-SAM and a CF_3-SAM show that the mass of the incident gas molecule is the most important factor in determining the energy exchange dynamics in this case.[20] However, the mass difference in the small hydrocarbon molecules studied in this thesis is much smaller compared to the mass differences in Ne, Ar, and Kr. Thus, before considering any other factors that may affect the energy transfer between small hydrocarbon molecules and organic surfaces, I explored how very small mass differences affect the scattering dynamics.

In my previous research, experiments of $^{14}N_2$ and $^{15}N_2$ scattering on identical OH-SAMs were performed to learn how small mass differences affect collision dynamics with surfaces. These scattering experiments exhibited very similar TD fractions (0.62 and 0.61 for $^{15}N_2$ and $^{14}N_2$, respectively) as demonstrated in Figure 3.14, in which the TD distributions of the two scattering experiments almost perfectly overlap with each other. Thus, the small mass difference of the gas molecules does not play a significant role in energy transfer during the gas-surface interactions. The same results should also apply to the small hydrocarbon scattering.

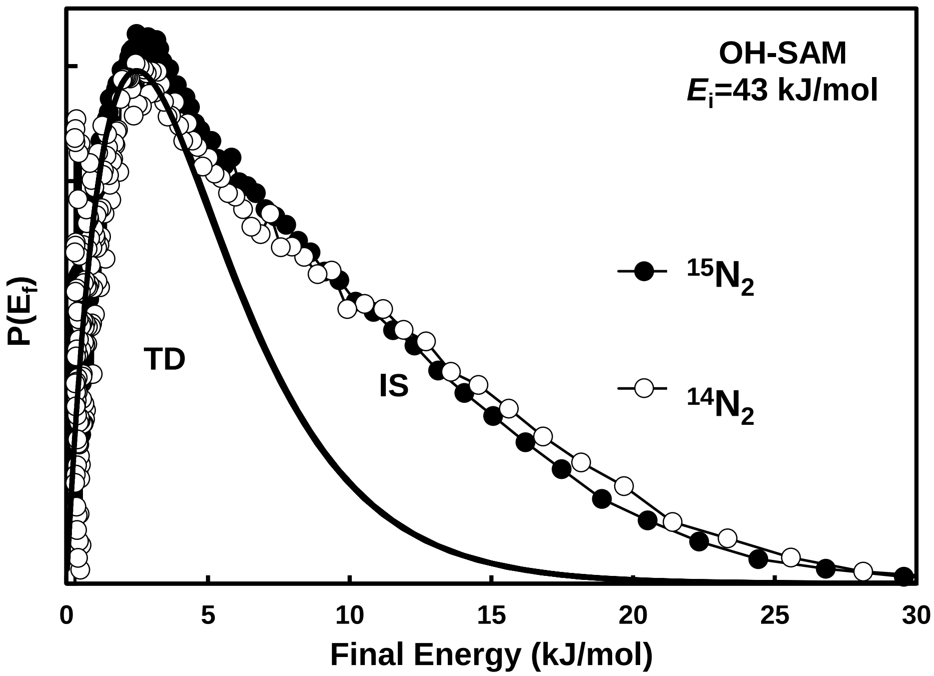

Figure 3.14 Final energy distributions of $^{15}N_2$ and $^{14}N_2$ scattering from OH-SAM. Solid lines represent the TD components.

3.4.2 Scattering Dynamics of C_2H_6, C_2H_4, and C_2H_2 on OH- and CH_3-SAMs and the correlation with the solubility

3.4.2.1 Overview

Solubility is the property that predicts the extent to which a solid, liquid or gaseous chemical dissolves into a solvent to form a homogeneous solution. The value of solubility defines how much a specific solute can be dissolved into a unit amount (volume or mass) of solvent. The solubility of a substance depends on the physical and chemical properties of both the solute and the solvent. As previously mentioned, a correlation has been observed with the diatomic molecules energy transfer in collisions with SAMs with their solubilities in a specific solvent of comparable chemistry to the SAMs. However, with different degrees of freedom, and various electronic structures, it would be interesting to see if such correlations stand. My goal here is to establish and understand the correlation between small hydrocarbon (C_2H_6, C_2H_4, and C_2H_2)-surface (CH_3-SAM and OH-SAM) energy transfer efficiency and the gas solubility in analogous solvents (hexane and water).

3.4.2.2 Correlation between Gas-Surface Interactions and Solubilities in *n*-Hexane and Water

The solubilities of C_2H_6, C_2H_4, and C_2H_2 in both water and *n*-hexane were shown earlier in Table 1.1. This data clearly shows that the solubilities of these three gases follow the trend of $S_{C2H2} < S_{C2H4} < S_{C2H6}$ in *n*-hexane. The CH_3-SAM, because it presents non-polar groups to the incoming gas molecule, may be used as an analog of hexane. I, therefore, hypothesize that molecules with higher solubility in hexane have higher thermal accommodation efficiencies in collisions with non-polar surfaces.

Upon analyzing the final energy distributions of C_2H_6, C_2H_4, and C_2H_2 after scattering on the CH_3-SAM, I found that solubility in hexane tracks the relative TD fractions for these molecules scattering from the CH_3-SAM. Figure 3.15 provides a plot of TD fraction on the CH_3-SAM versus solubility of gas molecules in *n*-hexane. The figure demonstrates that a higher solubility corresponds to a higher TD fraction, indicating more efficient energy transfer. This result is consistent with my hypothesis and the correlation established in previous research regarding the scattering of simple diatomic molecules on the CH_3-SAM.

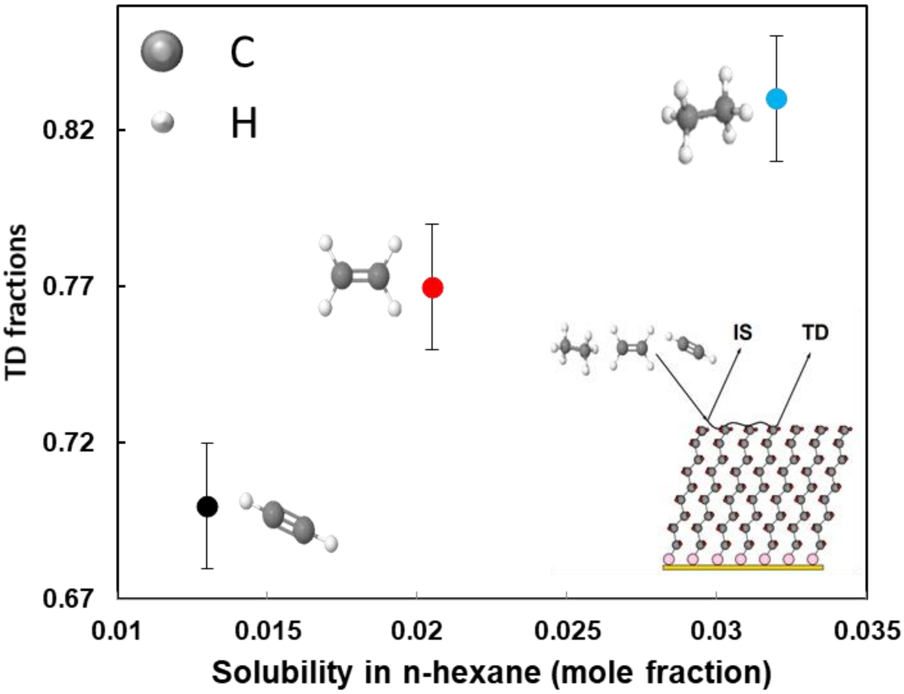

Figure 3.15 Thermal desorption fractions of gas scattering on a CH_3-SAM versus the solubilities of gas molecules in *n*-hexane.

Compared with the solubilities in hexane, the solubilities of these three small hydrocarbon gas molecules in water show a completely inverted order, $S_{C2H6} < S_{C2H4} < S_{C2H2}$. The OH-SAM, because it presents polar groups to the incoming gas molecule, may be used as an analog of water, I, therefore, hypothesize that molecules with higher solubility in water have higher thermal accommodation efficiencies in collisions with polar surfaces. However, as shown in Figure 3.17, the energy transfer efficiency (TD fraction) does not appear to be directly correlated with solubility in the analogous solvent. In this case, the solvent water, being a polar molecule, interacts with the solute molecules through London dispersion forces. With the double bond in C_2H_4 and the triple bond in C_2H_2, the major interactions between solute and water molecules will be electrostatic. The high electron density in C_2H_4 and C_2H_2 makes them good electron donors for the formation of π-OH hydrogen bonds with water molecules. Hydrogen bonding, as the strongest intermolecular force for neutral species, plays a dominant role in determining the relative solubility, as highlighted in Figure 3.17.

Since C_2H_6 is a non-polar molecule without π electrons, it has the weakest interactions with the water. This phenomenon was explained by Frank and Evans in 1945, ‘‘the nature of deviation found for non-polar solutes in water leads to the idea that the water forms frozen patches or microscopic icebergs around such solute molecules. The word ‘iceberg’ represents a microscopic region, surrounding the solute molecule, in which water molecules are tied together in some sort of quasi-solid structure’’.[142] The water molecules interact more strongly with each other due to the existence of hydrogen bonds than with saturated compounds like C_2H_6. As a result, the water molecules form somewhat structured shells around C_2H_6. This makes the whole system more ordered upon dissolution and therefore leads to a decrease in entropy. At a constant temperature, based on equation **(27),** the decrease of entropy corresponds to increase of Gibbs free energy of solvation.

$$\Delta G = \Delta H - T\Delta S \qquad \textbf{(27)}$$

Thus, compared with C_2H_4 and C_2H_2, C_2H_6 in water has a more positive Gibbs free energy of solvation and lower solubility. C_2H_2 has a higher electron density than C_2H_4; therefore, it is more likely to interact with water molecules to form hydrogen bonds. Previous research has been done by JE Del Bene to study the hydrogen bonds between water molecules and small hydrocarbon molecules.[143] As shown in Table 3.5, considering H_2O as the proton donor, despite the π electrons are more tightly bound in C_2H_2 than C_2H_4, the dimer formed through hydrogen bonding having C_2H_2 as the proton acceptor is more stable than the dimer having C_2H_4 as the proton acceptor. The angles listed in Table 3.5 are defined in Figure 3.16. Unlike hydrogen bonds form through a lone pair of electrons, there isn't a definite energetic preference for bond formation through π dimers having H_2O as a single or double proton donor.[143]

Table 3.5 Structures and energies of dimers containing C_2H_2 and C_2H_4 as proton acceptors and water as the proton donor. Table adapted from ref.[143]

Dimer	R (Å) a)	θ1 (deg)	Θ2 (deg)	χ2(deg)	Φ1 (deg)	ΔE (Kcal/mol)b)
H_2O-C_2H_2						
A	3.63	31 c)	90	-	90	-0.79691
B d)	3.69	46	95	-	0	-0.69024
C e)	3.58	0	90	-	90	-0.77181
H_2O-C_2H_4						
A	3.65	42	90	0	0	-0.62749
B	3.65	42	90	2	90	-0.62122
C e)	3.63	0	90	0	0	-0.50199
D e)	3.67	0	90	0	90	-0.48944

a) R is the intermolecular distance measured from the oxygen of water to the midpoint of the C-C bond.

b) ΔE is the intermolecular (hydrogen bond) energy.

c) θ1 = 50° places the O-H bond along the intermolecular line, as shown in Figure 3.16.

d) This dimer is not an equilibrium structure with respect to rotation by Φ.

e) These dimmers are not equilibrium structures. They represent particular structures in which water is a double proton donor and illustrate the flatness of the potential curves associated with θ1 and Φ rotations.

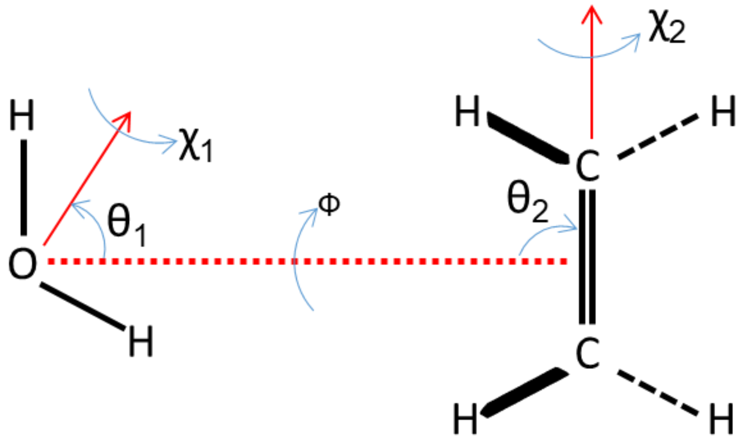

Figure 3.16 H_2O-C_2H_4 π dimer A showing principal axes and intermolecular coordinates. For this particular structure, R=3.65 Å, θ_1 = 42°, χ_1 = 0°, θ_2 = 90°, χ_2 = 0°, Φ = 0°.[143]

The stronger the water-solute interactions are, the more disordered the system will be (higher the ΔS), and the lower the Gibbs free energy of solvation. Thus, the solubility of these three molecules increases in the order of $S_{C2H6} < S_{C2H4} < S_{C2H2}$.

The hydrogen bonds in liquid bulk (water) affect solubility; likewise, the hydrogen bonds on solid surfaces (OH-SAM) affect energy transfer. However, the reasons behind these effects are fundamentally different. Therefore, I find that the TD fractions of the three organic gas molecules under investigation do not follow the same trend as their solubilities in water. As shown in Figure 3.17, C_2H_6 shows the highest TD fraction although it possesses the lowest solubility in water. Even though the solubility of C_2H_2 in water is smaller than the solubility of C_2H_4, C_2H_2 shows higher TD than C_2H_4 in the gas-solid surface interactions. Therefore, factors beyond hydrogen bonding, which plays a major role in solubility, must affect the gas-surface collision dynamics for scattering from the OH-SAM.

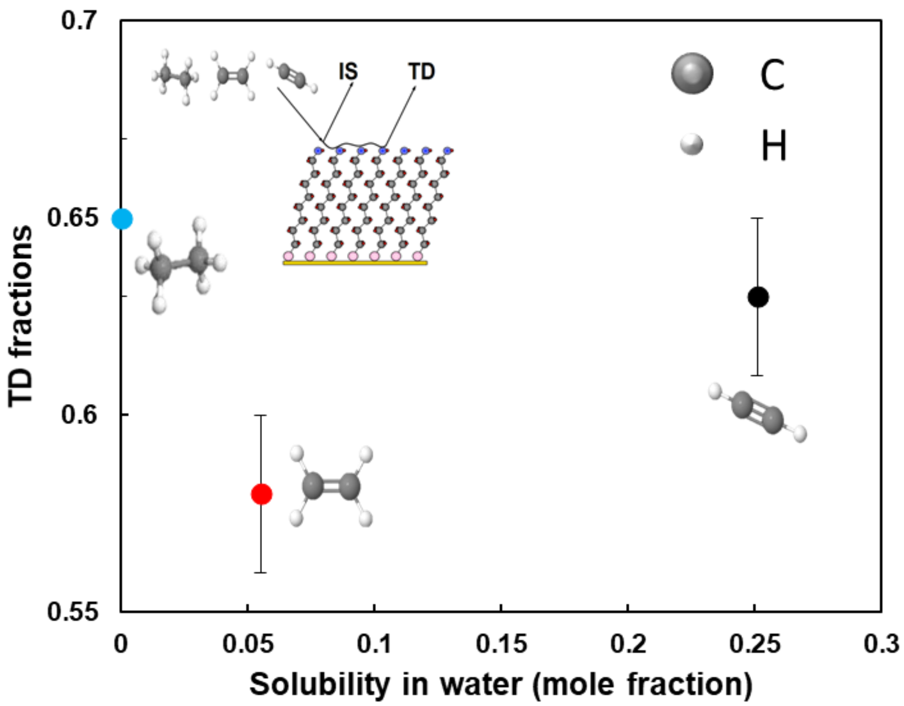

Figure 3.17 Thermal desorption fractions of gas scattering on an OH-SAM versus the solubilities of gas molecules in water.

3.4.3 **The Effect of Gas Properties**

As shown in the previous section, with the more complex molecular structure, the energy transfer between small hydrocarbon molecules and organic surfaces cannot be simply predicted by using their solubilities in specific analogous solvents. The electronic structure and degrees of freedom of the gas molecules likely contribute to the energy transfer efficiency. Among the three gas molecules, C_2H_6 has the highest degrees of freedom, which is 18, while C_2H_4 and C_2H_2 have degrees of freedom of 12 and 7, respectively. In the incident molecular beam, all the vibration and rotation modes of the gas molecules are not excited. Upon collision on an organic surface, the excess translational energy may be transferred to the energetically accessible rotations and vibrations of the gas molecule. Hence, with more vibrational and rotational modes, molecules may benefit from higher degrees of freedom regarding the energy transfer between gas molecules and organic surfaces. Although this is a possible factor affecting the gas-surface energy transfer, the translational-to-vibrational energy transfer for the gas molecules has been proven to be very inefficient. The final scattering result is clearly due to a combination of factors such as degrees of freedom, intermolecular forces, molecular size, electronic structure, and gas-surface attractive forces.

The C_2H_6 molecule, possessing the largest degrees of freedom, may be able to interact with the surface more efficiently and yield a more significant energy transfer. Also, the electronic structure of the gas molecule may also affect energy transfer dynamics. C_2H_4, with lower degrees of freedom, is more rigid than ethane, and therefore, yields less efficient energy transfer (lower TD fraction) upon colliding on organic surfaces. Interestingly, C_2H_2, although possessing the fewest degrees of freedom, shows higher energy transfer efficiency than C_2H_4. This effect may be due to the fact that the high electron density at the triple bond in C_2H_4 leads to the formation of hydrogen bonds with the surface functional groups, and therefore increases energy transfer (TD fraction)–despite the increased rigidity of the gas molecule. Future studies into the potential energy landscape of the gas-surface interaction will help further develop the understanding of these complex collision dynamics.

3.4.4 **The Effect of Terminal Groups**

Previously, the interactions between condensed phase solvents and the small hydrocarbon molecules were discussed to facilitate the understanding of the energy transfer between gas molecules and organic surfaces. However, a direct study of the solid surface could provide more specific information regarding the effect of surface properties on gas-surface energy transfer.

The experiments of small hydrocarbon scattering were performed on both an OH-SAM and a CH_3-SAM.

To show a direct comparison of gas scattering on the polar and non-polar surfaces, the time-of-flight distributions and final energy distributions of C_2H_6 upon collisions with CH_3-SAM and OH-SAM (with an incident beam energy of 95 kJ/mol), are shown in Figure 3.18. After normalization, it is obvious that the TD component in the data collected from the gas scattering on the CH_3-SAM (green line in Figure 3.18) is much bigger than the one from the OH-SAM scattering (red line in Figure 3.18). This indicates that, for the same incident energy, the energy transfer from C_2H_6 to CH_3-SAM is much more efficient than to OH-SAM. The same plots are presented for C_2H_4 and C_2H_2 in Figure 3.19 and Figure 3.20, respectively. For both C_2H_4 and C_2H_2, the same conclusion can be drawn that the energy transfers more efficiently to the CH_3-SAM than the OH-SAM. Even though, as previously discussed, the π electrons in the C_2H_4 and C_2H_2 may interact with polar molecules through the formation of hydrogen bonds, this intermolecular force is not strong enough in the gas-surface interactions to be the dominant factor.

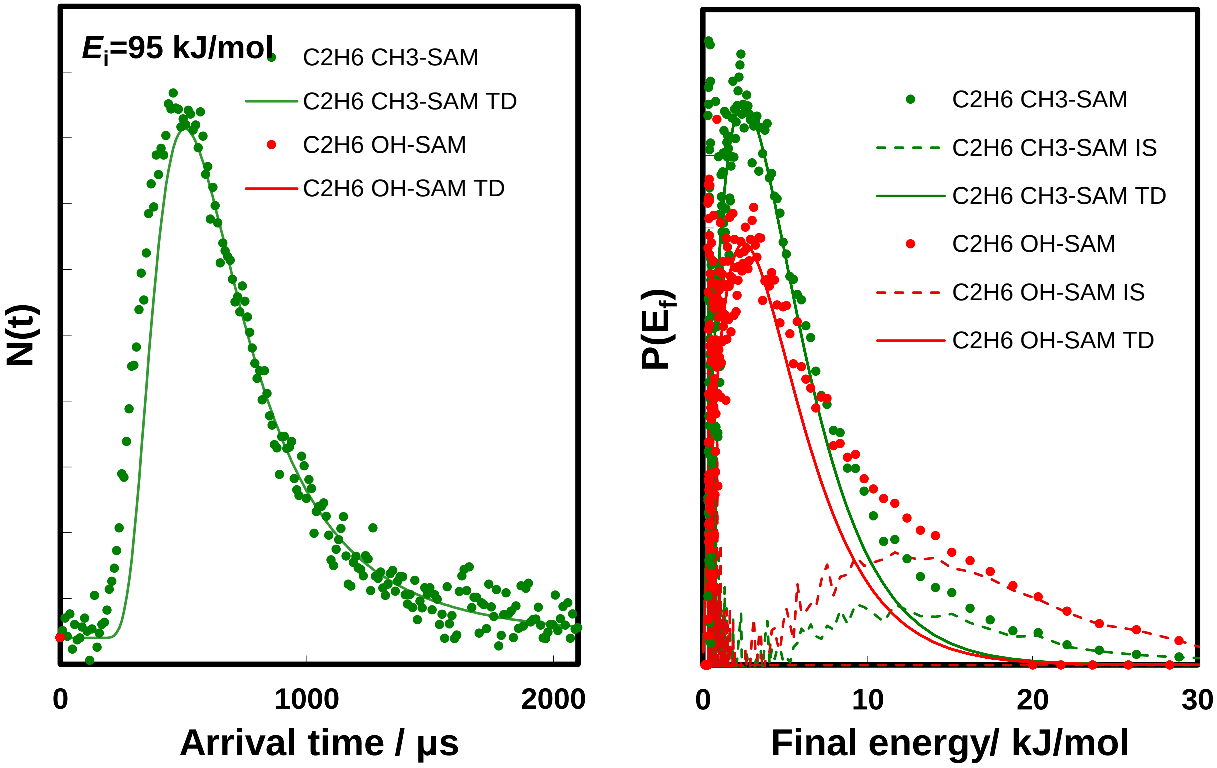

Figure 3.18 The time-of-flight distribution (left) and final energy distribution (right) of C_2H_6 scattering from OH-SAM and CH_3-SAM with the incident energy of 95 kJ/mol. Solid lines represent the TD components, dashed lines represent the IS components, and the solid circles represent the experimental time-of-flight and final energy distributions.

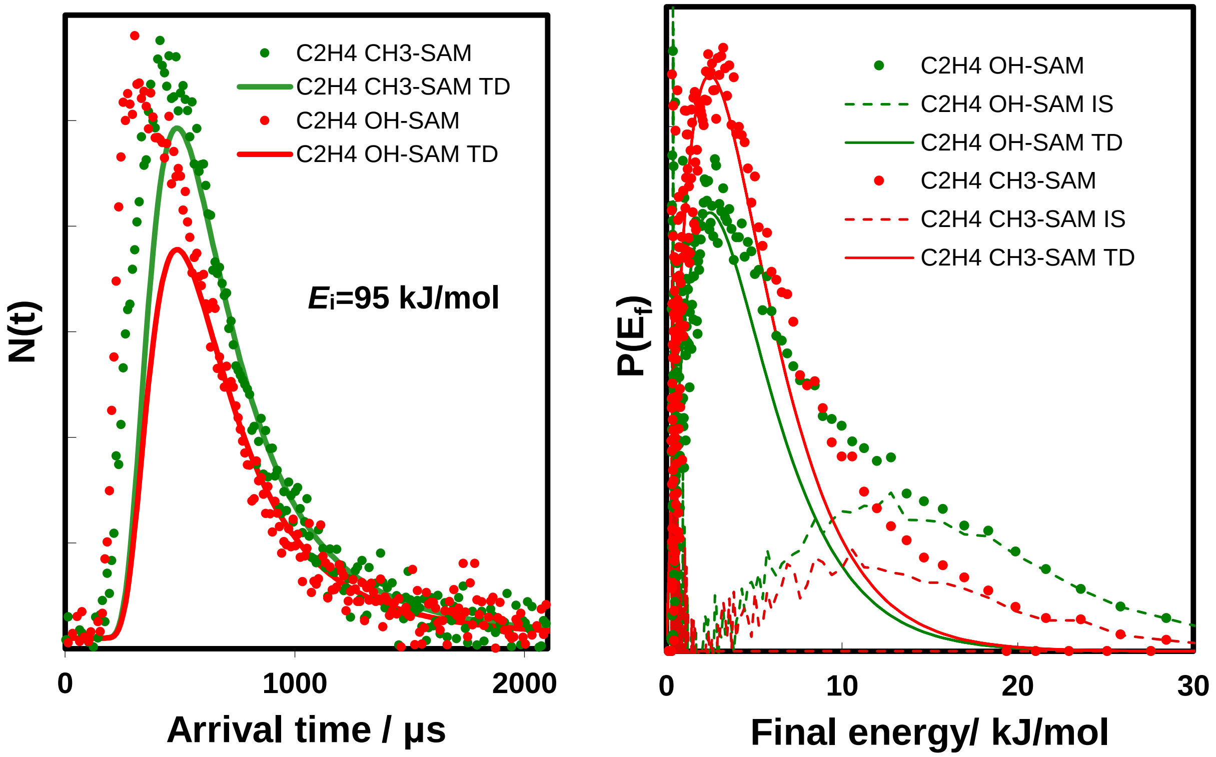

Figure 3.19 The time-of-flight distribution (left) and final energy distribution (right) of C_2H_4 scattering from OH-SAM and CH_3-SAM with the incident energy of 95 kJ/mol. Solid lines represent the TD components, dashed lines represent the IS components, and the solid circles represent the experimental time-of-flight and final energy distributions.

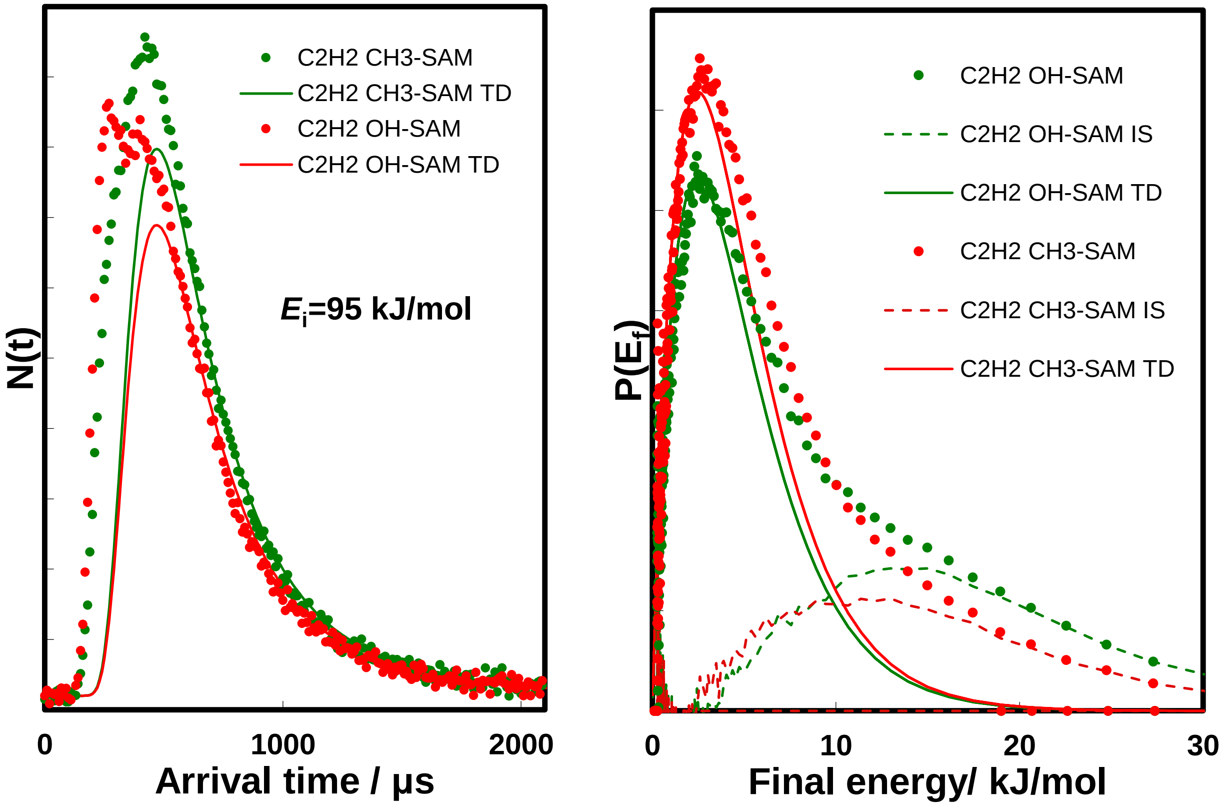

Figure 3.20 The time-of-flight distribution (left) and final energy distribution (right) of C_2H_2 scattering from OH-SAM and CH_3-SAM with the incident energy of 95 kJ/mol. Solid lines represent the TD components, dashed lines represent the IS components, and the solid circles represent the experimental time-of-flight and final energy distributions.

The TD fractions of C_2H_6, C_2H_4, and C_2H_2 scattering on a CH_3-SAM and an OH-SAM are tabulated in Table 3.6. For each molecule, the ratio of the TD fractions from CH_3-SAM scattering over the TD fractions from OH-SAM scattering was calculated. As shown in Figure 3.21 and Table 3.6, the energy transfer of the same gas molecules on two surfaces are dramatically different.

Table 3.6 TD fractions of C_2H_6, C_2H_4, and C_2H_2 scattering on a CH_3-SAM and an OH-SAM (incident energy = 95 kJ/mol).

Gas	TD (CH_3-SAM) (±0.02)	TD (OH-SAM) (±0.02)	TD (CH_3-SAM)/ TD (OH-SAM)
C_2H_6	0.85	0.65	1.308
C_2H_4	0.78	0.58	1.345
C_2H_2	0.70	0.61	1.148

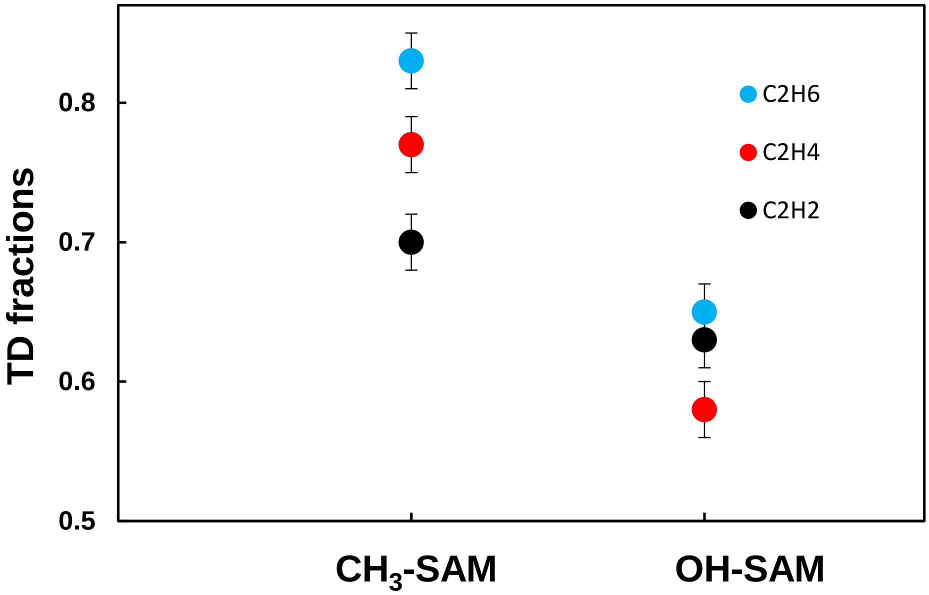

Figure 3.21 TD fractions of C_2H_6, C_2H_4, and C_2H_2 scattering on an OH-SAM and a CH_3-SAM (Incident energy=95 kJ/mol, error bar ±0.02).

Based on the results shown above, the gas-surface interaction dynamics depend on not only the properties of gas molecules but also the characteristics of the surface. The experimental results of gas scattering from CH_3-SAMs and OH-SAMs show that, with the same incident gas species and energy, the TD fraction in CH_3-SAM scattering is always higher than the TD fraction in OH-SAM scattering. This is because, compared with the OH-SAM, the CH_3-SAM is more flexible. In OH-SAMs, the terminal OH groups form intra-monolayer hydrogen bonds. The formation of the hydrogen bond "network" makes the surface relatively rigid.[144] The surface hydrogen bonds may significantly increase the effective surface mass, relative to the CH_3-SAM. As mentioned in section 1.1.3, the most efficient energy transfer occurs when the effective surface mass is the same as the mass of the imping gas molecules. Therefore, the increased surface mass may lower the efficiency of energy transfer between gas molecules and the OH-SAM.

The intra-monolayer hydrogen bond network in the OH-SAM anchors the end groups of the SAM and decrease the vibrational degrees of freedom of the surface. Therefore, some of the low-energy modes that are active in the CH_3-SAM may be restricted in the OH-SAM. As previously published by Naaman and Sagiv, [145-146] when the incident gas molecules hit the solid surface, part of the incident energy is transferred to the surface from the gas molecules and distributed into the subtle motions of the surface chains, such as end-group rotations and the low-energy waving motions. With the existence of intra-monolayer hydrogen bonds on the OH-SAMs, and some of those possible motions restricted, the energy transfer will be less efficient. Therefore, the rigid surface structure will significantly limit the energy transfer between the gas molecules and the OH-SAMs.[147] Also, because the chains on the CH_3-SAMs are freer to wag, twist, and become disordered, it is easier for energy to be dissipated into the low-energy vibrational modes upon gas molecules impinge on the CH_3-SAMs. A previous publication by Shuler et al. shows that comparing with an OH-SAM, the surface of a CH_3-SAM has additional energy modes, into which the kinetic energy of the incident gas molecules may be dissipated. These modes include the CH_3 torsional mode (2 kJ/mol), the stretching mode (37 kJ/mol), and the deformation mode (15 kJ/mol).[145] Furthermore, research has been done to show that decreasing the extent of hydrogen bonding frees up the otherwise anchored low-energy motions of the chains. These freed motions can then participate in the energy transfer between gas molecules and organic surfaces, which increases the energy transfer efficiency. Overall, the low-energy motions available on the SAM surface help to explain the physics governing the observation that the energy transfer between small hydrocarbon gas molecules and the CH_3-SAM is more efficient than the energy transfer to the OH-SAM.

3.5 Summary

The goal of this chapter was to investigate the effect of molecular rigidity, electron density, and surface functionality on the energy transfer between small hydrocarbon molecules and organic surfaces, as well as study how the molecular scattering behavior may be correlated with the solubility of the compounds in an analogous solvent.

Under ultrahigh vacuum conditions, I used molecular beams as a well-controlled gas source and self-assembled monolayers as well-characterized model surfaces. The TOF distributions of the scattered gas molecules upon gas-surface collisions were recorded by a quadrupole mass spectrometer and then converted to the final energy distributions. By assigning two components, thermal desorption, and impulsive scattering, to each final energy distribution, the energy transfer between gas molecules and organic surfaces were quantified (TD fraction and IS fraction) and used to evaluate the energy transfer efficiency.

I scattered C_2H_6, C_2H_4, and C_2H_2 on both a CH_3-SAM and OH-SAM. Each scattering experiment was performed with two incident beam energies (76 kJ/mol and 95 kJ/mol). The TD fractions for each experimental study are listed in Table 3.7. For each gas, with the same incident beam energy, the TD fraction upon collision on a CH_3-SAM was found to be higher than the TD fraction for scattering from the OH-SAM. So, for small hydrocarbon molecules, the gas-surface energy transfer is more efficient on the CH_3-SAM. This result is due to the formation of intramonolayer hydrogen bonding in the OH-SAM, which restricts the low-energy motions on the surface and therefore limits the energy transfer.

By comparing the TD fractions of C_2H_6, C_2H_4, and C_2H_2 scattering on the CH_3-SAM, I found the energy transfer efficiency decreases in the order of $C_2H_6 > C_2H_4 > C_2H_2$. The effect of degrees of freedom may play an important role in the overall scattering dynamics. With a more flexible structure and more degrees of freedom, C_2H_6 yields the most efficient energy transfer with the CH_3-SAM. This trend changes for the scattering on the OH-SAM. Even though C_2H_6 still transfers most of the energy, due to its high degrees of freedom, to the surface, C_2H_2 shows a higher TD than C_2H_4. The lower energy transfer of C_2H_4 compared to C_2H_6 is the result of the double bond in the chemical structure, which makes the molecule more rigid. And for C_2H_2, even though it has the lowest degrees of freedom among the three hydrocarbon molecules studied here, the high electron density in its triple bond may act as a hydrogen bond acceptor, and form a relatively strong H-bond with the electron positive hydrogen atoms on the surface of the OH-SAM, which leads to a high TD fraction despite the increased rigidity.

My original hypothesis that the thermal accommodation efficiency of gas molecules colliding with organic surfaces correlates with molecular solubility in analogous solvents proved to be valid for the small hydrocarbons impinging on the CH_3-SAM. However, the dynamics are more complex for scattering at the OH-SAM. Other than intermolecular forces, the energy transfer between small hydrocarbon molecules and organic surfaces are determined by a balance of factors such as degrees of freedom, electronic structure, and intermolecular forces.

Table 3.7 TD fractions of C_2H_6, C_2H_4, and C_2H_2 scattering on a CH_3-SAM and an OH-SAM with the incident beam energy of 76 and 95 kJ/mol.

Gas source	Incident beam energy (±2 kJ/mol)	TD (±0.02)	IS (±0.02)	TD (±0.02)	IS (±0.02)
		CH3-SAM		OH-SAM	
C_2H_6/H_2	76	0.87	0.13	0.70	0.30
C_2H_4/H_2	76	0.82	0.18	0.63	0.37
C_2H_2/H_2	76	0.75	0.25	0.67	0.33
C_2H_6/H_2	95	0.85	0.15	0.65	0.35
C_2H_4/H_2	95	0.78	0.22	0.58	0.42
C_2H_2/H_2	95	0.70	0.30	0.61	0.39

Chapter 4 Mechanism and Kinetics for Reaction of the Chemical Warfare Agent Simulants, DMMP(g) and DMCP (g), with Zirconium (IV) Metal-Organic Frameworks

This chapter is mostly a reprint of a manuscript published in the Journal of Physical Chemistry C to which the author, Guanyu Wang, was the primary scientific contributor and author. Dr. Weiwei Guo and Prof. Craig Hill synthesized the materials. The XPS experiments were performed by Cecilia Smith, and the data was analyzed by Guanyu Wang. Dr. Diego Troya performed the theoretical calculations and the corresponding writing. Dr. Wang, Dr. Plonka, and Prof. Frenkel performed PXRD characterizations of the MOFs employed in this research. Mr. Conor Sharp and Mr. James Kollar helped with experiments. Prof. Morris supervised the research presented in this chapter. This chapter is reprinted with permission from (Wang, G.; Sharp, C.; Plonka, A. M.; Wang, Q.; Frenkel, A. I.; Guo, W.; Hill, C.; Smith, C.; Kollar, J.; Troya, D.; Morris, J. R., Mechanism and Kinetics for Reaction of the Chemical Warfare Agent Simulant, DMMP(g), with Zirconium(IV) MOFs: An Ultrahigh-Vacuum and DFT Study. *J. Phys. Chem. C* **2017,** *121*, 11261-11272.) Copyright (2017) American Chemical Society.

The uptake and decomposition of organophosphonate-based chemical warfare nerve agents within Zr_6-based MOFs have been investigated by tracking the real-time uptake of the more benign simulant molecule, DMMP, and DMCP, within three systems. Specifically, infrared spectroscopy, X-ray photoelectron spectroscopy, and DFT calculations provided insight into how the chemistry of DMMP within UiO-66, UiO-67, and MOF-808 depends on MOF structure and SBU connectivity.

4.1 **Hydrogen Bonding of DMMP on UiO-66**

All three MOFs investigated yield rich infrared spectra with narrow bands characteristic of highly crystalline materials. For UiO-66, the IR bands in the low wavenumber region (Figure 4.1B spectrum in black), are well known to be due to the excitation of vibrational motions associated with the 1,4-benzenedicarboxylate (BDC) linkers, of which there are twelve linkers per node.[148-150] In addition, several features have been previously assigned to collective motions of the node itself.[151] A particularly noteworthy aspect of the infrared spectra is the abundance of bands in the mid-IR range from 1800 cm^{-1} to 2700 cm^{-1} (Figure 4.1A), which are due to overtones and combination bands associated with lower frequency motions. The high wavenumber region is characterized by absorbances due to excitation of the C-H stretches around the BDC. The narrow band at 3673 cm^{-1} is assigned to the stretches of the four bridging hydroxyl groups associated with each node (See Figure 4.1). The band assignments are summarized in Table 4.1.

.

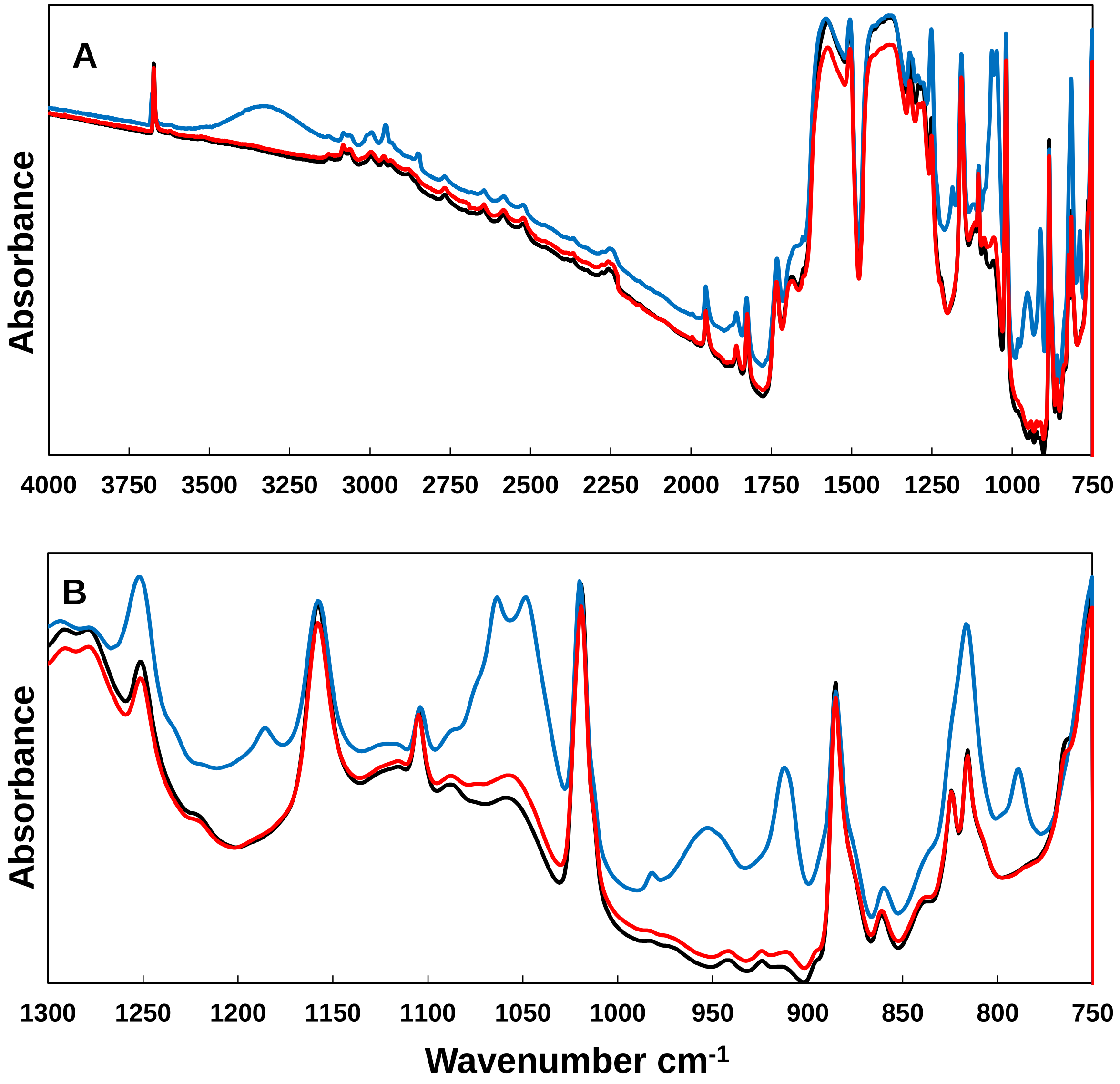

Figure 4.1 IR spectra for the entire mid-IR region (A) and the "fingerprint" region (B) of UiO-66 before DMMP exposure (black), after DMMP exposure (blue), and after post-exposure thermal treatment to 600 K (red).

Upon exposure to DMMP, the infrared bands associated with the UiO-66 remain largely unaffected, but new bands, which can be assigned to the DMMP adsorbate, emerge. The spectra shown in blue in Figure 4.1A and Figure 4.1B were recorded following exposure of UiO-66 to 2×10^4 L (where 1 L is equivalent to 10^{-6} Torr·s of exposure) of DMMP while the MOF was maintained at 298 K. One of the most significant changes upon exposure is the emergence of a broad band at 3250 cm^{-1}. This band, which is accompanied by a reduction in the intensity of the free OH band, is attributed to the formation of a hydrogen bond between DMMP and the hydroxyl groups at the nodes. Previous infrared studies of DMMP (and a variety of other CWA simulant) adsorption on hydroxylated silica demonstrated that DMMP is an excellent hydrogen bond acceptor.[123-124] On silica, the energy of those hydrogen bonds was found to be in excess of 50 kJ/mol.[124] Here, I observe similar types of hydrogen bonding interactions, but they seem to occupy only a small fraction of the total number of free OH groups within the MOF. Note that, even after prolonged exposure, the intensity of the free hydroxyl groups originally present at the nodes was not reduced beyond 20% of the original intensity, implying that the bridging node–OH groups appear to be largely inaccessible to DMMP. The majority of the uptake therefore likely occurs on the surface of the MOF crystallites, and little penetration into the MOF accompanies uptake. This interpretation is consistent with previous suggestions that the pore apertures for UiO-66 are too small for a molecule like DMMP to freely access the interior of the MOF.[77] The aperture size for the octahedral pore is only 12 Å, while that of the tetrahedral pore, where the OH groups reside, is even smaller at 6 Å.[152-153]

The features in the lower wavenumber region of the spectrum corroborate DMMP physisorption to the MOF through the formation of hydrogen bonds. The many new bands in the region from 750 cm^{-1} to 1300 cm^{-1} (Figure 4.1B) are consistent with prior work into DMMP interfacial hydrogen bonding and can be assigned to molecular DMMP.[81]

Table 4.1 Observed vibrational wavenumbers (cm^{-1}) for clean Zr$_6$-based MOFs and band assignments.[151-152, 154-164]

Mode	UiO-66 cm^{-1}	UiO-67 cm^{-1}	MOF-808 cm^{-1}
ν(ZrO−H)$_{\text{node, free}}$	3674	3674	3674
ν(COO−H)$_{\text{linker, free}}$		3616	3585
ν(CH)$_{\text{linker}}$	3130 3083 3061	3075 3061 3048 3015	3087
Overtone	2800-2000	2800-2000	
ν(COZr)$_{\text{bidentate}}$+ν(COO)$_{\text{i.p}}$+ν(C=C)+β(CH)	1662-1520	1638-1471	1646-1500
β(CH)+ν(C=C)	1507		
ν(COZr)$_{\text{bidentate}}$+ν(COO)$_{\text{o.o.p}}$+δ(OH)+β(CH)	1477-1329	1471-1321	1500-1219
ν(C=C)+δ(C=C-C)	1320	1315	
ν(CO)	1300-1260	1269	
ν(C-C)+β(CCH)+ δ(OH)+γ(CCC)ϕ χ(ring)		1180	
β(CH)+δ(OH)+χ(ring)	1158	1154	
β(CH)+ν(C=C)+χ(ring)	1105	1121	1112
β(CH)+ν(C=C)+γ(CCC)ϕ χ(ring)		1106	
ν(CO)+δ(OH)	1088		
ν(CO)+δ(OH)	1058		
γ(CCC)ϕ+δ(OH)+χ(ring)	1019	1021	1054
χ(ring)+ γ(ring)		1007 974 964	942
ρ(CH)	885 824 816	876 856 843 801	823 804
ν(Zr-O)+γ(CCC)ϕ+ρ(CH)		771	790
ν(Zr-O)+γ(COO)ϕ+ρ(CH)		753	760

ν: bond stretching, ρ: rocking (in-plane), δ: planar angle bending, β: in planar bending, γ: out-of-plane bending (wagging), ϕ: deformation, χ: aromatic ring breathing, i.p: in-plane, o.o.p: out-of-plane, sh: shoulder

The assignment of the bands that emerge upon exposure is aided by direct comparison to the IR spectrum for gas-phase DMMP (Figure 4.2). The spectrum shown in blue in Figure 4.2 was recorded following exposure of UiO-66 to DMMP with the original MOF used as the background such that the new bands represent changes in absorbance due to the vibrational excitations associated with new adsorbates, and negative features are due to changes to bands associated with the original MOF. The resulting difference spectrum for the MOF upon exposure shows a near 1:1 correlation with the bands for molecular DMMP in the gas phase. This correlation indicates that the types of interactions responsible for DMMP uptake are sufficiently weak that they have little to no effect on the electronic structure of the adsorbate. One notable exception is that the band assigned to the P=O stretch at 1275 cm^{-1} in the gas phase shifts to 1252 cm^{-1} upon adsorption. This shift is consistent with charge redistribution within the P=O bond as some charge transfers to the ZrO-H bond upon hydrogen bond formation (i.e., creation of P=O---HOZr hydrogen bonds). A further indication that the uptake is driven by hydrogen bonding, as opposed to chemistry within the MOF, comes from the absence of significant changes in absorbance of bands originally present in the MOF. That is, the IR data indicate that the framework is largely unaffected by the presence of DMMP.

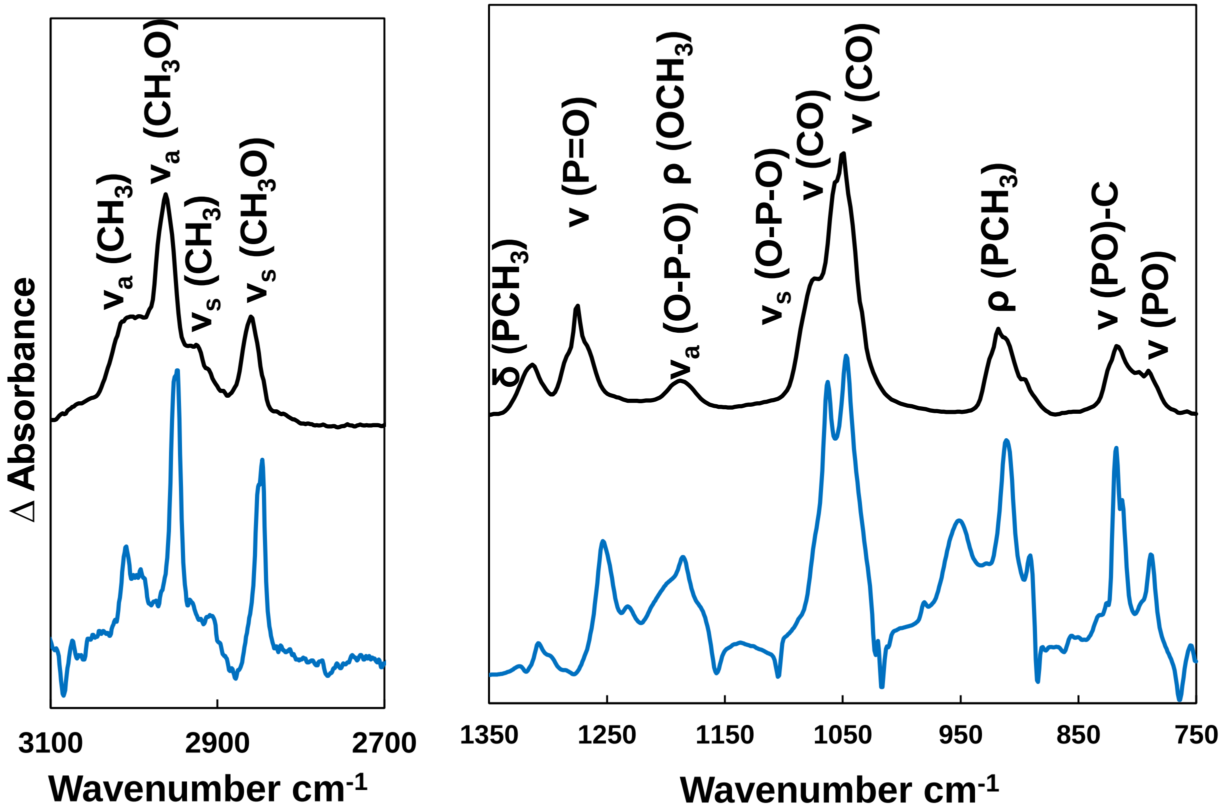

Figure 4.2 Gas phase DMMP (black) and difference spectra of DMMP adsorbed onto UiO-66 (blue) at high wavenumber region (left) and low wavenumber region (right).

Following exposure, the MOF was heated to drive off weakly bound adsorbates. The spectra shown in red in Figure 4.1A and Figure 4.1B reveal that the original IR spectrum for UiO-66 is recovered following heating. That is, the IR spectra indicate that DMMP thermally desorbs from the UiO-66 and the MOF returns to its original state.

While the current results show that reactivity is below my limit of detection in this UHV-based experiment, I have previously shown that DMMP can access the pores and affect the MOF structure if given sufficient time and exposure. Specifically, under prolonged exposure of UiO-66 to DMMP under atmospheric conditions, the MOF structure was found to change measurably.[82] The difference between the prior work and that described here is related to the level of exposure–

10^4 L versus 10^{12} L, which further evidences the very low reaction probability for vaporous DMMP with UiO-66.

4.2 **Uptake and Reactions of DMMP within UiO-67**

The other MOF, UiO-67, is isoreticular with UiO-66 but is composed of longer 4,4' biphenyl-dicarboxylate (BPDC) linkers that expand the pore apertures relative to UiO-66 (to 11.5 Å for tetrahedral and 23 Å for octahedral cavities). The more open structure of UiO-67, therefore, provides avenues through which reactants may access the SBUs.[100] My results demonstrate that the larger pore structure provides reactants with access to sites where chemistry and irreversible binding occur.

Chemisorption of DMMP into UiO-67 is revealed in the IR spectra shown in Figure 4.3. The spectrum shown in black in Figure 4.3 is that of the pristine UiO-67 sample. As for UiO-66, many of the bands for this spectrum have been previously assigned (Table 4.1). Upon exposure to a controlled flux of gas-phase DMMP (2×10^4 L), several new bands develop in the infrared spectra, while key features in the OH region, assigned to molecular water and free hydroxyl groups, diminish in intensity. However, the bands assigned to linker and node vibrational motions within the MOF remain largely unaffected (see the spectrum shown in blue in Figure 4.3). Several of the new bands are nearly identical in wavenumber to those assigned to physisorbed DMMP (see the above discussion associated with UiO-66); however, many previously unobserved bands appear in the post-exposure IR spectra for UiO-67, suggesting unique bond breaking or formation may have accompanied DMMP uptake. Following the room temperature DMMP exposure, the MOF was heated in an effort to drive the physisorbed molecules from the framework, as was done for the UiO-66 sample. I found that the majority of the new bands for the DMMP-exposed UiO-67 sample that could not be assigned to physisorbed DMMP persisted throughout the thermal annealing procedure even when the sample was maintained at 600 K for 60 min (see Figure 4.3, red). The new bands are hypothesized to be due to the formation of a highly stable chemisorbed methyl methylphosphonic acid species. Many prior studies have shown that DMMP and other organophosphonates react and irreversibly bind at the type of strong Lewis acid sites that may be present at missing-linker defects within the UiO-67 MOF. This hypothesis was tested by repeating the DMMP-exposure study with MOF-808, which possesses the same SBU as UiO-67, but is linked by benzene-1,3,5-tricarboxylates (BTCs) that produce a very large pore structure and a band of exposed Zr-OH and Zr-OH_2 sites that decorate the circumference of the node (See Figure 1.10).

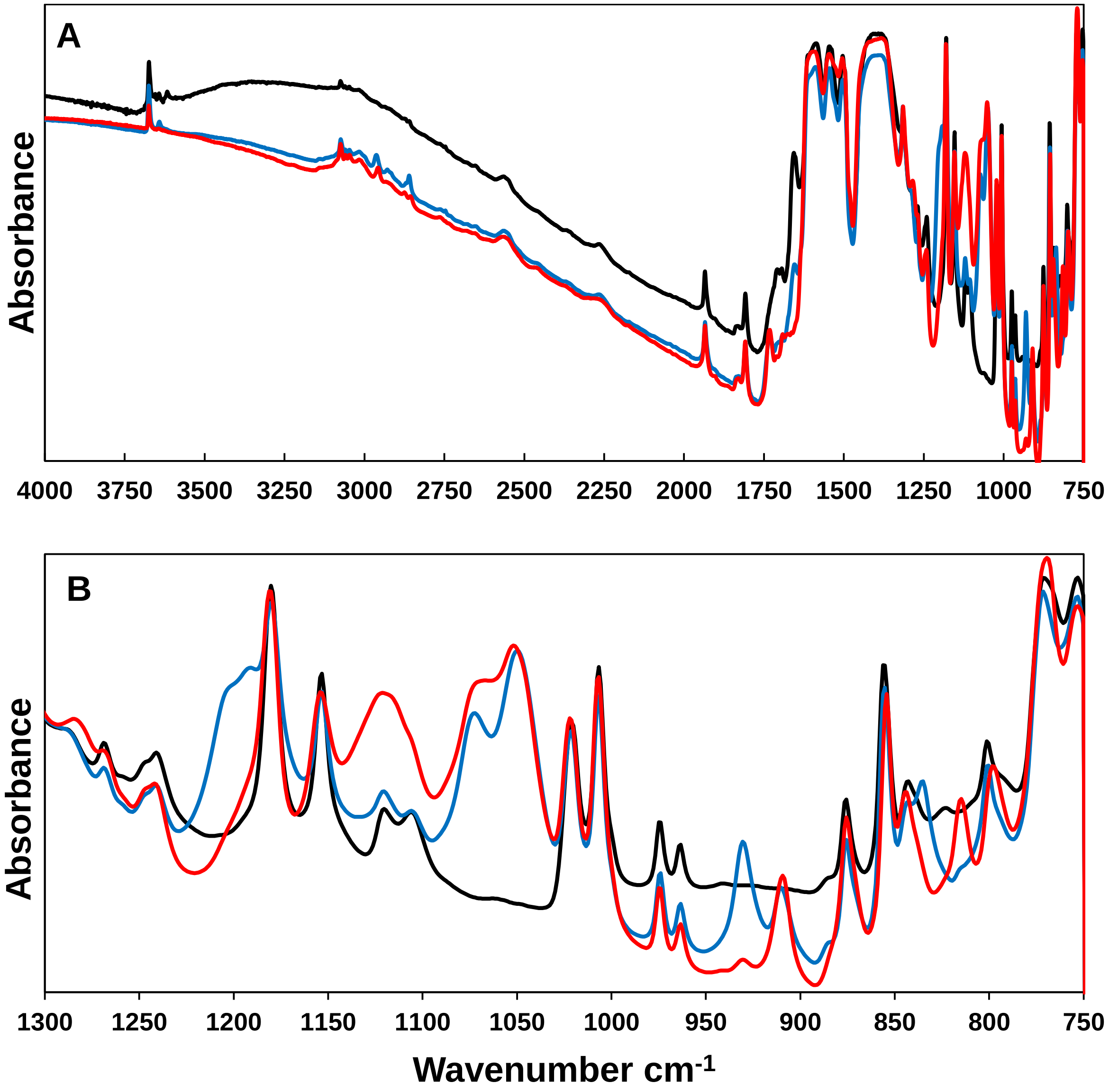

Figure 4.3 IR spectra for the entire mid-IR region (A) and the "fingerprint" region (B) of UiO-67 before DMMP exposure (black), after DMMP exposure (blue), and after post-exposure thermal treatment to 600 K (red).

4.3 Uptake and Reactions of DMMP within MOF-808

As described in the introduction, MOF-808 has been shown to be one of the most effective MOF-based catalysts for the hydrolysis of organophosphonates in buffered solutions.[104] Previous studies attribute the high activity of MOF-808 to an open pore structure, the consequence of only six (as opposed twelve for the UiO-MOFs discussed above) linkers per Zr_6 node.[105] The pore sizes of MOF-808 (18 Å)[104-105] are even larger than those of UiO-67 (11.5 Å)[100]. My results show that MOF-808 reacts irreversibly with the simulant DMMP to produce a significant concentration of node-bound methyl methylphosphonic acid and methyl phosphonic acid.

Similar to the MOFs described above, the infrared spectra of the pristine MOF-808 (Figure 4.4, black) is rich in spectral bands for both the linkers and the nodes (see Table 4.1 for assignments). Most notably, MOF-808 exhibits a narrow band at 3675 cm^{-1} indicative of the free hydroxyl groups that complete the coordination sphere of the node Zr atoms, and a broad band in the 3600-3100 cm^{-1} range that is likely due to hydrogen-bonded hydroxyl groups and aqua ligands.[124] As described below, these sites are likely initial docking points for DMMP, where the molecules are sequestered through strong hydrogen bonding interactions.

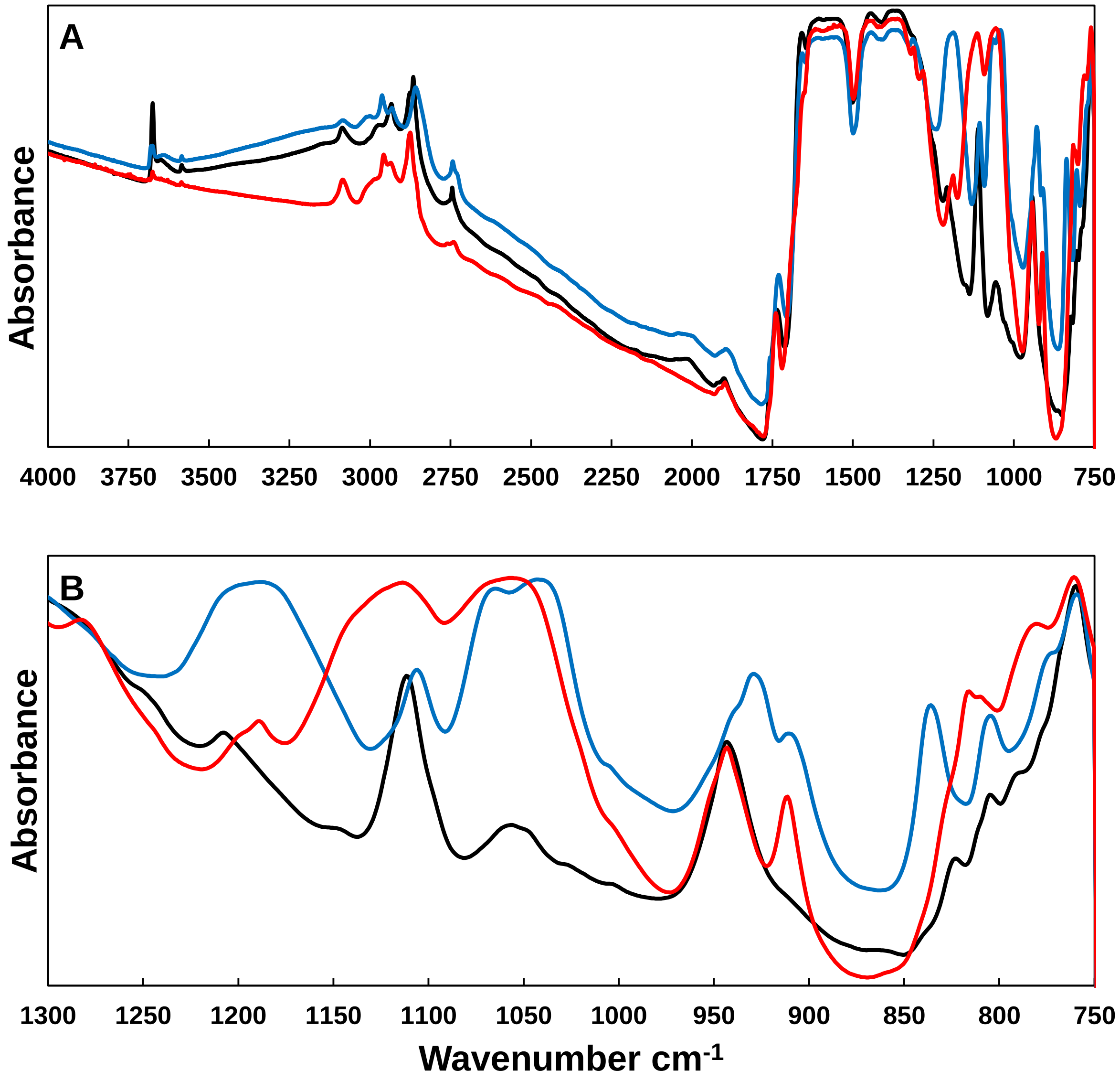

Figure 4.4 IR spectra for the entire mid-IR region (A) and the "fingerprint" region (B) of MOF-808 before DMMP exposure (black), after DMMP exposure (blue), and after post-exposure thermal treatment to 600 K (red)

Upon exposure to DMMP, the free hydroxyl groups diminish in intensity while new bands emerge. The new bands are very similar to those described above for exposure to UiO-67. The detailed difference spectra for MOF-808 and UiO-67 are presented in Figure 4.5, accommodated with corresponding peak assignments in Table 4.2.

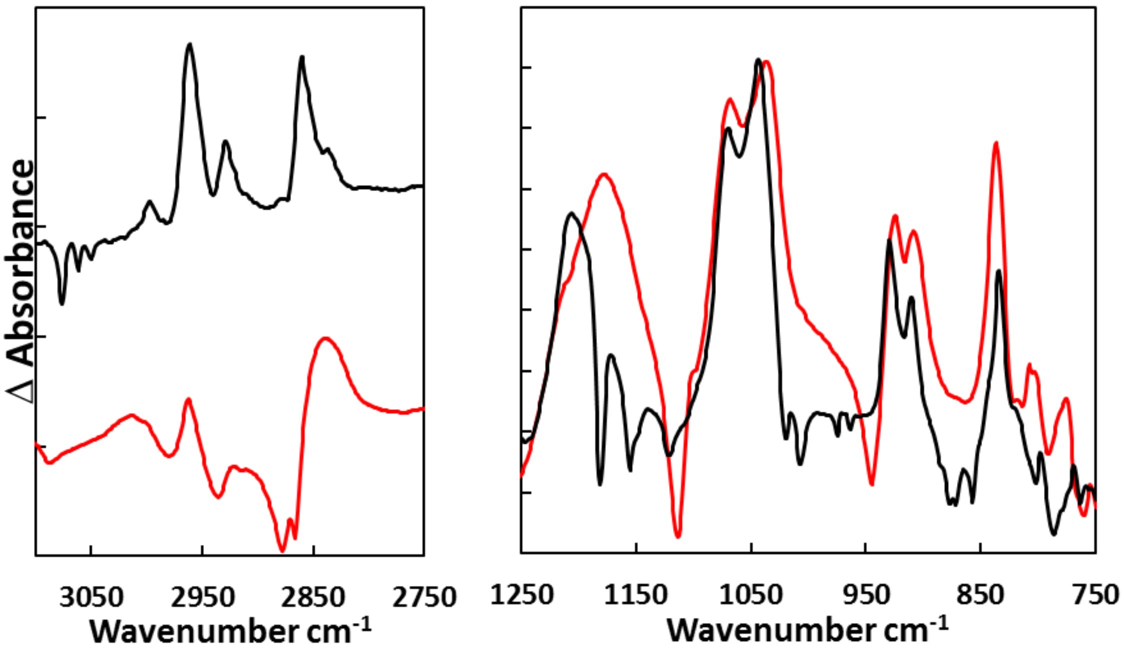

Figure 4.5 Difference IR spectra of MOF-808(Red) and UiO-67 (Black) upon DMMP exposure at room temperature (298 K)

In the C-H region, bands due to physisorbed DMMP, as well as chemisorbed methoxy groups, develop upon exposure. These signals are accompanied by the emergence of bands in the low wavenumber region of the spectrum (Figure 4.4B). The strongly chemisorbed species were isolated within the MOF by heating to 600 K, and the resulting IR spectrum following heating is shown by the red trace in Figure 4.4.

Table 4.2 Observed vibrational frequencies (cm^{-1}) in difference IR spectra of Zr_6 MOFs upon DMMP exposure and their assignments.[165]

Mode	UiO-66-DMMP cm^{-1}	UiO-67-DMMP cm^{-1}	MOF-808-DMMP cm^{-1}
$\nu(\mathrm{ZrO{-}H})_{\mathrm{SBU,\ H\text{-}bounded}}$	3313		
$\nu_{as}(\mathrm{CH_3})$	3009	2997	3012
$\nu_{as}(\mathrm{CH_3O})$	2950	2961	2962
$\nu_{s}(\mathrm{CH_3})$	2950sh	2961sh	2962sh
$\nu_{as}(\mathrm{ZrOCH_3})$		2928	2913
$\nu_{s}(\mathrm{CH_3O})$	2846	2860	2839
$\nu_{s}(\mathrm{ZrOCH_3})$		2836	2839sh
$\delta(\mathrm{PCH_3})+\delta(\mathrm{P{=}O})+\nu_{as}(\mathrm{O\text{-}P\text{-}O})+\rho(\mathrm{OCH_3})$			1178
$\delta(\mathrm{PCH_3})$	1308	1207	
$\upsilon(\mathrm{P{=}O})$	1255	1171	
$\nu_{as}(\mathrm{O\text{-}P\text{-}O})+\rho(\mathrm{OCH_3})$	1186	1138	
$\nu_{s}(\mathrm{O\text{-}P\text{-}O})$	1064sh	1070sh	1068sh
$\nu_{as}(\mathrm{CO})$	1064	1070	1068
$\nu_{s}(\mathrm{CO})$	1048	1043	1038
$\rho(\mathrm{PCH_3})_{\mathrm{P{=}O\ bounded\ to\ SBU}}$	952	926	925
$\rho(\mathrm{PCH_3})$	912	910	909
$\nu(\mathrm{P\text{-}C})$	819	834	837
$\nu(\mathrm{P\text{-}O})$	789	819	775

ν: bond stretching, ρ: rocking (in-plane), δ: angle bending

With two broad bands around 1130 and 1050 cm^{-1} and smaller bands in the 905-750 cm^{-1} region, the difference spectra for MOF-808 and UiO-67 following heating are very similar, suggesting that the same product is formed on each MOF. Figure 4.6 is a reproduction of the annealed spectra shown in Figure 4.3 and Figure 4.4, but with the original MOFs employed as the background such that the primary features in the spectra can be assigned to the MOF-bound reaction products. As the comparison indicates, the adsorbates are strongly bound (i.e., they do not desorb from the MOF even after heating to 600 K) and exhibit similar vibrational spectra for both MOFs.

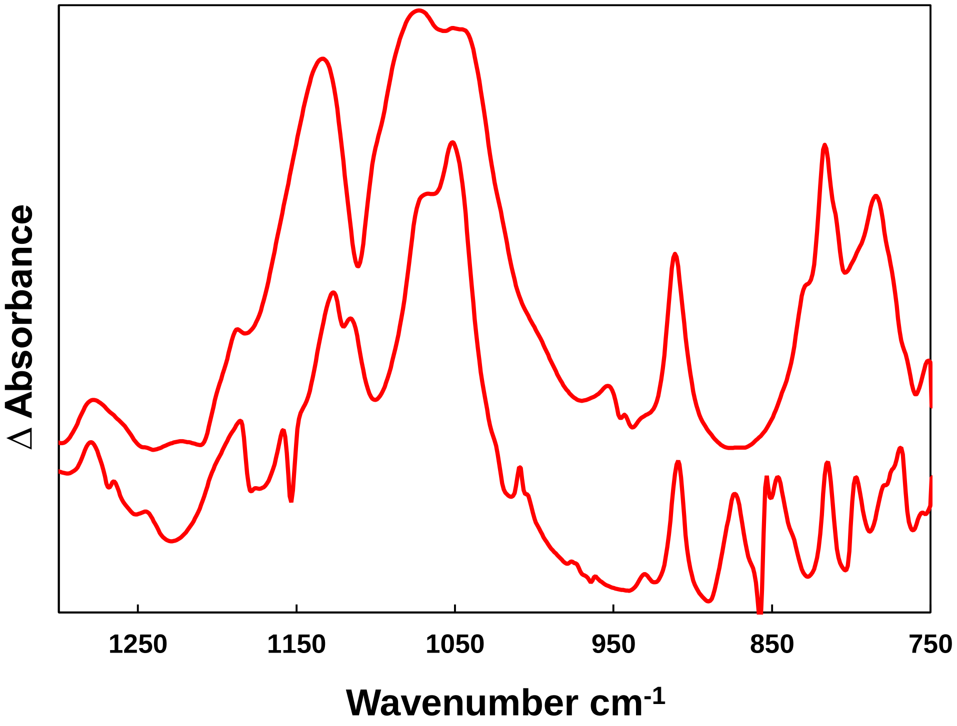

Figure 4.6 Difference IR spectra of MOF-808 (top) and UiO-67 (bottom) upon DMMP exposure then thermal treatment to 600 K for 60 minutes.

For both UiO-67 and MOF-808, the most likely MOF-bound product is methyl methylphosphonic acid (MMPA), which I hypothesize may bind to the nodes in its deprotonated form following the hydrolysis of DMMP. In fact, recent theoretical work showed that Sarin, which has a structure similar to DMMP, decomposes to isopropyl methyl phosphonic acid (IMPA) and methyl phosphonofluoridic acid (MPFA) upon reaction with the SBU of UiO-MOFs[166] and another metal-oxide based cluster, $Cs_8Nb_6O_{19}$.[167] Therefore, we performed energy minimization calculations of a Zr_6 SBU-bound MMPA species. The structure and calculated infrared spectrum, compared to that of the post-annealed MOF, are shown in Figure 4.7. The calculations help assign the O-P-O asymmetric, and O-P-O symmetric stretching modes to bands at 1155, and 1058 cm^{-1}, respectively, and the P-C stretching motion to the band at 791 cm^{-1}, which also agree with previously published work.[165, 168] Together, the experimental and computational results strongly suggest that the irreversibly bound product of DMMP + Zr_6-MOF reactions is MMPA at the SBU.

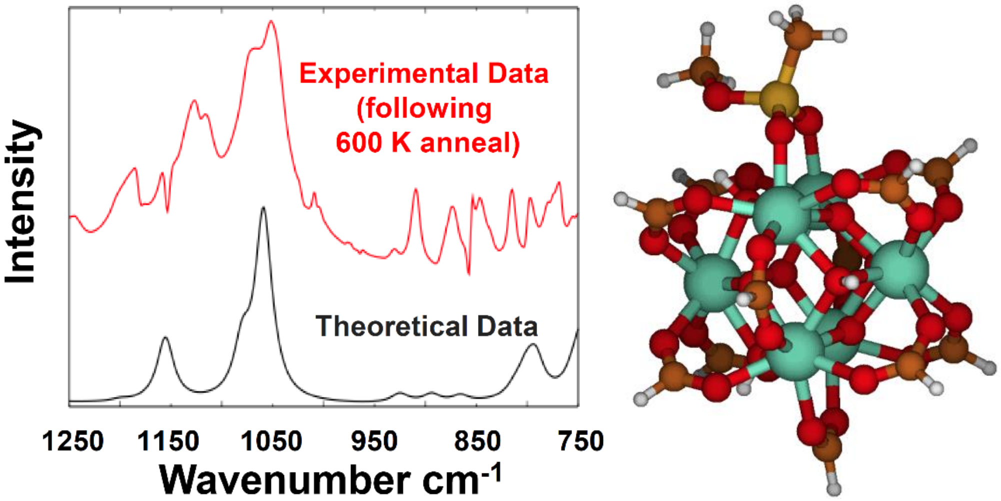

Figure 4.7 Left: Experimental (red) difference spectrum and theoretically calculated spectrum (reaction products, black, 10 cm^{-1} linewidth) of post-exposure UiO-67 after thermal treatment at 600 K; Right: Schematic of DMMP-UiO-67 reaction product. Color code: Zr: teal, C: brown; P: gold; H: white; O: red.

4.4 X-ray Photoelectron Characterization of MOF-bound Products after DMMP Exposure

While infrared spectra provide insight into the vibrational motions of the MOF-bound species, XPS reveals information about the elemental composition and electronic characteristics of the system. XPS spectra of Zr 3*d* electrons for MOF-808 before DMMP exposure indicate that the binding energy of Zr $3d_{3/2}$ and Zr $3d_{5/2}$ electrons are 185.61 and 183.27 eV, respectively (Figure 4.8A). These assignments and binding energies are consistent with previous reports.[169] Upon DMMP exposure, followed by 60-minutes of thermal treatment at 600 K to remove the physisorbed molecules, the Zr *3d* peaks shift slightly to lower binding energy, indicating the Zr atoms are less positively charged after DMMP reacts with the MOF, which provides evidence for charge redistribution within the node during covalent bond formation with the hypothesized MMPA product.

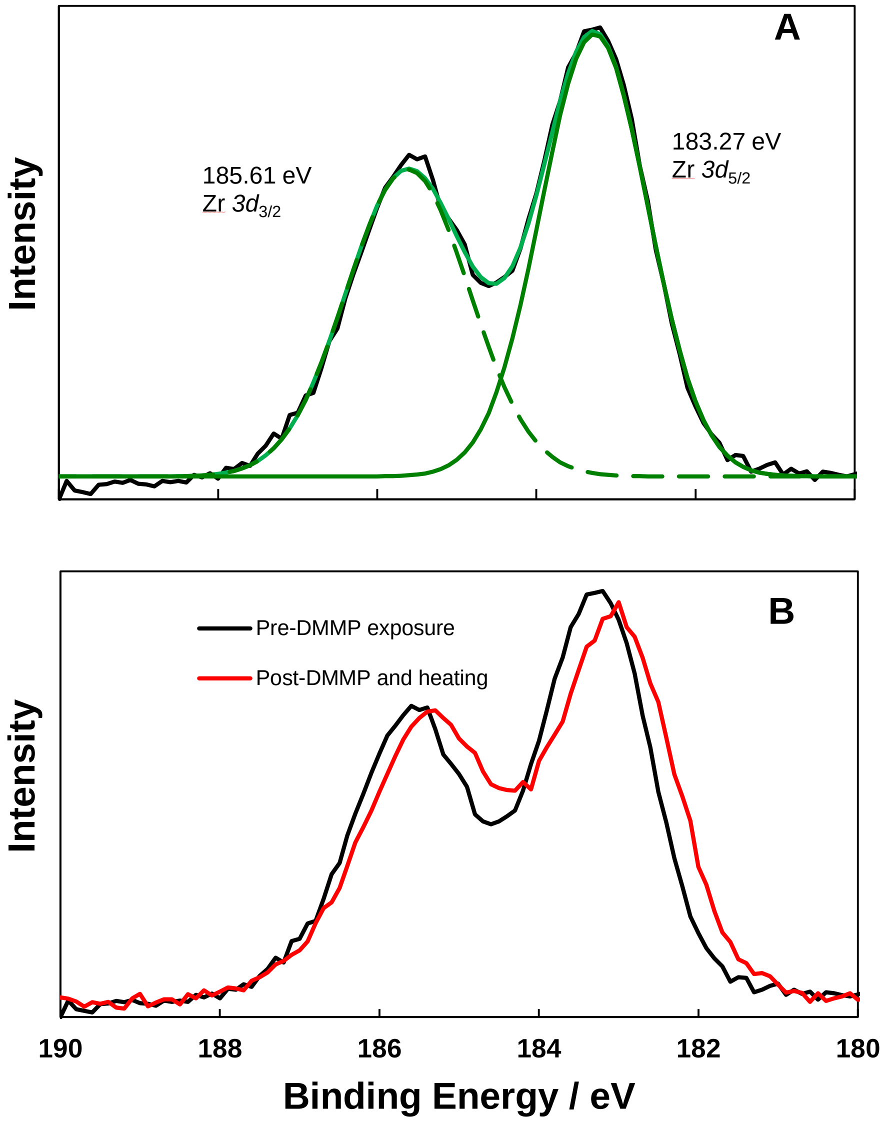

Figure 4.8 XPS spectra of Zr 3d on MOF-808 before DMMP exposure (top) fitted with two Gaussian components (green), and comparison of pre-DMMP exposure with after post-exposure thermal treatment at 600 K (bottom)

The XPS spectra for the phosphorus atoms following DMMP exposure to the MOF reveal two binding energy features that suggest the reaction is more complex than simple MMPA formation. More specifically, upon DMMP exposure to MOF-808, a feature in the photoelectron spectrum near 134 eV appears that likely corresponds to the *2p* electrons of phosphorus. The P *2p* peak can only be adequately modeled with two Gaussian components, which are most likely not due to spin-orbit splitting. That is, not only is the intensity ratio of the peaks inconsistent with the spin-orbit splitting of the P *2p* electrons, but also the energy difference for these components is only expected to be 0.2 eV, well below that observed here.[170] Therefore, there are likely two types of phosphorus within the MOF, each with a different bonding configuration.

Previous studies into the reaction mechanisms of DMMP on the surface of aluminum, cerium, iron, magnesium, calcium, yttrium and titanium oxide suggest that multiple phosphorus-containing products form upon uptake. For example, researchers have shown that, at room temperature on Al_2O_3, DMMP losses one methoxy group to form MMPA on the surface, which binds through two O-P bonds. Upon further thermal treatment to near 600 K, part of the MMPA further reacts with the aluminum oxide to shed the other methoxy group and form MPA, which binds to the surface through three O-P bonds. At temperatures below 700 K, MMPA and MPA have been shown to coexist on several of these oxide surfaces.[165, 171-176] Based upon the previous studies, I hypothesize that one component of P *2p* XPS spectrum (Figure 4.9) is due to DMMP molecules are partially hydrolyzed (i.e., lose one methoxy group) to form MMPA. The second component may arise from the continued reaction of the MMPA product to form MPA. This hypothesis is supported by the observation of IR bands that can be assigned to C-H stretching motions for the DMMP-exposed MOF-808 (2924 cm^{-1} and 2837 cm^{-1}) and UiO-67 (2927 cm^{-1} and 2835 cm^{-1}). The IR and XPS data strongly suggest that one of the products of this reaction is surface methoxides bound to the MOF nodes. These results suggest an overall reaction mechanism that requires initial interactions with Lewis acid sites, which activate the molecule toward nucleophilic attack by water or labile hydroxyl groups. Computational studies have been employed to test this hypothesis.

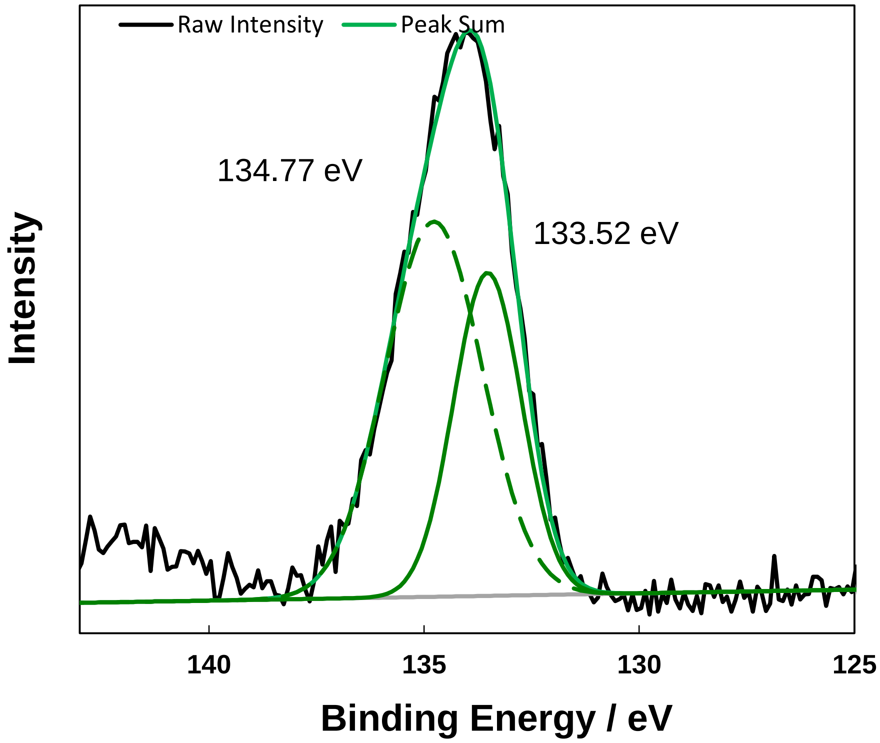

Figure 4.9 XPS spectra of P 2p on MOF-808 after post-exposure thermal treatment at 600 K (fitted with two Gaussian components, green)

4.5 Computational Studies of the DMMP Overall Reaction Pathway

To augment the measurements, Prof. Troya has performed electronic structure calculations of the stationary points of the decomposition reaction of DMMP with the SBU of UiO-66/67. All of the DFT calculations employed the M06L functional[177] with an ultrafine integration grid as implemented in the Gaussian09[178] code. Geometry optimizations and harmonic frequencies were obtained with the 6-31G** basis set for main-group elements and the Lanl2dz basis set and pseudopotentials for Zr. The stationary-point energies were further refined at via addition of diffuse functions in the main-group basis set (6-31++G**). All reported energies in this paper, therefore, correspond to electronic energies obtained at the M06L/(6-31++G**+Lanl2dz) level, corrected by M06L/(6-31G**+Lanl2dz) zero-point energies. [103]

Formally, the decomposition reaction follows base hydrolysis in which a hydroxide moiety adds nucleophilically to the phosphorus center of DMMP. This addition generates a phosphorus pentacoordinated intermediate that undergoes subsequent elimination of a methanol molecule to yield MMPA. The reaction occurs at the nodes of the MOFs, which feature a $Zr_6(\mu_3\text{-}O)_4(\mu_3\text{-}OH)_4$ SBU. In UiO-67, the presence of 12 BPDC linkers fully saturates the coordination sphere of the Zr atoms, rendering the node catalytically inactive. Thus, the reaction in this MOF occurs at missing linker defects, whose structure has been recently described experimentally[101] and computationally.[102] Removal of one linker generates two adjacent undercoordinated Zr atoms (nodes with several linkers missing would likely present additional undercoordinated reactive Zr atoms). Under ambient conditions and in the most stable configuration, one of these Zr atoms coordinates a hydroxide moiety while the other coordinates a water molecule. A second water molecule is present in the defect and forms hydrogen bonds to both the Zr–OH and Zr–OH_2, and a μ_3-OH group in the SBU.[102] In this work, the thermal treatment of the MOFs prior to DMMP exposure likely removes a majority of the coordinated water, leaving a Zr–OH moiety, and an adjacent undercoordinated Zr site to which DMMP binds to start the reaction.

Prior computational work has revealed that the most stable binding of DMMP to metal sites is through the O atom of sp^2 hybridization,[179-182] and consequently this binding arrangement has been used to model the interaction of DMMP to the undercoordinated Zr atom of the defective UiO-67 SBU in this work. Figure 4.10 and Figure 4.11 show the potential-energy profile and stationary-point geometries of the minimum-energy reaction path, which corresponds to a collinear arrangement of the forming P–OH bond and the P–CH_3 group at the addition transition state.

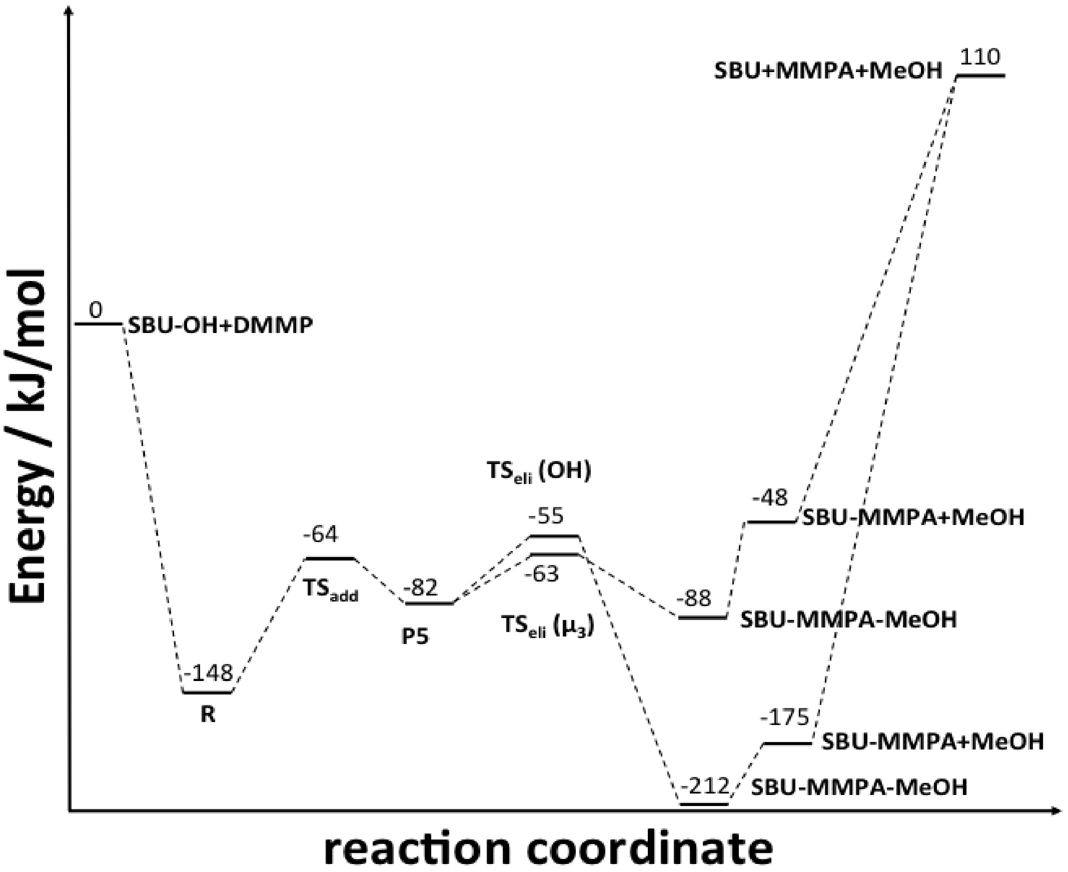

Figure 4.10 Potential-energy profile for the reaction of DMMP with a defective SBU of UiO-67 along the approach in which the P–CH_3 bond of DMMP is collinear to the forming P–OH bond at the addition transition state.[103]

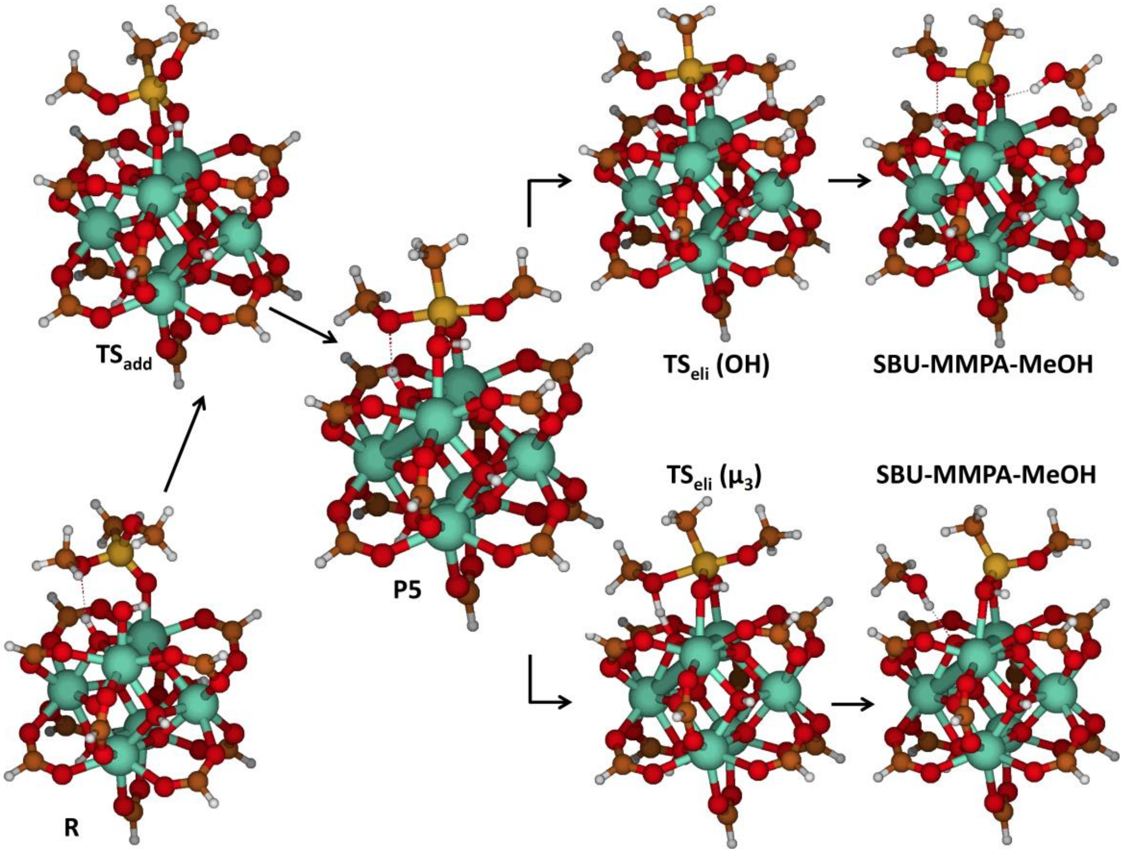

Figure 4.11 Geometries of the central stationary points in the decomposition of DMMP with a defective SBU of UiO-67 along the approach in which the P–CH_3 bond of DMMP is collinear to the forming P–OH bond at the addition transition state. Same color code as Figure 4.7.[103]

As mentioned above, the reaction starts upon the binding of DMMP to the SBU to form a reaction complex (Structure R in Figure 4.11). This binding is exothermic by 148 kJ/mol and coordinates DMMP to a Zr atom adjacent to the Zr–OH group. The first reaction step corresponds to the addition of the coordinated OH ligand to the phosphorus atom of DMMP. The transition-state energy for this step is 84 kJ/mol and generates a pentacoordinated phosphorus intermediate (P5). This addition reaction is endothermic by 66 kJ/mol. Proton transfer to the P5 intermediate results in the elimination of a methanol molecule, and formation of MMPA. There are two elimination pathways, which differ in the source of the proton transferred to the leaving methoxy group. In the lowest-energy elimination pathway, the proton emerges from a μ_3-OH group of the SBU through a barrier of 19 kJ/mol. The second pathway involves proton transfer from the –OH ligand that has mounted the nucleophilic addition and exhibits a slightly larger barrier of 27 kJ/mol. Both elimination pathways yield methanol and MMPA molecules adsorbed on the SBU. Methanol is only bound to the SBU through a hydrogen bond and exhibits desorption energies of ~40 kJ/mol for the two pathways. Conversely, the MMPA product is strongly bound to the SBU, but the desorption energy depends on the pathway. The elimination process involving proton transfer from the μ_3-OH group generates a protonated MMPA product with two dissimilar Zr–O bond lengths of 2.31 and 2.59 Å, with the longer bond corresponding to the protonated O atom of MMPA. The binding energy of this MMPA product to the SBU is 158 kJ/mol. The proton of the methanol product in the second elimination pathway is transferred from the –OH ligand, and generates an aprotic MMPA product that is bound to the SBU in a bidentate manner, with nearly identical Zr–O bond distances of 2.22 and 2.23 Å. MMPA is extraordinarily strongly bound to the SBU, with an enthalpic well depth of 285 kJ/mol relative to the separated products.

The experimental IR spectra in Figure 4.3 also show the presence of Zr–OCH_3 groups generated during the reaction, but the reaction pathways in Figure 4.11 do not provide a source for that moiety. Figure 4.12 exhibits an alternative reaction pathway that leads to Zr–OCH_3 formation. There are two major differences between this mechanism and the one presented in Figure 4.11. First, the initial binding of DMMP to the Lewis-acid undercoordinated Zr site is through one of the O(sp^3) atoms of DMMP, and not through the O(sp^2) atom of the phosphoryl group. The DMMP-MOF binding in Figure 4.12 is 37.8 kJ/mol weaker than that in Figure 4.11 but allows for the formation of Zr–OCH_3 products. From this binding arrangement, the reaction is also initiated via nucleophilic addition of a neighboring Zr–OH group, but the elimination of the methoxy moiety occurs directly, without an intervening pentacoordinated phosphorus intermediate. The absence of this intermediate provides the second major difference between the mechanisms in Figure 4.12 and Figure 4.11. The products of the addition-elimination process are a Zr–OCH$_3$ group, and an MMPA product that is bound to the UiO-67 MOF SBU in a monodentate manner and also forms a hydrogen bond with a μ_3–OH group. The barrier for the Zr–OCH$_3$ formation pathway is only slightly larger than the overall barrier for methanol elimination (Figure 4.10). Therefore, both pathways may play a role in the experiment.

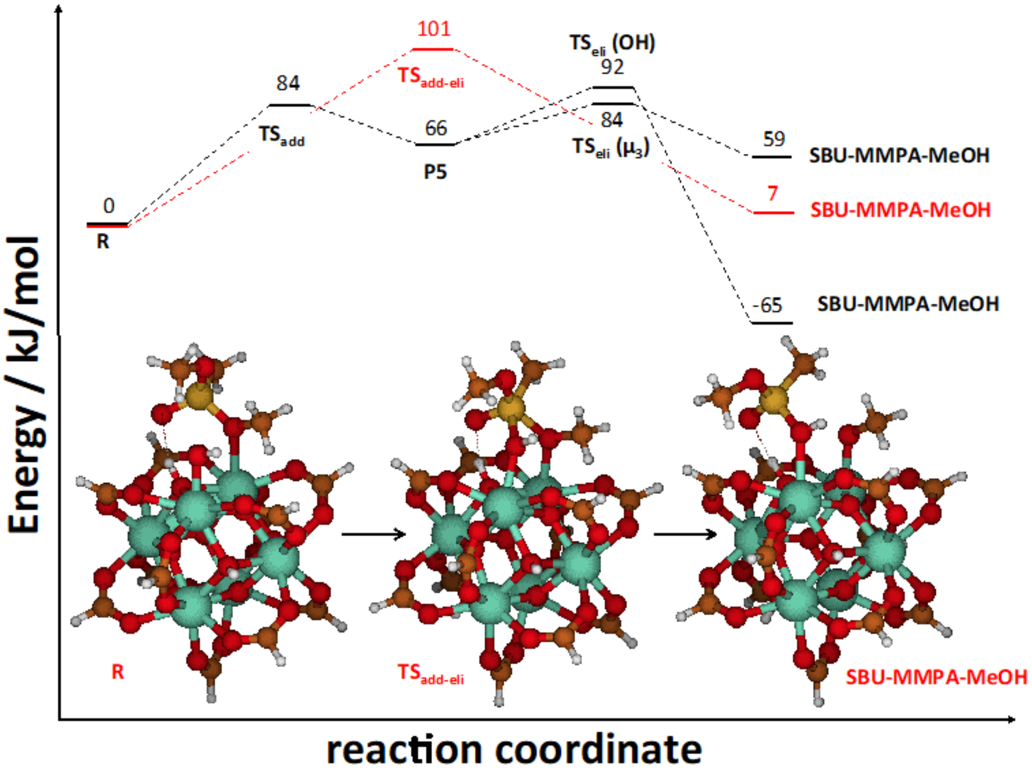

Figure 4.12 Comparison between the reaction mechanism for decomposition of DMMP on the UiO-67 SBU shown in Figure 4.10 and Figure 4.11 (black), and an alternative reaction pathway that results in Zr–OCH$_3$ formation (red). Energies are referred to the DMMP–MOF reagent complex for each pathway. Insets correspond to reaction along the Zr–OCH$_3$ pathway. Same color code as Figure 4.7.[103]

4.6 DMMP-MOF-808 Reaction Kinetics

The kinetics, which provides further insight into the reaction mechanism, was tracked by time-resolved infrared spectra of MOF-808 during DMMP exposure. Upon exposure of the MOF to DMMP, the intensity of the free hydroxyl groups decreases with time, while several new bands simultaneously rise in the low wavenumber region (see Figure 4.13).

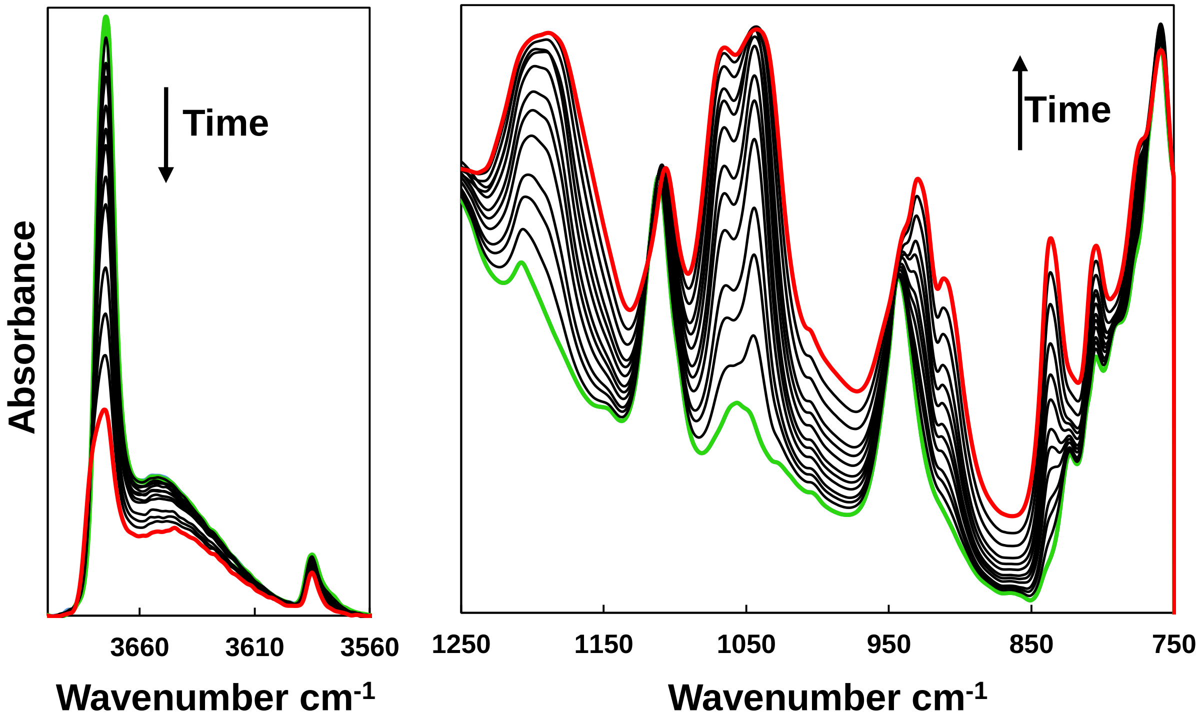

Figure 4.13 Time-resolved IR spectra are shown of MOF-808 upon DMMP exposure at room temperature (298 K). The high wavenumber region is shown on the left, and the low wavenumber region appears on the right. The spectrum in green was recorded before DMMP exposure, and the spectrum in red represents the final spectrum after DMMP exposure.

As described above, the consumption of the free hydroxyl groups is integral to the decomposition of DMMP into MMPA and MPA. Therefore, one may hypothesize that the features assigned to hydroxyl groups should decrease at the same rate as the rise in product bands. The absorbance for the free OH groups has been integrated and plotted versus exposure time in Fig. 14, which also provides the rate of increase for the band at 1175 cm^{-1} (assigned to physisorbed DMMP: The H-C-H and O-C-H bends) and the band at 1050 cm^{-1} assigned to the reaction product, MMPA (O-P-O symmetric stretch in MMPA).

Clearly depicted in Figure 4.13 is the fast decrease in intensity for the OH groups accompanied by a similarly rapid rise in bands assigned to MOF adsorbates. The initial changes in band intensities upon exposure of the MOF to DMMP are so rapidly relative to the changes at later times that the data cannot be modeled by a single exponential rise indicative of pseudo-first order kinetics, as one might expect for a process where impinging molecules react in a single step. Rather, there appear to be two exponential components to the reaction rates. The solid lines in Figure 4.14 model the data as a sum of two exponential components and the non-linear least squares fitting parameters yield observed rate constants for the various components (see Table 4.3).

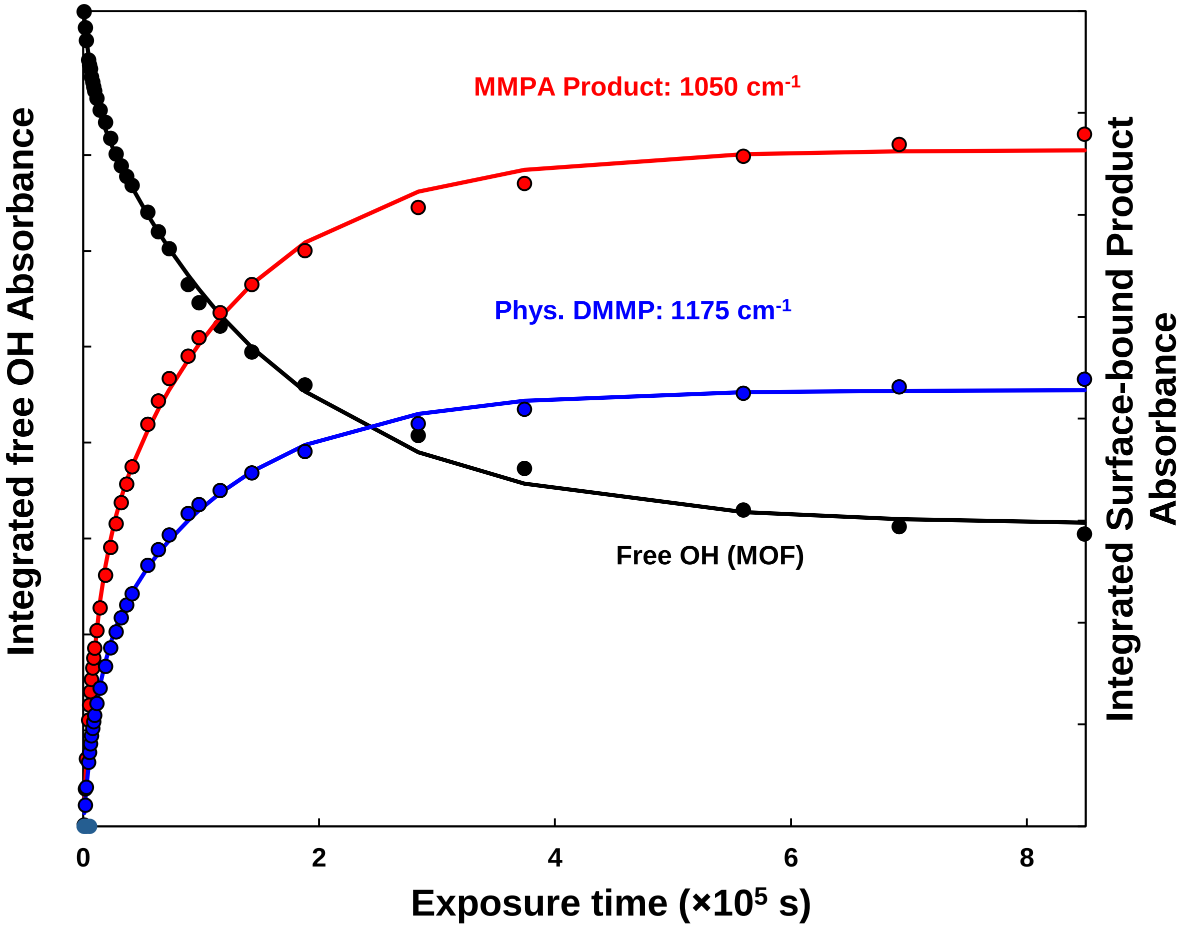

Figure 4.14 The integrated absorbance of the free OH groups in MOF-808 (black), physisorbed DMMP (blue), and the reaction product (red) versus the DMMP exposure time. The solid lines model the data with two exponential functions that are necessary to capture the fast rise (fall) at early times and the slow development in the data at later times. The fitting parameters are provided in Table 4.3.

The two rate constants required to adequately describe the kinetics for the development of the main reaction product, MMPA, reveal that there are two reaction pathways. However, the two pathways appear to lead to the same products, as evidenced by the consistency in the wavenumber and bandwidths of these features throughout the experiment (see Figure 4.13). Therefore, I speculate that the rapid pathway, open at early times, is due to reactions at the most accessible Zr sites and OH groups. The slow reaction component is then due to reactions at sites that are much less accessible, perhaps because they are blocked by the irreversibly bound MMPA products that are generated at short reaction times.

Table 4.3 Rate Constants (s^{-1}) for the DMMP + MOF-808 kinetics

Component	**OH (3674 cm^{-1})**	**Phys. DMMP (1175 cm^{-1})**	**MMPA (1050 cm^{-1})**
Fast rise	1.3 (± 0.3) x 10^{-3}	8.4 (± 2.0) x 10^{-4}	9.3 (± 2.0) x 10^{-4}
Slow plateau	6.3 (± 1.3) x 10^{-5}	8.7 (± 2.0) x 10^{-5}	8.3 (± 2.0) x 10^{-5}

Interestingly, the rate of development of the bands assigned to physisorbed DMMP track the rate for OH consumption and product formation. That is, there appear to exist physisorption sites that are both readily accessible and sites that provide some steric hindrance to physisorption. More importantly, the magnitudes of the rate constants are very similar for both DMMP physisorption and DMMP reactions within the MOF. Because the rate of physisorption likely depends primarily on the incident flux and the diffusion rate of DMMP within the MOF, the similarities of the rates for the various components strongly suggest that the reaction rate is diffusion limited. This observation further supports the mechanism identified by the computational studies, which indicates that the transition states that separate DMMP from the MMPA product have relatively low energies.

4.7 Hydrogen Bonding of DMCP on UiO-66

The interactions between DMCP and UiO-66 are quite similar to DMMP. Upon exposure to DMCP, the infrared bands associated with the UiO-66 remain largely unaffected, but new bands, which can be assigned to the DMCP adsorbate, emerge. The spectra shown in blue in Figure 4.15A and Figure 4.15B were recorded following exposure of UiO-66 to 2×10^4 L of

DMCP while the MOF was maintained at 298 K. One of the most significant changes upon exposure is the emergence of a broad band at 3425 cm^{-1}. This band, which is accompanied by a reduction in the intensity of the free OH band, is attributed to the formation of a hydrogen bond between DMCP and the hydroxyl groups at the nodes. The infrared studies of earlier have demonstrated that DMMP is an excellent hydrogen bond acceptor. Here, I observe similar types of hydrogen bonding interactions with DMCP. but they seem to occupy only a small fraction of the total number of free OH groups within the MOF. Note that, even after prolonged exposure, the intensity of the free hydroxyl groups originally present at the nodes was not reduced beyond 30% of the original intensity, implying that the bridging node–OH groups appear to be largely inaccessible to DMMP. Just like the DMMP, the majority of the uptake therefore likely occurs on the surface of the MOF crystallites, and little penetration into the MOF accompanies uptake. This interpretation is consistent with previous suggestions that the pore apertures for UiO-66 are too small for a molecule like DMCP to freely access the interior of the MOF.[77] The aperture size for the octahedral pore is only 12 Å, while that of the tetrahedral pore, where the OH groups reside, is even smaller at 6 Å.[152-153]

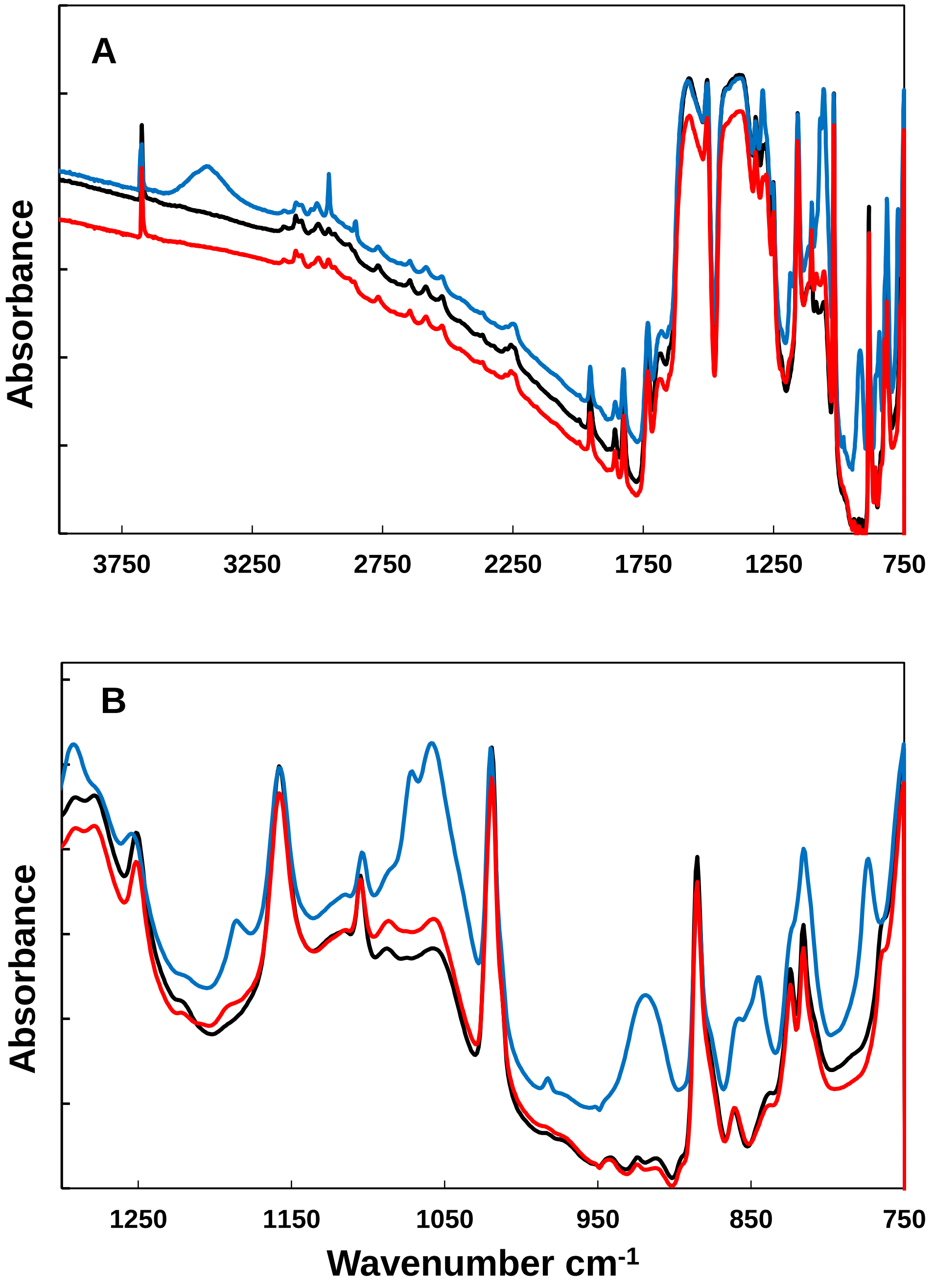

Figure 4.15 IR spectra for the entire mid-IR region (A) and the "fingerprint" region (B) of UiO-66 before DMCP exposure (black), after DMCP exposure (blue), and after post-exposure thermal treatment to 600 K (red).

The assignment of the bands that emerge upon exposure is aided by direct comparison to the IR spectrum for gas-phase DMCP (Figure 4.16). The spectrum shown in blue was recorded following exposure of UiO-66 to DMCP with the original MOF used as the background such that the new bands represent changes in absorbance due to the vibrational excitations associated with new adsorbates, and negative features are due to changes to bands associated with the original MOF.

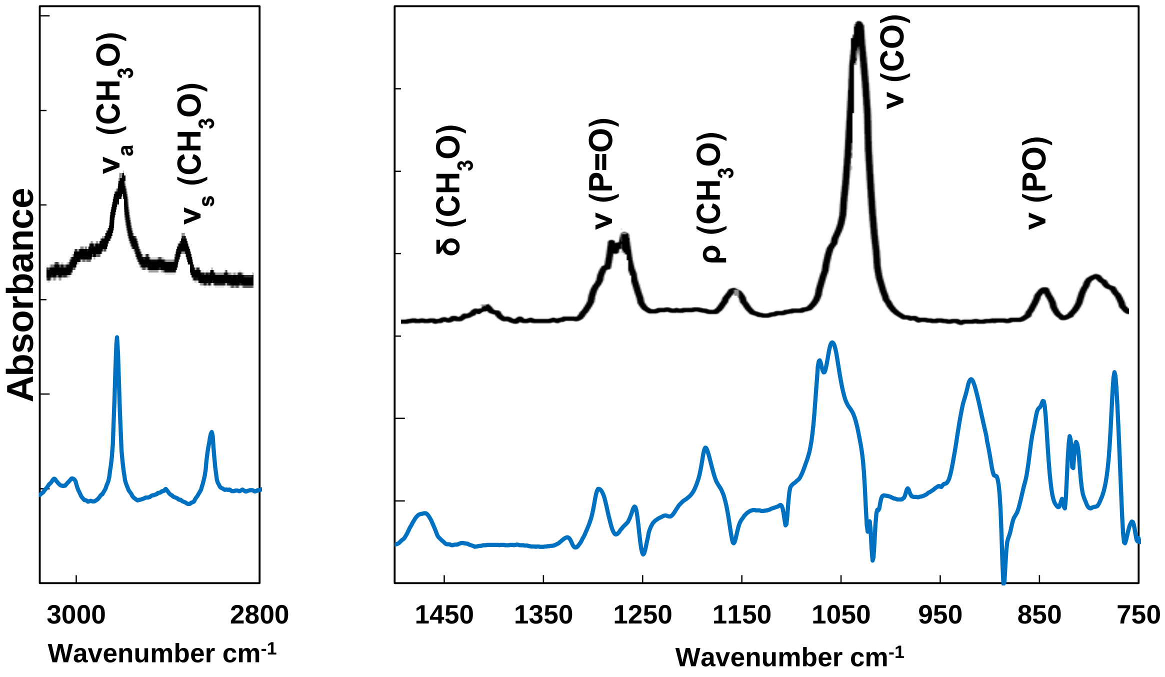

Figure 4.16 Gas phase DMCP (black) and difference spectra of DMMP adsorbed onto UiO-66 (blue) at high wavenumber region (left) and low wavenumber region (right).

4.8 Uptake and Reactions of DMCP within MOF-808

As previously mentioned, DMMP reversibly binds the UiO-66 through the formation of hydrogen bonds while chemisorbs to the MOFs with larger pore sizes (UiO-67 and MOF-808). Therefore, the experiments of exposing MOF-808 to DMCP was performed under the same conditions to compare the reactivity of DMMP and DMCP.

My results demonstrate that the larger pore structure provides reactants with access to sites where chemistry and irreversible binding occur. Chemisorption of DMCP into MOF-808 is revealed in the IR spectra shown in Figure 4.17. The spectrum shown in black in Figure 4.17 is that of the pristine MOF-808 sample. As for UiO-66, many of the bands for this spectrum have been previously assigned (Table 4.1). Upon exposure to a controlled flux of gas-phase DMCP (2×10^4 L), several new bands develop in the infrared spectra, while key features in the OH region, assigned to molecular water and free hydroxyl groups, diminish in intensity. However, the bands assigned to linker and node vibrational motions within the MOF remain largely unaffected (see the spectrum shown in blue in Figure 4.17). Several of the new bands are nearly identical in wavenumber to those assigned to physisorbed DMCP (see the above discussion associated with UiO-66); however, many previously unobserved bands appear in the post-exposure IR spectra for MOF-808, suggesting unique bond breaking or formation may have accompanied DMCP uptake. Following the room temperature DMMP exposure, the MOF was heated in an effort to drive the physisorbed molecules from the framework, as was done for the UiO-66 sample. I found that the majority of the new bands for the DMCP-exposed MOF-808 sample that could not be assigned to physisorbed DMCP persisted throughout the thermal annealing procedure even when the sample was maintained at 600 K for 60 min (see Figure 4.17, red). Based on the results acquired from DMMP experiments and calculations and the IR spectra shown in Figure 4.17, I think that MOF-808 reacts irreversibly with the simulant DMCP to produce a significant concentration of node-bound methyl phosphonochloridic acid (MPCA).

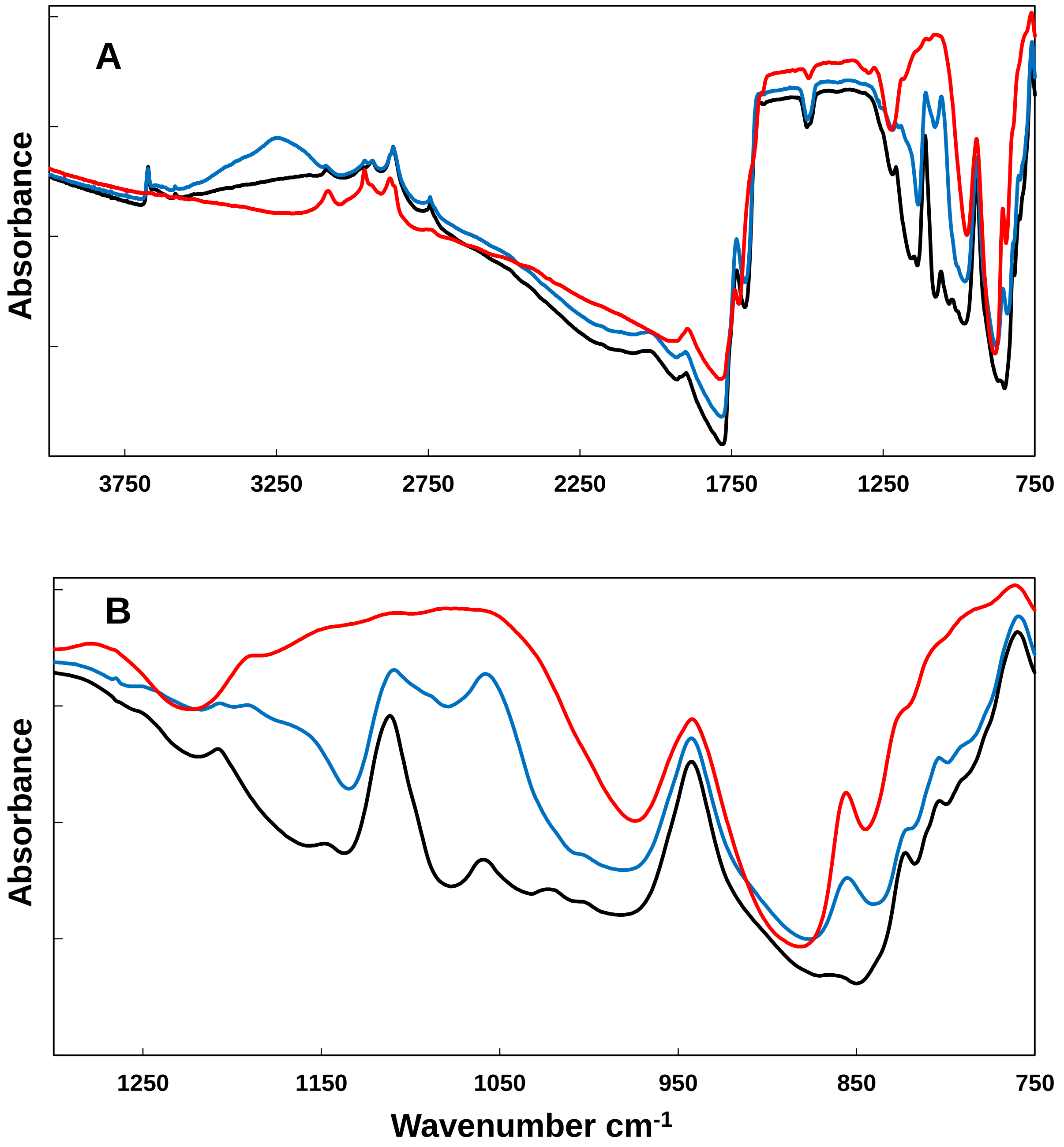

Figure 4.17 IR spectra for the entire mid-IR region (A) and the "fingerprint" region (B) of MOF-808 before DMCP exposure (black), after DMCP exposure (blue), and after post-exposure thermal treatment to 600 K (red).

Upon exposure to DMCP, the free hydroxyl groups diminish in intensity while new bands emerge. The new bands are very similar to those described above for DMMP exposure to MOF-

808. The detailed difference spectra for MOF-808 upon exposure to DMMP and DMCP are presented in Figure 4.18. The spectra in Figure 4.18 is recorded with the original MOFs employed as the background such that the primary features in the spectra can be assigned to the MOF-bound reaction products. As the comparison indicates, the adsorbates are strongly bound (i.e., they do not desorb from the MOF even after heating to 600 K) and exhibit similar vibrational spectra for both nerve agent simulants.

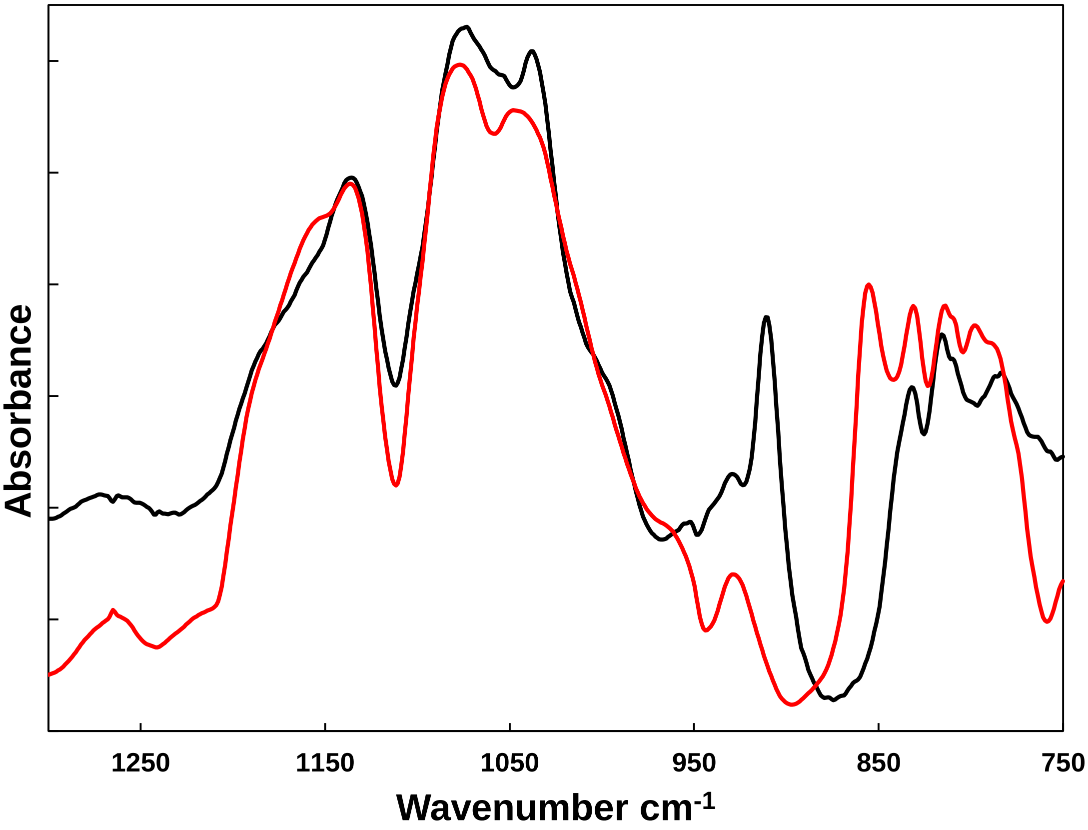

Figure 4.18 Difference IR spectra of MOF-808 upon DMMP (black) and DMCP (red) exposure then thermal treatment to 600 K for 60 minutes.

As previously discussed, upon DMMP exposure, the most likely MOF-bound product is methyl methylphosphonic acid (MMPA), which may bind to the nodes in its deprotonated form following the hydrolysis of DMMP. Based on Figure 4.18, it is reasonable to make the hypothesis that the product formed upon DMCP exposure has a similar structure to MMPA, in this case, methyl phosphonochloridic acid (A in Figure 4.19) or methyl methylphosphonic acid (B in Figure 4.19), depending on the reaction pathway. Based on the theoretical electronic structure calculation of the stationary points presented above for DMMP-SBU reactions, the decomposition reaction of DMCP on Zr_6 MOFs are hypothesized to follow a similar pathway, as shown in Figure 4.19. The peak assignment will be similar to the ones mentioned in the DMMP-UiO-67 calculations in section 4.2.

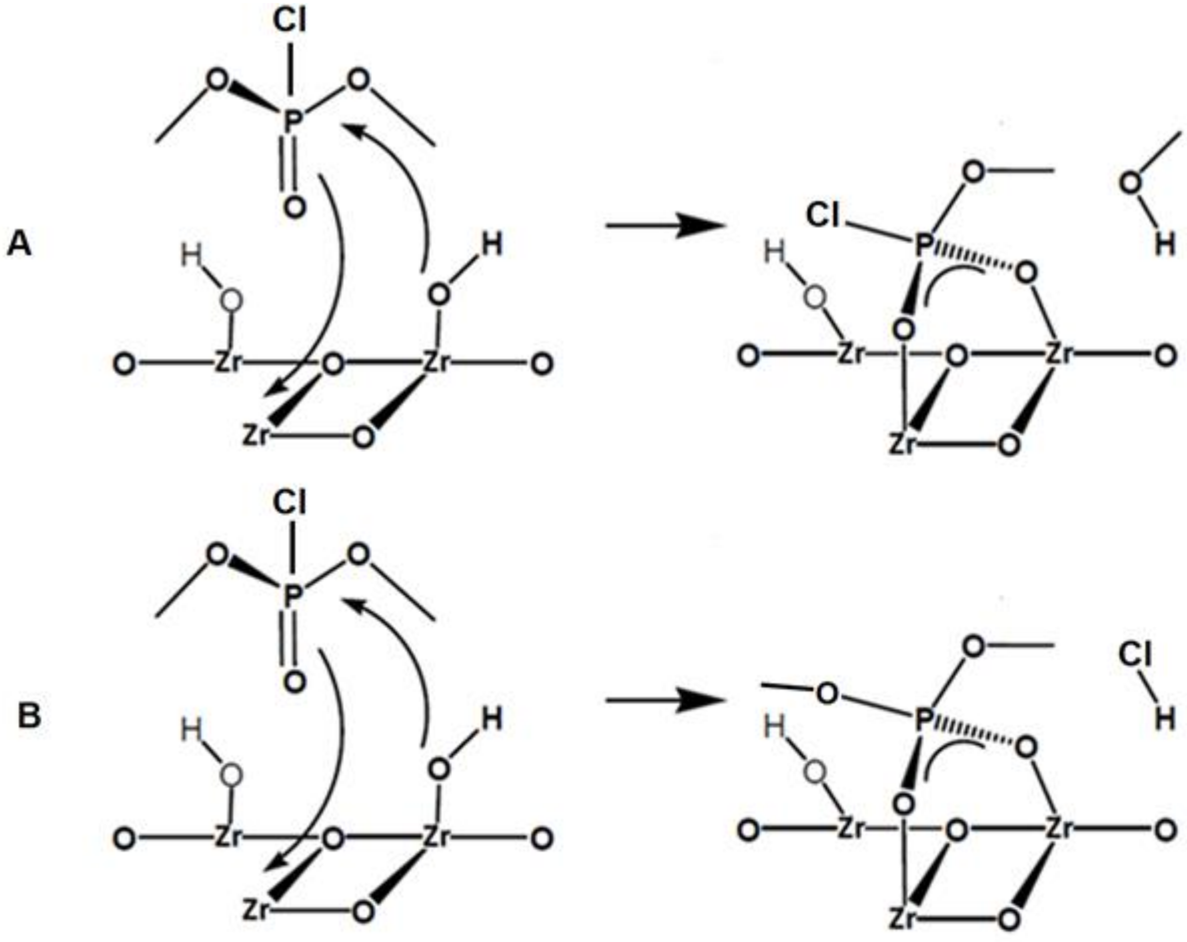

Figure 4.19 Hypothesized reaction pathway for DMCP decomposition on Zr_6 MOFs

Chapter 5 Summary and Conclusions

5.1 Summary of Results

The objectives of the research described in this thesis were to develop a fundamental understanding of gas-surface interactions to help to predict the fate of atmospheric interactions, as well as the investigation of potential catalysts for chemical warfare destruction. This knowledge is important for the control of environmental contaminants, and the development of new materials for the protection of personnel from nerve agents in potential chemical warfare attacks.

Initial studies were focused on investigating the dynamics of small hydrocarbons scattered from organic surfaces. All experiments were conducted in an ultra-high vacuum chamber to maintain clean surfaces as well as generate the well-controlled incident gas source. The time of flight distribution of the scattered gas molecules after interacting with the surfaces was then recorded by the quadrupole mass spectrometer. Then a final energy distribution was derived from the time of flight distribution, to illustrate how much energy was transferred to the surface from the gas molecules during the collisions.

The results show that upon gas-surface collisions, the energy transfer was affected by both the properties of the gas molecules and surfaces. Compared with the methyl-terminated self-assembled monolayer (CH_3-SAM), the hydroxyl-terminated self-assembled monolayer (OH-SAM) is more rigid due to the formation of the intra-monolayer hydrogen bonds. The surface hydrogen bonding “network” limits the low-energy vibrational modes, which are considered as possible ways to dissipate the excess translational energy of the incident gas molecules. As a result, the energy transfer is less efficient on an OH-SAM. The electronic structures of ethane

(C_2H_6), ethene (C_2H_4), and ethyne (C_2H_2) also appear to play a role in affecting the energy transfer process. The π electrons in the double bond of C_2H_4 and the triple bond of C_2H_2 may act as hydrogen bond acceptors when interacts with the OH-SAM, and therefore, facilitate the energy transfer. In my previous study of diatomic gas molecules' interactions with organic surfaces, a positive correlation between thermal desorption (TD) fractions in gas-surface scattering and solubility for analogous solute-solvent combinations was observed. The similar trend does persist in small hydrocarbon interactions with a CH_3-SAM (TD fractions: C_2H_6 > C_2H_4 > C_2H_2), but not an OH-SAM (C_2H_6 > C_2H_2 > C_2H_4). The energy transfers between C_2H_6, C_2H_4, and C_2H_2 and the CH_3-SAM appear to be affected by factors such as degrees of freedom and molecular size, while the electronic structure is also decisive regarding their interactions with the OH-SAM.

Then the experiments were furthered and focused on the investigation of decomposing nerve agents on metal organic frameworks (MOF). This research was also conducted in an ultra-high vacuum chamber. Nerve agent simulants were used to mimic the physical or chemical properties of the "live" agents, but with significantly lower toxicity. The interactions between dimethyl methylphosphonate (DMMP), dimethyl chlorophosphate (DMCP), and three Zr_6-based MOFs have been explored at a fundamental level through *in situ* infrared spectroscopy, X-ray photoelectron spectroscopy, and DFT calculations.

The interactions between DMMP and DMCP with UiO-66 appear to be weak and reversible. The infrared spectra show evidence for hydrogen bonding between free hydroxyl groups on the nodes and the simulants, with the sp^2 oxygen atom of DMMP and DMCP serving as the primary electron donor; however, the interactions are likely limited to the surface of crystallites rather than within the pore structure of the MOF. In contrast, UiO-67 and MOF-808, both with significantly larger pore apertures or channels, are both capable of sequestering DMMP through reversible physisorption and irreversible chemisorption processes. [100, 104, 132] Evidence was also provided for irreversible chemisorption of DMCP on MOF-808. The rates for both chemisorption and physisorption were found to be very similar upon DMMP exposure, suggesting that the reaction rates for the chemisorption pathway are limited only by the rate of diffusion throughout the MOFs. Calculations suggest that the reaction mechanism consists of nucleophilic attack to the phosphorous atom in the node-bound DMMP by an adjacent Zr-OH group, which ultimately leads to the formation of methyl methylphosphonic acid (MMPA) and methanol or a Zr-bound methoxy. MMPA is strongly bound to the MOF and appears to partially decompose to methyl phosphonic acid (MPA) upon heating. By comparing the difference IR spectra of MOF-808 upon DMMP and DMCP exposure then thermal treatment, the similar features in the IR bands observed in the spectra indicate similar MOF-bound products, methyl phosphonochloridic acid (MPCA) and MMPA were formed upon DMCP following similar reaction pathways.

5.2 **Future Studies**

To further understand the dynamics of small hydrocarbons scattering from organic surfaces, potential energy surfaces (PES) for small hydrocarbons approaching the hydroxyl groups of an OH-SAM, and the methyl groups of a CH_3-SAM may be calculated. My experimental results show that the gas-surface energy transfer between small hydrocarbon molecule and organic surfaces are controlled by a combination of several factors such as degrees of freedom, size, and attractive intermolecular forces. Therefore, to draw a more convincing conclusion, theoretical work would play a very important role in facilitating the interpretation of the experimental results.

The work on the adsorption and decomposition of chemical warfare agent (CWA) with MOFs presented here was an important component of a multi-university collaboration program that is the first research program in fundamental surface science geared entirely toward developing a comprehensive understanding of the reaction mechanisms and kinetics of chemical warfare agents within MOFs.

The results and discussion presented here provide a fundamental framework and experimental benchmarks for future work aimed at elucidating the dynamics of CWA reactions within MOFs. Infrared band assignments and signatures of reactions will aid other work in this area. Importantly, I have shown that open pore structures and the presence of defects are key requirements for building Zr_6-based MOFs that may react with organophosphonate-based CWAs. Finally, the tight binding of the MMPA reaction product at the nodes of open Zr_6-based MOFs may inhibit further chemistry and render these MOFs ineffective as gas-phase catalysts for CWA hydrolysis.

Chapter 6 References

1. Lee, D. Y.; Kautz, N. A.; Kandel, S. A., Reactivity of Gas-Phase Radicals with Organic Surfaces. *The Journal of Physical Chemistry Letters* **2013,** *4* (23), 4103-4112.

2. Moe, K.; Moe, M. M.; Levin, D. A.; Wysong, I. J.; Garcia, A. L. In *Gas-surface interactions in low-Earth orbit,* AIP Conference Proceedings-American Institute of Physics, 2011; p 1313.

3. Ghosh, L.; Kinoshita, H.; Ohmae, N., Degradation on a mechanical property of high-modulus aramid fiber due to hyperthermal atomic oxygen beam exposures. *Composites science and technology* **2007,** *67* (7), 1611-1616.

4. Buczala, D. M.; Brunsvold, A. L.; Minton, T. K., Erosion of Kapton H® by Hyperthermal Atomic Oxygen. *Journal of spacecraft and rockets* **2006,** *43* (2), 421-425.

5. Grossman, E.; Gouzman, I., Space environment effects on polymers in low earth orbit. Nuclear Instruments and Methods in Physics Research Section B: Beam Interactions with Materials and Atoms **2003,** 208, 48-57.

6. Moe, K.; Moe, M. M., Gas–surface interactions and satellite drag coefficients. *Planetary and Space Science* **2005,** *53* (8), 793-801.

7. Minton, T. K.; Garton, D. J., Dynamics of atomic-oxygen-induced polymer degradation in low earth orbit. *Chemical dynamics in extreme environments* **2001,** *11*, 420-489.

8. Murad, E., Spacecraft interaction with atmospheric species in low earth orbit. *Journal of spacecraft and rockets* **1996,** *33* (1), 131-136.

9. Caledonia, G. E.; Krech, R. H.; Green, B. D., A high flux source of energetic oxygen atoms for material degradation studies. *AIAA journal* **1987,** *25* (1), 59-63.

10. Moe, M. M.; Moe, K., The roles of kinetic theory and gas-surface interactions in measurements of upper-atmospheric density. *Planetary and Space Science* **1969,** *17* (5), 917-922.

11. Mhadeshwar, A.; Aghalayam, P.; Papavassiliou, V.; Vlachos, D., Surface reaction mechanism development for platinum-catalyzed oxidation of methane. *Proceedings of the Combustion Institute* **2002,** *29* (1), 997-1004.

12. Veser, G.; Ziauddin, M.; Schmidt, L. D., Ignition in alkane oxidation on noble-metal catalysts. *Catalysis Today* **1999,** *47* (1), 219-228.

13. Veser, G.; Schmidt, L. D., Ignition and extinction in the catalytic oxidation of hydrocarbons over platinum. *AIChE Journal* **1996,** *42* (4), 1077-1087.

14. Vlachos, D., Homogeneous-heterogeneous oxidation reactions over platinum and inert surfaces. *Chemical Engineering Science* **1996,** *51* (10), 2429-2438.

15. Kühnle, A.; Linderoth, T. R.; Besenbacher, F., Self-assembly of monodispersed, chiral nanoclusters of cysteine on the Au (110)-(1× 2) surface. *Journal of the American Chemical Society* **2003,** *125* (48), 14680-14681.

16. Bain, C. D.; Troughton, E. B.; Tao, Y. T.; Evall, J.; Whitesides, G. M.; Nuzzo, R. G., Formation of monolayer films by the spontaneous assembly of organic thiols from solution onto gold. *Journal of the American Chemical Society* **1989,** *111* (1), 321-335.

17. Cygan, M.; Dunbar, T.; Arnold, J.; Bumm, L.; Shedlock, N.; Burgin, T.; Jones, L.; Allara, D.; Tour, J.; Weiss, P., Insertion, conductivity, and structures of conjugated organic oligomers in self-assembled alkanethiol monolayers on Au {111}. *Journal of the American Chemical Society* **1998,** *120* (12), 2721-2732.

18. Nathanson, G. M.; Davidovits, P.; Worsnop, D. R.; Kolb, C. E., Dynamics and kinetics at the gas-liquid interface. *The Journal of Physical Chemistry* **1996,** *100* (31), 13007-13020.

19. Davidovits, P.; Kolb, C. E.; Williams, L. R.; Jayne, J. T.; Worsnop, D. R., Mass accommodation and chemical reactions at gas-liquid interfaces. *Chemical reviews* **2006,** *106* (4), 1323-1354.

20. Alexander, W. A.; Day, B. S.; Moore, H. J.; Lee, T. R.; Morris, J. R.; Troya, D., Experimental and theoretical studies of the effect of mass on the dynamics of gas/organic-surface energy transfer. *The Journal of chemical physics* **2008,** *128* (1), 014713.

21. Alexander, W. A.; Zhang, J.; Murray, V. J.; Nathanson, G. M.; Minton, T. K., Kinematics and dynamics of atomic-beam scattering on liquid and self-assembled monolayer surfaces. *Faraday discussions* **2012,** *157*, 355-374.

22. Bosio, S. B.; Hase, W. L., Energy transfer in rare gas collisions with self-assembled monolayers. *The Journal of chemical physics* **1997,** *107* (22), 9677-9686.

23. Darling, S.; Rosenbaum, A.; Sibener, S., Surface vibrations of a highly ordered low-density alkanethiol monolayer measured using inelastic helium atom scattering. *Surface science* **2001,** *478* (1), L313-L319.

24. Day, B. S.; Morris, J. R., Packing density and structure effects on energy-transfer dynamics in argon collisions with organic monolayers. *The Journal of chemical physics* **2005,** *122* (23), 234714.

25. Day, B. S.; Morris, J. R.; Alexander, W. A.; Troya, D., Theoretical study of the effect of surface density on the dynamics of Ar+ alkanethiolate self-assembled monolayer collisions. *The Journal of Physical Chemistry A* **2006,** *110* (4), 1319-1326.

26. Day, B. S.; Shuler, S. F.; Ducre, A.; Morris, J. R., The dynamics of gas-surface energy exchange in collisions of Ar atoms with ω-functionalized self-assembled monolayers. *The Journal of chemical physics* **2003,** *119* (15), 8084-8096.

27. Fiegland, L. R.; McCorn Saint Fleur, M.; Morris, J. R., Reactions of C C-terminated self-assembled monolayers with gas-phase ozone. *Langmuir* **2005,** *21* (7), 2660-2661.

28. Garton, D. J.; Minton, T. K.; Alagia, M.; Balucani, N.; Casavecchia, P.; Volpi, G. G., Comparative dynamics of Cl (2P) and O (3P) interactions with a hydrocarbon surface. *The Journal of Chemical Physics* **2000,** *112* (13), 5975-5984.

29. Gibson, K.; Isa, N.; Sibener, S., Experiments and simulations of Ar scattering from an ordered 1-decanethiol–Au (111) monolayer. *The Journal of chemical physics* **2003,** *119* (24), 13083-13095.

30. Gibson, K.; Isa, N.; Sibener, S., Experiments and simulations of hyperthermal Xe interacting with an ordered 1-decanethiol/Au (111) monolayer: Penetration followed by high-energy, directed ejection. *The Journal of Physical Chemistry A* **2006,** *110* (4), 1469-1477.

31. Li, G.; Bosio, S.; Hase, W., A QM/MM model for O (< sup> 3</sup> P) reaction with an alkyl thiolate self-assembled monolayer. *Journal of Molecular Structure* **2000,** *556* (1), 43-57.

32. Lu, J. W.; Day, B. S.; Fiegland, L. R.; Davis, E. D.; Alexander, W. A.; Troya, D.; Morris, J. R., Interfacial energy exchange and reaction dynamics in collisions of gases on model organic surfaces. *Progress in Surface Science* **2012,** *87* (9), 221-252.

33. Minton, T. K.; Zhang, J.; Garton, D. J.; Seale, J. W., Collision-assisted erosion of hydrocarbon polymers in atomic-oxygen environments. *High Performance Polymers* **2000,** *12* (1), 27-42.

34. Tasic, U.; Day, B. S.; Yan, T.; Morris, J. R.; Hase, W. L., Chemical dynamics study of intrasurface hydrogen-bonding effects in gas-surface energy exchange and accommodation. *The Journal of Physical Chemistry C* **2008,** *112* (2), 476-490.

35. Tasic, U. S.; Yan, T.; Hase, W. L., Dynamics of energy transfer in collisions of O (3P) atoms with a 1-decanethiol self-assembled monolayer surface. *The Journal of Physical Chemistry B* **2006,** *110* (24), 11863-11877.

36. Troya, D., Dynamics of collisions of hydroxyl radicals with fluorinated self-assembled monolayers. *Theoretical Chemistry Accounts* **2012,** *131* (1), 1-12.

37. Troya, D.; Schatz, G. C., Theoretical studies of hyperthermal O (3P) collisions with hydrocarbon self-assembled monolayers. *The Journal of chemical physics* **2004,** *120* (16), 7696-7707.

38. Troya*, D.; Schatz†, G. C., Hyperthermal chemistry in the gas phase and on surfaces: theoretical studies. *International Reviews in Physical Chemistry* **2004,** *23* (3), 341-373.

39. Waring, C.; Bagot, P. A.; Bebbington, M. W.; Raisanen, M. T.; Buck, M.; Costen, M. L.; McKendrick, K. G., How penetrable are thioalkyl self-assembled monolayers? *The Journal of Physical Chemistry Letters* **2010,** *1* (13), 1917-1921.

40. Waring, C.; Bagot, P. A.; Räisänen, M. T.; Costen, M. L.; McKendrick, K. G., Dynamics of the Reaction of O (3P) Atoms with Alkylthiol Self-assembled Monolayers†. *The Journal of Physical Chemistry A* **2009,** *113* (16), 4320-4329.

41. Yan, T.; Hase, W. L., Origin of the Boltzmann translational energy distribution in the scattering of hyperthermal Ne atoms off a self-assembled monolayer. *Physical Chemistry Chemical Physics* **2000,** *2* (4), 901-910.

42. Yan, T.; Hase, W. L., Comparisons of models for simulating energy transfer in Ne-atom collisions with an alkyl thiolate self-assembled monolayer. *The Journal of Physical Chemistry B* **2002,** *106* (33), 8029-8037.

43. Yan, T.; Isa, N.; Gibson, K.; Sibener, S.; Hase, W. L., Role of Surface Intramolecular Dynamics in the Efficiency of Energy Transfer in Ne Atom Collisions with an-Hexylthiolate Self-Assembled Monolayer. *The Journal of Physical Chemistry A* **2003,** *107* (49), 10600-10607.

44. Yuan, H.; Gibson, K.; Li, W.; Sibener, S., Modification of Alkanethiolate Monolayers by O (3P) Atomic Oxygen: Effect of Chain Length and Surface Temperature. *The Journal of Physical Chemistry B* **2012,** *117* (16), 4381-4389.

45. Day, B. S. The Dynamics of Gas-Surface Energy Transfer in Collisions of Rare Gases with Organic Thin Films. Virginia Polytechnic Institute and State University, 2005.

46. Lu, J. W.; Morris, J. R., Gas–Surface Scattering Dynamics of CO2, NO2, and O3 in Collisions with Model Organic Surfaces. *The Journal of Physical Chemistry A* **2011,** *115* (23), 6194-6201.

47. Alexander, W. A.; Day, B. S.; Moore, H. J.; Lee, T. R.; Morris, J. R.; Troya, D., Experimental and theoretical studies of the effect of mass on the dynamics of gas/organic-surface energy transfer. *The Journal of chemical physics* **2008,** *128*, 014713.

48. Saecker, M. E.; Nathanson, G. M., Collisions of protic and aprotic gases with hydrogen bonding and hydrocarbon liquids. *The Journal of chemical physics* **1993,** *99*, 7056.

49. Abo Riziq, A.; Trainic, M.; Erlick, C.; Segre, E.; Rudich, Y., Extinction efficiencies of coated absorbing aerosols measured by cavity ring down aerosol spectrometry. *Atmospheric Chemistry and Physics* **2008,** *8* (6), 1823-1833.

50. Reisen, F.; Arey, J., Atmospheric reactions influence seasonal PAH and nitro-PAH concentrations in the Los Angeles basin. *Environmental science & technology* **2005,** *39* (1), 64-73.

51. Goodman, F. O., *Dynamics of gas-surface scattering*. Elsevier: 2012.

52. Grimmelmann, E. K.; Tully, J. C.; Cardillo, M. J., Hard-cube model analysis of gas-surface energy accommodation. *The Journal of Chemical Physics* **2008,** *72* (2), 1039-1043.

53. Logan, R. M.; Keck, J. C., Classical theory for the interaction of gas atoms with solid surfaces. *The Journal of Chemical Physics* **2003,** *49* (2), 860-876.

54. Logan, R. M.; Stickney, R. E., SIMPLE CLASSICAL MODEL FOR SCATTERING OF GAS ATOMS FROM A SOLID SURFACE. *Journal of Chemical Physics* **1966,** *44* (1), 195-&.

55. Kalberer, M.; Morrical, B.; Sax, M.; Zenobi, R., Picogram quantitation of polycyclic aromatic hydrocarbons adsorbed on aerosol particles by two-step laser mass spectrometry. *Analytical chemistry* **2002,** *74* (14), 3492-3497.

56. Nathanson, G. M., Molecular beam studies of gas-liquid interfaces. *Annu. Rev. Phys. Chem.* **2004,** *55*, 231-255.

57. King, M. E.; Fiehrer, K. M.; Nathanson, G. M.; Minton, T. K., Effects of thermal roughening on the angular distributions of trapping and scattering in gas-liquid collisions. *The Journal of Physical Chemistry A* **1997,** *101* (36), 6556-6561.

58. Tully, J. C., Washboard model of gas–surface scattering. *The Journal of chemical physics* **1990,** *92* (1), 680-686.

59. Yan, T.; Hase, W. L.; Tully, J. C., A washboard with moment of inertia model of gas-surface scattering. *The Journal of chemical physics* **2003,** *120* (2), 1031-1043.

60. Logan, R. M.; Stickney, R., Simple classical model for the scattering of gas atoms from a solid surface. *The Journal of Chemical Physics* **1966,** *44* (1), 195-201.

61. Kondo, T.; Kato, H.; Yamada, T.; Yamamoto, S.; Kawai, M., Effect of the molecular structure on the gas-surface scattering studied by supersonic molecular beam. *The European Physical Journal D-Atomic, Molecular, Optical and Plasma Physics* **2006,** *38* (1), 129-138.

62. LeFèvre, R. J. W., Dipole moments, their measurement and application in chemistry. **1953**.

63. Atkins, P.; De Paula, J., *Atkins' physical chemistry*. Oxford University Press: 2014.

64. London, F., The general theory of molecular forces. *Transactions of the Faraday Society* **1937,** *33*, 8b-26.

65. Gough, K., Theoretical analysis of molecular polarizabilities and polarizability derivatives in hydrocarbons. *The Journal of chemical physics* **1989,** *91* (4), 2424-2432.

66. Protocol for the Prohibition of the Use in War of Asphyxiating, Poisonous or Other Gases, and of Bacteriological Methods of Warfare (Geneva Protocol). United Nations: Geneva, 1925.

67. Erickson, R. J., Protocol I: A Merging of the Hague and Geneva Law of Armed Conflict. *Va. J. Int'l L.* **1978,** *19*, 557-594.

68. Yingling, R. T.; Ginnane, R. W., The Geneva Conventions of 1949. *The American Journal of International Law* **1952,** *46* (3), 393-427.

69. Yang, Y. C.; Baker, J. A.; Ward, J. R., Decontamination of Chemical Warfare Agents. *Chemical Reviews* **1992,** *92* (8), 1729-1743.

70. Stone, H.; See, D.; Smiley, A.; Ellingson, A.; Schimmoeller, J.; Oudejans, L., Surface Decontamination for Blister Agents Lewisite, Sulfur Mustard and Agent Yellow, a Lewisite and Sulfur Mustard Mixture. *J. Hazard. Mater.* **2016,** *314*, 59-66.

71. Seto, Y., Decontamination of Chemical and Biological Warfare Agents. *Yakugaku Zasshi-J. Pharm. Soc. Jpn.* **2009,** *129* (1), 53-69.

72. Prasad, G. K.; Ramacharyulu, P.; Singh, B., Nanomaterials Based Decontaminants Against Chemical Warfare Agents. *J. Sci. Ind. Res.* **2011,** *70* (2), 91-104.

73. Raber, E.; McGuire, R., Oxidative Decontamination of Chemical and Biological Warfare Agents Using L-Gel. *J. Hazard. Mater.* **2002,** *93* (3), 339-352.

74. Wagner, G. W., Decontamination of Chemical Warfare Agents Using Household Chemicals. *Ind. Eng. Chem. Res.* **2011,** *50* (21), 12285-12287.

75. Talmage, S. S.; Watson, A. P.; Hauschild, V.; Munro, N. B.; King, J., Chemical Warfare Agent Degradation and Decontamination. *Curr. Org. Chem.* **2007,** *11* (3), 285-298.

76. Moon, S. Y.; Proussaloglou, E.; Peterson, G. W.; DeCoste, J. B.; Hall, M. G.; Howarth, A. J.; Hupp, J. T.; Farha, O. K., Detoxification of Chemical Warfare Agents Using a Zr-6-Based Metal-Organic Framework/Polymer Mixture. *Chem.-Eur. J.* **2016,** *22* (42), 14864-14868.

77. Mondloch, J. E.; Katz, M. J.; Isley, W. C.; Ghosh, P.; Liao, P. L.; Bury, W.; Wagner, G.; Hall, M. G.; DeCoste, J. B.; Peterson, G. W.; Snurr, R. Q.; Cramer, C. J.; Hupp, J. T.; Farha, O. K., Destruction of Chemical Warfare Agents Using Metal-Organic Frameworks. *Nat. Mater.* **2015,** *14* (5), 512-516.

78. Moon, S. Y.; Wagner, G. W.; Mondloch, J. E.; Peterson, G. W.; DeCoste, J. B.; Hupp, J. T.; Farha, O. K., Effective, Facile, and Selective Hydrolysis of the Chemical Warfare Agent VX Using Zr-6-Based Metal-Organic Frameworks. *Inorg. Chem.* **2015,** *54* (22), 10829-10833.

79. Li, P.; Klet, R. C.; Moon, S. Y.; Wang, T. C.; Deria, P.; Peters, A. W.; Klahr, B. M.; Park, H. J.; Al-Juaid, S. S.; Hupp, J. T.; Farha, O. K., Synthesis of Nanocrystals of Zr-Based Metal-Organic Frameworks with csq-net: Significant Enhancement in the Degradation of a Nerve Agent Simulant. *Chem. Commun.* **2015,** *51* (54), 10925-10928.

80. Katz, M. J.; Mondloch, J. E.; Totten, R. K.; Park, J. K.; Nguyen, S. T.; Farha, O. K.; Hupp, J. T., Simple and Compelling Biomimetic Metal-Organic Framework Catalyst for the Degradation of Nerve Agent Simulants. *Angew. Chem.-Int. Edit.* **2014,** *53* (2), 497-501.

81. Kanan, S. M.; Tripp, C. P., An Infrared Study of Adsorbed Organophosphonates on Silica: A Prefiltering Strategy for the Detection of Nerve Agents on Metal Oxide Sensors. *Langmuir* **2001,** *17* (7), 2213-2218.

82. Plonka, A. M.; Wang, Q.; Gordon, W. O.; Balboa, A.; Troya, D.; Guo, W. W.; Sharp, C. H.; Senanayake, S. D.; Morris, J. R.; Hill, C. L.; Frenkel, A. I., In Situ Probes of Capture and Decomposition of Chemical Warfare Agent Simulants by Zr-Based Metal Organic Frameworks. *Journal of the American Chemical Society* **2017,** *139* (2), 599-602.

83. Tucker, J. B., War of nerves: chemical warfare from World War I to Al-Qaeda. Anchor: 2007.

84. Kim, K.; Tsay, O. G.; Atwood, D. A.; Churchill, D. G., Destruction and Detection of Chemical Warfare Agents. *Chemical Reviews* **2011,** *111* (9), 5345-5403.

85. Delfino, R. T.; Ribeiro, T. S.; Figueroa-Villar, J. D., Organophosphorus Compounds as Chemical Warfare Agents: a Review. *J. Braz. Chem. Soc.* **2009,** *20* (3), 407-428.

86. Wilmsmeyer, A. R. Ultrahigh Vacuum Studies of the Fundamental Interactions of Chemical Warfare Agents and
Their Simulants with Amorphous Silica. Virginia Tech, 2012.

87. Lu, J. W.; Alexander, W. A.; Morris, J. R., Gas–surface energy exchange and thermal accommodation of CO2 and Ar in collisions with methyl, hydroxyl, and perfluorinated self-assembled monolayers. *Physical Chemistry Chemical Physics* **2010,** *12* (39), 12533-12543.

88. Ceyer, S. T.; Gladstone, D. J.; McGonigal, M.; Schulberg, M. T., Molecular beams: probes of the dynamics of reactions on surfaces. *Investigations of Surfaces and Interfaces-Part A* **1993**, 383-452.

89. Buchanan, J. H.; Sumpter, K. B.; Abercrombie, P. L.; Tevault, D. E. *Vapor pressure of GB*; EDGEWOOD CHEMICAL BIOLOGICAL CENTER ABERDEEN PROVING GROUND MD RESEARCH AND TECHNOLOGY DIR: 2009.

90. Lohr, J. R.; Day, B. S.; Morris, J. R., Scattering, accommodation, and trapping of HCl in collisions with a hydroxylated self-assembled monolayer. *The Journal of Physical Chemistry B* **2005,** *109* (32), 15469-15475.

91. Isa, N.; Gibson, K.; Yan, T.; Hase, W.; Sibener, S., Experimental and simulation study of neon collision dynamics with a 1-decanethiol monolayer. *The Journal of chemical physics* **2004,** *120*, 2417.

92. Siu, E. Y.; Andino, J. M., Vapor Pressure of Organophosphorus Nerve Agent Simulant Compounds (vol 54, pg 1876, 2009). *J. Chem. Eng. Data* **2011,** *56* (9), 3713-3713.

93. Li, H.; Eddaoudi, M.; O'Keeffe, M.; Yaghi, O. M., Design and Synthesis of an Exceptionally Stable and Highly Porous Metal-Organic Framework. *Nature* **1999,** *402* (6759), 276-279.

94. Furukawa, H.; Ko, N.; Go, Y. B.; Aratani, N.; Choi, S. B.; Choi, E.; Yazaydin, A. O.; Snurr, R. Q.; O'Keeffe, M.; Kim, J.; Yaghi, O. M., Ultrahigh Porosity in Metal-Organic Frameworks. *Science* **2010,** *329* (5990), 424-428.

95. Eddaoudi, M.; Moler, D. B.; Li, H. L.; Chen, B. L.; Reineke, T. M.; O'Keeffe, M.; Yaghi, O. M., Modular Chemistry: Secondary Building Units As a Basis for the Design of Highly Porous and Robust Metal-Organic Carboxylate Frameworks. *Accounts Chem. Res.* **2001,** *34* (4), 319-330.

96. Lee, J.; Farha, O. K.; Roberts, J.; Scheidt, K. A.; Nguyen, S. T.; Hupp, J. T., Metal-Organic Framework Materials as Catalysts. *Chem. Soc. Rev.* **2009,** *38* (5), 1450-1459.

97. Grissom, T. G.; Sharp, C. H.; Usov, P. M.; Troya, D.; Morris, A. J.; Morris, J. R., Benzene, Toluene, and Xylene Transport through UiO-66: Diffusion Rates, Energetics, and the Role of Hydrogen Bonding. *The Journal of Physical Chemistry C* **2018,** *122* (28), 16060-16069.

98. Valenzano, L.; Civalleri, B.; Chavan, S.; Bordiga, S.; Nilsen, M. H.; Jakobsen, S.; Lillerud, K. P.; Lamberti, C., Disclosing the Complex Structure of UiO-66 Metal Organic Framework: A Synergic Combination of Experiment and Theory. *Chem. Mat.* **2011,** *23* (7), 1700-1718.

99. Wu, H.; Yildirim, T.; Zhou, W., Exceptional Mechanical Stability of Highly Porous Zirconium Metal-Organic Framework UiO-66 and Its Important Implications. *J. Phys. Chem. Lett.* **2013,** *4* (6), 925-930.

100. Katz, M. J.; Brown, Z. J.; Colon, Y. J.; Siu, P. W.; Scheidt, K. A.; Snurr, R. Q.; Hupp, J. T.; Farha, O. K., A Facile Synthesis of UiO-66, UiO-67 and Their Derivatives. *Chem. Commun.* **2013,** *49* (82), 9449-9451.

101. Trickett, C. A.; Gagnon, K. J.; Lee, S.; Gandara, F.; Burgi, H. B.; Yaghi, O. M., Definitive Molecular Level Characterization of Defects in UiO-66 Crystals. *Angew. Chem.-Int. Edit.* **2015,** *54* (38), 11162-11167.

102. Ling, S. L.; Slater, B., Dynamic Acidity in Defective UiO-66. *Chem. Sci.* **2016,** *7* (7), 4706-4712.

103. Wang, G.; Sharp, C.; Plonka, A. M.; Wang, Q.; Frenkel, A. I.; Guo, W.; Hill, C.; Smith, C.; Kollar, J.; Troya, D.; Morris, J. R., Mechanism and Kinetics for Reaction of the Chemical Warfare Agent Simulant, DMMP(g), with Zirconium(IV) MOFs: An Ultrahigh-Vacuum and DFT Study. *J. Phys. Chem. C* **2017,** *121* (21), 11261-11272.

104. Moon, S. Y.; Liu, Y. Y.; Hupp, J. T.; Farha, O. K., Instantaneous Hydrolysis of Nerve-Agent Simulants with a Six-Connected Zirconium-Based Metal-Organic Framework. *Angew. Chem.-Int. Edit.* **2015,** *54* (23), 6795-6799.

105. Li, Z. Q.; Yang, J. C.; Sui, K. W.; Yin, N., Facile Synthesis of Metal-Organic Framework MOF-808 for Arsenic Removal. *Mater. Lett.* **2015,** *160*, 412-414.

106. Liang, W. B.; Chevreau, H.; Ragon, F.; Southon, P. D.; Peterson, V. K.; D'Alessandro, D. M., Tuning Pore Size in a Zirconium-Tricarboxylate Metal-Organic Framework. *Crystengcomm* **2014,** *16* (29), 6530-6533.

107. Day, B. S.; Shuler, S. F.; Ducre, A.; Morris, J. R., The dynamics of gas-surface energy exchange in collisions of Ar atoms with ω-functionalized self-assembled monolayers. *The Journal of chemical physics* **2003,** *119*, 8084.

108. Saecker, M. E.; Nathanson, G. M., Collisions of protic and aprotic gases with a perfluorinated liquid. *The Journal of chemical physics* **1994,** *100*, 3999.

109. Moore, J. H.; Davis, C. C.; Coplan, M. A., Building Scientific Apparatus. *American Journal of Physics* **1984,** *52* (7), 669-670.

110. Vattuone, L.; Bracco, G.; Smerieri, M.; Savio, L.; Rocca, M., Supersonic Molecular Beams Studies of Surfaces. In *Dynamics of Gas-Surface Interactions*, Springer: 2013; pp 1-23.

111. Sherman, F. S., The transition from continuum to molecular flow. *Annual Review of Fluid Mechanics* **1969,** *1* (1), 317-340.

112. Auerbach, D. J. C., G.; Poelsema, B.; Asscher, M.; Somorjai, G., *Atomic and Molecular Beam Methods*. Oxford University: New York, 1998.

113. Love, J. C.; Estroff, L. A.; Kriebel, J. K.; Nuzzo, R. G.; Whitesides, G. M., Self-assembled monolayers of thiolates on metals as a form of nanotechnology. *Chemical reviews* **2005,** *105* (4), 1103-1170.

114. Cohen, S. R.; Naaman, R.; Sagiv, J., TRANSLATIONAL ENERGY-TRANSFER FROM MOLECULES AND ATOMS TO ADSORBED ORGANIC MONOLAYERS OF LONG-CHAIN AMPHIPHILES. *Phys. Rev. Lett.* **1987,** *58* (12), 1208-1211.

115. Pan, S.; Castner, D. G.; Ratner, B. D., Multitechnique surface characterization of derivatization efficiencies for hydroxyl-terminated self-assembled monolayers. *Langmuir* **1998,** *14* (13), 3545-3550.

116. Greenler, R. G., Infrared study of adsorbed molecules on metal surfaces by reflection techniques. *The Journal of Chemical Physics* **1966,** *44* (1), 310-315.

117. Nuzzo, R. G.; Dubois, L. H.; Allara, D. L., Fundamental studies of microscopic wetting on organic surfaces. 1. Formation and structural characterization of a self-consistent series of polyfunctional organic monolayers. *Journal of the American Chemical Society* **1990,** *112* (2), 558-569.

118. Day, B. S.; Morris, J. R., Even-odd orientation and chain-length effects in the energy exchange of argon collisions with self-assembled monolayers. *The Journal of Physical Chemistry B* **2003,** *107* (29), 7120-7125.

119. Lu, J. W.; Fiegland, L. R.; Davis, E. D.; Alexander, W. A.; Wagner, A.; Gandour, R. D.; Morris, J. R., Initial Reaction Probability and Dynamics of Ozone Collisions with a Vinyl-Terminated Self-Assembled Monolayer. *The Journal of Physical Chemistry C* **2011,** *115* (51), 25343-25350.

120. Bosio, S. B.; Hase, W. L., Energy transfer in rare gas collisions with self-assembled monolayers. *The Journal of chemical physics* **1997,** *107,* 9677.

121. Auerbach, D., Atomic and molecular beam methods. *by G. Scoles, Oxford Univ. Press, New York* **1988,** *1*, 362.

122. Zhang, Y. F.; Chapleski, R. C.; Lu, J. W.; Rockhold, T. H.; Troya, D.; Morris, J. R., Gas-surface reactions of nitrate radicals with vinyl-terminated self-assembled monolayers. *Physical Chemistry Chemical Physics* **2014,** *16* (31), 16659-16670.

123. Wilmsmeyer, A. R.; Uzarski, J.; Barrie, P. J.; Morris, J. R., Interactions and Binding Energies of Dimethyl Methylphosphonate and Dimethyl Chlorophosphate with Amorphous Silica. *Langmuir* **2012,** *28* (30), 10962-10967.

124. Wilmsmeyer, A. R.; Gordon, W. O.; Davis, E. D.; Troya, D.; Mantooth, B. A.; Lalain, T. A.; Morris, J. R., Infrared Spectra and Binding Energies of Chemical Warfare Nerve Agent Simulants on the Surface of Amorphous Silica. *J. Phys. Chem. C* **2013,** *117* (30), 15685-15697.

125. Abelard, J.; Wilmsmeyer, A. R.; Edwards, A. C.; Gordon, W. O.; Durke, E. M.; Karwacki, C. J.; Troya, D.; Morris, J. R., Adsorption of Substituted Benzene Derivatives on Silica: Effects of Electron Withdrawing and Donating Groups. *J. Phys. Chem. C* **2016,** *120* (24), 13024-13031.

126. Abelard, J.; Wilmsmeyer, A. R.; Edwards, A. C.; Gordon, W. O.; Durke, E. M.; Karwacki, C. J.; Troya, D.; Morris, J. R., Adsorption of 2-Chloroethyl Ethyl Sulfide on Silica: Binding Mechanism and Energy of a Bifunctional Hydrogen-Bond Acceptor at the Gas Surface Interface. *J. Phys. Chem. C* **2015,** *119* (1), 365-372.

127. Yates Jr, J. T., Experimental innovations in surface science. *Springer, New York* **1998,** *27*, 181-0013.

128. Toby, B. H.; Von Dreele, R. B., GSAS-II: the genesis of a modern open-source all purpose crystallography software package. *Journal of Applied Crystallography* **2013,** *46* (2), 544-549.

129. Petříček, V.; Dušek, M.; Palatinus, L., Crystallographic computing system JANA2006: general features. *Zeitschrift für Kristallographie-Crystalline Materials* **2014,** *229* (5), 345-352.

130. Øien, S.; Wragg, D.; Reinsch, H.; Svelle, S.; Bordiga, S.; Lamberti, C.; Lillerud, K. P., Detailed Structure Analysis of Atomic Positions and Defects in Zirconium Metal–Organic Frameworks. *Crystal Growth & Design* **2014,** *14* (11), 5370-5372.

131. Ko, N.; Hong, J.; Sung, S.; Cordova, K. E.; Park, H. J.; Yang, J. K.; Kim, J., A significant enhancement of water vapour uptake at low pressure by amine-functionalization of UiO-67. *Dalton Transactions* **2015,** *44* (5), 2047-2051.

132. Furukawa, H.; Gandara, F.; Zhang, Y. B.; Jiang, J. C.; Queen, W. L.; Hudson, M. R.; Yaghi, O. M., Water Adsorption in Porous Metal-Organic Frameworks and Related Materials. *Journal of the American Chemical Society* **2014,** *136* (11), 4369-4381.

133. Chapleski, R. C.; Zhang, Y.; Troya, D.; Morris, J. R., Heterogeneous chemistry and reaction dynamics of the atmospheric oxidants, O 3, NO 3, and OH, on organic surfaces. *Chem. Soc. Rev.* **2016,** *45* (13), 3731-3746.

134. Scharlin, P.; Battino, R.; Silla, E.; Tunon, I.; Pascual-Ahuir, J., Solubility of gases in water: correlation between solubility and the number of water molecules in the first solvation shell. *Pure and applied chemistry* **1998,** *70* (10), 1895-1904.

135. Koelliker, R.; Thies, H., Solubility of carbon monoxide in n-hexane between 293 and 473 K and carbon monoxide pressures up to 200 bar. *J. Chem. Eng. Data* **1993,** *38* (3), 437-440.

136. Mizerovskii, L.; Smirnova, K., Solubility of noble gases and nitrogen in n-alkanes at 298.15 K and atmospheric pressure. Correlation analysis. *Russian Chemical Bulletin* **2009,** *58* (8), 1547-1561.

137. Shaw, A. W.; Vosper, A. J., Solubility of nitric oxide in aqueous and nonaqueous solvents. *Journal of the Chemical Society, Faraday Transactions 1: Physical Chemistry in Condensed Phases* **1977,** *73*, 1239-1244.

138. Dias, A. M.; Bonifacio, R. P.; Marrucho, I. M.; Pádua, A. A.; Gomes, M. C., Solubility of oxygen in n-hexane and in n-perfluorohexane. Experimental determination and prediction by molecular simulation. *Physical Chemistry Chemical Physics* **2003,** *5* (3), 543-549.

139. Bennett, M. E.; Alexander, W. A.; Lu, J. W.; Troya, D.; Morris, J. R., Collisions of polar and nonpolar gases with hydrogen bonding and hydrocarbon self-assembled monolayers. *The Journal of Physical Chemistry C* **2008,** *112* (44), 17272-17280.

140. Scoles, G., *Atomic and molecular beam methods*. Oxford university press: 1988.

141. Lohr, J. R.; Day, B. S.; Morris, J. R., Scattering, accommodation, and trapping of HCl in collisions with a hydroxylated self-assembled monolayer. *J. Phys. Chem. B* **2005,** *109* (32), 15469-15475.

142. Reichardt, C.; Welton, T., *Solvents and solvent effects in organic chemistry*. John Wiley & Sons: 2011.

143. Del Bene, J. E., Molecular orbital theory of the hydrogen bond. PI electrons as proton acceptors. *Chemical Physics Letters* **1974,** *24* (2), 203-207.

144. Shuler, S. F.; Davis, G. M.; Morris, J. R., Energy transfer in rare gas collisions with hydroxyl-and methyl-terminated self-assembled monolayers. *Journal of Chemical Physics* **2002,** *116* (21), 9147-9150.

145. Cohen, S. R.; Naaman, R.; Sagiv, J., Translational energy transfer from molecules and atoms to adsorbed organic monolayers of long-chain amphiphiles. *Phys. Rev. Lett.* **1987,** *58* (12), 1208.

146. Paz, Y.; Naaman, R., Energy distribution in aniline scattered from various low energy surfaces. *The Journal of chemical physics* **1991,** *94* (7), 4921-4927.

147. Alexander, W. A.; Morris, J. R.; Troya, D., Experimental and theoretical study of CO collisions with CH3- and CF3-terminated self-assembled monolayers. *The Journal of Chemical Physics* **2009,** *130* (8), 084702.

148. Cliffe, M. J.; Wan, W.; Zou, X. D.; Chater, P. A.; Kleppe, A. K.; Tucker, M. G.; Wilhelm, H.; Funnell, N. P.; Coudert, F. X.; Goodwin, A. L., Correlated Defect Nanoregions in a Metal-Organic Framework. *Nat. Commun.* **2014,** *5*, 8.

149. Nishida, J.; Tamimi, A.; Fei, H. H.; Pullen, S.; Ott, S.; Cohen, S. M.; Fayer, M. D., Structural Dynamics Inside a Functionalized Metal-Organic Framework Probed by Ultrafast 2D IR Spectroscopy. *Proc. Natl. Acad. Sci. U. S. A.* **2014,** *111* (52), 18442-18447.

150. DeCoste, J. B.; Peterson, G. W.; Jasuja, H.; Glover, T. G.; Huang, Y. G.; Walton, K. S., Stability and Degradation Mechanisms of Metal-Organic Frameworks Containing the Zr6O4(OH)(4) Secondary Building Unit. *J. Mater. Chem. A* **2013,** *1* (18), 5642-5650.

151. Bensitel, M.; Moravek, V.; Lamotte, J.; Saur, O.; Lavalley, J. C., Infrared Study of Alcohols Adsorption on Zirconium Oxide: Reactivity of Alkoxy Species Towards CO2. *Spectroc. Acta Pt. A-Molec. Biomolec. Spectr.* **1987,** *43* (12), 1487-1491.

152. Cavka, J. H.; Jakobsen, S.; Olsbye, U.; Guillou, N.; Lamberti, C.; Bordiga, S.; Lillerud, K. P., A New Zirconium Inorganic Building Brick Forming Metal Organic Frameworks with Exceptional Stability. *Journal of the American Chemical Society* **2008,** *130* (42), 13850-13851.

153. Chavan, S.; Vitillo, J. G.; Gianolio, D.; Zavorotynska, O.; Civalleri, B.; Jakobsen, S.; Nilsen, M. H.; Valenzano, L.; Lamberti, C.; Lillerud, K. P.; Bordiga, S., H-2 Storage in Isostructural UiO-67 and UiO-66 MOFs. *Physical Chemistry Chemical Physics* **2012,** *14* (5), 1614-1626.

154. Sharma, A.; Kaur, S.; Mahajan, C. G.; Tripathi, S. K.; Saini, G. S. S., Fourier Transform Infrared Spectral Study of N,N '-Dimethylformamide-Water-Rhodamine 6G Mixture. *Mol. Phys.* **2007,** *105* (1), 117-123.

155. Yamamoto, H.; Yano, H.; Kouchi, H.; Obora, Y.; Arakawa, R.; Kawasaki, H., N,N-Dimethylformamide-Stabilized Gold Nanoclusters As a Catalyst for the Reduction of 4-Nitrophenol. *Nanoscale* **2012,** *4* (14), 4148-4154.

156. Deep, A.; Jain, S.; Sharma, P. C.; Verma, P.; Kumar, M.; Dora, C. P., Design and Biological Evaluation of Biphenyl-4-Carboxylic Acid Hydrazide-Hydrazone for Antimicrobial Activity. *Acta Pol. Pharm.* **2010,** *67* (3), 255-259.

157. Tellez, C. A.; Hollauer, E.; Mondragon, M. A.; Castano, V. M., Fourier Transform Infrared and Raman Spectra, Vibrational Assignment and Ab Initio Calculations of Terephthalic Acid and Related Compounds. *Spectroc. Acta Pt. A-Molec. Biomolec. Spectr.* **2001,** *57* (5), 993-1007.

158. Lee, M. W.; Kim, M. S.; Kim, K., Infrared and Raman Spectroscopic Study of Terephthalic Acid Adsorbed on Silver Surfaces. *Journal of Molecular Structure* **1997,** *415* (1-2), 93-100.

159. Zerbi, G.; Sandroni, S., Fundamental Frequencies and Molecular Configuration of Biphenyl—II Normal Coordinates. *Spectrochimica Acta Part a-Molecular Spectroscopy* **1968,** *A 24* (5), 511-&.

160. Kaliszewski, M. S.; Heuer, A. H., Alcohol Interaction with Zirconia Powders. *J. Am. Ceram. Soc.* **1990,** *73* (6), 1504-1509.

161. Bensitel, M.; Saur, O.; Lavalley, J. C.; Mabilon, G., Acidity of Zirconium Oxide and Sulfated ZrO2 Samples. *Mater. Chem. Phys.* **1987,** *17* (3), 249-258.

162. Hertl, W., Surface Chemistry of Zirconia Polymorphs. *Langmuir* **1989,** *5* (1), 96-100.

163. Yamaguchi, T.; Nakano, Y.; Tanabe, K., Infrared Study of Surface Hydroxyl Groups on Zirconium Oxide. *Bulletin of the Chemical Society of Japan* **1978,** *51* (9), 2482-2487.

164. Dang, Z.; Anderson, B. G.; Amenomiya, Y.; Morrow, B. A., Silica-Supported Zirconia. 1. Characterization by Infrared Spectroscopy, Temperature-Programmed Desorption, and X-ray Diffraction. *J. Phys. Chem.* **1995,** *99* (39), 14437-14443.

165. Gordon, W. O.; Tissue, B. M.; Morris, J. R., Adsorption and Decomposition of Dimethyl Methylphosphonate on Y2O3 Nanoparticles. *J. Phys. Chem. C* **2007,** *111* (8), 3233-3240.

166. Troya, D., Reaction Mechanism of Nerve-Agent Decomposition with Zr-Based Metal Organic Frameworks. *J. Phys. Chem. C.* **2016**.

167. Chapleski, R. C.; Musaev, D. G.; Hill, C. L.; Troya, D., Reaction Mechanism of Nerve-Agent Hydrolysis with the Cs8Nb6O19 Lindqvist Hexaniobate Catalyst. *J. Phys. Chem. C* **2016,** *120* (30), 16822-16830.

168. Kuiper, A. E. T.; Vanbokhoven, J.; Medema, J., The Role of Heterogeneity in the Kinetics of a Surface Reaction: I. Infrared Characterization of the Adsorption Structures of Organophosphonates and Their Decomposition. *J. Catal.* **1976,** *43* (1-3), 154-167.

169. Fu, Y. Y.; Yang, C. X.; Yan, X. P., Incorporation of Metal-Organic Framework UiO-66 into Porous Polymer Monoliths to Enhance the Liquid Chromatographic Separation of Small Molecules. *Chem. Commun.* **2013,** *49* (64), 7162-7164.

170. Head, A. R.; Tsyshevsky, R.; Trotochaud, L.; Eichhorn, B.; Kuklja, M. M.; Bluhm, H., Electron Spectroscopy and Computational Studies of Dimethyl Methylphosphonate. *J. Phys. Chem. A* **2016,** *120* (12), 1985-1991.

171. Templeton, M. K.; Weinberg, W. H., Adsorption and Decomposition of Dimethyl Methylphosphonate on an Aluminum Oxide Surface. *Journal of the American Chemical Society* **1985,** *107* (1), 97-108.

172. Templeton, M. K.; Weinberg, W. H., Decomposition of Phosphonate Esters Adsorbed on Aluminum-Oxide *Journal of the American Chemical Society* **1985,** *107* (4), 774-779.

173. Kim, C. S.; Lad, R. J.; Tripp, C. P., Interaction of Organophosphorous Compounds with TiO2 and WO3 Surfaces Probed by Vibrational Spectroscopy. *Sens. Actuator B-Chem.* **2001,** *76* (1-3), 442-448.

174. Mitchell, M. B.; Sheinker, V. N.; Mintz, E. A., Adsorption and Decomposition of Dimethyl Methylphosphonate on Metal Oxides. *J. Phys. Chem. B* **1997,** *101* (51), 11192-11203.

175. Aurianblajeni, B.; Boucher, M. M., Interaction of Dimethyl Methylphosphonate with Metal Oxides. *Langmuir* **1989,** *5* (1), 170-174.

176. Chen, D. A.; Ratliff, J. S.; Hu, X. F.; Gordon, W. O.; Senanayake, S. D.; Mullins, D. R., Dimethyl Methylphosphonate Decomposition on Fully Oxidized and Partially Reduced Ceria Thin Films. *Surface Science* **2010,** *604* (5-6), 574-587.

177. Zhao, Y.; Truhlar, D. G., A new local density functional for main-group thermochemistry, transition metal bonding, thermochemical kinetics, and noncovalent interactions. *Journal of Chemical Physics* **2006,** *125* (19), 194101.

178. Frisch, M. J.; Trucks, G. W.; Schlegel, H. B.; Scuseria, G. E.; Robb, M. A.; Cheeseman, J. R.; Scalmani, G.; Barone, V.; Mennucci, B.; Petersson, G. A.; Nakatsuji, H.; Caricato, M.; Li, X.; Hratchian, H. P.; Izmaylov, A. F.; Bloino, J.; Zheng, G.; Sonnenberg, J. L.; Hada, M.; Ehara, M.; Toyota, K.; Fukuda, R.; Hasegawa, J.; Ishida, M.; Nakajima, T.; Honda, Y.; Kitao, O.; Nakai, H.; Vreven, T.; Montgomery Jr., J. A.; Peralta, J. E.; Ogliaro, F. ß.; Bearpark, M. J.; Heyd, J.; Brothers, E. N.; Kudin, K. N.; Staroverov, V. N.; Kobayashi, R.; Normand, J.; Raghavachari, K.; Rendell, A. P.; Burant, J. C.; Iyengar, S. S.; Tomasi, J.; Cossi, M.; Rega, N.; Millam, N. J.; Klene, M.; Knox, J. E.; Cross, J. B.; Bakken, V.; Adamo, C.; Jaramillo, J.; Gomperts, R.; Stratmann, R. E.; Yazyev, O.; Austin, A. J.; Cammi, R.; Pomelli, C.; Ochterski, J. W.; Martin, R. L.; Morokuma, K.; Zakrzewski, V. G.; Voth, G. A.; Salvador, P.; Dannenberg, J. J.; Dapprich, S.; Daniels, A. D.; Farkas, ñ. n.; Foresman, J. B.; Ortiz, J. V.; Cioslowski, J.; Fox, D. J. *Gaussian 09,* Revision E.01; Gaussian, Inc.: Wallingford, CT, 2009.

179. Bermudez, V. M., Quantum-Chemical Study of the Adsorption of DMMP and Sarin on Gamma-Al2O3. *J. Phys. Chem. C* **2007,** *111* (9), 3719-3728.

180. Bermudez, V. M., Computational Study of Environmental Effects in the Adsorption of DMMP, Sarin, and VX on gamma-Al2O3: Photolysis and Surface Hydroxylation. *J. Phys. Chem. C* **2009,** *113* (5), 1917-1930.

181. Bermudez, V. M., Ab Initio Study of the Interaction of Dimethyl Methylphosphonate with Rutile (110) and Anatase (101) TiO2 Surfaces. *J. Phys. Chem. C* **2010,** *114* (7), 3063-3074.

182. Bermudez, V. M., Computational Study of the Adsorption of Dimethyl Methylphosphonate (DMMP) on the (010) Surface of Anatase TiO2 with and without Faceting. *Surface Science* **2010,** *604* (7-8), 706-712.